Non-intuitive Design of Compliant Mechanisms Possessing Optimized Flexure Hinges

Von der Fakultät für Maschinenbau der
Helmut-Schmidt-Universität/ Universität der Bundeswehr Hamburg
zur Erlangung des akademischen Grades eines Doktor-Ingenieurs
genehmigte

DISSERTATION

vorgelegt von

Dipl.-Ing. Frank Dirksen, M.Sc.

aus Meißen

Hamburg, 2013

Referent:
Professor Dr.-Ing. Rolf Lammering
Helmut-Schmidt-Universität/
Universität der Bundeswehr Hamburg

Korreferent:
Professor Dr.-Ing. Wolfgang Seemann
Karlsruhe Institute of Technology

Tag der mündlichen Prüfung: 20. Dezember 2013

Non-intuitive Design of Compliant Mechanisms Possessing Optimized Flexure Hinges

DOCTORAL THESIS

approved by the Department of Mechanical Engineering of the
Helmut-Schmidt-University/ University of the Federal Armed Forces
Hamburg for obtaining the academic degree of
Doktor-Ingenieur (Dr.-Ing.)
presented by

Dipl.-Ing. Frank Dirksen, M.Sc.

from Meißen, Germany

Hamburg, 2013

Committee in charge:
Professor Dr.-Ing. Rolf Lammering (chair)
Helmut-Schmidt-University/
University of the Federal Armed Forces Hamburg, Germany

Professor Dr.-Ing. Wolfgang Seemann
Karlsruhe Institute of Technology, Germany

Day of completion of the oral examination: December 20, 2013

Abstract

As a part of the priority programme "Small machine tools for small work pieces" initiated by the German Research Foundation, this dissertation focuses on the synthesis of compliant mechanisms. It addresses two major challenges: first, the difficult, non-intuitive design process and, second, the hardly-predictable influence of incorporated flexure hinges.

In order to address the first challenge, a staggered topology optimization algorithm, that includes a nonlinear finite element analysis, optimality criteria method and globally convergent method of moving asymptotes, is developed. This algorithm is tested on different common load cases resulting in different topologies corresponding to the boundary conditions and motion specifications. As one key result of the topology optimization process, the designed compliant mechanisms with its hinge positions and deflections are obtained yielding the desired motion specifications.

In order to address the second challenge, analytical expressions are derived and tested providing explicit relations between the hinge geometry and the mechanical properties, such as precision, deflection range and fatigue life under static and dynamic loading conditions and meeting the desired performance specifications resulting from the topology synthesis or application purpose. These relations can be applied in both directions, i.e. the mechanical properties can be determined directly from the geometry, and an optimal geometry can be found meeting certain mechanical performance criteria including the highly desirable prediction on the fatigue life.

Finally, the appropriate flexure hinges are incorporated in the optimized topology yielding a prototype of a compliant gripping device.

Kurzfassung

Die vorliegende Dissertation befasst sich mit der Entwicklung von nachgiebigen Mechanismen im Rahmen des DFG-geförderten Schwerpunktprogrammes "Kleine Werkzeugmaschinen für kleine Werkstücke". Gegenstand dieser Arbeit sind dabei vor allem die derzeit größten Herausforderungen: Erstens, die Entwicklung von nachgiebigen Mechanismen unter Anwendung systematischer, nicht-intuitiver Verfahren, sowie zweitens, das Verhalten von unterschiedlich geformten Festkörpergelenken.

Zunächst wird ein gestaffelter Topologieoptimierungsalgorithmus entwickelt, programmiert und auf unterschiedliche Lastfälle angewendet. Der Algorithmus besteht aus einer nicht-linearen finiten Elemente Berechnung sowie zweier Optimierungsalgorithmen, die einerseits auf gradientenbasierte und anderseits auf approximationsbasierte Verfahren[1] zurückgreifen. Dadurch werden Topologien nachgiebiger Mechanismen mit bekannten Gelenkpositionen und -verformungen, welche die kinematischen Zielvorgaben ermöglichen, systematisch und erfolgreich generiert.

Anschließend werden analytische Gleichungen hergeleitet, die die relevanten, mechanischen Eigenschaften von elastischen Festkörpergelenken, wie Präzision, maximale (elastische) Durchbiegung sowie Materialermüdung abhängig von der Gelenkgeometrie explizit beschreiben. Darauf aufbauend wird eine Vorgehensweise zur Lebensdauervorhersage und zur Geometrieoptimierung von langlebigen Festkörpergelenken entwickelt.

Abschließend werden der entwickelte Topologieroptimierungsalgorithmus und die hergeleiteten Gleichungen angewendet, um einen Prototypen eines nachgiebigen Greifmechanismus systematisch herzustellen.

[1] Optimality Criteria Method, Globally Convergent Method of Moving Asymptotes

Acknowledgements

To Professor Rolf Lammering for encouraging and supporting me during my time at the Helmut-Schmidt-University/ University of the Federal Armed Forces Hamburg (HSU) and throughout the entire research project. Numerous ideas have been developed together and countless hints have found their way into this thesis.

To Professor Wolfgang Seemann for supporting me, particularly, at the final stage of the graduation process. The outcome of interesting conversations at the Karlsruhe Institute of Technology (KIT) and many helpful suggestions on the draft version of the dissertation have been very beneficial.

To Professor Tarek I. Zohdi for advising and guiding me during my research semesters at the University of California at Berkeley (UCB) and beyond. In particular, the discussions about different numerical aspects and the prompt support during the preparation of this thesis and several research publications have been very helpful.

To my friends, colleagues and students at the HSU and UCB for having many valuable discussions on interesting (research) topics and providing a very pleasant working atmosphere.

To the German Academic Exchange Service for supporting my work with an individual post-graduate research grant (DAAD-D/10/46834).

To my family for the help and forbearance.

Contents

1 Introduction

1.1 Motivation

Nowadays, most machine tools and mechanisms are designed and engineered as multi-body systems. The desired motion is gained from the relative motion of several parts that are connected by conventional pin-joints. These systems are easy to design due to the kinematically-decoupled structures and motions and, thus, the common choice for design engineers, so far. However, these conventional mechanisms may reach their precision limits in small scale applications as explained shortly.

Therefore, the German Research Foundation has initiated a six years priority programme "Small machine tools for small work pieces" (DFG SPP 1476) that bridges the gap between established large scale applications and more recent micro- and nanoscale applications. As one part of a research project within the priority programme, this thesis focuses on fundamental issues and aims to provide pioneering work.

1.2 Why Compliant mechanisms?

In order to design machine tools for small scale applications, compliant mechanisms (CM) have become more popular in the last years competing against multi-body systems. In contrast to conventional multi-body systems, CM gain their motion from the *elastic deformation* of certain parts called flexure hinges (FH). Fig. 1.1 shows two medical gripping devices in comparison based on a multi-body system connected by a standard

Figure 1.1: Medical gripping devices in comparison based on multi-body system connected by a standard pin-joint hinge (left) and based on a monolithic compliant mechanism (right) from [1]

pin-joint hinge (left) and based on a monolithic CM (right).

CM have several advantages compared to their multi-body-based counterparts. Table 1.1 lists the most significant advantages and drawbacks in terms of performance, costs and the design process. In terms of performance, CM are: frictionless due to the absence of slipping parts. Noiseless due to the small number of parts and the absence of slipping parts. Cleaner due to the absence of any lubricants making them highly suitable for applications that stipulate a clean environment, such as minimal invasive medical devices. More precise due to the absence of an un-

Table 1.1: Comparison between conventional multi-body systems and CM in terms of performance and costs in small scale applications

	Multi-body systems	Compliant mechanism
Friction	−	+ +
Noise	∘	+ +
Cleanliness	−	+ +
Precision	−	+ +
Performance	**−**	**+**
Number of parts	− −	+ +
Manufacturing costs	−	+
Maintenance costs	−	+
Costs	**−**	**+**
Simplicity to design	+	− −
Influence of hinges	+ +	∘
Design process	**+**	**−**

predictable and deviating bearing play. In terms of costs, CM are: potentially cheaper caused by the small number of parts due to the monolithic structure. Less expensive in manufacturing, assembling and maintenance due to small number of parts and the typically planar structure.

Thus, particularly in small scale applications, CM may provide better performance while being less expensive due to the aforementioned benefits.

However, there are two major disadvantages: first, designing CM is more difficult and non-intuitive, due to its inherent complex overall deformation. Second, the influence of flexure hinges in terms of motion performance and fatigue effects is still hardly-predictable. These drawbacks make CM not yet fully suitable to more complex applications. Particularly, any long-lasting employments are still uncertain since there exist no fatigue predictions regarding the key elements of CM: flexure hinges.

In a fairly recent review paper [2], it is pointed out that

"...there are too little of previous results on analysis of fatigue failure in the compliant mechanisms",

and the conclusion is drawn that

"In future, there should be the analysis of fatigue failure to prevent premature failure in the [compliant] device",

which immediately motivates the following thesis' objectives.

1.3 Thesis' objectives and outline

The main objective of this work is to address the two mentioned challenges: the difficult design process of CM and the hardly-predictable influence of the FH geometry on its performance, particularly in long-lasting applications.

- In order to address the first challenge, an algorithm will be developed to design the topology of CM in a non-intuitive and systematic manner. This topology optimization algorithm will be tested on different common load cases resulting in different topologies, i.e. different CM corresponding to the boundary conditions and motion specifications.

- Then, the second challenge will be addressed: the size and shape of the FH will be designed carefully to provide desired mechanical properties, such as precision, deflection range, fatigue life, etc. under static and dynamic loading conditions and to meet performance specifications resulting from topology synthesis or application purpose. For this purpose, analytical expressions on FH will be derived and tested providing explicit relations between the hinge geometry and the resulting mechanical properties. These relations should be applicable in both directions, i.e. the mechanical properties need

to be determined directly from the geometry, and an optimal geometry needs to be found meeting certain mechanical performance criteria including the highly desirable prediction on the fatigue life.

The thesis is outlined as follows: In Chapter 2, the current state of the art of relevant topology optimization techniques, FH and CM is summarized. In Chapter 3, the own topology optimization algorithm is described, numerically implemented and tested within a MATLAB environment. In Chapter 4, the relevant expressions on the static and dynamic, mechanical properties of flexure hinges are derived, summarized and tested. In Chapter 5, the topology optimization process and the gained knowledge on FH are applied to a final example, where a rapid-prototyped CM with incorporated FH is developed. Finally, in Chapter 6, a conclusion is drawn, the main achievements are pointed out and an outlook on future prospects is given.

Further details on the presented topology optimization and flexure hinges are given in the Appendix A.

2 State of the art

In contrast to the sequential design of most engineering structures, the synthesis of CM is more ambitious since the topology of the entire mechanism needs to be designed simultaneously. A brief description of present structural optimization techniques, i.e. optimization of size, shape and topology, as illustrated in Fig. 2.1, that focusses on CM is given in Sect. 2.1. These techniques result in the CM's overall skeleton providing the positions of FH meeting the kinematical specifications but not an optimal shape of these FH. For this purpose, relevant research on FH is reviewed in Sect. 2.2.

2.1 Current state of topology optimization techniques

Many current CM have been created by engineers' intuition and experience without using any systematic techniques. Usually, numerous trial and error iterations are necessary to obtain a final CM that meets the desired performance specification. Since this intuitive design process is time-consuming and results in working – but usually non-optimal – solutions, a variety of systematic design and optimization techniques have been proposed by several research groups from different backgrounds in the last two decades. In order to provide a systematic literature review, a rough subdivision into general approaches, design domains, optimization techniques and solution algorithms is beneficial, as illustrated in Fig. 2.2. A general review on structural optimization from a product development standpoint can be found in [4].

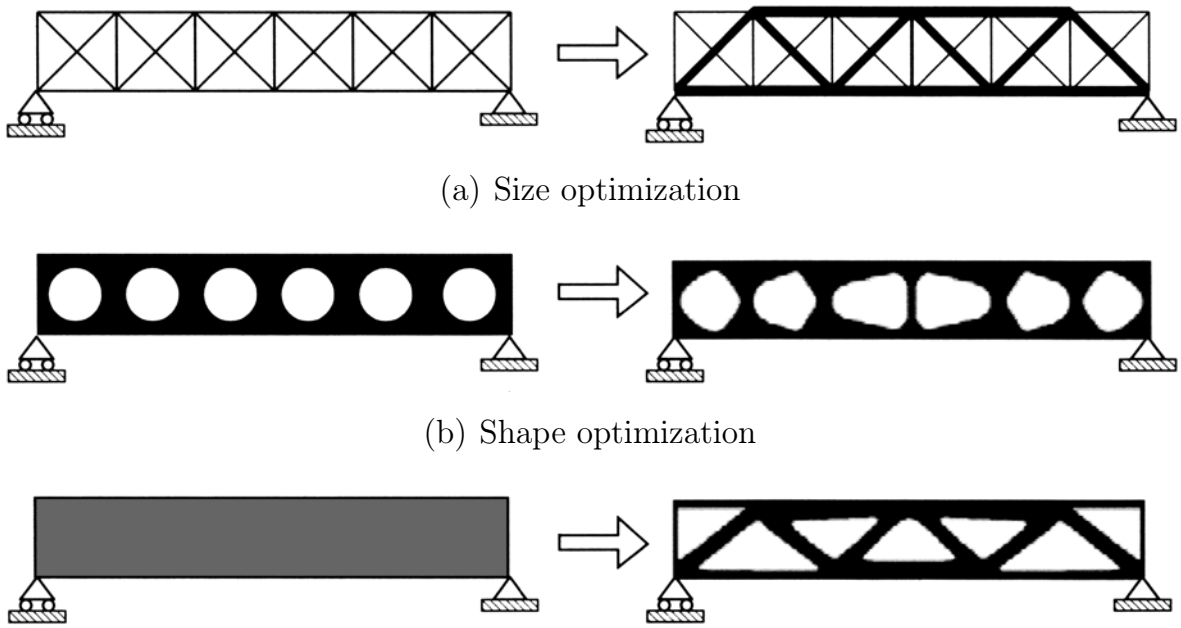

(a) Size optimization

(b) Shape optimization

(c) Topology optimization

Figure 2.1: Different types of structural optimization [3]

2.1.1 General approach

There are two established general approaches addressing the systematic synthesis of CM known in literature: kinematics-based approach and structural-optimization-based approach.

In the **kinematics-based approach**, the flexible members of a known compliant mechanism are modeled by several rigid bodies connected by pin-joints with added torsional stiffnesses which need to be optimized. This method was introduced by Howell in [5] using small length flexure hinges. For other flexure members, such as flexure pivots, cantilever beams and initially curved beams closed-loop equations of the force-deflection behavior were derived for different boundary conditions by Howell and Midha [6, 7], and used to develop commercially valuable CM such as a parallel CM by Mattson [8] or a micro-positioning mechanism by Handley [9], as illustrated in Fig. 2.3. Dynamic modeling for a simple parallel CM was given by Yu [10]. The kinematics-based approach is well-suited to model large, non-linear deformations. However,

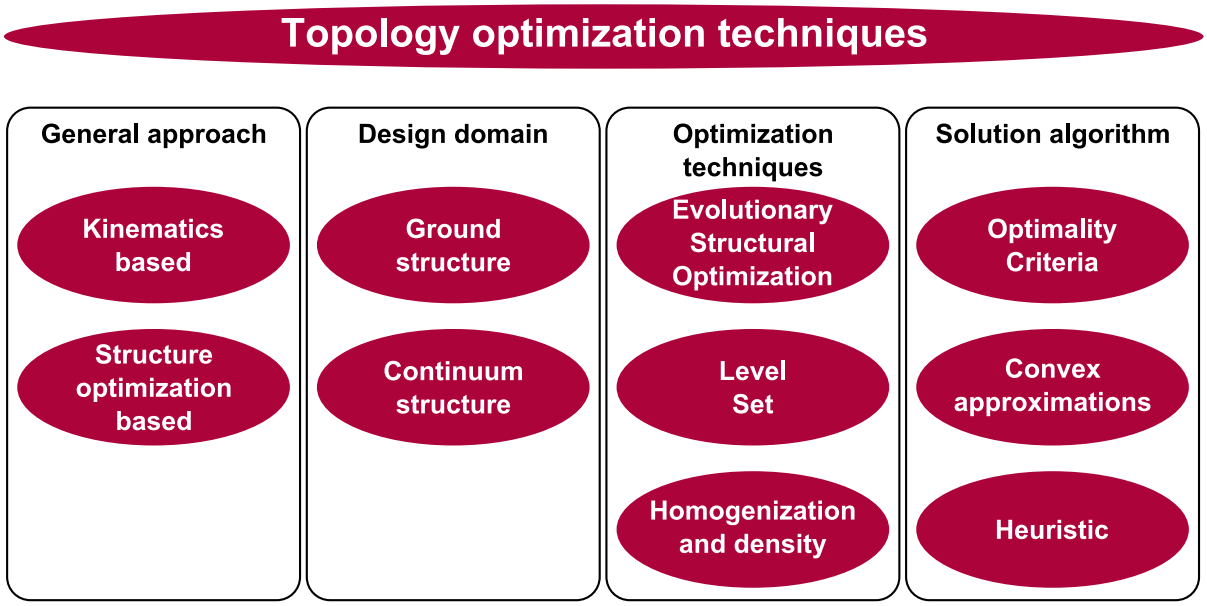

Figure 2.2: Rough categorization of current topology optimization techniques

it is based on a known initial rigid-link mechanism, i.e. the initial setup of a CM needs to be known. This approach is not suitable for a non-intuitive approach since an initial setup is not available and, thus, the kinematics-based approach is not further considered in this work. A more detailed description of this approach is given in Howell's monograph [11].

In the **structure-optimization-based approach,** no initial setup is required. It starts from a certain material (design) domain and aims to find an optimal shape, size and topology based on specified external loads and boundary conditions. This approach is used in this work and is further explained in the following subsections.

2.1.2 Design domain

The design domain used in structure-optimization-based approaches is represented by either a ground structure or continuum structure as illustrated in Fig. 2.4.

The **ground structure** domain is modeled by an exhaustive finite set of truss or beam elements, where the cross section of each element is

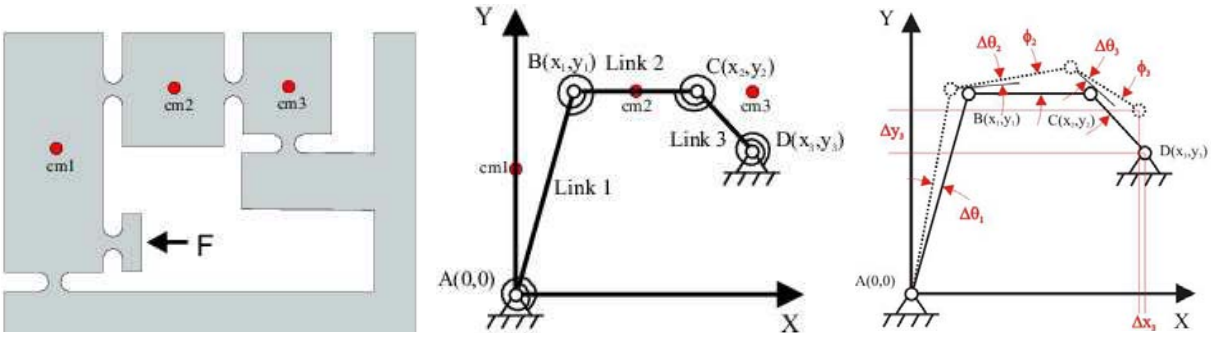

(a) (b) (c)

Figure 2.3: Kinematics-based approach: (a) Initial compliant mechanism, (b) corresponding pseudo-rigid-body-model and (c) deflected pseudo-rigid body-model [9]

the design variable. Fig. 2.4(a) shows an initial (reduced) set of trusses. The design variables are changed individually during an optimization process from (almost) zero to unity where zero values of cross-section means a removal of the element from the set. After several iterations, the set of elements is gradually reduced leading to the final topology.

Various research groups have adopted the ground structure approach to CM for different applications. Frecker, Kota, Kikuchi, Saxena and Ananthasuresh developed fundamentals of this approach [12], proposed multi-criteria formulations [13, 14], designed a smart (adaptive) structure [15], proposed an extension to multiple outputs [16], designed an amplification mechanism for piezoceramic stack actuators [17, 18] and micro-electrical-mechanical-systems (MEMS) [19], and proposed an approach that selects the optimal topology based on a kinetostatic design specification [20]. Ramrakhyani introduced hinged beam elements instead of rigidly-connected beam elements [21]. Joo and Kota considered different actuators [22, 23], developed some surgical tools [24] and compared the ground approach using linear beam elements with nonlinear beam elements [25, 26].

In the **continuum structure**, the design domain is divided into appropriate finite elements as shown in Fig. 2.4(b). Except Talischi [27], rectangular elements are used in literature due to numerical advantages.

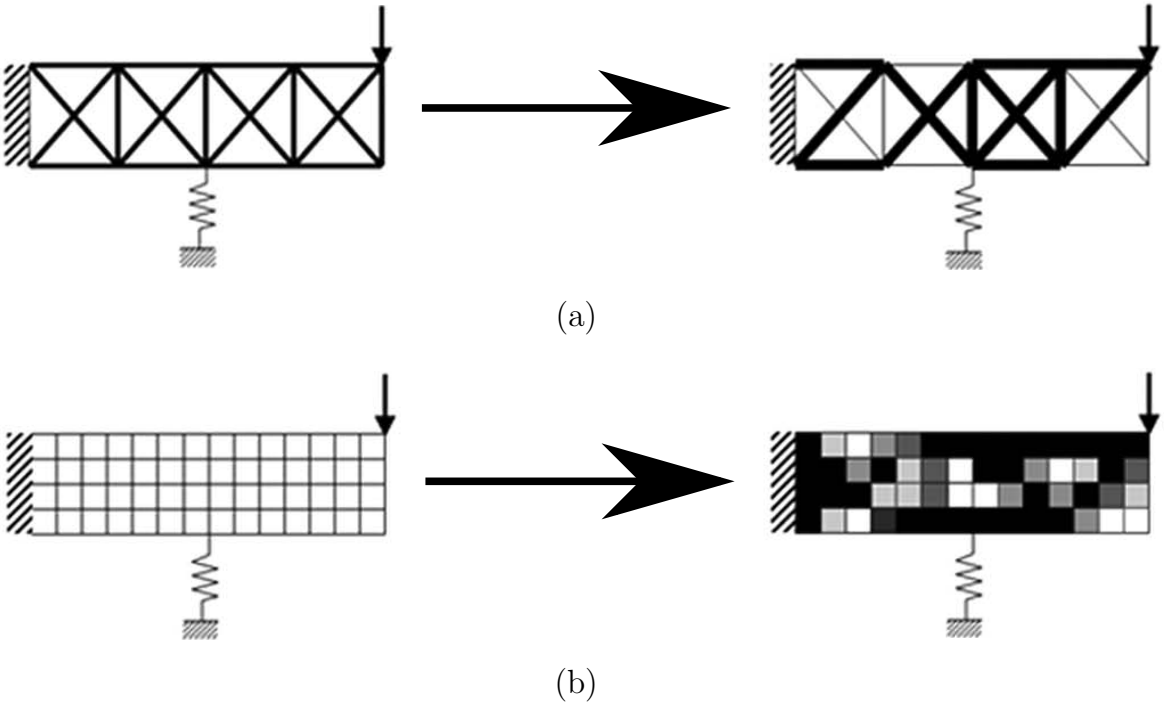

Figure 2.4: Different material domains: (a) ground structure and (b) continuum structure

A comprehensive review on topology optimization on continuum structures was given by Eschenhauer [28]. During the optimization process, the design variables are changed individually between almost zero and unity, representing void and solid elements, respectively. The mechanical properties, e.g. stiffness, of each individual element depend on different variable(s) depending on the optimization technique, as explained in the following subsection.

2.1.3 Optimization techniques

There are different, established optimization techniques that have been applied successfully to structural optimization problems: evolutionary structural optimization methods, level set methods, cellular automata and homogenization techniques. A modified version of the latter ones called the density technique, is implemented in this work and further described in Sect. 3.

Evolutionary structural optimization (ESO) methods optimize a structure by adding and removing material without using any sensitivities as illustrated in Fig. 2.5(a). ESO methods are based on purely heuristic algorithms, as described shortly in Sect. 2.1.4, and seem to be advantageous due to simplicity and efficiency. ESO was introduced by Xie [29] demonstrating its potential on some (stiff) structures. Later, a detailed monograph on ESO is given in his famous book [30] or more recently by Huang [31]. Different modifications and extensions have been proposed, e.g. bi-directional ESO (BESO) [32], additive ESO (AESO) [33], group ESO (GESO) [34] and multi-objective ESO (MESO) [35]. Edwards applied ESO to a tie-beam showing the sensitivity to different finite element mesh sizes [36]. ESO has been applied to the synthesis of CM for single loading conditions by Ansola [37]. However, there is an ongoing discussion lead by research teams around Zhou and Rozvany [38, 39] about drawbacks of ESO methods such as the lack of a sound mathematical basis and the occasional convergence to non-optimal solutions.

Level Set methods (LS) are based on multi-dimensional embedding functions where only a specific layer, namely the level set, defines the topology as illustrated in Fig. 2.5(b). LS methods have been applied to topology optimization problems by only a few authors. Stiff structures, such as a cantilever beam, an MBB-Beam, a Michell-type structure were designed by Sethian and Wiegmann [40], Wang [41, 42], and Allaire [43, 44], Sokolowski [45] and Norato [46], extended to multiple loads by Allaire [47] and reformulated using radial basis functions by Wang [48]. Recently, Xing proposed a finite element based LS formulation [49] and Shu addressed vibrations of structures and their frequency response [50]. CM were designed using LS methods by Allaire [44], Wang [51], Luo [52–54], and more recently Chen [55] and Otomori [56,57].

The **homogenization method**, is based on a microstructure divided into unit cells possessing several rectangular voids as illustrated in Fig. 2.5(c). The design variables are the dimensions α, β of the voids and the orientation θ of the unit cell. In a slightly modified version, referred as the **density method**, the material density of each finite element represents the design variable. The values of the design variables range from (almost) zero to unity representing void or solid material, re-

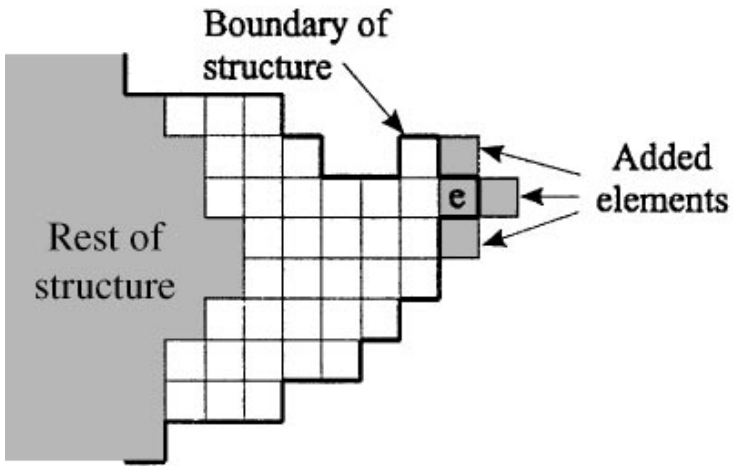

(a) Evolutionary structural optimization method [33]

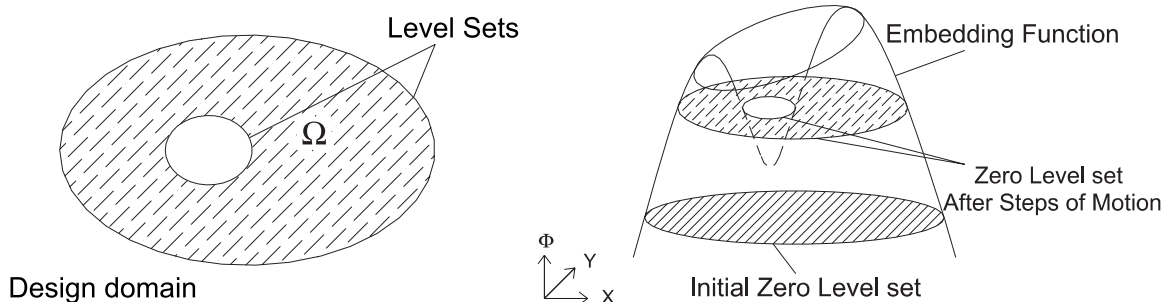

(b) Level Set method [42]

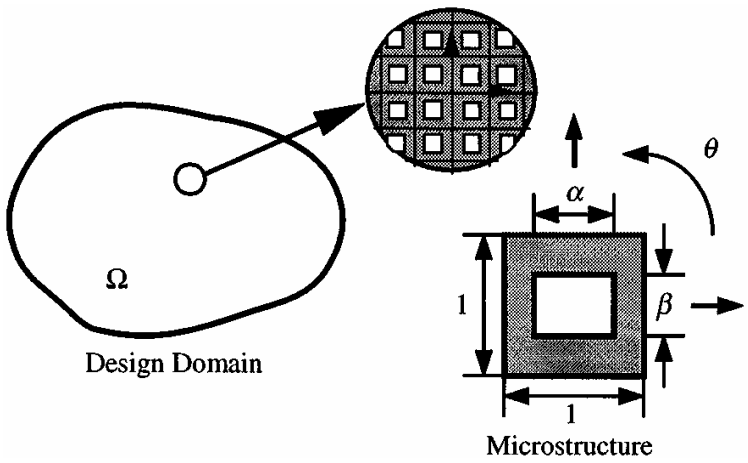

(c) Homogenization method [58]

Figure 2.5: Different topology optimization techniques

spectively. Originally proposed by Bendsøe and Kikuchi in a milestone paper [59], this method has been used for numerous optimizations of stiff structures and objects, e.g. by Ansola for three-dimensional shells [60] or by Kikuchi and Ma to eigenfrequency problems [61–65]. A basic 99 line code was published by Sigmund providing a helpful introduction to topology optimization of stiff structures [66]. In CM, the homogenization method was applied by Nishiwaki, Suzuki and recently Hongwei [58, 67, 68]. Detailed information are given in Bendsøe's book [3, 69], in Hassani's reviews [70–73] and in Le's recent dissertation [74].

2.1.4 Solution algorithms

There is a variety of solution algorithms that have been applied to general optimization problems. Detailed descriptions can be found in several textbooks, such as Gill [75] or Fletcher [76]. Here, only a few solution algorithms are described that have been applied successfully on structural optimization-based problems such as optimality criteria (OC) methods, methods based on explicit convex approximations and purely heuristic methods.

The **OC method** solves the optimization problem directly resulting from optimal conditions if closed-form expressions are available. It is very efficient if the number of constraints is small compared to the number of variables. The OC method has been well-developed and successfully applied to weight minimization problems for different structures, for example, based on a ground structure by Zhou and Rozvany [77, 78] and Hassani [72] or based on a continuum structure by Chiandussi [79] and Gheami [80]. In CM, OC methods have been applied successfully to compliant amplification devices by Saxena [14] and Canfield [81]. In summary, the OC method seems to be advantageous due to its efficiency and straightforward implementation.

Convex approximation algorithms, such as sequential linear programming (SLP), the sequential quadratic programming (SQP), convex linearization (CONLIN) and the method of moving asymptotes (MMA), can be described as iterative processes of approximated optimizations. In SLP, linear approximations of a Taylor series expansion of the objective

function and constraint equations are used, e.g. by Bremicker for different truss structures [82]. SLP can handle several objective functions and a large number of design variables. However, the computational efficiency strongly depends on a certain move limit. Kumar proposed an adaptive control of the move limit to improve the convergence for topology optimization problems [83]. In SQP, quadratic approximations are used providing a potentially more robust and accurate solver. However, the Hessian matrix, i.e. the second-order derivative of the objective function, needs to be calculated in each iteration which becomes cumbersome for a high number of design variables, as shown by Herskovits [84] and Morin [85]. In CONLIN, the optimization problems are solved taking specific characteristics of a structural-optimization-based problem into account, i.e. it uses intervening variables to obtain better approximations as proposed by Fleury [86, 87]. In MMA, slightly different intervening variables are used resulting in an even higher convergence rate. MMA was developed [88], extended to a globally convergent MMA (GCMMA) [89] and compared with each other by Svanberg [90]. A computational comparison of all aforementioned convex approximation algorithms applied to weight minimization of 79 structures was given by Schittkowski [91]. In summary, the GCMMA seems to be highly useful and advantageous to structural optimization problems, in particular, due to its simple handling of additional constraints.

Heuristic algorithms, such as genetic algorithms (GA), simulated annealing (SA), ant colony optimization (ACO) and particle swarm optimization (PSO) and cellular automata (CA), are non-gradient-based algorithms based on natural phenomena and have been applied to topology optimization problems that can hardly be solved by conventional, gradient-based methods. CA methods are inspired by the biological process of bone remodeling where only elements on the surface of a current design are modified. CA were applied to cantilever structures by Kita [92] and Abdalla [93], to tower structures by Kicinger [94, 95], to crashworthiness by Guo [96] and extended to eigenvalue problems by Abdalla [97]. Tovar applied CA to airfoil structures [98], introduced local control rules [99] and proposed CA specific optimality conditions [100]. A ground structure was used and compared for CA by Gürdal [101] and

Tatting [102]. As shown recently by Penninger in [103]. GA are also widely used in topology optimization and based on selection, crossover and mutation. Erbatur, Hajela, Jakiela, Lin, Rajeev and Wu applied GA to different stiff structures [104–111]. Comparisons of GA to other heuristic algorithms were drawn by Zitzler [112] and Botello [113]. Multi-objective algorithms were introduced by Srinivas [114], Coello [115, 116] and Tai [117], and reviewed by Veldhuizen [118]. Adaptive penalty schemes were introduced by Nanakorn [119], Lemonge [120] and Yeniay [121]. Bit array representation were used by Wang [122], harmony search algorithm was implemented by Lee [123] and a two-stage adaptive algorithm was proposed by Balamurugan [124]. Other algorithms have been applied less widely, for example, SA by Kirkpatrick [125] and Suppaptnarm [126], PSO by Perez [127], Padhye [128] and by Li [129], and ACO by Camp [130, 131] and Kaveh [132]. In order to design CM systematically, heuristic methods have been applied by different research groups, such as, Parson [133] and Saxena [134] by applying GA to a ground structure, Lu [135, 136] aiming to morph adaptive shapes, Sharma [137–140] applying different heuristic methods to a continuum structure, and Liu [141] by applying GA to binary strings that represent different multi-link mechanisms. An overview on the mentioned heuristic algorithms is given by Lagaros [142] and more recently by Li [143]. As a common tendency, heuristic methods may have a slow convergence and are not necessarily globally convergent to an optimal design.

Based on the aforementioned literature research and a numerical comparison of the different solution algorithms in own sample scenarios, the OC method, as a limited but very efficient solution technique, and the GCMMA method, as a successful and very versatile solution technique, are adopted and implemented in a staggered topology optimization algorithm in this work. A detailed description of each method's mathematical background and implementation is given in Sect. 3.1.

2.1.5 Research needs

The aforementioned topology optimization techniques lead in a systematic manner to final, optimized topologies, i.e. an optimal distribution of

material over the design domain is obtained. As a key result, the positions of hinges but not their optimal shape is obtained. Thus, one-node hinges (or often called pseudo-hinges) with doubtful physical meaning arise. Although some techniques exist circumventing this critical issue, e.g. [144], [145] or [146], a more consequent way is to use the already known data from the finite element calculation used in the topology optimization process. Since nodal displacements for a given topology are known, the required deflection range are available without additional costs, as well. Using these information would be beneficial to replace one-node hinges with real flexure hinges that meet the deflection and load bearing requirements as a result of their specific shape, dimension and material data.

2.2 Current state of flexure hinges and compliant mechanisms

Compliant mechanisms have been designed, manufactured and applied to small, micro and nanoscale problems by several research and engineering groups. Besides the design of the CM's skeleton using either systematic or intuitive techniques, a special focus is on the FH that enable the desired overall motion of CM through a permanent deformation but become highly stressed and, thus, susceptible to material failure. A brief overview of relevant research on common types of FH and current applications of CM is presented now.

Remark. This work focuses on *planar* CM with incorporated *planar* FH, since most three-dimensional applications can be performed by a combination of planar and perpendicularly-oriented CM. Therefore, non-planar CM are not discussed here.

2.2.1 Flexure hinges

There exist different types of FH, such as planar FH, rotational symmetric FH and compliant joints that consist of a system of FH. In terms

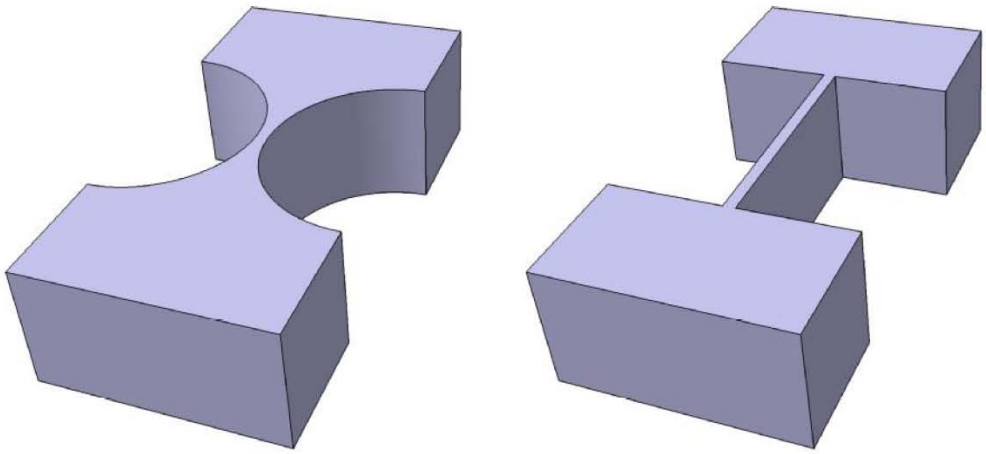

(a) Circular notch hinge (b) Rectangular leaf hinge

Figure 2.6: Common shapes of planar flexure hinges [148]

of topology optimization of in-plane mechanisms, planar FH are more relevant and, thus, are reviewed here. A review of rotational symmetric FH is given by Trease [147].

Many different types of FH have been investigated by several research groups. Paros and Weisbord did pioneer work yielding approximate compliances of differently shaped FH as early as in 1965 [149]. In the last decade, the design of FH has gained more attention due to a growing number of applications of CM. Several research groups proposed analytical, numerical and experimental studies: Researchers around Chen, Hsioa, Lobontiu, Smith, Tian, Tseytlin, Xu and Zhang presented analytical equations and numerical finite element (FE) calculations for circular and corner-filleted (i.e. rectangular) [150–154], symmetric conic [155], parabolic and hyperbolic [156], V-shaped [157], elliptical and conical [158–160], concave [161], half corner-filleted [162], variable rectangular [163], corner [164] and three segment FH [165]. However, the most common shapes of FH implemented in CM are circular and rectangular FH due to manufacturability, as shown in Fig. 2.6.

Mostly, compliances are derived for discrete points by using Castigliano's theorem, as suggested and extensively applied by Lobontiu in his milestone book on the design and modeling of FH [166], which has

been frequently cited and has been taken as a starting point for further developments by the aforementioned authors. Smith published another landmark book providing an excellent description of flexure elements and flexure systems [167] from a broader engineering standpoint. Recent comparisons and reviews on different FH's performances were given by Yong [168, 169] and Tain [170].

Other literature has been published addressing relevant properties of flexure hinges, such as the effect of the accuracies of analytic equations on CM by Yong [171], the error due to machining imperfections by Ryu [172] and avoiding buckling failure due to high compressive loads by Guerinot [173].

An inverse design of FH, i.e. finding the optimal shape of an FH, based on required performance specifications such as deflection range and infinite fatigue life is not known to the author's knowledge.

2.2.2 Compliant mechanisms

The majority of CM have been designed by using time intensive, intuitive approaches instead of systematic techniques as described in Sect.2.1. For this purpose, Howell provided design engineers with a milestone monograph on CM [11]. Besides a few early CM devices, e.g. by Scire in 1978 [174], CM have become popular since the mid 1990s. In particular, high and ultra precision problems accelerated the development of new techniques based on CM that are able to provide higher precision than existing multi-body systems.

Gripping devices for nano and micro applications were proposed, for example, a force and position controlled 1-degree-of-freedom micro gripper by Goldfarb [175] or an ultra precise micro gripper by Zubir [176] as shown in Fig. 2.7(a) and Fig. 2.7(b), respectively.

Several positioning and motion devices for nano and micro applications were proposed: a wafer stage mechanism providing translational and rotational motion by Ryu [180] and by Yi [177] as shown in Fig. 2.7(c), a two-grade amplifying parallel CM by Gao [181], a 3-translational-DOF CM has been developed and benchmarked in terms of accuracy by Niaritsiry [182], a microscopy scanning device based on 3-translational-DOF

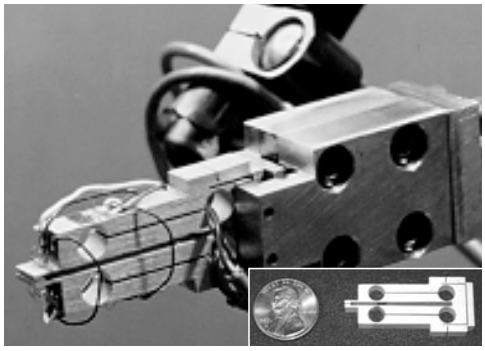

(a) Micro-gripper [175]

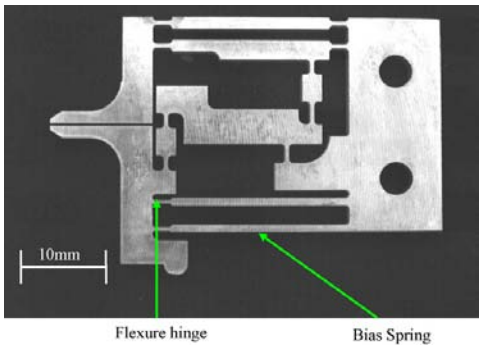

(b) Micro-gripper [176]

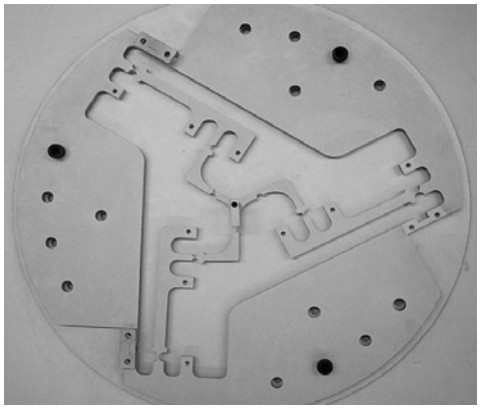

(c) 3-DOF mechanism [177]

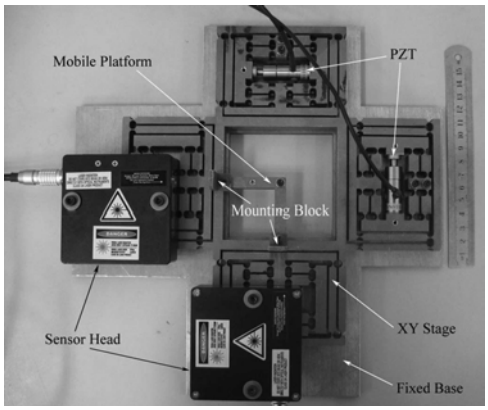

(d) Decoupled parallel CM [129]

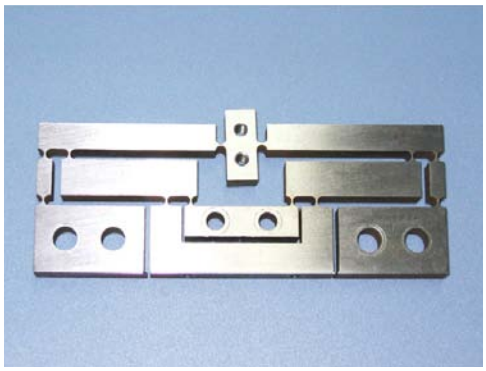

(e) Compliant magnifier [178]

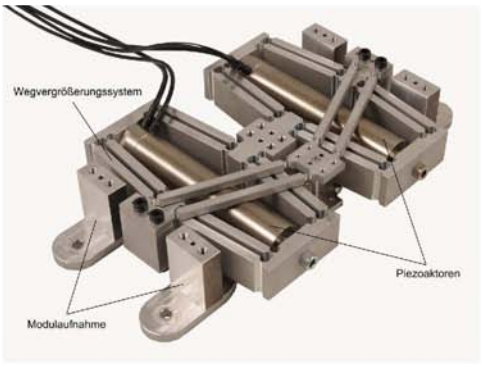

(f) Compliant feed unit [148]

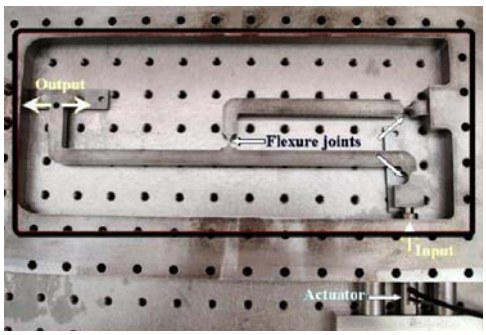

(g) Scott-Russel CM [179]

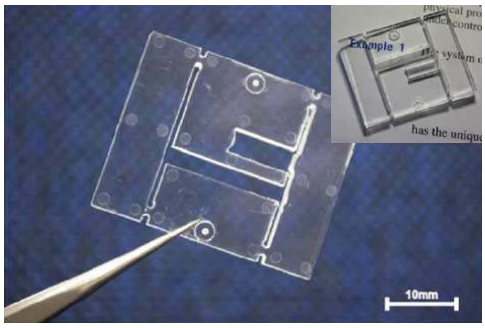

(h) Transparent positioner [129]

Figure 2.7: Current compliant mechanisms possessing flexure hinges

CM was developed by Kim [183]. Tian modeled a Scott-Russel mechanism under dynamic conditions and proposed another five-bar CM as shown in Fig. 2.7(g) [179, 184]. Chang developed a large travel range CM [185]. Yong developed a 3-RRR mechanism [186] and Yao designed and tested a compliant, parallel XY stage [187]. Tang developed a parallel CM with large-displacements and a decoupled kinematic structure [188, 189]. Ma and Kim analyzed the amplification of bridge-type CM [190, 191].

Li proposed a decoupled parallel micro positioning device [129] as shown in Fig. 2.7(d). Choi introduced a magnification device [178], as shown in Fig. 2.7(e). Recently, Kohrs developed and tested a compliant feed unit [148] as shown in Fig. 2.7(f). Callegari designed and tested a spherical micro positioning device [192]. An ortho-planar linear motion spring was proposed and patented by Howell and Parise [193, 194].

Steel or aluminum alloys were used in most CM, whereas a polymer-based, transparent positioner was presented by Chae [195] shown in Fig. 2.7(h) and a CM with implemented (superelastic) shape memory alloy FH by Raatz [196]. A review from a technological standpoint is given by Ouyang [197].

2.2.3 Research needs

Compliant mechanisms and, particularly, the implemented FH are permanently deformed and, thus, susceptible to fracture and fatigue failure. In a fairly recent review paper, Shuib pointed out rightly that there are currently too few fatigue data on flexure hinges used in CM and further research is necessary to prevent premature failure in CM [2]. Analytical studies on the fatigue life of FH is not known to the author's knowledge. Therefore, the derivation of relevant mechanical properties is of great interest and is addressed in Sect. 4.

3 Topology optimization of compliant mechanisms

The design and optimization of CM performed in this work is described now. Necessary and relevant fundamentals are derived in Sect. 3.1. The implementation of the algorithm into a MATLAB environment is described in Sect. 3.2. The results of the topology optimization are shown and discussed in Sect. 3.3. A summary is given in Sect. 3.4.

3.1 Relevant fundamentals

Fundamental knowledge on continuum mechanics, finite element analysis, and topology optimization techniques can be found in various textbooks [3, 198, 199]. Here, only relevant fundamentals that are applied in this work, are recalled.

The aim of topology optimization is to find an optimal material distribution for a given design domain Ω_0 under certain boundary and loading conditions, e.g. stresses $\boldsymbol{t}$ and displacements $\boldsymbol{u}$. A sample topology optimization problem is illustrated by Fig. 3.1: a general design domain with specified solid and void areas is adapted to match a specific load scenario, as shown in Fig. 3.1(a) and Fig. 3.1(b). Then, a systematic optimization of the material distribution leads to a final topology as presented in Fig. 3.1(c).

Remark. Any body forces are omitted due to their negligible role in the later modeling of CM.

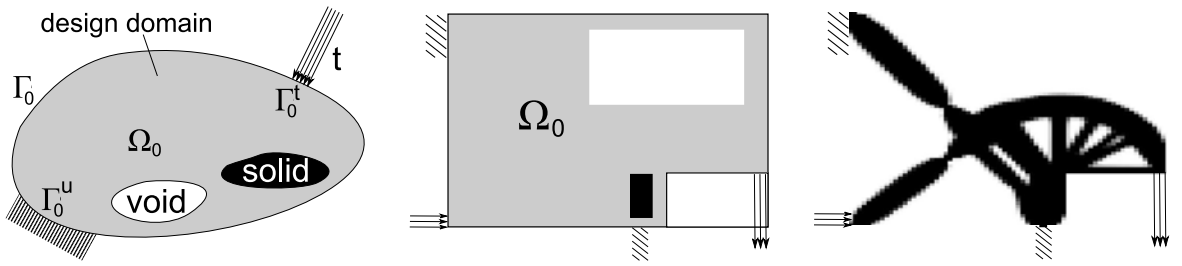

(a) (b) (c)

Figure 3.1: General topology optimization problem of designing an optimal material distribution: (a) general design domain, (b) sample rectangular design domain and (c) optimal topology of a compliant mechanism based on a 6,400 finite element discretization

3.1.1 Fundamentals of continuum mechanics

The topology optimization algorithm described and implemented in this work is based on a planar finite element (FE) discretization of the continuous material domain. In order to obtain a valid numerical formulation later, some fundamentals of continuum mechanics need to be derived beforehand.

Remark. For better understanding, most equations are listed by two lines, representing concise vector notation and explicit Einstein notation, respectively. Details on these notations can be found in standard continuum mechanics literature, e.g. in [200].

3.1.1.1 Deformation and motion

The material domain in an initial state is denoted by Ω_0. This initial configuration is chosen to be the *reference configuration*, i.e. the equations that describe the deformations and motions refer to this configuration. Fig. 3.2 illustrates a material domain in its reference and current configuration, i.e. in its undeformed and deformed state. The material domain in an *undeformed state* and all its material points can be described by material coordinates

$$\boldsymbol{X} = X_i \boldsymbol{e}_i \in \Omega_0, \tag{3.1}$$

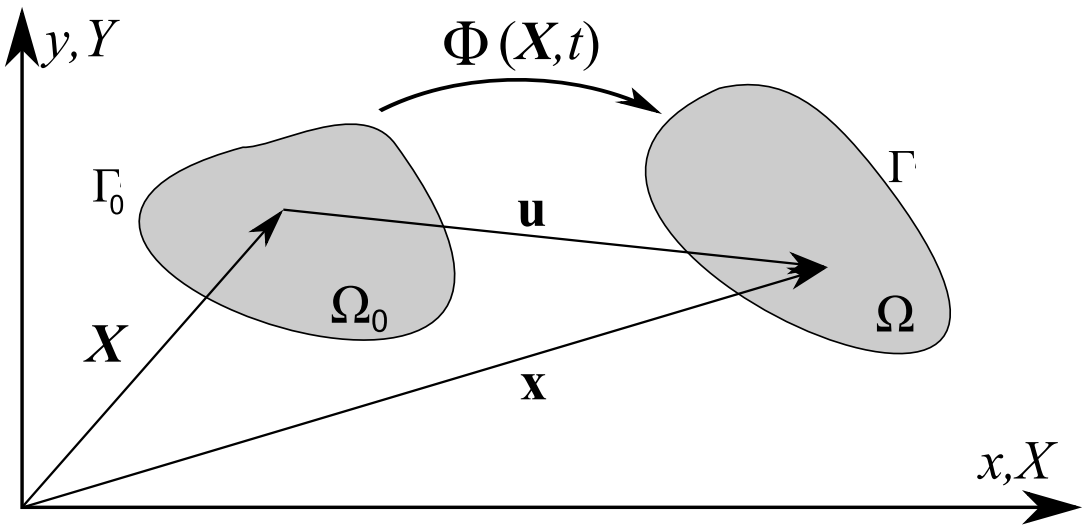

Figure 3.2: Undeformed (reference) configuration and deformed (current) configuration of a material domain

that do not change with time. Here, X_i are the components of the position vector in the reference configuration and $\boldsymbol{e}_i$ are the unit base vectors of a Cartesian coordinate system.

In contrast to this, the position of a point in the *current configuration* (after undergoing some motion) is described by

$$\boldsymbol{x} = x_i \boldsymbol{e}_i \in \Omega, \tag{3.2}$$

where x_i are the components of the position vector in the current configuration. The **motion** $\boldsymbol{\phi}$ that links the deformed state to the undeformed state is

$$\begin{aligned} \boldsymbol{x} &= \boldsymbol{\phi}(\boldsymbol{X}, t), \\ x_i &= \phi_i(\boldsymbol{X}, t). \end{aligned} \tag{3.3}$$

The **displacement** $\boldsymbol{u}$ of a material point caused by a motion is given by

$$\begin{aligned} \boldsymbol{u} &= \boldsymbol{x} - \boldsymbol{X}, \\ u_i &= x_i - X_i. \end{aligned} \tag{3.4}$$

The **deformation gradient** $\boldsymbol{F}$ is defined as

$$\begin{aligned} \boldsymbol{F} &= \frac{\partial \boldsymbol{\phi}}{\partial \boldsymbol{X}} = \frac{\partial \boldsymbol{x}}{\partial \boldsymbol{X}} = (\nabla_0 \boldsymbol{\phi})^T, \\ F_{ij} &= \frac{\partial \phi_i}{\partial X_j} = \frac{\partial x_i}{\partial X_j}, \end{aligned} \tag{3.5}$$

where ∇_0 is the gradient with respect to the material coordinates. In terms of displacements it can be expressed as

$$\begin{aligned} \boldsymbol{F} &= \boldsymbol{I} + \nabla_0 \boldsymbol{u}, \\ F_{ij} &= \delta_{ij} + \frac{\partial u_i}{\partial X_j}. \end{aligned} \tag{3.6}$$

The determinant of $\boldsymbol{F}$ is denoted by

$$J = \det(\boldsymbol{F}), \tag{3.7}$$

and is used to link the integrals between different configurations, e.g.

$$\int_{\Omega} (.) d\Omega = \int_{\Omega_0} (.) J d\Omega_0. \tag{3.8}$$

3.1.1.2 Strain measures

The **Green strain tensor** $\boldsymbol{E}$ (sometimes referred as Green-Lagrange strain) is a symmetric, second-order tensor and is defined as

$$\begin{aligned} \boldsymbol{E} &= \frac{1}{2} \left(\boldsymbol{F}^T \boldsymbol{F} - \boldsymbol{I} \right), \\ E_{ij} &= \frac{1}{2} \left(F_{ki} F_{kj} - \delta_{ij} \right), \end{aligned} \tag{3.9}$$

and it can be expressed in terms of displacements as

$$\begin{aligned} \boldsymbol{E} &= \frac{1}{2} \left(\nabla_0 \boldsymbol{u} + (\nabla_0 \boldsymbol{u})^T + (\nabla_0 \boldsymbol{u})^T \cdot \nabla_0 \boldsymbol{u} \right), \\ E_{ij} &= \frac{1}{2} \left(\frac{\partial u_i}{\partial X_j} + \frac{\partial u_j}{\partial X_i} + \frac{\partial u_k}{\partial X_i} \frac{\partial u_k}{\partial X_j} \right). \end{aligned} \tag{3.10}$$

The **Almansi strain tensor** $\boldsymbol{e}$ is a second-order tensor and is defined as

$$\boldsymbol{e} = \tfrac{1}{2}\left(\boldsymbol{I} - \boldsymbol{F}^{-T}\boldsymbol{F}^{-1}\right), \tag{3.11}$$

and it can be expressed in terms of displacements as

$$\begin{aligned} \boldsymbol{e} &= \frac{1}{2}\left(\nabla\boldsymbol{u} + (\nabla\boldsymbol{u})^T - (\nabla\boldsymbol{u})^T \cdot \nabla\boldsymbol{u}\right), \\ e_{ij} &= \frac{1}{2}\left(\frac{\partial u_i}{\partial x_j} + \frac{\partial u_j}{\partial x_i} - \frac{\partial u_k}{\partial x_i}\frac{\partial u_k}{\partial x_j}\right). \end{aligned} \tag{3.12}$$

Both strain tensors are linked with each other by the (push-forward) relation

$$\boldsymbol{e} = \boldsymbol{F}^{-T} \cdot \boldsymbol{E} \cdot \boldsymbol{F}^{-1}. \tag{3.13}$$

In the case of small strains, the *linearized* strain tensors $\boldsymbol{E}^{lin}$ and $\boldsymbol{e}^{lin}$ are used, where the nonlinear terms are omitted. Based on the assumption that there is a negligible difference in the material and spatial coordinates of a given material point, the gradients with respect to material and spatial coordinates coincide. Thus,

$$\begin{aligned} \boldsymbol{E}^{lin} \approx \boldsymbol{e}^{lin} \approx \boldsymbol{\epsilon} &= \frac{1}{2}\left((\nabla\boldsymbol{u})^T + \nabla\boldsymbol{u}\right), \\ E_{ij}^{lin} \approx e_{ij}^{lin} \approx \epsilon_{ij} &= \frac{1}{2}\left(\frac{\partial u_i}{\partial x_j} + \frac{\partial u_j}{\partial x_i}\right), \end{aligned} \tag{3.14}$$

with $\boldsymbol{\epsilon}$ as the second-order (linear) small strain tensor.

3.1.1.3 Stress measures

Three different stress measures are used later: the Cauchy stress tensor $\boldsymbol{\sigma}$, the nominal (first Piola-Kirchhoff) stress tensor $\boldsymbol{P}$ and the second Piola-Kirchhoff (PK2) stress tensor $\boldsymbol{S}$. Fig. 3.3 illustrates the different stress measures in their corresponding configuration.

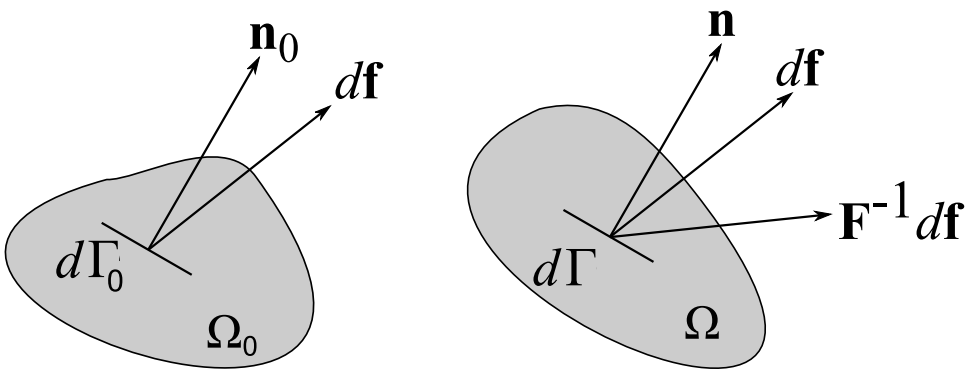

Figure 3.3: Definition of stress measures in the reference and current configuration [201]

The **Cauchy-stress tensor** $\boldsymbol{\sigma}$ is a symmetric, second-order tensor defined in the current configuration by

$$\begin{aligned} \boldsymbol{n} \cdot \boldsymbol{\sigma} d\Gamma &= \quad \boldsymbol{t} d\Gamma, \\ n_i \sigma_{ij} d\Gamma &= \quad t_j d\Gamma. \end{aligned} \tag{3.15}$$

The **nominal stress tensor** $\boldsymbol{P}$ is a non-symmetric, second-order tensor defined in the reference configuration by

$$\begin{aligned} \boldsymbol{n}_0 \cdot \boldsymbol{P} d\Gamma_0 &= \quad \boldsymbol{t}_0 d\Gamma_0, \\ n_{0i} P_{ij} d\Gamma_0 &= \quad t_{0j} d\Gamma_0. \end{aligned} \tag{3.16}$$

It can be seen, that $\boldsymbol{\sigma}$ and $\boldsymbol{P}$ are defined similarly except that they refer to different configurations.

The **second Piola-Kirchhoff stress tensor** $\boldsymbol{S}$ is a symmetric, second-order tensor defined by

$$\begin{aligned} \boldsymbol{n}_0 \cdot \boldsymbol{S} d\Gamma_0 &= \quad \boldsymbol{F}^{-1} \cdot \boldsymbol{t}_0 d\Gamma_0, \\ n_{0i} S_{ij} d\Gamma_0 &= \quad F_{ij}^{-1} t_{0i} d\Gamma_0. \end{aligned} \tag{3.17}$$

The three stress measures are linked with each other by the relations

$$\begin{aligned} \boldsymbol{P} &= \quad J \boldsymbol{F}^{-1} \cdot \boldsymbol{\sigma} = \boldsymbol{S} \cdot \boldsymbol{F}^T, \\ P_{ij} &= \quad J F_{ik}^{-1} \sigma_{kj} = S_{ik} F_{jk}. \end{aligned} \tag{3.18}$$

In the case of $\boldsymbol{F} = \boldsymbol{I}$, all three stress measures coincide.

3.1.1.4 Conservation equation and weak formulation

There are several conservation equations where the conservation of linear momentum, as the most relevant one in this work, is briefly described. Neglecting any body forces and accelerations, the conservation of linear momentum is reduced to the equilibrium equation that is with respect to the *reference configuration*

$$\begin{aligned} \nabla_0 \cdot \boldsymbol{P} &= \mathbf{0}, \\ \frac{\partial P_{ij}}{\partial X_i} &= 0. \end{aligned} \tag{3.19}$$

The general optimization problem already shown in Fig. 3.1(a) has to satisfy the equilibrium equation given by Eq. (3.19). Since differentiability of the stress is often a too strong requirement, an equivalent *weak* formulation will be developed from the strong formulation.

Forming a scalar product with an arbitrary, smooth, vector-valued test function $\delta\boldsymbol{v} = \delta\boldsymbol{v}(\boldsymbol{X})$ and integrating over the entire design domain Ω_0 leads to

$$\begin{aligned} \int_{\Omega_0} (\nabla_0 \cdot \boldsymbol{P}) \cdot \delta\boldsymbol{v} \, d\Omega_0 &= 0, \\ \int_{\Omega_0} \frac{\partial P_{ij}}{\partial X_i} \delta v_j \, d\Omega_0 &= 0. \end{aligned} \tag{3.20}$$

Applying the product rule of differentiation

$$\begin{aligned} (\nabla_0 \cdot \boldsymbol{P}) \cdot \delta\boldsymbol{v} &= \nabla_0 \cdot (\boldsymbol{P} \cdot \delta\boldsymbol{v}) - (\nabla_0 \delta\boldsymbol{v}) : \boldsymbol{P}, \\ \frac{\partial P_{ij}}{\partial X_i} \delta v_j &= \frac{\partial (P_{ij} \delta v_j)}{\partial X_i} - P_{ij} \frac{\partial \delta v_j}{\partial X_i}, \end{aligned} \tag{3.21}$$

yields

$$\begin{aligned} \int_{\Omega_0} (\nabla_0 \cdot (\boldsymbol{P} \cdot \delta\boldsymbol{v}) - (\nabla_0 \delta\boldsymbol{v}) : \boldsymbol{P}) \, d\Omega_0 &= 0, \\ \int_{\Omega_0} \left(\frac{\partial (P_{ij} \delta v_j)}{\partial X_i} - \frac{\partial (\delta v_j)}{\partial X_i} P_{ij} \right) d\Omega_0 &= 0. \end{aligned} \tag{3.22}$$

By applying Gauss' divergence theorem on the first term, recalling the stress vector as introduced in Eq. (3.17), and considering nonzero tension only at the surface Γ_t^0 the first term of Eq. (3.22) can be manipulated to

$$\begin{aligned} \int_{\Omega_0} \nabla_0 \cdot (\boldsymbol{P} \cdot \delta\boldsymbol{v}) d\Omega = & \int_{\Gamma_0} (\boldsymbol{P}_0 \cdot \delta\boldsymbol{v}) \cdot \boldsymbol{n} \, d\Gamma_0 = \int_{\Gamma_{t_i}^0} \boldsymbol{t}^0 \cdot \delta\boldsymbol{v} \, d\Gamma_0, \\ \int_{\Omega_0} \frac{\partial (P_{ij} \delta v_j)}{\partial X_i} d\Omega = & \int_{\Gamma_0} P_{ij} \delta v_j n_i^0 \, d\Gamma_0 = \sum_{j=1}^{2} \int_{\Gamma_t^0} t_j^0 \delta v_j \, d\Gamma_0. \end{aligned} \tag{3.23}$$

Considering two-dimensional problems, Eq. (3.22) can be rewritten as

$$\begin{aligned} \int_{\Omega_0} (\nabla_0 \delta\boldsymbol{v}) : \boldsymbol{P} \, d\Omega_0 &= \sum_{j=1}^{2} \int_{\Gamma_{t_j}^0} (\boldsymbol{t}^0 \cdot \boldsymbol{e}_j) \cdot (\delta\boldsymbol{v} \cdot \boldsymbol{e}_j) \, d\Gamma_0, \\ \int_{\Omega_0} P_{ij} \frac{\partial \delta v_j}{\partial X_i} \, d\Omega_0 &= \sum_{j=1}^{2} \int_{\Gamma_t^0} t_j^0 \delta v_j \, d\Gamma_0. \end{aligned} \tag{3.24}$$

By using Eq. (3.5), the first term of Eq. (3.24) is substituted by

$$\begin{aligned} (\nabla_0 \delta\boldsymbol{v}) : \boldsymbol{P} = & \quad \delta(\nabla_0 \boldsymbol{v}) : \boldsymbol{P} = (\delta \boldsymbol{F}) : \boldsymbol{P}, \\ \frac{\partial (\delta u_j)}{\partial X_i} P_{ij} = & \quad \delta \left(\frac{\partial u_j}{\partial X_i} \right) P_{ij} = (\delta F_{ji}) P_{ij}, \end{aligned} \tag{3.25}$$

yielding

$$\begin{aligned} \int_{\Omega_0} (\delta \boldsymbol{F}^T) : \boldsymbol{P} \, d\Omega_0 = & \sum_{j=1}^{2} \int_{\Gamma_{t_j}^0} (\boldsymbol{t}^0 \cdot \boldsymbol{e}_j) \cdot (\delta\boldsymbol{v} \cdot \boldsymbol{e}_j) \, d\Gamma_0, \\ \int_{\Omega_0} (\delta F_{ji}) P_{ij} \, d\Omega_0 = & \sum_{j=1}^{2} \int_{\Gamma_t^0} t_j^0 \delta v_j \, d\Gamma_0, \end{aligned} \tag{3.26}$$

representing the weak formulation of the equilibrium equation which is equivalent to the strong formulation given in Eq. (3.19) but the differentiability requirements have been weakened. This formulation is also called the potential of virtual work where the LHS and RHS are related to the internal and external forces, respectively.

3.1.2 Fundamentals of finite element analysis

A numerical formulation of the weak formulation of the equilibrium equation given in Eq. (3.26) is now developed, which finally leads to a set of equations that later is solved numerically. Following [201], isoparametric finite elements (FE) are introduced, a numerical formulation is given and the constitutive equation is presented. Finally, explicit matrix expressions of the tangent stiffness are derived.

3.1.2.1 Isoparametric two-dimensional finite elements

The material domain, i.e. the design domain, is discretized by two-dimensional, quadrilateral FE, where the shape functions N_I with the nodal indices $I = 1..4$ are

$$N_I = \frac{1}{4}\left(1 + \xi_I \xi\right)\left(1 + \eta_I \eta\right), \tag{3.27}$$

as illustrated in Fig. 3.4.

The material coordinates of an arbitrary point within the FE are expressed by these shape functions and the nodal coordinates $\boldsymbol{x}_I$

$$\begin{aligned} \boldsymbol{x}(\boldsymbol{\xi}) &= N_I(\boldsymbol{\xi})\boldsymbol{x}_I, \\ x_i(\boldsymbol{\xi}) &= N_I(\boldsymbol{\xi})x_{iI}, \\ \begin{bmatrix} x(\boldsymbol{\xi}) \\ y(\boldsymbol{\xi}) \end{bmatrix} &= N_I(\boldsymbol{\xi}) \begin{bmatrix} x_I \\ y_I \end{bmatrix}, \end{aligned} \tag{3.28}$$

with the element coordinates $\boldsymbol{\xi} = [\xi, \eta]^T$. The displacements of an arbitrary point within the FE are expressed similarly by the nodal displacements $\boldsymbol{u}_I$

$$\begin{aligned} \boldsymbol{u}(\boldsymbol{\xi}) &= N_I(\boldsymbol{\xi})\boldsymbol{u}_I, \\ \begin{bmatrix} u(\boldsymbol{\xi}) \\ v(\boldsymbol{\xi}) \end{bmatrix} &= N_I(\boldsymbol{\xi}) \begin{bmatrix} u_I \\ v_I \end{bmatrix}. \end{aligned} \tag{3.29}$$

The derivatives of the shape functions with respect to the material coordinates are

$$\underset{[2\times 4]}{\boldsymbol{\mathcal{B}}_0} = \begin{bmatrix} N_{1,X} & N_{2,X} & N_{3,X} & N_{4,X} \\ N_{1,Y} & N_{2,Y} & N_{3,Y} & N_{4,Y} \end{bmatrix}, \tag{3.30}$$

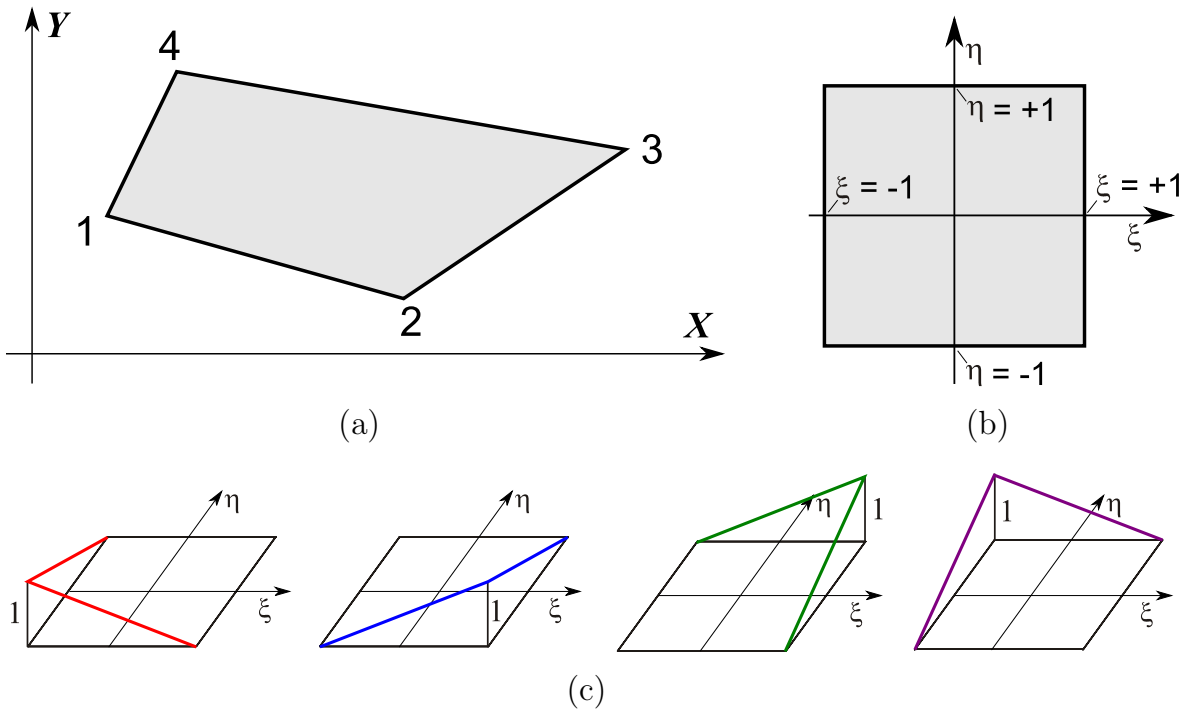

Figure 3.4: Mapping from original element (a) to squared, master element (b) using bilinear shape functions $N_I(\xi,\eta), I = 1,...,4$ (c); adopted and modified from [202]

and can be calculated for each shape function N_I by

$$\boldsymbol{\mathcal{B}}_{0I}^T = \boldsymbol{N}_{I,\boldsymbol{X}}^T = [N_{I,X}\ N_{I,Y}] = \boldsymbol{N}_{I,\boldsymbol{\xi}}^T \boldsymbol{X}_{,\boldsymbol{\xi}}^{-1} = \boldsymbol{N}_{I,\boldsymbol{\xi}}^T \left(\boldsymbol{F}_{\boldsymbol{\xi}}^0\right)^{-1}, \qquad (3.31)$$

The latter term represents inverse of the Jacobian matrix of the mapping between the material and the (master) element coordinates. The gradients $\boldsymbol{N}_{I,\boldsymbol{\xi}}^T$ for the considered four-node quadrilateral FE are

$$\boldsymbol{N}_{I,\boldsymbol{\xi}}^T = \begin{bmatrix} \partial N_1/\partial\xi & \partial N_1/\partial\eta \\ \partial N_2/\partial\xi & \partial N_2/\partial\eta \\ \partial N_3/\partial\xi & \partial N_3/\partial\eta \\ \partial N_4/\partial\xi & \partial N_4/\partial\eta \end{bmatrix} = \frac{1}{4}\begin{bmatrix} \xi_1(1+\eta_1\eta) & \eta_1(1+\xi_1\xi) \\ \xi_2(1+\eta_2\eta) & \eta_2(1+\xi_2\xi) \\ \xi_3(1+\eta_3\eta) & \eta_3(1+\xi_3\xi) \\ \xi_4(1+\eta_4\eta) & \eta_4(1+\xi_4\xi) \end{bmatrix}, \qquad (3.32)$$

later, the derivatives of the shape functions are expressed in a short hand notation as $\mathcal{B}_{jI}^0 = \partial N_I/\partial X_j$.

3.1.2.2 Finite element formulation

Following [201], the continuous weak formulation given in Eq. (3.26) is now discretized by the aforementioned FE, where the coordinates and displacements are expressed by using the shape functions as given in Eq.(3.28) and (3.29). Similarly, the test functions, also called variations, are described by

$$\begin{aligned} \delta\boldsymbol{u}(\boldsymbol{X}) = &\ \delta\boldsymbol{u_I} N_I(\boldsymbol{X}), \\ \delta u_i(\boldsymbol{X}) = &\ \delta u_{iI} N_I(\boldsymbol{X}). \end{aligned} \tag{3.33}$$

The deformation gradient, given in Eq. (3.5), is described by

$$\begin{aligned} \boldsymbol{F} &= \boldsymbol{x}\boldsymbol{\mathcal{B}}_o^T, \\ F_{ij} &= \mathcal{B}_{jI}^0 x_{iI} = \frac{\partial N_I}{\partial X_j} x_{iI}, \end{aligned} \tag{3.34}$$

or

$$\begin{aligned} \boldsymbol{F} &= \boldsymbol{I} + \nabla_0 \boldsymbol{u} = \boldsymbol{I} + \boldsymbol{u}\boldsymbol{\mathcal{B}}_0^T, \\ F_{ij} &= \delta_{ij} + \frac{\partial N_I}{\partial X_j} u_{iI}, \end{aligned} \tag{3.35}$$

since $\delta x_{iI} = \delta(X_{iI} + u_{iI}) = \delta u_{iI}$. The variation of the deformation gradient is described by

$$\begin{aligned} \delta\boldsymbol{F} &= \delta\boldsymbol{u}\boldsymbol{\mathcal{B}}_o^T, \\ \delta F_{ij} &= \mathcal{B}_{jI}^0 \delta u_{iI} = \frac{\partial N_I}{\partial X_j} \delta u_{iI}, \end{aligned} \tag{3.36}$$

The internal virtual work, given by the LHS of the weak formulation from Eq. (3.26), is then reformulated to

$$\delta u_{iI} f_{iI}^{int} = \int_{\Omega_0} (\delta F_{ij}) P_{ji}\, d\Omega_0 = \ \delta u_{iI} \int_{\Omega_0} \frac{\partial N_I}{\partial X_j} P_{ji}\, d\Omega_0, \tag{3.37}$$

and due to the arbitrariness of the test function δu_{iI} this yields the *internal forces*

$$\begin{aligned} \boldsymbol{f}^{int} &= \int_{\Omega_0} \boldsymbol{\mathcal{B}}_0^T \boldsymbol{P}(\boldsymbol{u})\, d\Omega_0, \\ f_{iI}^{int} &= \int_{\Omega_0} \frac{\partial N_I}{\partial X_j} P_{ji}\, d\Omega_0 = \int_{\Omega_0} \mathcal{B}_{jI}^0 P_{ji}\, d\Omega_0, \end{aligned} \tag{3.38}$$

and its infinitesimal increment $d\boldsymbol{f}^{int}$ as

$$d\boldsymbol{f}^{int} = \int_{\Omega_0} \boldsymbol{\mathcal{B}}_0^T d\boldsymbol{P}(\boldsymbol{u}) d\Omega_0, \tag{3.39}$$

where, again, $\boldsymbol{\mathcal{B}}_0$ contains the derivatives of the shape functions as given in Eq.(3.31). By using $\boldsymbol{P}(\boldsymbol{u}) = \boldsymbol{S}\boldsymbol{F}^T$ yields

$$\boldsymbol{f}^{int} = \int_{\Omega_0} \boldsymbol{\mathcal{B}}_0^T \boldsymbol{S}\boldsymbol{F}^T d\Omega_0, \tag{3.40}$$

$$d\boldsymbol{f}^{int} = \underbrace{\int_{\Omega_0} \boldsymbol{\mathcal{B}}_0^T (d\boldsymbol{S})\boldsymbol{F}^T d\Omega_0}_{d\boldsymbol{f}_{mat}^{int}} + \underbrace{\int_{\Omega_0} \boldsymbol{\mathcal{B}}_0^T \boldsymbol{S}(d\boldsymbol{F})^T d\Omega_0}_{d\boldsymbol{f}_{geo}^{int}}. \tag{3.41}$$

The internal load vector $\boldsymbol{f}^{int}$ can be computed explicitly by Eq. (3.40).

The external virtual work, given by the RHS of the weak formulation from Eq. (3.26), is reformulated to

$$\delta u_{iI} f_{iI}^{ext} = \int_{\Gamma_{t_i}^0} t_i^0 \delta u_i\, d\Gamma_0 = \delta u_{iI} \left(\int_{\Gamma_{t_i}^0} N_I t_i^0\, d\Gamma_0 \right), \tag{3.42}$$

and, again, due to the arbitrariness of the test function δu_{iI} this yields the *external forces*

$$f_{iI}^{ext} = \int_{\Gamma_{t_i}^0} N_I t_i^0\, d\Gamma_0. \tag{3.43}$$

3.1.2.3 Constitutive equation

The stresses are expressed by the material properties and the occurring strains $\boldsymbol{E} = \boldsymbol{E}(\boldsymbol{u})$ at each material point based on the displacements. In compliant mechanisms, where large deformations may occur in the flexure hinges, the material response can be properly modelled by extending Hooke's linear law of elasticity $\boldsymbol{\sigma} = \mathbb{C} : \boldsymbol{\epsilon}$ by replacing the Cauchy stress by the PK2 stress $\boldsymbol{S}$ and the small strain tensor by the nonlinear Green strain tensor $\boldsymbol{E}$

$$\begin{aligned} \boldsymbol{S}(\boldsymbol{u}) &= \quad \mathbb{C} : \boldsymbol{E}(\boldsymbol{u}), \\ S_{ij}(\boldsymbol{u}) &= \; C_{ijkl} E_{kl}(\boldsymbol{u}), \end{aligned} \tag{3.44}$$

where $\mathbb{C}$ represents the fourth-order elasticity tensor. For isotropic materials, as usually used in applications of CM, this relation can be simplified and rewritten in Voigt notation, as outlined in Appendix A.1 as

$$\begin{aligned} \boldsymbol{S}(\boldsymbol{u}) &= \quad \frac{E\nu}{1-\nu^2}\mathrm{tr}(\boldsymbol{E}(\boldsymbol{u}))\boldsymbol{I} + \frac{E}{1+\nu}\boldsymbol{E}(\boldsymbol{u}), \\ S_{ab}(\boldsymbol{u}) &= \; \frac{E\nu}{1-\nu^2}E_{kk}(\boldsymbol{u})\delta_{ab} + \frac{E}{1+\nu}E_{ab}(\boldsymbol{u}). \end{aligned} \tag{3.45}$$

In the case of a plane stress state, one obtains

$$\underbrace{\begin{Bmatrix} S_{11} \\ S_{22} \\ S_{12} \end{Bmatrix}}_{\{\boldsymbol{S}(\boldsymbol{u})\}} = \underbrace{\frac{E}{1-\nu^2}\begin{bmatrix} 1 & \nu & 0 \\ \nu & 1 & 0 \\ 0 & 0 & (1-\nu)/2 \end{bmatrix}}_{[\boldsymbol{C}]} \underbrace{\begin{Bmatrix} E_{11} \\ E_{22} \\ 2E_{12} \end{Bmatrix}}_{\{\boldsymbol{E}(\boldsymbol{u})\}} \tag{3.46}$$

with E and ν as the Young's modulus and the Poisson's ratio, respectively.

Remark. Further details on the reduction of the forth-order elasticity tensor are given in standard continuum mechanics textbooks, e.g. [200].

After computing the stresses as given in Eq. (3.45), the internal forces are available as well, leading to the set of equations

$$\underbrace{\int_{\Omega_0} \boldsymbol{\mathcal{B}}_0^T \boldsymbol{S}(\boldsymbol{u}) \boldsymbol{F}^T d\Omega_0}_{f^{int} = \boldsymbol{K}(\boldsymbol{u})\,\boldsymbol{u}} = \underbrace{\int_{\Gamma_{t_i}^0} N_I t_i^0 \, d\Gamma_0}_{\boldsymbol{f}^{ext}}. \tag{3.47}$$

3.1.2.4 Tangent stiffness matrix formulation

In Eq. (3.41), the first part $d\boldsymbol{f}_{mat}^{int}$ depends on the material response since it involves the change of stress $d\boldsymbol{S}$. The second part $d\boldsymbol{f}_{geo}^{int}$ accounts for geometric effects of the deformation. Using the identity given in Eq. (3.31), the two parts can be written in standard index notation as

$$df_{mat\,iI}^{int} = \int_{\Omega_0} \frac{\partial N_I}{\partial X_k} dS_{kl} F_{il} d\Omega_0, \tag{3.48}$$

$$df_{geo\,iJ}^{int} = \int_{\Omega_0} \frac{\partial N_J}{\partial X_k} S_{kl} dF_{il} d\Omega_0. \tag{3.49}$$

Now, both increments are reformulated as $d\boldsymbol{f}_{mat}^{int} = \boldsymbol{K}^{mat} d\boldsymbol{u}$ and $d\boldsymbol{f}_{geo}^{int} = \boldsymbol{K}^{geo} d\boldsymbol{u}$ introducing material and geometric tangent stiffness matrices.

Material tangent stiffness matrix

Since the stress will be expressed by the fourth-order elasticity tensor $\mathbb{C}_{ijkl}$, rewriting Eq. (3.48) is helpful

$$d\boldsymbol{f}_{mat}^{int} = \int_{\Omega_0} \boldsymbol{B}_0^T \{d\boldsymbol{S}\} d\Omega_0 \tag{3.50}$$

where the increment of the PK2 stress is $\{d\boldsymbol{S}\} = [\boldsymbol{C}]\{d\boldsymbol{E}\}$ and a $\boldsymbol{B_0}$ matrix is introduced following [201] with

$$B_{jliI}^0 = \operatorname*{sym}_{j,l} \left(\frac{\partial N_I}{\partial X_j} F_{il} \right). \tag{3.51}$$

Note, that $\boldsymbol{B_0} \neq \boldsymbol{\mathcal{B}_0}$. Furthermore, it incorporates the deformation gradient $\boldsymbol{F}$, that can be easily computed by

$$\underset{[2\times2]}{\boldsymbol{F}} = \underset{[2\times2]}{\boldsymbol{I}} + \underset{[2\times2]}{\boldsymbol{H}} = \begin{bmatrix} \frac{\partial x}{\partial X} & \frac{\partial x}{\partial Y} \\ \frac{\partial y}{\partial X} & \frac{\partial y}{\partial Y} \end{bmatrix}, \tag{3.52}$$

with

$$\underset{[2\times2]}{\boldsymbol{H}} = \nabla_0 \boldsymbol{u} = \begin{bmatrix} u_1 & u_2 & u_3 & u_4 \\ v_1 & v_2 & v_3 & v_4 \end{bmatrix} \begin{bmatrix} N_{1,X} & N_{1,Y} \\ N_{2,X} & N_{2,Y} \\ N_{3,X} & N_{3,Y} \\ N_{4,X} & N_{4,Y} \end{bmatrix}. \tag{3.53}$$

Thus, for instance, the first part of $\boldsymbol{B}_0$ is calculated by

$$\underset{[3\times 2]}{\boldsymbol{B}_{0I}} = \begin{bmatrix} N_{I,X}\frac{\partial x}{\partial X} & N_{I,X}\frac{\partial y}{\partial X} \\ N_{I,Y}\frac{\partial x}{\partial Y} & N_{I,Y}\frac{\partial y}{\partial Y} \\ N_{I,X}\frac{\partial x}{\partial Y} + N_{I,Y}\frac{\partial x}{\partial X} & N_{I,X}\frac{\partial y}{\partial Y} + N_{I,Y}\frac{\partial y}{\partial X} \end{bmatrix}. \tag{3.54}$$

Using $\{d\boldsymbol{E}\} = \boldsymbol{B_0 du}$ leads to

$$d\boldsymbol{f}^{int}_{mat} = \int_{\Omega_0} \boldsymbol{B}_0^T[\boldsymbol{C}]\ \boldsymbol{B}_0 d\Omega_0\ \boldsymbol{du}, \tag{3.55}$$

and, thus, the *material* tangent stiffness matrix becomes

$$\underset{[8x8]}{\boldsymbol{K}^{\,mat}} = \int_{\Omega_0} \underset{[8x3][3x3][3x8]}{\boldsymbol{B}_0^T[\boldsymbol{C}]\,\boldsymbol{B}_0}\, d\Omega_0. \tag{3.56}$$

It can be seen, that the material tangent stiffness matrix connects the increments of the internal nodal forces to the increment of the displacements based on the material response.

Geometric tangent stiffness matrix

Similarly, the geometric stiffness matrix becomes from Eq. (3.49)

$$\begin{aligned} df^{int}_{geo\,iI} &= \int_{\Omega_0} \frac{\partial N_I}{\partial X_k} S_{kl} dF_{il} d\Omega_0, \\ &= \int_{\Omega_0} \mathcal{B}^0_{Ik} S_{kl} \mathcal{B}^0_{lS} d\Omega_0\ du_{iS}, \\ &= \int_{\Omega_0} \mathcal{B}^0_{Ik} S_{kl} \mathcal{B}^0_{lS} d\Omega_0\ \delta_{it} du_{tS}, \\ d\boldsymbol{f}^{int}_{geo\,I} &= \boldsymbol{I} \int_{\Omega_0} \boldsymbol{\mathcal{B}}^T_{0I} \boldsymbol{S} \boldsymbol{\mathcal{B}}_{0S} d\Omega_0\ d\boldsymbol{u}_S, \end{aligned} \tag{3.57}$$

where the identity $dF_{il} = \mathcal{B}^0_{lS}\ du_{iS}$ is applied. Thus, the geometric tangent stiffness matrix becomes

$$\boldsymbol{K}^{geo}_{IJ} = \boldsymbol{I} \int_{\Omega_0} \boldsymbol{\mathcal{B}}^T_{0I} \boldsymbol{S} \boldsymbol{\mathcal{B}}_{0J} d\Omega_0, \tag{3.58}$$

where the identity applies as a submatrix operator on each scalar α_{IJ} with

$$\alpha_{IJ} = \int_{\Omega_0} \underset{[1x2]}{\boldsymbol{\mathcal{B}}_{0I}^T} \underset{[2x2]}{\boldsymbol{S}} \underset{[2x1]}{\boldsymbol{\mathcal{B}}_{0J}^T} d\Omega_0. \tag{3.59}$$

leading to the geometric tangent stiffness matrix written as

$$\boldsymbol{K}^{geo} = \begin{bmatrix} \alpha_{11} & 0 & \alpha_{12} & 0 & \alpha_{13} & 0 & \alpha_{14} & 0 \\ 0 & \alpha_{11} & 0 & \alpha_{12} & 0 & \alpha_{13} & 0 & \alpha_{14} \\ \alpha_{21} & 0 & \alpha_{22} & 0 & \alpha_{23} & 0 & \alpha_{24} & 0 \\ 0 & \alpha_{21} & 0 & \alpha_{22} & 0 & \alpha_{23} & 0 & \alpha_{24} \\ \alpha_{31} & 0 & \alpha_{32} & 0 & \alpha_{33} & 0 & \alpha_{34} & 0 \\ 0 & \alpha_{31} & 0 & \alpha_{32} & 0 & \alpha_{33} & 0 & \alpha_{34} \\ \alpha_{41} & 0 & \alpha_{42} & 0 & \alpha_{43} & 0 & \alpha_{44} & 0 \\ 0 & \alpha_{41} & 0 & \alpha_{42} & 0 & \alpha_{43} & 0 & \alpha_{44} \end{bmatrix}. \tag{3.60}$$

Finally, the tangent stiffness matrix $\boldsymbol{K_T}$ can be computed by Eqs. (3.56) and (3.58).

3.1.3 Fundamentals of topology optimization techniques

The optimization techniques implemented in this work aim to find an optimal distribution of the design variables to maximize a specific objective function under certain constraints, which will be explained first. Then, two different techniques implemented in this work are outlined: the closed-form optimality criteria method and the globally convergent method of moving asymptotes.

3.1.3.1 Design variables, objective functions and constraints

Design variables

Motivated by already established optimization techniques aiming to maximize the stiffness of structures, artificial, dimensionless densities ρ_e for

Figure 3.5: Graphical interpretation of different values of the design variables ranging from solid (black, $\rho_e = 1$) to void (white, $\rho_e \approx 0$)

each FE are introduced as design variables. The design variables ρ_e are bounded by unity and (almost) zero, where the lower bound $\underline{\rho} = 1 \cdot 10^{-3}$ is introduced to avoid numerical difficulties, such as singularity of the global stiffness matrix

$$0 \quad < \quad \underline{\rho} \quad \leq \quad \rho_e \quad \leq \quad \overline{\rho} = 1. \tag{3.61}$$

Thus, density values of (almost) zero or unity represent void or solid material of the corresponding FE, as illustrated in Fig. 3.5.

The global stiffness matrix $\boldsymbol{K}$ is assembled by density-weighted, local stiffnesses of each FE, i.e. solid FE are counted in, whereas void FE are practically not

$$\boldsymbol{K} = \bigcup_{e=1}^{N} \rho_e \boldsymbol{K}_e. \tag{3.62}$$

Objective functions

Topology optimization techniques of *stiff structures* often aim to maximize the stiffness of the entire structure. An objective function that describes this stiffness is the overall strain energy (SE) that has to be minimized in the domain:

$$SE = \frac{1}{2} \int_{\Omega_0} \boldsymbol{\sigma}_{\text{in}} \boldsymbol{E}_{\text{in}} d\Omega_o, \tag{3.63}$$

where $\boldsymbol{\sigma}_{\text{in}}$ is the stress field when only the input load at the input point P_{in} is applied. This or similar formulations are often minimized to design a nearly rigid structure with maximum stiffness.

In contrast to this, topology optimization of *compliant mechanisms* needs to yield flexible mechanisms that are very compliant while being able to resist certain loads. An objective function that describes the flexibility of the domain is the mutual potential energy (MPE) that has to be maximized

$$MPE = \int_{\Omega} \boldsymbol{\sigma}_{\text{out}} \boldsymbol{E}_{\text{in}} d\Omega, \tag{3.64}$$

where $\boldsymbol{\sigma}_{\text{out}}$ is the stress field due to a unit (dummy) load at the output point P_{out}, and $\boldsymbol{\epsilon}_{\text{in}}$ is the strain field due to the input load at the input point P_{in}. Numerically, it can be computed by using a FE discretization

$$MPE = \boldsymbol{v}^T \boldsymbol{K} \boldsymbol{u}, \tag{3.65}$$

where $\boldsymbol{u}$ and $\boldsymbol{v}$ are the nodal displacements caused by the forces $\boldsymbol{f}_{in}$ and $\boldsymbol{f}_{out}$ at the input point P_{in} and output point P_{out}, respectively.

Since CM have to withstand applied forces as well as provide sufficient motion, different approaches combining SE and MPE have been investigated, such as maximizing the ratio, i.e. max $\frac{MPE}{SE}$, or minimizing a convex combination, i.e. $min\ [-\alpha MPE + (1-\alpha)SE]$ for different $0 < \alpha < 1$, as described in [13].

However, since the main purpose of CM is to meet a specific motion performance, the MPE representing the output motion is further considered as the most relevant objective function.

Constrained optimization problem

The topology optimization problem aims to find the optimal design variables that maximize the aforementioned objective function. However, there are different mathematical, material and mechanical constraints that have to be considered yielding a *constrained* optimization problem.

Besides the mathematical limitation on the design variables given in Eq. (3.61), the most important constraint is given by the vector-valued, quasi-static equilibrium equation, that represent the mechanical behavior of the entire FE system. These equations ultimately depend on the

design variables and must hold for all intermediate and final solutions of the optimization problems

$$\boldsymbol{K}\left(\boldsymbol{u},\boldsymbol{\rho}\right)\ \boldsymbol{u}=\boldsymbol{f}. \tag{3.66}$$

Another relevant material constraint is the limitation of the overall material that can be used. Without a material constraint an optimal solution is typically not found. In stiffness maximization, it would lead to the obvious solution of a full solid material domain, i.e. $\rho_e = 1\ \forall\ e = 1 \ldots N$. In flexibility maximization it would lead to a void material domain $\rho_e \approx 0\ \forall\ e = 1 \ldots N$, which is obviously unusable. Therefore, an overall material specification V is introduced

$$\sum_{e=1}^{N} \left(\rho_e - V\right) = 0, \tag{3.67}$$

where $0 < V < 1$ is typically chosen based on numerical experience to $V = 0.3$, i.e. three out of ten FE are set to be solid.

Remark. Further constraints, such as specific output motions are explained in Sect. 3.2.

3.1.3.2 Optimality criteria method

The optimality criteria (OC) method is well suited for topology optimization purposes due to its simplicity and efficiency. Here, it is explained using the following, relevant optimization problem

$$(\mathbb{P})_{\mathrm{OC}} = \begin{cases} \max\limits_{\rho} & g_0(\boldsymbol{\rho}) = \sum_{e=1}^{N} \boldsymbol{u}_e^T \rho_e \boldsymbol{K}_e \boldsymbol{v}_e \\ \text{s.t.} & g_1(\boldsymbol{\rho}) = \sum_{e=1}^{N} \left(\rho_e - V\right) = 0 \\ & \boldsymbol{K}(\boldsymbol{\rho})\boldsymbol{u} = \boldsymbol{f} \\ & \{\boldsymbol{\rho} \in \mathbb{R}^N : \underline{\rho} \leq \rho_e \leq \overline{\rho}, e = 1, \ldots, N\}, \end{cases} \tag{3.68}$$

where $g_0(\boldsymbol{\rho})$ is the MPE which represents the output motion of a compliant mechanism caused by a unit dummy load, and $g_1(\boldsymbol{\rho})$ the volume

constraint. The derivative with respect to the (unknown) design variables is

$$\frac{\partial g_0(\boldsymbol{\rho})}{\partial \rho_e} = \boldsymbol{u}_e^T \boldsymbol{K}_e \boldsymbol{v}_e. \tag{3.69}$$

Following standard literature such as [198], a linearization of $g_0(\boldsymbol{\rho})$ in the intervening variable

$$y_e = \rho_e^{-\alpha}, \tag{3.70}$$

is beneficial. Here, the positive scalar α is introduced. Then, the linearized objective function becomes

$$g_0(\boldsymbol{\rho}) \approx g_0(\boldsymbol{\rho}^{(k)}) + \sum_{e=1}^{N} \left.\frac{\partial g_0(\boldsymbol{\rho})}{\partial y_e}\right|_{\boldsymbol{\rho}=\boldsymbol{\rho}^{(k)}} (y_e - y_e^{(k)}), \tag{3.71}$$

where the derivative is calculated using the chain rule

$$\frac{\partial g_0(\boldsymbol{\rho})}{\partial y_e} = \frac{\partial g_0(\boldsymbol{\rho})}{\partial \rho_e}\frac{\partial \rho_e}{\partial y_e} = \frac{\partial g_0(\boldsymbol{\rho})}{\partial \rho_e}\frac{1}{\frac{\partial \rho_e^{-\alpha}}{\partial \rho_e}} = -\frac{\rho_e^{1+\alpha}}{\alpha}\frac{\partial g_0(\boldsymbol{\rho})}{\partial \rho_e}. \tag{3.72}$$

Substituting Eqs. (3.69) and (3.72) into Eq. (3.71) yields

$$g_0(\boldsymbol{\rho}) \approx g_0 + \sum_{e=1}^{N} b_e^k \rho_e^{-\alpha}, \tag{3.73}$$

with

$$g_0 = const. \qquad \text{and} \qquad b_e^k = \frac{\boldsymbol{u}_e^T \boldsymbol{K}_e \boldsymbol{v}_e}{\alpha} \rho_e^{1+\alpha}. \tag{3.74}$$

This new subproblem becomes

$$(\mathbb{P})_{\text{OC, sub}} = \begin{cases} \min\limits_{\rho} & \sum_{e=1}^{N} b_e^k \rho_e^{-\alpha} \\ \text{s.t.} & g_1(\underline{\boldsymbol{\rho}}) = \sum_{e=1}^{N} (\rho_e - V) = 0 \\ & \boldsymbol{K}(\boldsymbol{\rho})\boldsymbol{u} = \boldsymbol{f} \\ & \{\boldsymbol{\rho} \in \mathbb{R}^N : \underline{\rho} \leq \rho_e \leq \overline{\rho}, e = 1, \ldots, N\}, \end{cases} \tag{3.75}$$

is convex and can be solved using Lagrangian duality. The Lagrangian function of Eq. (3.75) can be formulated as

$$\mathcal{L}(\boldsymbol{\rho}, \lambda) = \sum_{e=1}^{N} b_e^k \rho_e^{-\alpha} + \lambda \sum_{e=1}^{N} (\rho_e - V) = \sum_{e=1}^{N} \left(b_e^k \rho_e^{-\alpha} + \lambda \rho_e - \lambda V \right), \tag{3.76}$$

and the corresponding dual function is

$$\phi(\lambda) = \inf_{\underline{\rho} \leq \rho_e \leq \overline{\rho}} \mathcal{L}(\boldsymbol{\rho}, \lambda) = \inf_{\underline{\rho} \leq \rho_e \leq \overline{\rho}} \sum_{e=1}^{N} \left(\underbrace{b_e^k \rho_e^{-\alpha} + \lambda \rho_e - \lambda V}_{\phi_e} \right). \tag{3.77}$$

The dual function can be evaluated by finding separate minima for N element-wise functions

$$\phi_e(\boldsymbol{\rho}, \lambda) = b_e^k \rho_e^{-\alpha} + \lambda \rho_e - \lambda V. \tag{3.78}$$

The stationary point can be found by

$$\frac{\partial \phi_e(\boldsymbol{\rho}, \lambda)}{\partial \rho_e} = -\alpha b_e^k \rho_e^{-\alpha - 1} - \lambda \stackrel{!}{=} 0, \tag{3.79}$$

which is a minimum since the second derivative is always non-negative, throughout this work, i.e.

$$\frac{\partial^2 \phi_e(\boldsymbol{\rho}, \lambda)}{\partial \rho_e^2} = \alpha(\alpha + 1) b_e^k \rho_e^{-\alpha - 2} \geq 0. \tag{3.80}$$

The Eq. (3.79) leads to

$$\rho_e = \left(\frac{\alpha b_e^k}{\lambda} \right)^{\frac{1}{1+\alpha}}. \tag{3.81}$$

Considering the interval $\underline{\rho} \leq \rho_e \leq \overline{\rho}$ yields the primal-dual relation

$$\rho_e(\lambda) = \begin{cases} \underline{\rho} & \text{if} \quad \left(\frac{\alpha b_e^k}{\lambda} \right)^{\frac{1}{1+\alpha}} < \underline{\rho} \\ \left(\frac{\alpha b_e^k}{\lambda} \right)^{\frac{1}{1+\alpha}} & \text{if} \quad \underline{\rho} \leq \left(\frac{\alpha b_e^k}{\lambda} \right)^{\frac{1}{1+\alpha}} \leq \overline{\rho} \\ \overline{\rho} & \text{if} \quad \left(\frac{\alpha b_e^k}{\lambda} \right)^{\frac{1}{1+\alpha}} > \overline{\rho}. \end{cases} \tag{3.82}$$

The appropriately chosen $\rho_e(\lambda)$ is now inserted into Eq. (3.77) to obtain the dual function $\phi(\lambda)$ explicitly, leading to the dual problem

$$\phi(\lambda) = \mathcal{L}(\boldsymbol{\rho}(\lambda), \lambda) = \sum_{e=1}^{N} \phi_e(\rho_e(\lambda), \lambda). \tag{3.83}$$

The optimal value λ^* is determined by the stationary point of $\phi(\lambda)$ given by

$$\frac{\partial \phi(\lambda)}{\partial \lambda} = \sum_{e=1}^{N} \left(\frac{\partial \phi_e}{\partial \rho_e} \frac{\partial \rho_e}{\partial \lambda} + \frac{\partial \phi_e}{\partial \lambda} \right) \stackrel{!}{=} 0. \tag{3.84}$$

The product in the brackets is always zero, since

$$\frac{\partial \phi_e}{\partial \rho_e} = 0 \quad \text{if } \underline{\rho} \leq \rho_e \leq \overline{\rho}, \tag{3.85}$$

$$\frac{\partial \rho_e}{\partial \lambda} = 0 \quad \text{elsewhere} \tag{3.86}$$

as indicated by Eqs. (3.79) and (3.82). This leads to

$$\frac{\partial \phi(\lambda)}{\partial \lambda} = \sum_{e=1}^{N} \left(\rho_e(\lambda) - V \right) \stackrel{!}{=} 0, \tag{3.87}$$

showing that the dual problem has a stationary point if the volume constraint is satisfied. Due to the monotonic behavior of Eq. (3.87), it can be easily solved by, e.g. bisection method, leading to a unique solution λ^*.

Plugging λ^* into the primal-dual relation given by Eq. (3.82) yields an updated design variable for each element

$$\rho_e^{(k+1)} = \rho_e(\lambda^*). \tag{3.88}$$

Recalling Eqs. (3.74), (3.81) and the interval limitation given in Eq. (3.82) result in an update of the design variables

$$\rho_e^{(k+1)} = \min \left\{ \max \left[\left(\frac{\left(\boldsymbol{u}_e^{(k)} \right)^T \boldsymbol{K}_e \boldsymbol{v}_e^{(k)}}{\lambda} \right)^{\eta} \rho_e^{(k)}, \underline{\rho} \right], \overline{\rho} \right\}, \tag{3.89}$$

where a numerical damping term $\eta = \frac{1}{1+\alpha}$ is introduced to coincide with standard literature, e.g. [198].

3.1.3.3 Globally convergent method of moving asymptotes

The globally convergent method of moving asymptotes (GCMMA) is applied to nonlinear optimization problems with several inequality restrictions. It uses explicit, conservative, convex, separable approximations, where only function values $f_k(\boldsymbol{x})$ and first derivatives $\nabla f_k(\boldsymbol{x})$ of the objective function and the restriction inequalities are evaluated. The approximations and the corresponding moving asymptotes are calculated heuristically as described in detail in [89, 90]. A brief overview and a simple example are given here:

$$(\mathbb{P})_{\text{GCMMA}} = \begin{cases} \min & f_0(\boldsymbol{x}) + a_0 z + \sum_{k=1}^{m} (c_k y_k + \frac{1}{2} d_k y_k^2) \\ \text{s.t.} & f_k(\boldsymbol{x}) - a_k z - y_k \leq 0, k = 1, \ldots, m \\ & \boldsymbol{x} \in X = \{\boldsymbol{x} \in \mathbb{R}^N : x_i^{\min} \leq x_i \leq x_i^{\max}, i = 1, \ldots, n\} \\ & \boldsymbol{y} \in \mathbb{R}^m, \boldsymbol{y} \geq \boldsymbol{0} \\ & z \in \mathbb{R}, z \geq 0. \end{cases} \tag{3.90}$$

where $x_i^{\min}$ and $x_i^{\max}$ are the extremal values of the design variables, $f_0, f_1, \ldots, f_m$ are known, differentiable functions, e.g. cost and restriction functions, a_0, a_k, c_k and d_k non-negative, real numbers with $a_0 > 0, a_k \geq 0, c_k \geq 0, d_k \geq 0$ and $c_k + d_k > 0$ and for $a_k > 0$ with $a_k c_k > a_0$, $y_1, \ldots, y_m$ and z are artificial variables that are introduced for simplicity.

The GCMMA uses inner and outer loops, where the indices κ and ν denote the iteration number of the outer and inner loops. The optimization process is outlined here:

1. Choose a feasible initial point $\boldsymbol{x}^{(1)}, \boldsymbol{y}^{(1)}$ and $z^{(1)}$.
2. Perform an **outer iteration** from $\left(\boldsymbol{x}^{(\kappa)},\ \boldsymbol{y}^{(\kappa)},\ z^{(\kappa)}\right)$ to $\left(\boldsymbol{x}^{(\kappa+1)},\ \boldsymbol{y}^{(\kappa+1)},\ z^{(\kappa+1)}\right)$:

(a) Create a subproblem by replacing the functions $f_k(\boldsymbol{x})$ by convex approximations $\tilde{f}_k^{(\kappa,\nu)}(\boldsymbol{x})$.

(b) Calculate the optimum of the subproblem yielding $\left(\hat{\boldsymbol{x}}^{(\kappa,0)}, \hat{\boldsymbol{y}}^{(\kappa,0)}, \hat{z}^{(\kappa,0)}\right)$.

(c) Check if $\tilde{f}_k^{(\kappa,0)}(\hat{\boldsymbol{x}}^{(\kappa,0)}) \geq f_k(\hat{\boldsymbol{x}}^{(\kappa,0)})\ \forall\ k = 0, 1, \ldots, m$.
If yes, next (outer) iteration step is reached $(\boldsymbol{x}^{(\kappa+1)}, \boldsymbol{y}^{(\kappa+1)}, z^{(\kappa+1)}) = (\hat{\boldsymbol{x}}^{(\kappa,0)}, \hat{\boldsymbol{y}}^{(\kappa,0)}, \hat{z}^{(\kappa,0)})$.
If no, perform an **inner iteration**:

i. Create a new subproblem by replacing the functions $f_k(\boldsymbol{x})$ with $\tilde{f}_k^{(\kappa,1)}(\boldsymbol{x})$, that are even more conservative than $\tilde{f}_k^{(\kappa,0)}(\boldsymbol{x})$, for each k where the inequality equations are not met and evaluate $\tilde{f}_k^{(\kappa,1)}(\boldsymbol{x})$ at $\boldsymbol{x}^{(\kappa)}$.

ii. Calculate the optimum of the (inner) subproblem yielding $\left(\hat{\boldsymbol{x}}^{(\kappa,1)}, \hat{\boldsymbol{y}}^{(\kappa,1)}, \hat{z}^{(\kappa,1)}\right)$.

iii. Check if $\tilde{f}_k^{(\kappa,1)}(\hat{\boldsymbol{x}}^{(\kappa,1)}) \geq f_k(\hat{\boldsymbol{x}}^{(\kappa,1)})\ \forall\ k = 0, 1, \ldots, m$.
If yes, inner iteration is finished and next (outer) iteration step is reached $(\boldsymbol{x}^{(\kappa+1)}, \boldsymbol{y}^{(\kappa+1)}, z^{(\kappa+1)}) = (\hat{\boldsymbol{x}}^{(\kappa,1)}, \hat{\boldsymbol{y}}^{(\kappa,1)}, \hat{z}^{(\kappa,1)})$, i.e. outer iteration loop is finished, as well.
If no, start another inner iteration with $\tilde{f}_k^{(\kappa,2)}(\boldsymbol{x})$, etc. After a finite number ν, $\tilde{f}_k^{(\kappa,\nu)}(\hat{\boldsymbol{x}}^{(\kappa,\nu)}) \geq f_k(\hat{\boldsymbol{x}}^{(\kappa,\nu)})\ \forall\ k = 0, 1, \ldots, m$, and thus $(\boldsymbol{x}^{(\kappa+1)}, \boldsymbol{y}^{(\kappa+1)}, z^{(\kappa+1)}) = (\hat{\boldsymbol{x}}^{(\kappa,\nu)}, \hat{\boldsymbol{y}}^{(\kappa,\nu)}, \hat{z}^{(\kappa,\nu)})$.

(d) Check if $(\boldsymbol{x}^{(\kappa+1)}, \boldsymbol{y}^{(\kappa+1)}, z^{(\kappa+1)}) = (\hat{\boldsymbol{x}}^{(\kappa)}, \hat{\boldsymbol{y}}^{(\kappa)}, \hat{z}^{(\kappa)})$.
If no, start another outer iteration.
If yes, outer iteration loop is finished and exit.

Example 3.1.1. *The stepwise calculation of the minimum of the function* $f_0(x) = x^3 + x^2$ *within* $x \in [-2,\ 1.5]$ *using the GCMMA is illustrated in Fig. 3.6. The function* $f_0(x)$ *(blue plot) is approximated by a subproblem* $\tilde{f}_k^{(\kappa,\nu)}(x)$ *(red plot) evaluated at the current step* $\left(\boldsymbol{x}^{(\kappa)}, \boldsymbol{y}^{(\kappa)}, z^{(\kappa)}\right)$ *(blue dot) within the moving asymptotes (green, dotted lines). The*

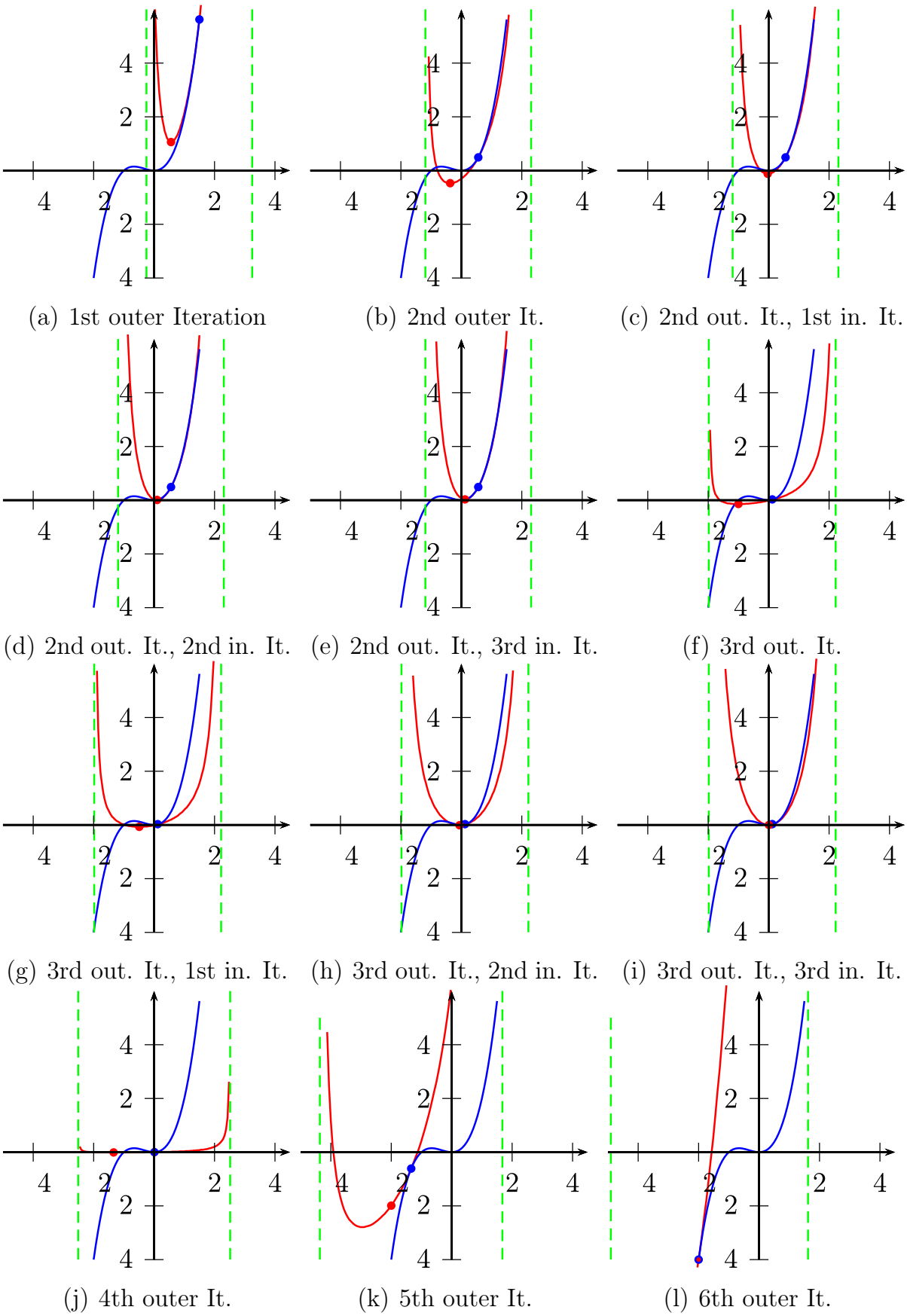

(a) 1st outer Iteration (b) 2nd outer It. (c) 2nd out. It., 1st in. It.

(d) 2nd out. It., 2nd in. It. (e) 2nd out. It., 3rd in. It. (f) 3rd out. It.

(g) 3rd out. It., 1st in. It. (h) 3rd out. It., 2nd in. It. (i) 3rd out. It., 3rd in. It.

(j) 4th outer It. (k) 5th outer It. (l) 6th outer It.

Figure 3.6: Stepwise minimization of function given in Ex. 3.1.1 using GCMMA adopted from [203]

minimum of the subproblem $\left(\hat{\boldsymbol{x}}^{(\kappa,0)}, \hat{\boldsymbol{y}}^{(\kappa,0)}, \hat{z}^{(\kappa,0)}\right)$ *(red dot) becomes the next (outer) iteration step.*

The minimum is found after six (outer) iterations, where the current and next iteration step coincide, i.e. $(\boldsymbol{x}^{(\kappa+1)}, \boldsymbol{y}^{(\kappa+1)}, z^{(\kappa+1)}) = (\hat{\boldsymbol{x}}^{(\kappa)}, \hat{\boldsymbol{y}}^{(\kappa)}, \hat{z}^{(\kappa)})$*, as shown in Fig. 3.6 (l).*

Remark. The GCMMA subroutines and the corresponding documentation were provided by K. Svanberg from Royal Institute of Technology, Sweden [88–90, 204, 205].

3.2 Implementation

The topology optimization algorithm is implemented into a MATLAB environment. The previously described methods, namely OC and GCMMA, are combined into a staggered, iterative topology optimization algorithm providing superior performance in terms of robustness and functionality than applied individually. The implemented algorithm is illustrated in Fig. 3.7. It

- starts with an **initialization step**,
- continues with the **optimization algorithms** and
- finishes with a **convergence check**.

Each optimization algorithm block, OC and GCMMA, consists of a similar scheme:

Performing a (non)linear *finite element analysis* (FEA), where the global stiffness matrix $\boldsymbol{K}$ is calculated and assembled as well as the displacements $\boldsymbol{u}$ are computed for given loads $\boldsymbol{f}$. Evaluating the *objective function*, where the scalar-valued objective function g_0 is calculated based on the displacements $\boldsymbol{u}$. Performing *sensitivity analysis*, where necessary derivatives $dg_0/d\rho_i$ are calculated based on the value of the objective function and the current design variables. *Updating* the design variables, where the new design variables are calculated based on the current values of the objective function and its derivative. An *exit check* if a maximum number of iterations is reached. If yes exit, if no start a new iteration (within the same optimization algorithm).

Relevant aspects of the implementation process and most significant parts of the source code are described here.

3.2.1 Initializing

In the initialization step, the 2D material design domain is discretized by $N = N_{elx} \times N_{ely}$ rectangular FE, where N_{elx} and N_{ely} correspond to

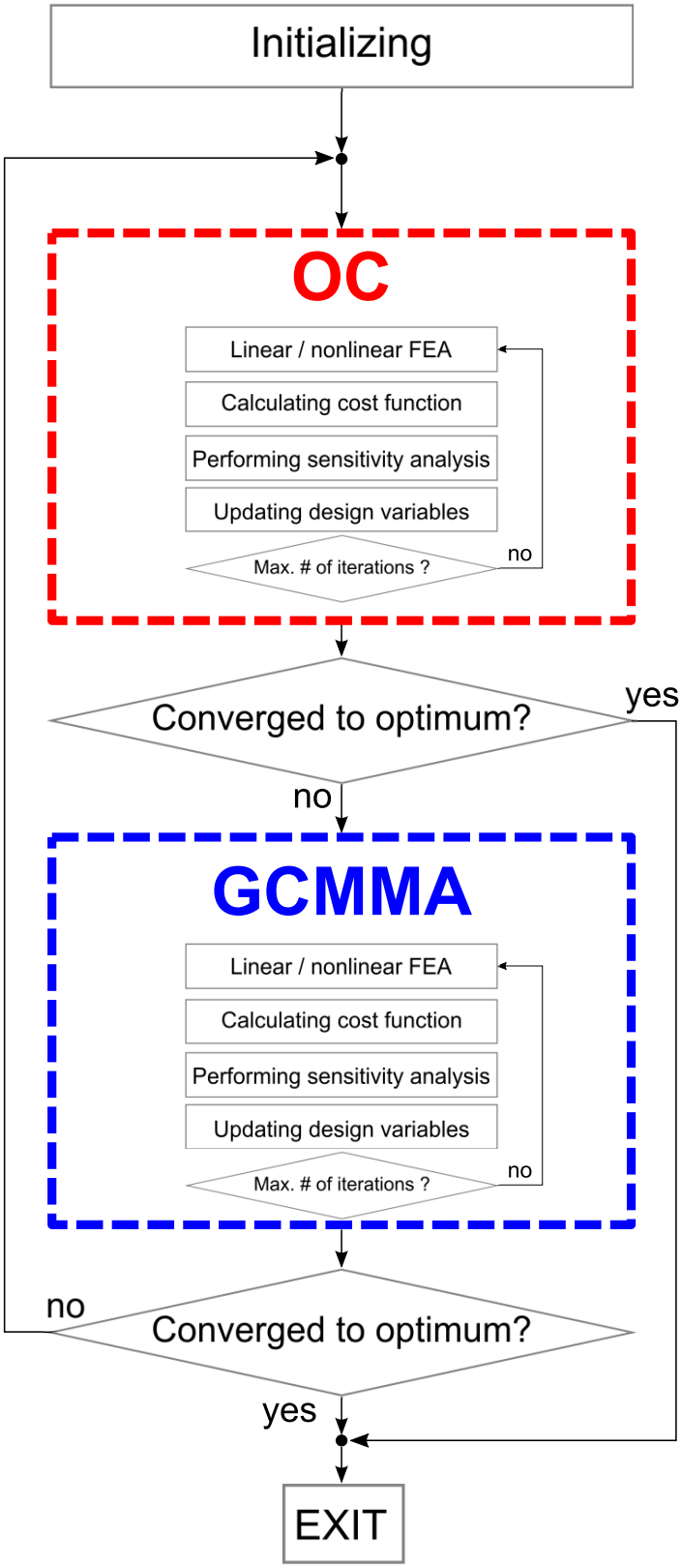

Figure 3.7: Overall scheme of the staggered, iterative topology optimization algorithm using optimality criteria (OC) method and globally convergent method of moving asymptotes (GCMMA)

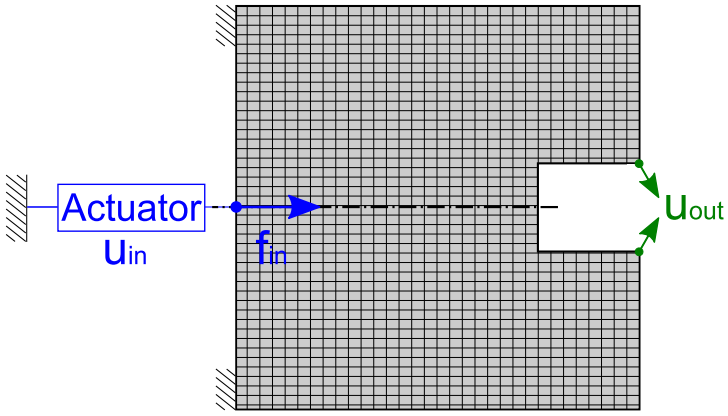

Figure 3.8: Specified input force $\boldsymbol{f_{in}}$, boundary conditions, actuator stiffness, material data and output direction $\boldsymbol{u_{out}}$

the number of FE in x-direction and y-direction, respectively. This leads to N design variables ρ_e with $e = 1 \ldots N$.

Certain areas are specified to be solid or void over the entire optimization process, i.e. the design variables are kept constant $\rho_{spec} = \underline{\rho}$ or $\rho_{spec} = \overline{\rho}$, respectively.

Then, the relevant, case-dependent boundary conditions (BC), real and dummy loads are applied on the FE nodes. Fig. 3.8 illustrates an example with specified, horizontal input load at the left center (blue) and a desired output direction at the right (green).

3.2.2 Finite element analysis

3.2.2.1 Solving linear FEA

The global stiffness matrix $\boldsymbol{K}_{lin}$ is obtained by assembling the element stiffness matrices $\boldsymbol{K}_{lin}^{e}$ depending on the numbering scheme and a design factor.

The global load vector $\boldsymbol{f}$ represents external loads that are – in this work – not calculated but pre-specified separately depending on the load case.

In order to calculate the objective function $g_0 = g_0(\boldsymbol{u}(\boldsymbol{\rho}))$, a finite element analysis (FEA) is performed in each optimization iteration i

yielding the nodal displacements $\boldsymbol{u}^{(i)} = \boldsymbol{u}^{(i)}(\boldsymbol{\rho}^{(i)})$ depending on the current design.

A linear FEA is implemented and applied in the early topology optimization process due to its high efficiency in terms of computation time and memory usage. First, the *local* stiffness matrix is computed and, then, the *global* stiffness matrix is assembled.

3.2.2.2 Computing local stiffness matrix

As explained in Sect. 3.1.2.1, a mapping to a master element domain is beneficial, i.e the element stiffness matrix becomes

$$\begin{aligned} \underset{[8\times8]}{\boldsymbol{K}^e_{lin}} &= \int_{-b}^{b}\int_{-a}^{a} \underset{[8\times3]}{\boldsymbol{B}}^T \underset{[3\times3]}{[\boldsymbol{C}]} \underset{[3\times8]}{\boldsymbol{B}}\, dx\, dy, \\ &= \underbrace{\int_{-1}^{+1}\int_{-1}^{+1} \underset{[8\times3]}{\boldsymbol{B}}^T \underset{[3\times3]}{[\boldsymbol{C}]} \underset{[3\times8]}{\boldsymbol{B}}\, \det \boldsymbol{J}(\xi,\eta)\, d\xi\, d\eta}_{\text{Calculation on master element}}. \end{aligned} \tag{3.91}$$

Instead of a numerically-expensive closed-form evaluation over the whole domain $\xi, \eta \in [-1, +1]$, a pointwise integration (Gauss quadrature) is used to calculate the element stiffness matrix. In order to ensure exact integration of a polynomial function with degree $p = 2n - 1$, the integrand is evaluated at n Gauss points.

$$\int_{-1}^{+1}\int_{-1}^{+1} f(\xi,\eta)\; d\xi\, d\eta = \sum_{i=1}^{n}\sum_{j=1}^{n} w_i w_j f(\xi_i,\eta_j). \tag{3.92}$$

In the case of the aforementioned Q4-elements, $n = 2$ Gauss points are chosen for each direction ξ, η to deal with the quadratic integrand $p = 2$. The Gauss points are illustrated in Fig. 3.9. Thus, the element stiffness matrix is calculated as

$$\underset{[8\times8]}{\boldsymbol{K}^e_{lin}} = \sum_{i=1}^{n=2}\sum_{j=1}^{n=2} w_i w_j \underset{[8\times3]}{\boldsymbol{B}}(\xi_i,\eta_j)^T \underset{[3\times3]}{[\boldsymbol{C}]} \underset{[3\times8]}{\boldsymbol{B}}(\xi_i,\eta_j) \det \boldsymbol{J}(\xi_i,\eta_j). \tag{3.93}$$

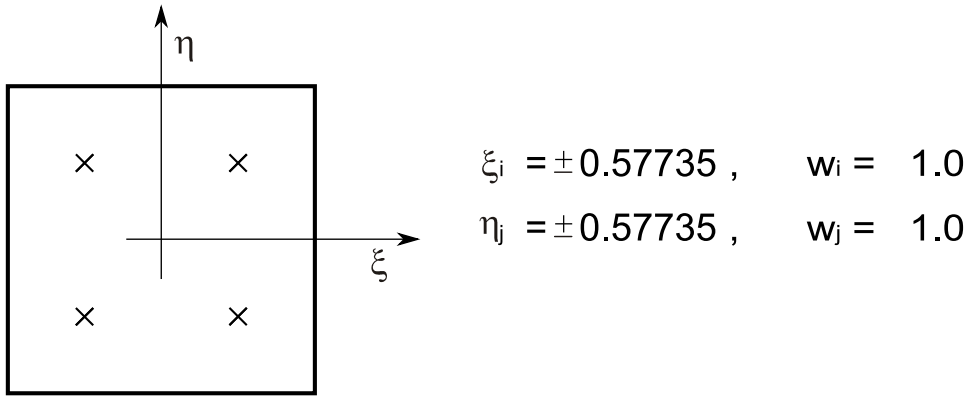

Figure 3.9: 2×2 pointwise integration using Gauss points ξ_i, η_j and weights w_i, w_j

Recalling that all FE are equally sized and any FE deformations are neglected in the linear FEA, $\boldsymbol{K}_{lin}^{e}$ is equal for all elements and, thus, it is computed only once.

3.2.2.3 Assembling global stiffness matrix

The global stiffness matrix $\boldsymbol{K}_{lin}$, i.e. the stiffness of the entire system, is assembled following a column-wise global numbering scheme of each FE and a counterclockwise global-local renumbering, as shown in Fig. 3.10.

The design variables ρ_e weighs each FE and, thus, its stiffness that is added to the entire CM.

$$\boldsymbol{K}_{lin} = \sum_{e=1}^{N} \rho_e \boldsymbol{K}_{lin}^{e}. \tag{3.94}$$

Simply following this assembling scheme leads in the later optimization process to topologies that consist of grey FE elements possessing intermediate design variables $\rho_e \approx 0.5$, which are hard to manufacture.

In order to get discrete solid-void solutions, intermediate design variables are penalized by using a power-law treatment ρ_e^p often referred as the Solid Isotropic Microstructure with Penalization (SIMP) approach that steers the design variables to zero or unity, as illustrated in Fig. 3.11.

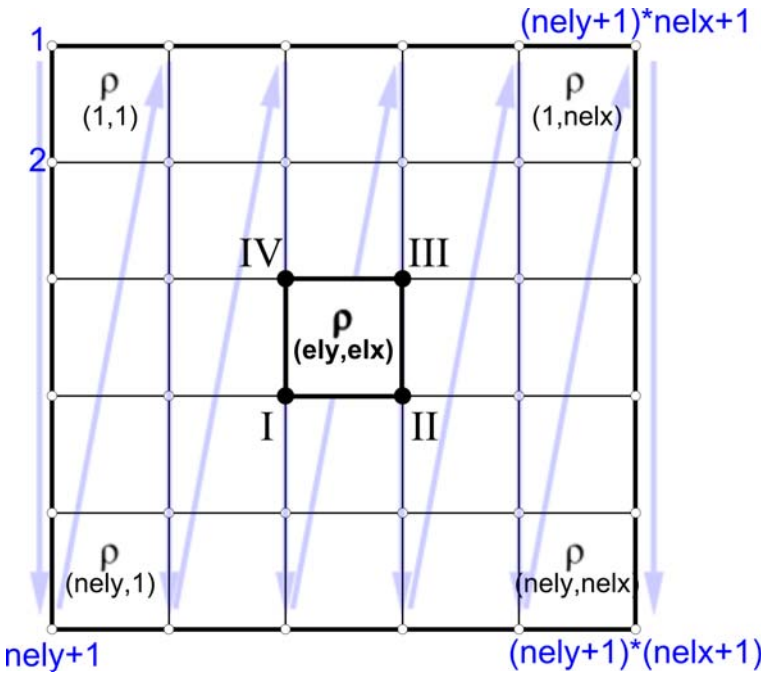

Figure 3.10: FE meshed material domain with global and local numbering scheme using a Cartesian frame

Therefore the global stiffness matrix is computed by

$$\boldsymbol{K}_{lin} = \sum_{e=1}^{N} \rho_e^p \boldsymbol{K}_{lin}^e. \tag{3.95}$$

The following excerpt of the source code shows the assembly of the global stiffness matrix $\boldsymbol{K}_{lin}$, which is simply written as `K`:

```
% Assembling global stiffness matrix
K = sparse(2*(nelx+1)*(nely+1), 2*(nelx+1)*(nely+1));
for elx = 1:nelx
 for ely = 1:nely
  n1 = (nely+1)*(elx-1)+ ely; % upper left global element node nr
  n2 = (nely+1)* elx   + ely; % upper right global element node nr
  % edof global/ local numbering
  edof = [2*n1+1;2*n1+2;2*n2+1;2*n2+2;2*n2-1;2*n2;2*n1-1;2*n1];
  % Assembling global stiffness matrix
  K(edof,edof) = K(edof,edof) + x(ely,elx)^penal*KE;
 end
end
```

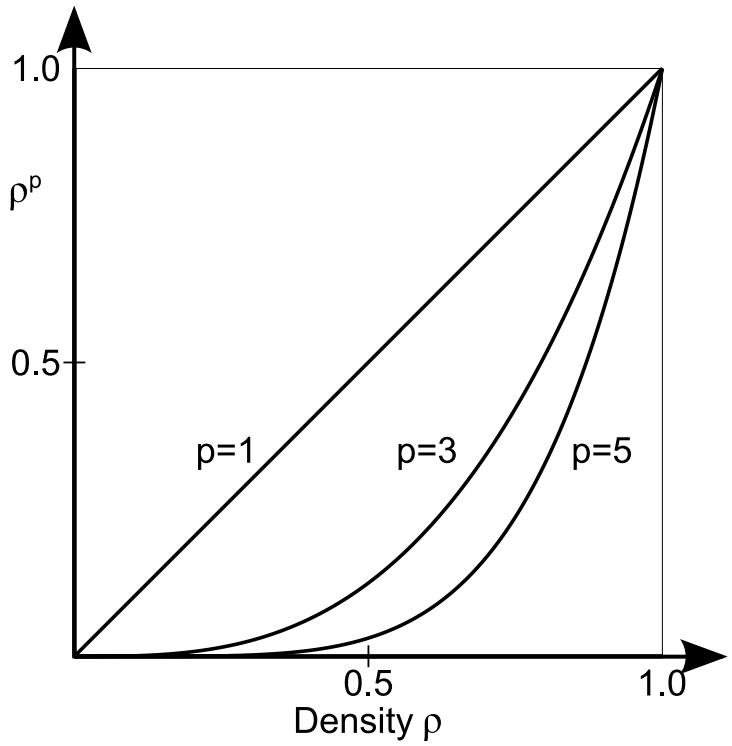

Figure 3.11: SIMP approach: Penalized design variables ρ_e^p (element densities) for different penalization values p

Remark. Further details on the SIMP approach can be found in [206]. Alternative methods suppressing intermediate densities were proposed by Stolpe and Svanberg [207], Fuchs [208] and Sigmund [209]. Those methods are less established in topology synthesis and are not considered in this work. A comparison between SIMP and ESO in terms of performance on a tie-beam was published in 2007 [36], where the SIMP approach was shown to be superior and, thus, implemented in this work.

After assembling the global stiffness matrix $\boldsymbol{K}_{lin}$ and setting the load vector $\boldsymbol{f}$ depending on the load case, the linear set of equation

$$\boldsymbol{K}_{lin}\,\boldsymbol{u} = \boldsymbol{F} \tag{3.96}$$

is solved for the displacements $\boldsymbol{u}$ considering the boundary conditions that, again, depend on the load case.

3.2.2.4 Solving nonlinear FEA

In the previously shown linear FE formulation, small (infinite) deformations as well as fixed loads are assumed yielding the linear equation $\boldsymbol{K}_{lin}\ \boldsymbol{u} = \boldsymbol{f}$. Here, the displacements $\boldsymbol{u}$ depend linearly on the external load, i.e. higher loads correspond to respective higher displacements $\boldsymbol{K}_{lin}\ \alpha\boldsymbol{u} = \alpha\boldsymbol{f}$. The stiffness matrix $\boldsymbol{K}_{lin} = const.$ is calculated on the undeformed body and, thus, do not depend on the nodal displacements $\boldsymbol{u}$.

In CM, where large deformations might occur, it is crucial to perform the FE calculations under consideration of non-negligible deformations. Therefore, the stiffness of each (deformed) FE is affected by the nodal displacements and, thus, the global stiffness matrix depends on the displacements $\boldsymbol{u}$, as well. This leads to the nonlinear set of equilibrium equations

$$\boldsymbol{K}_{nonlin}(\boldsymbol{u})\ \boldsymbol{u} = \boldsymbol{f} \tag{3.97}$$

where the stiffness $\boldsymbol{K}_{nonlin} \neq const.$ depends on the deformation of each element and, thus, ultimately on the nodal displacements $\boldsymbol{u}$.

As opposed in the aforementioned linear case, this nonlinear equilibrium equation needs to be solved iteratively as explained now.

Remark. Further details on efficient solving of (large-scale) nonlinear sets of equations can be found in standard literature, e.g. [210].

The Eq. (3.97) is reformulated to a residual expression

$$\boldsymbol{R}(\boldsymbol{u}) = \underbrace{\boldsymbol{K}_{nonlin}(\boldsymbol{u})\ \boldsymbol{u}}_{\boldsymbol{f}^{int}} - \underbrace{\boldsymbol{f}}_{\boldsymbol{f}^{ext}} = \boldsymbol{0}, \tag{3.98}$$

where, again, $\boldsymbol{f}^{ext}$ is the external force vector and $\boldsymbol{f}^{int} = \boldsymbol{f}^{int}(\boldsymbol{u})$ is the nonlinear, internal force vector. In order to solve this nonlinear equilibrium equation iteratively the Newton-Raphson method is advantageous due to its quadratic convergence. Therefore, a Taylor series expansion of the nonlinear term at the current displacement is performed

$$\boldsymbol{f}_{int}^{(1)}(\boldsymbol{u}_0 + \boldsymbol{\Delta u}_1) = \boldsymbol{f}_{int}(\boldsymbol{u}_0) + \left[\frac{d\boldsymbol{f}_{int}}{d\boldsymbol{u}}\right]_{\boldsymbol{u}_0} \Delta\boldsymbol{u}_1 \tag{3.99}$$

and follows these steps that are illustrated in Fig. 3.12:

1. Computing the tangent stiffness matrix $\boldsymbol{K}_T$ for a known $\boldsymbol{u}_{(i)}$ as shown in Fig. 3.12(a)

$$\frac{d\boldsymbol{f}_{int}}{d\boldsymbol{u}} = \frac{d\left(\boldsymbol{K}(\boldsymbol{u})\boldsymbol{u}\right)}{d\boldsymbol{u}} = \boldsymbol{K}_{T,i}. \tag{3.100}$$

2. Computing next step size $\Delta\boldsymbol{u}_{(i+1)}$ using the existing imbalance between internal and external forces $\Delta\boldsymbol{f}^{(i+1)} = \boldsymbol{f}_{ext} - \boldsymbol{f}_{int}^{(i)}$ as shown in Fig. 3.12(b)

$$\Delta\boldsymbol{u}_{(i+1)} = \left(\left[\boldsymbol{K}_T\right]_{\boldsymbol{u}_{(0)}}\right)^{-1} \Delta\boldsymbol{f}^{(i+1)} \tag{3.101}$$

3. Computing next displacements $\boldsymbol{u}_{(i+1)}$ and internal forces $\boldsymbol{f}_{int}^{(i+1)}$ as shown in Fig. 3.12(c)

$$\boldsymbol{u}_{(i+1)} = \boldsymbol{u}_{(i)} + \Delta\boldsymbol{u}_{(i+1)} \tag{3.102}$$

$$\boldsymbol{f}_{int}^{(i+1)} = \boldsymbol{f}_{int}^{(i+1)}\left(\boldsymbol{u}_{(i+1)}\right) \tag{3.103}$$

4. Repeating steps 2 and 3 without recalculating the tangent stiffness matrix $\boldsymbol{K}_T$ until $\boldsymbol{f}_{int}^{(i+1)} = \boldsymbol{f}_{ext}$, i.e. the residual term vanishes at the solution $\boldsymbol{u}_B$ as shown in Fig. 3.12(d)

$$\boldsymbol{R}(\boldsymbol{u}_B) = \boldsymbol{K}_{nonlin}(\boldsymbol{u}_B)\,\boldsymbol{u}_B - \boldsymbol{f} = \boldsymbol{0}. \tag{3.104}$$

Remark. The tangent stiffness matrix $\boldsymbol{K}_T$ is not calculated at each step of the nonlinear FEA, which causes a few more, but significantly faster iterations. Further details on the nonlinear FEA and including the efficient calculation of the tangent stiffness matrix, as implemented in this work, can be found in standard literature, e.g. [201].

The following excerpt of the source code shows the assembly of the nonlinear stiffness matrices and the solving for the new solution $\boldsymbol{u}_{(i+1)}$, which is simply written as `u_new`:

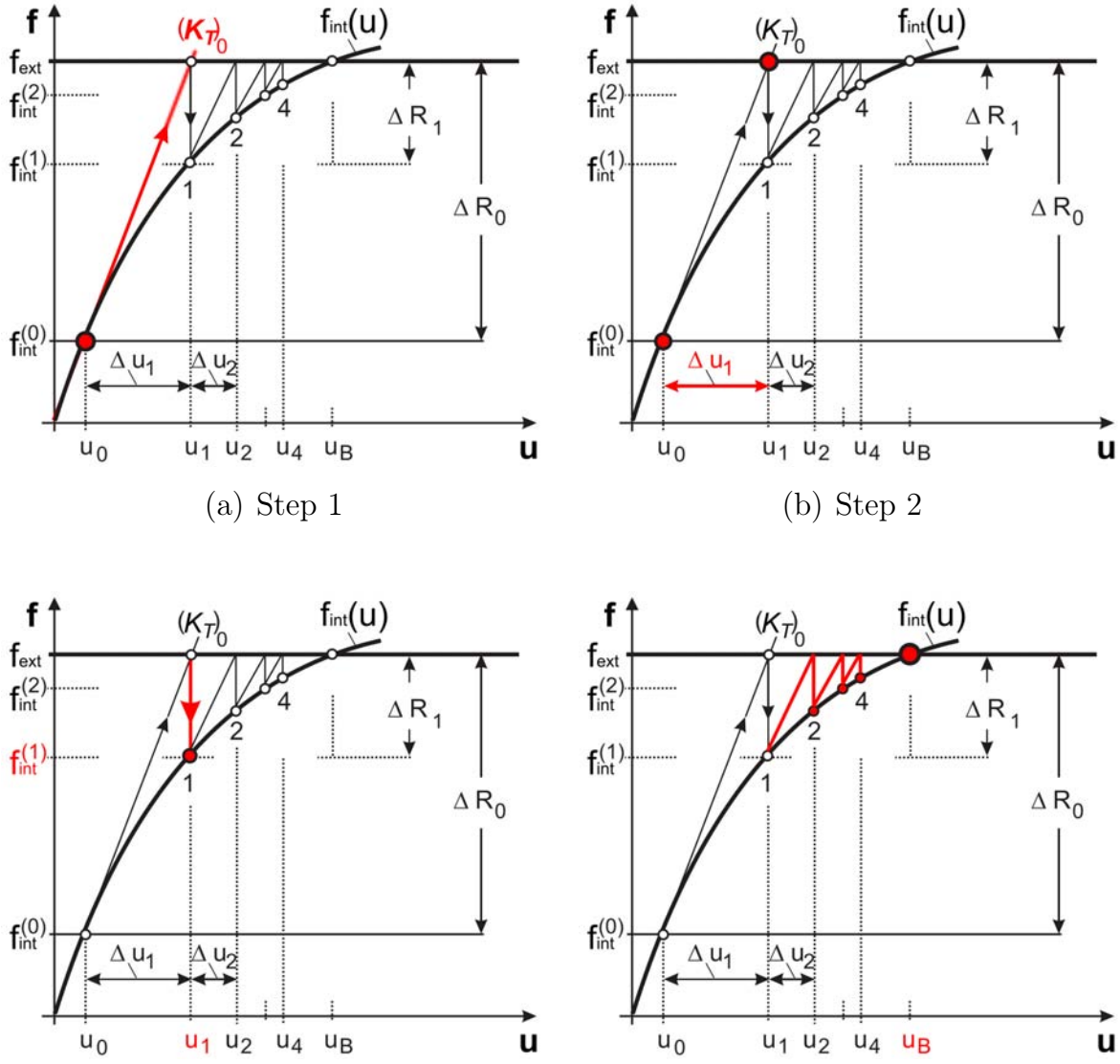

(a) Step 1

(b) Step 2

(c) Step 3

(d) Repeating steps 2 and 3

Figure 3.12: Solving nonlinear equation with the modified Newton-Raphson method

```
for elx = 1:nelx    % Assembling K_Global
 for ely = 1:nely
  ...
  % Computing element stiffness matrices
  [KE_mat, KE_geo] = getKE_nl(u_old(edof),pos(edof)
                     +u_old(edof),E_matrix,Ewidth,Eheight);

  % Assembling global stiffness matrix
  K_mat(edof,edof) = K_mat(edof,edof) + x(ely,elx)^penal*KE_mat;
  K_geo(edof,edof) = K_geo(edof,edof) + x(ely,elx)^penal*KE_geo;
 end
end
...
% Compute f^int = K_mat*u and f^ext with Boundary Conditions
f_int(freedofs,:) = K_mat(freedofs,freedofs)*u_old(freedofs,:);

% Solving for u_new
u_new(freedofs,:)
 = u_old(freedofs,:) + (K_mat(freedofs,freedofs)
 + K_geo(freedofs,freedofs))\(F(freedofs,:)-f_int(freedofs,:));
```

The tangent stiffness matrix with its material and geometric parts, $\boldsymbol{K}^{mat}$ and $\boldsymbol{K}^{geo}$, is calculated as described in Eq. (3.56) and (3.58). The source code is not printed here due to its extensive length.

3.2.3 Formulating the optimization problem

The optimization problem of designing CM with specific motion requirements is formulated by a vector-based motion restriction, denoted by a specified displacement vector $\boldsymbol{u}_{spec}$. Two different formulations of the vector-based motion restriction result in two slightly different formulations of the optimization problems that are implemented and tested.

Both optimization problems are solved by combining the robust, but less functional OC method and the broadly-functional, but often unstable GCMMA method to a staggered optimization scheme that provides both features: robustness and a broad functionality. It can be seen, that in both formulations the *functional* constraints are only addressed by the GCMMA algorithm.

Remark. Here, *broad functionality* refers to the ability to handle additional constraints such as motion restrictions.

3.2.3.1 Single criterion objective function

In the first formulation, the components of the output vector $\boldsymbol{u}_{\text{out}} = (u_{out1},\, u_{out2})^T$ are treated separately, maximizing one and constraining its perpendicular component by applying lower and upper bounds of the parasitic displacement, denoted by $u_{out\perp}^{\min}$ and $u_{out\perp}^{\max}$. Typically, this is of interest for the case of most common applications of CM.

The nodal displacements, u_{out1} and u_{out2}, are calculated for the different loads that are applied to the (current) topology. As shown in Fig. 3.13(a) and 3.13(b), these loads are either real loads $\boldsymbol{f}_{\text{in}}$ (blue) applied at the input DOF(s) or unit dummy loads $\boldsymbol{f}_{\text{out}}$ (green) at the output DOF(s), causing the displacements $\boldsymbol{u}$ and $\boldsymbol{v}$ of the current topology.

$$\boldsymbol{K}\boldsymbol{u} = \boldsymbol{f}_{\boldsymbol{in}}, \qquad \boldsymbol{K}\boldsymbol{v} = \boldsymbol{f}_{\boldsymbol{out}}. \tag{3.105}$$

The displacements $\boldsymbol{u}$ and $\boldsymbol{v}$ are, then, used to calculate the mutual potential energy (MPE) as given in Eq. (3.65), which is equal to the output motion u_{out} since

$$\begin{aligned} u_{out}(\boldsymbol{\rho}) &= \boldsymbol{u}^{\boldsymbol{T}}\boldsymbol{f}_{out} \\ &= \boldsymbol{u}^T\boldsymbol{K}(\boldsymbol{\rho})\boldsymbol{v} \\ &= \sum_{e=1}^{N} \rho_e^p \boldsymbol{u}_e^T \boldsymbol{K}_e \boldsymbol{v}_e, \end{aligned} \tag{3.106}$$

where $\boldsymbol{f}_{out} = [0, \ldots, 1, \ldots, 0]^T$ and the SIMP approach, as introduced in Eq. (3.95), were used.

Remark. Note, that $\boldsymbol{u}_{out}$ is the displacement vector caused by the *real* force at the input DOF. It is not to confuse with any displacements $\boldsymbol{v}$ caused by the dummy load that is applied at the output DOF.

The components of the output motion $\boldsymbol{u}_{\text{out}} = (u_{out1}, u_{out2})^T$ are now used to calculate the objective function. Hence, the first problem formu-

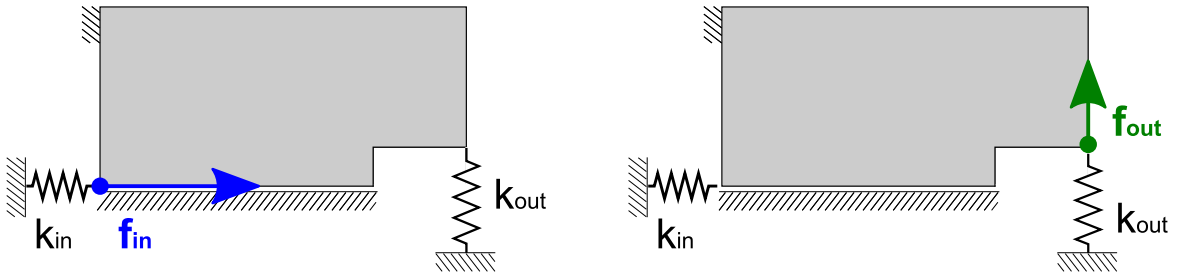

(a) Real load case (b) Dummy load case

Figure 3.13: Different loads applied on an example material domain with input and output stiffnesses for (a) real loads and (b) dummy loads

lation for the staggered optimization scheme can be written for the OC algorithm as

$$(\mathbb{P})^I_{\text{OC}} = \begin{cases} \max\limits_{\boldsymbol{\rho}} & g_0^I(\boldsymbol{\rho}) = u_{out}(\boldsymbol{\rho}) \\ \text{s.t.} & g_1^I(\boldsymbol{\rho}) = \sum\limits_{e=1}^{N} (\rho_e - V) \leq 0 \\ & \boldsymbol{K}(\boldsymbol{\rho})\boldsymbol{u} = \boldsymbol{f} \\ & \{\boldsymbol{\rho} \in \mathbb{R}^N : \underline{\rho} \leq \rho_e \leq \overline{\rho}, e = 1, \ldots, N\}, \end{cases} \tag{3.107}$$

and for the GCMMA algorithm as

$$(\mathbb{P})^I_{\text{GCMMA}} = \begin{cases} \max\limits_{\boldsymbol{\rho}} & g_0^I(\boldsymbol{\rho}) = u_{out}(\boldsymbol{\rho}) \\ \text{s.t.} & g_1^I(\boldsymbol{\rho}) = \sum\limits_{e=1}^{N} (\rho_e - V) \leq 0 \\ & g_2^I(\boldsymbol{\rho}) = u_{out\perp} - u_{out\perp}^{\max} \leq 0 \\ & g_3^I(\boldsymbol{\rho}) = u_{out\perp}^{\min} - u_{out\perp} \leq 0 \\ & \boldsymbol{K}(\boldsymbol{\rho})\boldsymbol{u} = \boldsymbol{f} \\ & \{\boldsymbol{\rho} \in \mathbb{R}^N : \underline{\rho} \leq \rho_e \leq \overline{\rho}, e = 1, \ldots, N\}, \end{cases} \tag{3.108}$$

where V is the total volume fraction, $\underline{\rho}$ is a small non-zero lower bound of the design variable, and $\boldsymbol{K}(\boldsymbol{\rho})\boldsymbol{u} = \boldsymbol{f}$ denotes the equilibrium equation.

In addition to maximize the objective function, further constraints need to be met for all intermediate and final topologies. The *mechanical* constraint

$$\boldsymbol{K}(\boldsymbol{\rho})\,\boldsymbol{u} = \boldsymbol{f}, \tag{3.109}$$

is guaranteed by the FEA that is implemented prior to the optimization in each iteration step, and, thus, is not explained here. The *mathematical* constraint

$$\sum_{e=1}^{N} (\rho_e - V) = 0, \tag{3.110}$$

is guaranteed by (a) an efficient bisection method that is implemented in the update algorithm of the OC method and (b) an added constraint to the GCMMA algorithm.

3.2.3.2 Multi criteria objective function

The second formulation maximizes a multi-criteria objective function, which is written as a quotient of the Euclidian norms of the actual output vector $\boldsymbol{u}_{out}$ and the difference of $\boldsymbol{u}_{out}$ and its projection on $\boldsymbol{u}_{spec}$, denoted by $\alpha\boldsymbol{u}_{spec}$. As a result, both criteria are optimized relatively to each other instead of absolutely, e.g. when taking weighted sum methods into consideration.

The second problem formulation for the staggered optimization problem becomes

$$(\mathbb{P})^{II}_{\mathrm{OC}} = \begin{cases} \max\limits_{\boldsymbol{\rho}} & g_0^{II}(\boldsymbol{\rho}) = \dfrac{\|\boldsymbol{u}_{out}\|}{\|\boldsymbol{u}_{out} - \alpha\boldsymbol{u}_{spec}\|} \\ \text{s.t.} & g_1^{II}(\boldsymbol{\rho}) = \sum\limits_{e=1}^{N} (\rho_e - V) \leq 0 \\ & \boldsymbol{K}(\boldsymbol{\rho})\boldsymbol{u} = \boldsymbol{f} \\ & \{\boldsymbol{\rho} \in \mathbb{R}^N : \underline{\rho} \leq \rho_e \leq \overline{\rho}, e = 1, \ldots, N\}, \end{cases} \tag{3.111}$$

and for the GCMMA algorithm as

$$(\mathbb{P})^{II}_{\text{GCMMA}} = \begin{cases} \max\limits_{\boldsymbol{\rho}} & g_0^{II}(\boldsymbol{\rho}) = \dfrac{\|\boldsymbol{u}_{out}\|}{\|\boldsymbol{u}_{out} - \alpha \boldsymbol{u}_{spec}\|} \\ \text{s.t.} & g_1^{II}(\boldsymbol{\rho}) = \sum\limits_{i=1}^{N} (\rho_e - V) \leq 0 \\ & g_2^{II}(\boldsymbol{\rho}) = -\text{sgn}(u_{spec1}) \cdot u_1 \leq 0 \\ & \boldsymbol{K}(\boldsymbol{\rho})\boldsymbol{u} = \boldsymbol{f} \\ & \{\boldsymbol{\rho} \in \mathbb{R}^N : \underline{\rho} \leq \rho_e \leq \overline{\rho}, e = 1, \ldots, N\}. \end{cases} \tag{3.112}$$

Remark. The additional constraint $g_2^{II}(\boldsymbol{\rho})$ is introduced to ensure a convenient mathematical handling of unique directions, otherwise $\boldsymbol{u}_{spec} = (1, -1)^T$ and $\boldsymbol{u}_{spec} = (-1, 1)^T$ yield the same results. It has no further impact on the optimization procedure.

3.2.4 Sensitivity analysis

The values of the objective functions, $g_0^I(\boldsymbol{\rho})$ and $g_0^{II}(\boldsymbol{\rho})$, provide only an indicator for the quality of the corresponding intermediate solution, i.e. how well performs the current design of the CM. In order to improve the solution with every iteration step, a sensitivity analysis, i.e. the derivative with respect to the design variables, is required.

Remark. A very comprehensive guide on sensitivity analysis for linear and nonlinear systems can be found in [211] and [212]. For this work, a detailed derivation of the relevant sensitivities is given in the Appendix A.2 based on the direct differentiation method and the adjoint method. The adjoint method was tested to be more efficient and, thus, is implemented in this work, since there is only one objective function compared to a very large number of design variables ρ_i.

As a final outcome, the derivative of the objective function of the

first formulation given in Eq. (3.106) can be calculated as

$$\frac{\partial g_0^I(\boldsymbol{\rho})}{\partial \rho_e} = \boldsymbol{f}_{out}^T \frac{\partial(\boldsymbol{u}(\boldsymbol{\rho}))}{\partial \rho_e}, \tag{3.113}$$

$$= \boldsymbol{v}(\boldsymbol{\rho})^T \boldsymbol{K}(\boldsymbol{\rho}) \frac{\partial(\boldsymbol{u}(\boldsymbol{\rho}))}{\partial \rho_e}. \tag{3.114}$$

The last term can be obtained by differentiation of the equilibrium equation $\boldsymbol{K}(\boldsymbol{\rho})\boldsymbol{u}(\boldsymbol{\rho}) = \boldsymbol{f}$ as

$$\frac{\partial \boldsymbol{K}(\boldsymbol{\rho})}{\partial \rho_e}\boldsymbol{u}(\boldsymbol{\rho}) + \boldsymbol{K}(\boldsymbol{\rho})\frac{\partial(\boldsymbol{u}(\boldsymbol{\rho}))}{\partial \rho_e} = \boldsymbol{0}, \tag{3.115}$$

which yields

$$\frac{\partial(\boldsymbol{u}(\boldsymbol{\rho}))}{\partial \rho_e} = -\boldsymbol{K}^{-1}(\boldsymbol{\rho}) \frac{\partial \boldsymbol{K}(\boldsymbol{\rho})}{\partial \rho_e}\boldsymbol{u}(\boldsymbol{\rho}) = -p\rho_e^{(p-1)}\boldsymbol{K}^{-1}(\boldsymbol{\rho})\, \boldsymbol{K_e}\boldsymbol{u}_e, \tag{3.116}$$

where $\frac{\partial \boldsymbol{K}(\boldsymbol{\rho})}{\partial \rho_e} = p\rho_e^{(p-1)}\ \boldsymbol{K_e}\boldsymbol{u}_e$ was used in the second step. Plugging Eq. (3.116) into Eq. (3.114) results in

$$\frac{\partial g_0^I(\boldsymbol{\rho})}{\partial \rho_e} = -\boldsymbol{v}_e^T \left(p\rho_e^{(p-1)}\boldsymbol{K}_e\right) \boldsymbol{u_e}, \tag{3.117}$$

which is the final expression that is to be calculated.

The following excerpt of the source code shows calculation of the derivative of objective function $\frac{\partial g_0(\boldsymbol{\rho})}{\partial \rho_e}$ with respect to each FE's design variable ρ_e and is simply written as `dcost(ely,elx)`:

```
for elx = 1:nelx
  for ely = 1:nely
   ...
   dcost(ely,elx) = -penal*x(ely,elx)^(penal-1)*Ue'*KE*Ve;
   ...
  end
end
```

The derivative of the objective function of the second, multi-criteria formulation given in Eq. (3.111) and (3.112) is printed in the Appendix A.3 due to its extensive length.

3.2.5 Update scheme

The design variables $\rho_e^{(k)}$ need to be updated after each iteration k based on the sensitivities in order to maximize the objective function, i.e. to improve the overall solution. The update schemes of both methods, OC and GCMMA, are described now.

3.2.5.1 Optimality criteria method

In order to improve the current (intermediate) topology of the CM, the design variables $\boldsymbol{\rho}^{(k)}$ are replaced by updated design variables $\boldsymbol{\rho}^{(k+1)}$ at each (outer) iteration step. Recalling the previously derived update scheme given in Eq. (3.89) and the introduced SIMP modification given in Eq. (3.95) yield

$$\begin{aligned}\rho_e^{(k+1)} &= \min\left\{\max\left[\left(\frac{-\frac{\partial g_0^{(k)}(\boldsymbol{\rho})}{\partial \rho_e}}{\lambda}\right)^{\eta}\rho_e^{(k)}, \underline{\rho}\right]\right\}, \\ &= \min\left\{\max\left[\left(\frac{\left(\boldsymbol{u}_e^{(k)}\right)^T\left(p\rho_e^{(p-1)}\boldsymbol{K}_e\right)\boldsymbol{v}_e^{(k)}}{\lambda}\right)^{\eta}\rho_e^{(k)}, \underline{\rho}\right], \overline{\rho}\right\},\end{aligned} \tag{3.118}$$

where the sensitivities from Eq. (3.117) were substituted in the second line. The Lagrange multiplier λ in the denominator is calculated by the volume constraint given in Eq. (3.87)

$$\sum_{e=1}^{N}\left(\rho_e^{(k+1)}(\lambda) - V\right) \stackrel{!}{=} 0, \tag{3.119}$$

which is solved very efficiently by a bisection method due to the monotonic behavior of Eq. (3.119). Fig. 3.14 illustrates the feasible range of values (green) of the updated design variables limited by certain bounds and limits. The red area is inaccessible at all times for all design variables due to the lower bound $\underline{\rho}$. The yellow area is inaccessible in this iteration step for this respective design variable $\rho_e^{(k)}$ due to a numerical move limit m. The following excerpt of the source code shows calculation of the updated design variables $\rho^{(k+1)}$ simply written as `xnew` while

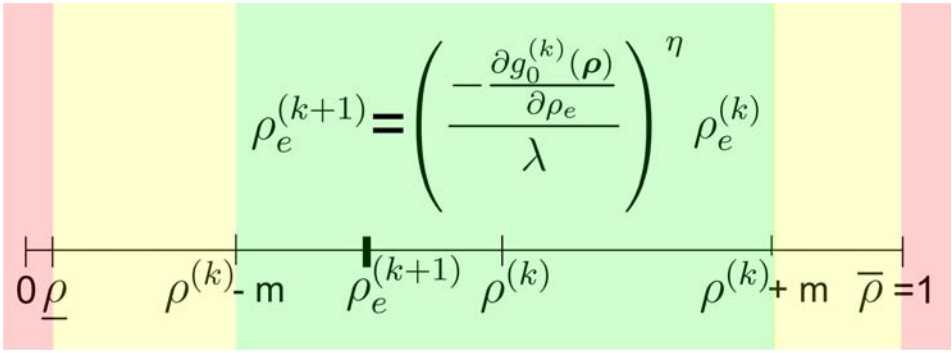

Figure 3.14: Range of values of the updated design variables $\rho^{(k+1)}$ based on the sensitivities, move limit m, and lower and upper bounds

solving for the Lagrange multiplier λ simply denoted by `lmid`:

```
while ((l2-l1)/(l2+l1) > convlim & l2 > 1E-15)
    ...
    xnew = max(xmin,
           max(x-move,
           min(1.,
           min(x+move,x.*(max(1e-10,-dc./lmid)).^0.3))));
    ...
    if sum(sum(xnew)) - volfrac*nelx*nely > 0
        l1 = lmid;
    else
        l2 = lmid;
    end
end
```

3.2.5.2 Globally convergent method of moving asymptotes

The update process of the design variables ρ in the GCMMA algorithm uses the sensitivities of the objective function $g_0(\boldsymbol{\rho})$ *as well as* the derivatives of the constraint equations $g_1(\boldsymbol{\rho})$ and $g_2(\boldsymbol{\rho})$. It is based on a mainly heuristic update scheme, which is outlined in Sect. 3.1.3.3. A detailed description of the update process is given in Svanberg's original papers [89, 204].

The relevant sensitivities of $g_0(\boldsymbol{\rho})$, $g_1(\boldsymbol{\rho})$ and $g_2(\boldsymbol{\rho})$ of both formulations are not derived here but are printed in the Appendix A.3 due to their extensive length.

3.3 Results and discussion

The implemented topology optimization algorithm yields optimized topologies of CM that meet the desired motion specifications under the predefined loading and boundary conditions. The results of the topological synthesis based on the implemented algorithm are shown and discussed now. First, the process of the topology optimization based on the OC algorithm is illustrated and the results are compared to those in literature. Second, the influence of linear and nonlinear computation is presented. Third, the topology synthesis is tailored to different applications. Fourth, the benefits of the introduced staggered optimization scheme are shown.

3.3.1 Topology optimization process

The stepwise process of the topology optimization based on the OC algorithm is illustrated on two different syntheses: first, a compliant displacement inverter and, second, a compliant gripping device are generated.

Here, the final topologies of the CM obtained by the own OC algorithm are compared to the results of the topological optimization achieved by other research groups, as mentioned in Sect. 2.1. However, a full comparison is not always possible due to different and sometimes not explicitly known boundary and loading conditions.

3.3.1.1 Compliant displacement inverter

Compliant displacement inverters transform an input motion into an output motion pointing to an opposite direction. Fig. 3.15 illustrates the initial design domain with specified boundary conditions, an input force f_{in} and a desired output motion u_{out}.

In this example, the objective is to design a CM that inverts a right-pointing input force into a left-pointing output motion. Input and output coordinates are set to the horizontal center, and a void area is prespecified at the center of the design domain. **No *intuitive* design specifications are made in the topology optimization process.**

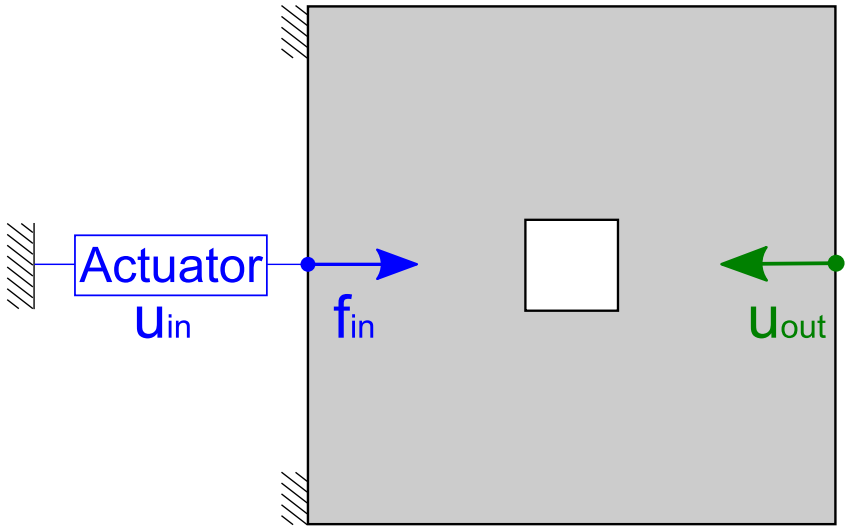

Figure 3.15: Initial design domain with specified boundary conditions, an input force $\boldsymbol{f}_{in}$ and a desired output motion $\boldsymbol{u}_{out}$ aiming to synthesize compliant displacement inverter

Figure 3.16 shows the topology optimization process of a compliant displacement inverter with 2×5,000 FE, starting from an initial design domain (Fig. 3.16(a)), running through several intermediate topologies (Fig. 3.16(b) - 3.16(k)) and resulting in a final topology (Fig. 3.16(l)). Here, all the computation is done on the upper half of the material domain which is discretized by 5,000 FE, the results are mirrored to the lower half afterwards.

The stepwise development is clearly illustrated. It can be seen that the first couple of iterations provide a substantial change whereas the later iterations simply ”fine-tune” the results.

Comparing the results of this work with the final topologies of compliant displacement inverters recently obtained by another research group [213] based on a different approach reveals similar topologies and, thus, supports the own algorithm. Fig. 3.17 shows the results, where the one-node hinges were smoothed by post-processing techniques.

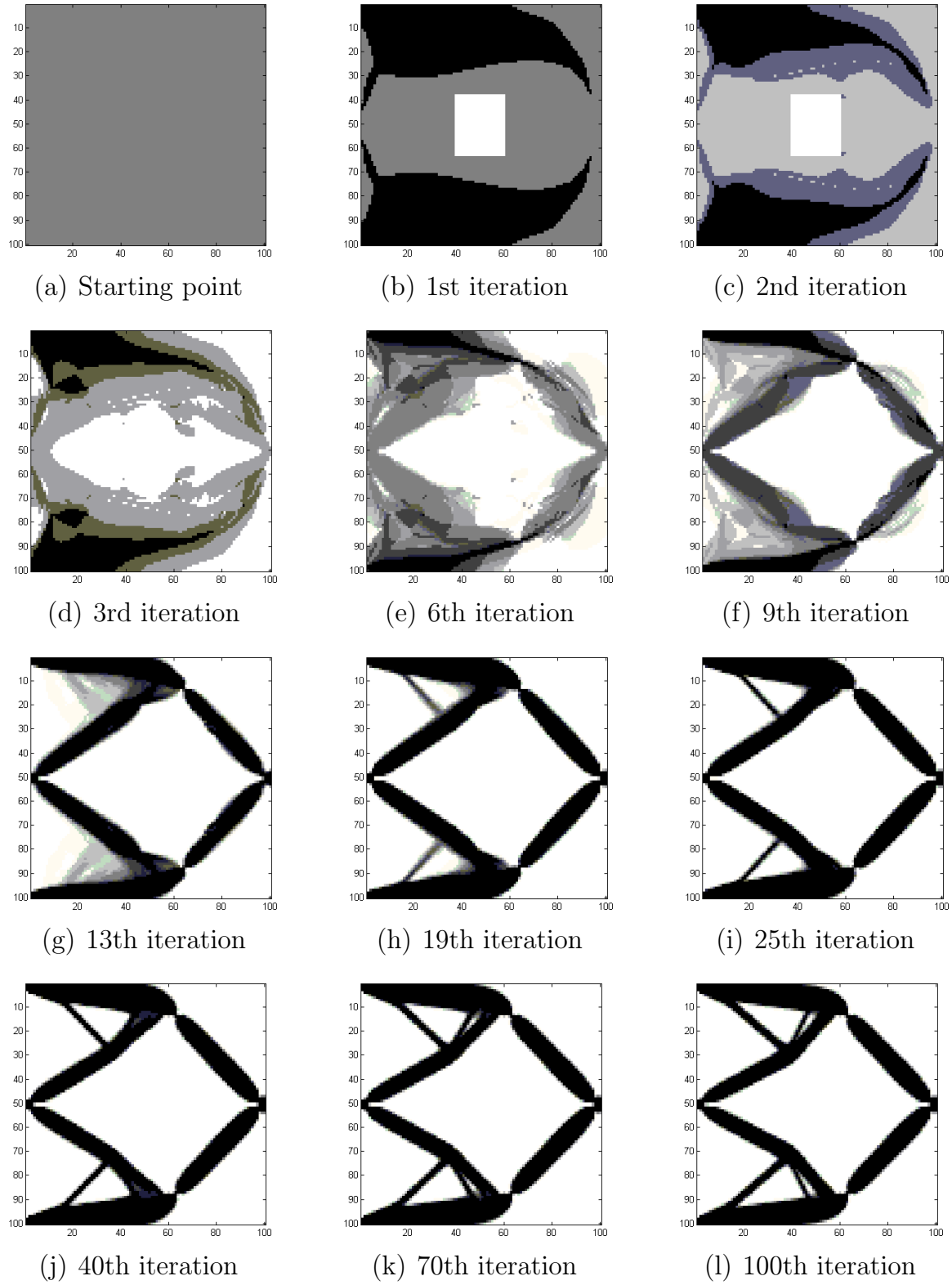

(a) Starting point (b) 1st iteration (c) 2nd iteration

(d) 3rd iteration (e) 6th iteration (f) 9th iteration

(g) 13th iteration (h) 19th iteration (i) 25th iteration

(j) 40th iteration (k) 70th iteration (l) 100th iteration

Figure 3.16: Stepwise topology optimization process of an compliant displacement inverter with 2×5,000 finite elements

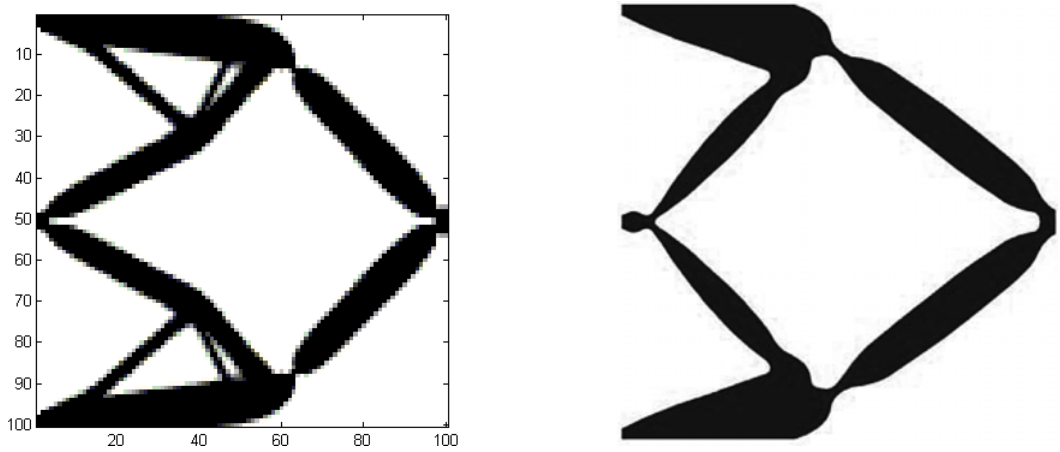

(a) Own final topology (b) From [213]

Figure 3.17: Final topologies of compliant displacement inverters in comparison obtained by own algorithm (a) and another research group (b)

3.3.1.2 Compliant gripping device

Compliant gripping devices transform a single input motion into a perpendicular gripping motion of two (or more) output points. Fig. 3.18 illustrates the initial design domain with specified boundary conditions, an input force f_{in} and a desired output motion u_{out}. In this example, the objective is to design a CM that transforms a right-pointing input force into a vertical gripping (output) motion. The input motion is set to the horizontal center, and a void area is pre-specified at the right center of the design domain to give space for later work pieces that are subject to the resulting gripping motion. **No *intuitive* design specifications are made in the topology optimization process.**

Comparing the results of this work with the final topologies of compliant gripping devices, as shown in Fig. 3.19, recently obtained by another research group [214] based on a ground structure design, as explained in Sect. 2.1.2, reveals similar topologies and, thus, supports the own algorithm, again.

Figure 3.20 shows the topology optimization process of a compliant gripping device with 2×20,000 FE: starting from an initial, material de-

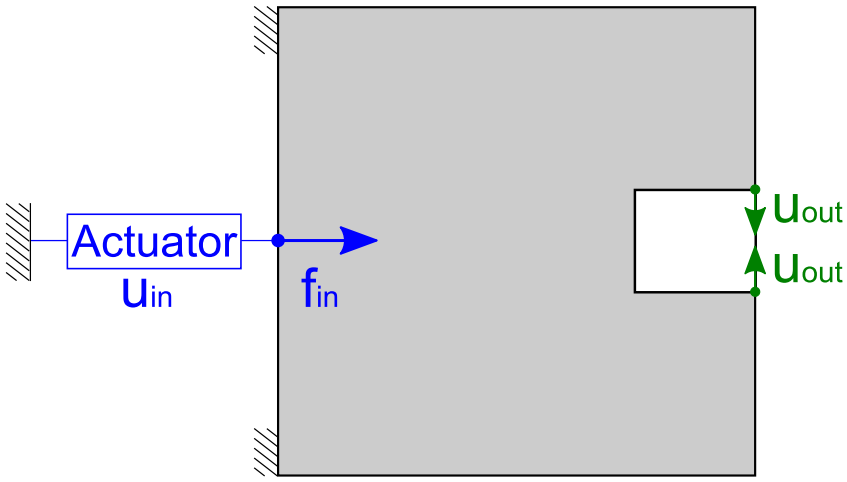

Figure 3.18: Initial design domain with specified boundary conditions, an input force $\boldsymbol{f}_{in}$ and a desired output motion $\boldsymbol{u}_{out}$ aiming to synthesize compliant gripping device

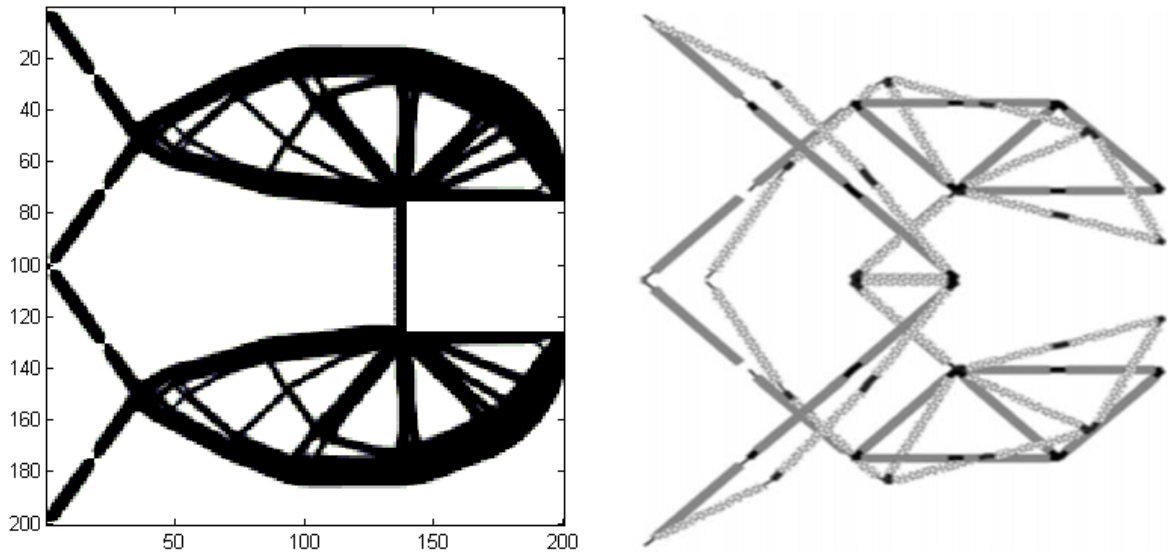

(a) Own final topology

(b) From [214]

Figure 3.19: Final topologies of compliant gripping devices in comparison obtained by own algorithm (a) and another research group (b)

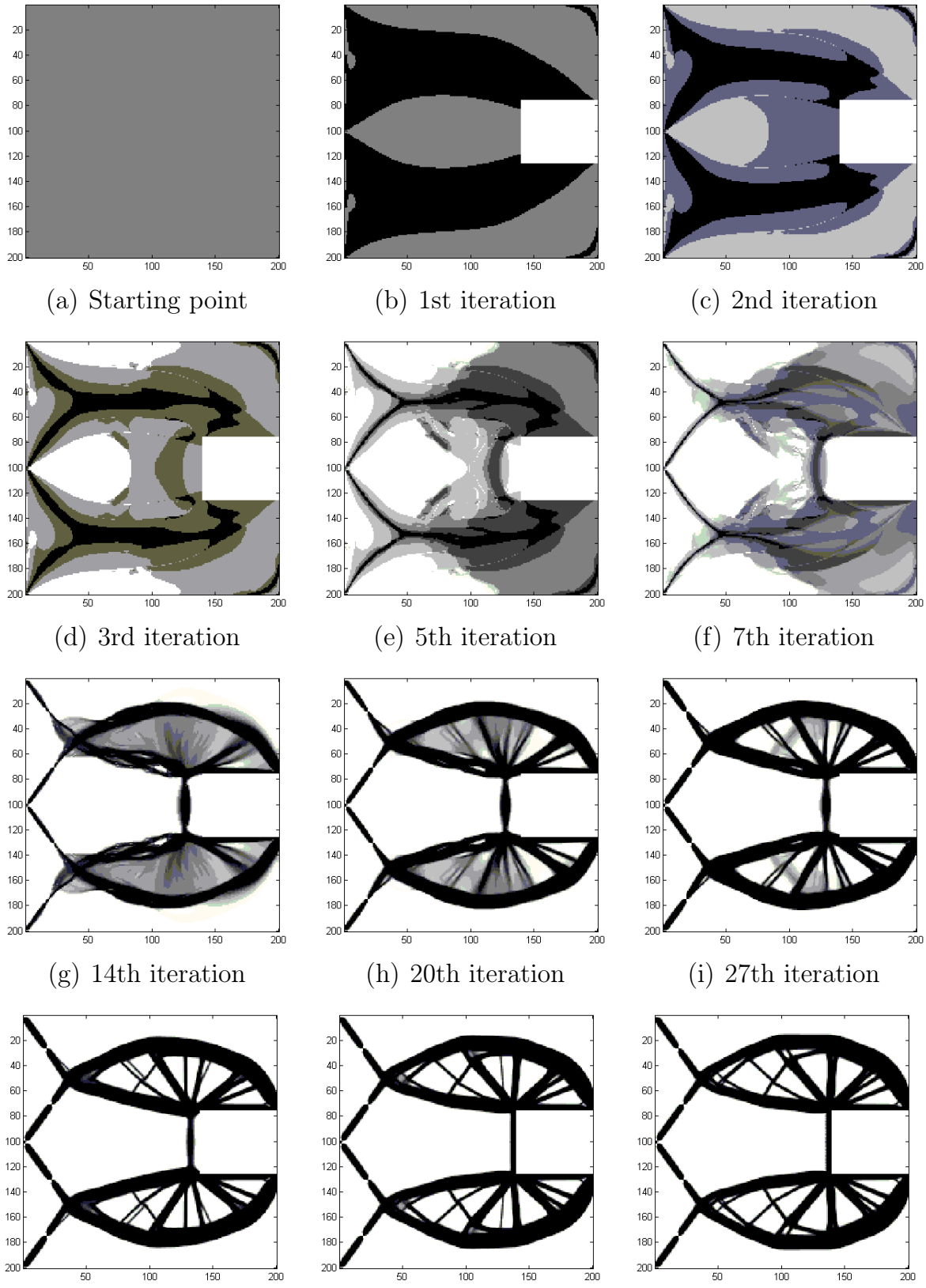

(a) Starting point (b) 1st iteration (c) 2nd iteration

(d) 3rd iteration (e) 5th iteration (f) 7th iteration

(g) 14th iteration (h) 20th iteration (i) 27th iteration

(j) 40th iteration (k) 70th iteration (l) 100th iteration

Figure 3.20: Stepwise topology optimization process of an compliant gripping device with 2×20,000 finite elements

sign domain (Fig. 3.20(a)), running through several intermediate topologies (Fig. 3.20(b) - 3.20(k)) and resulting in a final topology (Fig. 3.20(l)). The stepwise development is clearly illustrated. Again, it can be seen that the first couple of iterations provide a substantial change whereas the later iterations simply "fine-tune" the results.

3.3.2 Linear vs. nonlinear computation

The topology synthesis of CM relies on the nodal displacements caused by the external loads. Since the occurring deformations of each FE need to be considered, cost-intensive but more precise and more stable nonlinear FEA is performed, as suggested in [215]. Here, a comparison between the topology syntheses based on linear and nonlinear FEA is presented.

3.3.2.1 Computational cost

In terms of computational cost, the computation *time* is the most significant measure since *memory* has become inconsiderably cheap. Fig. 3.21 and Tab. 3.1 illustrate the computation time of the topology syntheses performed on a standard PC and a high-end workstation (WS) with linear and nonlinear FEA for different numbers of DOF.

It can be seen, that the computation time T strongly depends on various aspects: the number of DOF N_{DOF}, the choice of linear or nonlinear FEA and the hardware. In the cases considered here, it turned out that

- The computation time rises approximately quadratically with the number of DOF, i.e.
$$T \sim N_{DOF}^2.$$
- The nonlinear computation requires approximately the triple of the time for a linear computation, i.e.
$$T_{nonlin} \approx 3T_{lin}.$$
- The standard PC requires approximately the quadruple of the computation time of the workstation, i.e.
$$T^{PC} \approx 4T^{WS}.$$

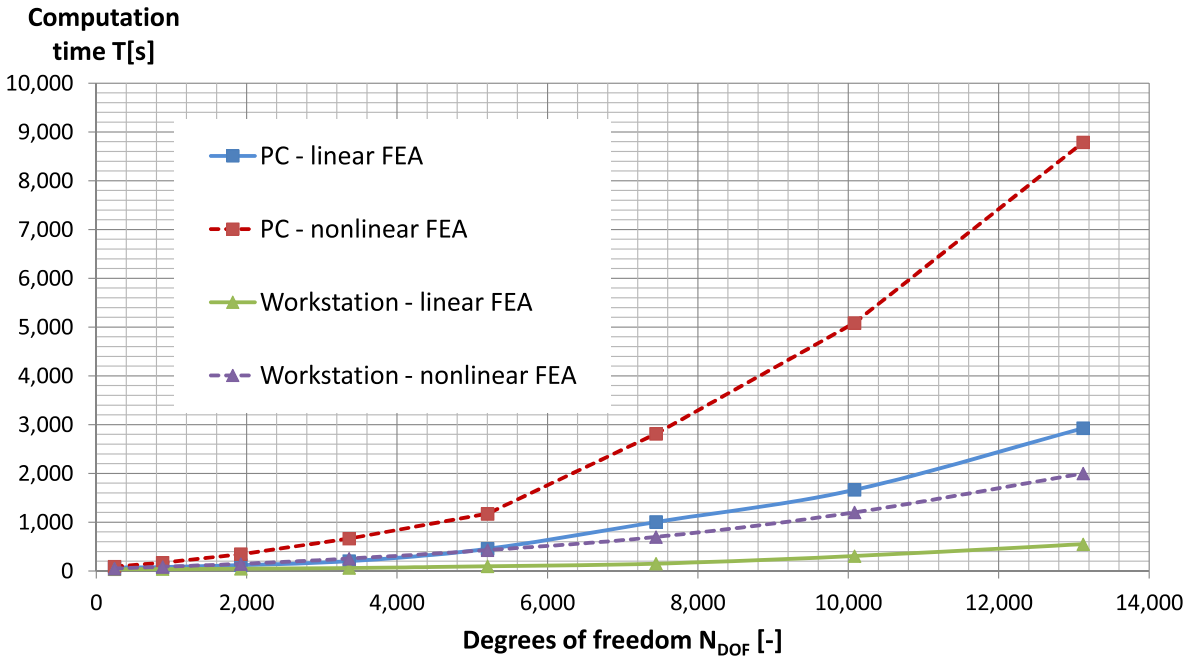

Figure 3.21: Computation time of topology syntheses on a standard PC and a high-end workstation with linear and nonlinear FEA for different numbers of finite elements

Table 3.1: Computation time T of topology syntheses on standard PC and high-end workstation (WS) with linear and nonlinear FEA for different numbers of finite elements N and the corresponding number of degrees of freedom N_{DOF}

N [-]	N_{DOF} [-]	T_{lin}^{PC} [s]	T_{nonlin}^{PC} [s]	T_{lin}^{WS} [s]	T_{nonlin}^{WS} [s]
100	242	69.8	91.2	36.1	47.6
400	882	82.2	168.3	40.9	84.3
900	1,922	122.2	343.9	45.5	144.3
1,600	3,362	203.7	663.5	62.1	252.5
2,500	5,202	455.1	1,171.9	96.2	427.2
3,600	7,442	1,005.3	2,811.7	150.1	696.3
4,900	10,882	1,665.0	5,084.6	305.4	1,200.5
6,400	13,122	2,927.5	8,786.6	548.4	1,998.8

Finally, a careful use of nonlinear FEA is recommended due to the significantly higher computation time.

Remark. The standard PC is an IBM ThinkPad T61 with Intel Core Duo processor (T7300, 2 GHz) and 2 GB DDR2 RAM (667 MHz). The workstation is a HP Z820 high-end workstation with Intel Xeon Eight Core processor (E5-2690, 2.9 GHz) and 256 GB DDR3 RAM (1.6 GHz).

3.3.2.2 Quality of linear and nonlinear computation

The differences in terms of the final topologies gained by fully linear or fully nonlinear computation are presented now. Figure 3.22 shows the results of the topology syntheses of displacement inverters based on different mesh sizes, where each figure compares the solution of fully linear and fully nonlinear computation. For instance, the two plots of Fig. 3.22(h) represent the final topology based on 2 × 6,400 FE for linear (left plot) and nonlinear (right plot) computation. The blue and green "x" highlights the input and output node, respectively.

It can be seen, that for all considered mesh sizes a solution is obtained. The obtained solutions are mesh dependent, i.e. different mesh sizes yield different (but working) topologies. Comparing the results of linear and nonlinear calculations, reveals similar topologies with minor but identifiable differences, e.g. the number and positions of the hinges are different in Fig. 3.22(h).

In order to ensure a mechanically-stable, time-efficient *and* accurate topology synthesis, a combination of linear and nonlinear FEA is recommended. Therefore, all optimization processes in this thesis start with linear FEA and are finalized using nonlinear FEA. The final results of this linear-nonlinear FEA converged in all considered cases to the results obtained by the fully nonlinear computation but in significantly less time.

3.3.3 Tailoring to different applications

A variety of different applications requires different CM that are adopted accordingly. In the following, CM are tailored systematically to a specific

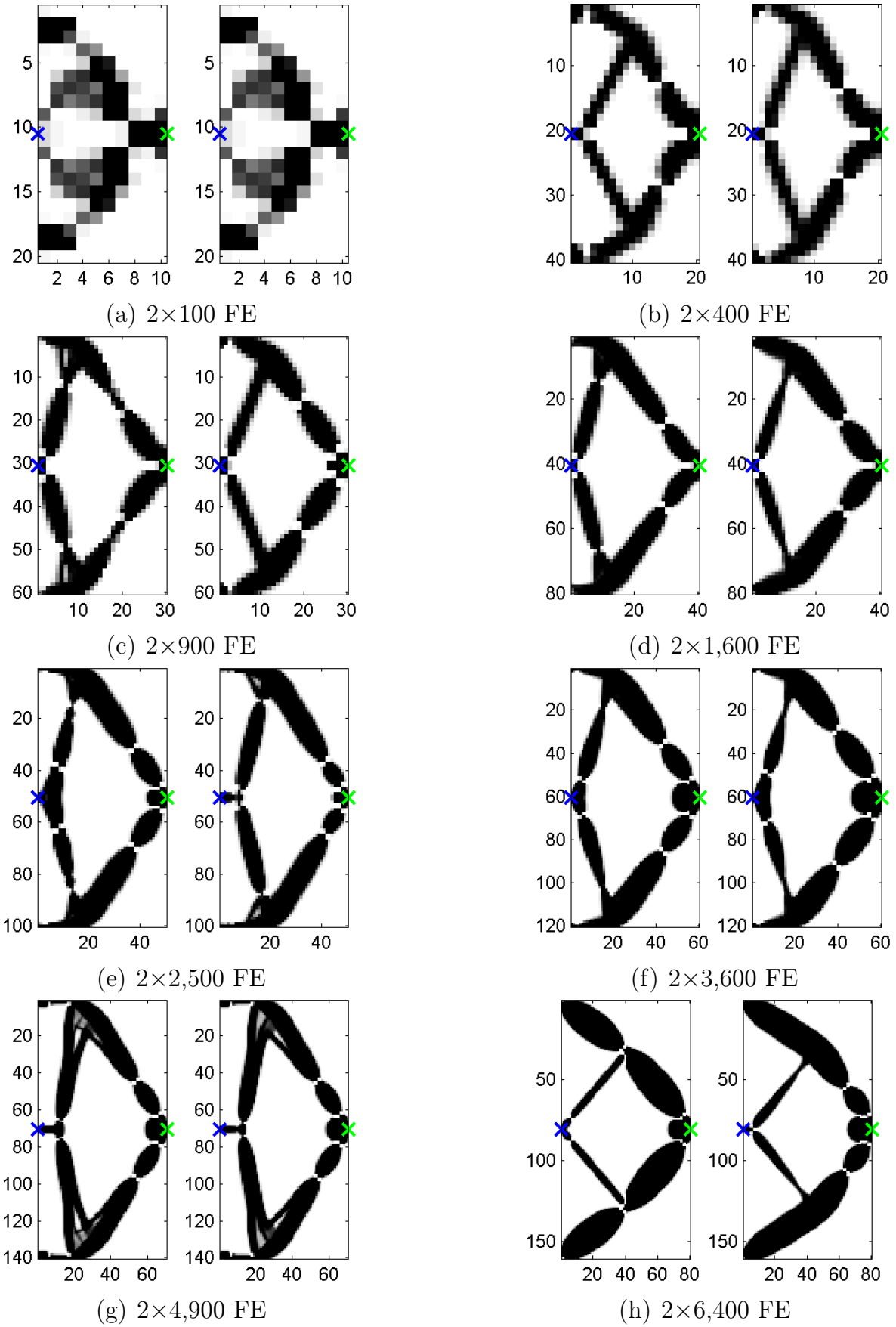

(a) 2×100 FE (b) 2×400 FE

(c) 2×900 FE (d) 2×1,600 FE

(e) 2×2,500 FE (f) 2×3,600 FE

(g) 2×4,900 FE (h) 2×6,400 FE

Figure 3.22: Optimized topologies of displacement inverters based on different mesh sizes for linear (left) and nonlinear computation (right)

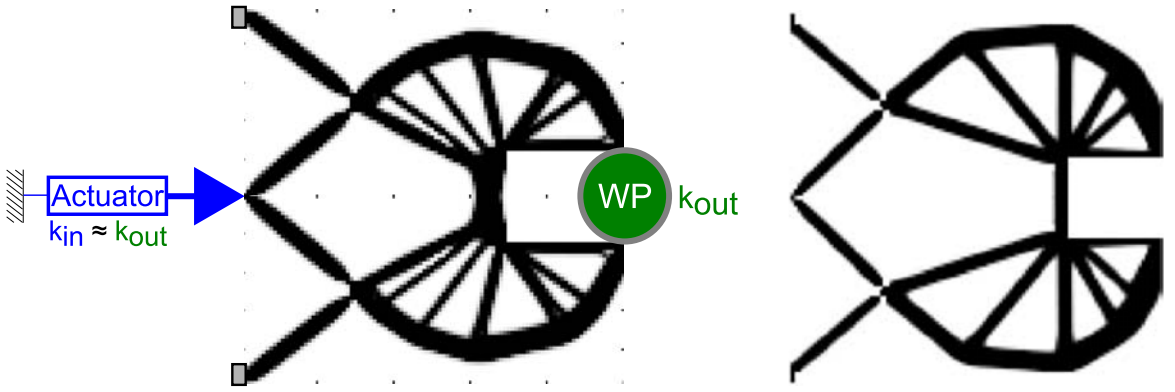

(a) Own final topology (b) From [216]

Figure 3.23: Final topologies of a compliant gripping device with stiff actuator and stiff work piece providing moderate GA and moderate MA obtained by own algorithm (a) and another research group (b)

application without any intuition, but solely based on the different prespecified forces and strokes at the input and output ports.

Stiff actuators, such as piezoceramic stack actuators, usually provide a small stroke and, thus, require a high geometric amplification (GA). In contrast to this, compliant actuators, such as electroactive polymers or the human hand, require a high mechanical amplification (MA) , i.e. a high amplification of the (input) force. Furthermore, the kind of work piece needs to be considered, as well. Stiff workpieces, e.g. diamond or titanium, need a lower output stroke. In contrast to this, compliant work pieces, such as rubber or wood, require higher output strokes.

Based on the specifications of actuator and workpiece, additional stiffnesses, k_{in} and k_{out}, are added to the global stiffness matrix $\boldsymbol{K}$ at the corresponding input and output DOF resulting in the fact that solving the (modified) set of equations $\boldsymbol{Ku} = \boldsymbol{f}$ within the topology optimization process yields CM tailored accordingly to provide an optimal performance.

Fig. 3.23 - 3.25 show different gripping mechanisms obtained by the own optimization algorithm and by other research groups: Fig. 3.23 is designed for similarly stiff actuators and work pieces providing moderate geometric and mechanical amplification. Fig. 3.24 is designed for stiff

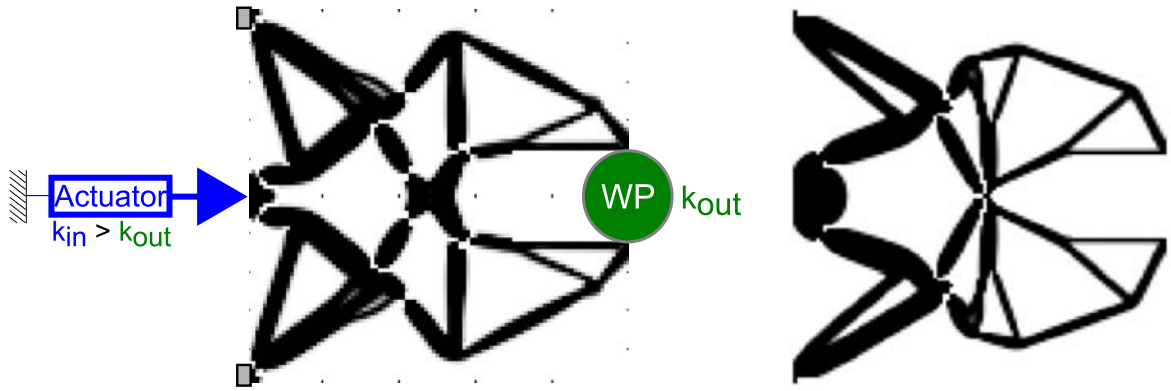

(a) Own final topology (b) From [216]

Figure 3.24: Final topologies of a compliant gripping device with *stiff actuator* and *compliant work piece* providing high GA obtained by own algorithm (a) and another research group (b)

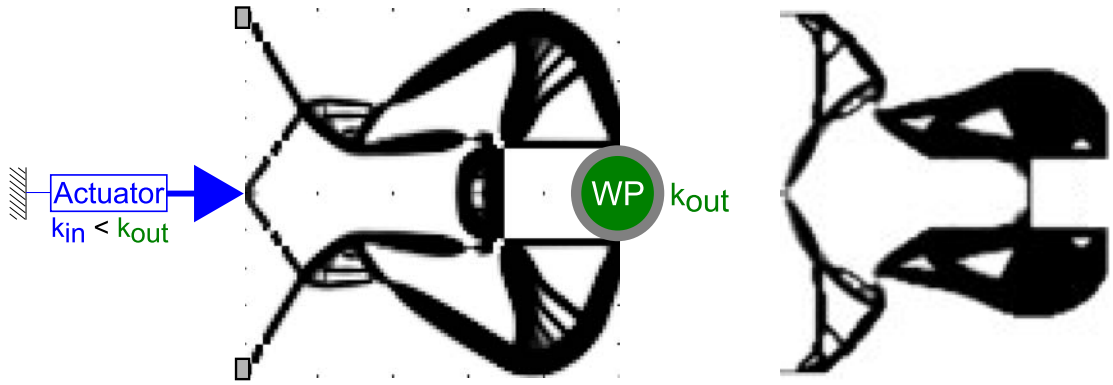

(a) Own final topology (b) From [217]

Figure 3.25: Final topologies of a compliant gripping device with *compliant actuator* and *stiff work piece* providing high MA obtained by own algorithm (a) and another research group (b)

actuators and compliant workpieces providing a high *geometric amplification* GA ≈ 10. Fig. 3.25 is designed for compliant actuators and stiff work pieces providing a high *mechanical amplification* MA ≈ 10.

Comparing the results of this work with the final topologies of the different compliant gripping devices obtained by other research groups reveals similar topologies and, thus, supports the own algorithm.

Therefore, it can be noted, that the proposed synthesis of CM can be applied successfully to a variety of applications providing specifically tailored CM meeting the requirements in terms of motion, stroke and forces of actuators and workpieces.

3.3.4 Staggering topology optimization algorithms

Applying topological optimization methods, purely based on the OC method, yield CM in an efficient and systematic manner. However, functionality is limited and, thus, further motion constraints can hardly be implemented. In contrast, the GCMMA algorithm provides powerful functionality in implementing further (motion) constraints but it lacks in terms of robustness and stability. Implementing both algorithms to a staggered topology optimization algorithm combines the advantages and compensates the drawbacks of each algorithm, as described in Sect. 3.2.

A comparison between an OC algorithm and staggered OC-GCMMA algorithm is presented. First, the influence of the intervals of each applied algorithm, namely n_{OC} and n_{GCMMA}, is shown. Then, the superiority of the staggered topology optimization algorithm compared to the OC algorithm is demonstrated.

3.3.4.1 Interval lengths

Staggering two different optimization algorithms may depend on the interval lengths, i.e. the number of iterations of one algorithm before it is switched over to the other algorithm. The influence of these interval lengths, n_{OC} and n_{GCMMA}, on the overall results is presented here.

Tab. 3.2 lists the output displacements $\boldsymbol{u}_{\mathrm{out}}$ and parasitic errors of the final topologies of a compliant gripping mechanism for the optimization

Table 3.2: Output displacements $\boldsymbol{u}_{\text{out}}$ and relative errors for optimization problems (3.107) and (3.108) for purely vertical output motion

N [−]	n_{OC} [−]	n_{GCMMA} [−]	u_{out1}^{Stagg} [µm]	u_{out2}^{Stagg} [µm]	Parasitic error [−]
6,400	1	1	-0.4	-130.9	0.32%
	2	2	-0.4	-191.9	0.19%
	10	4	-0.2	-221.0	0.08%

problem given in Eq. (3.107) for different intervals n_{OC} and n_{GCMMA}. Fig. 3.26 shows the corresponding final topologies, where a square design domain of 6,400 FE was used.

It can be seen, that different intervals lead to different final topolo-

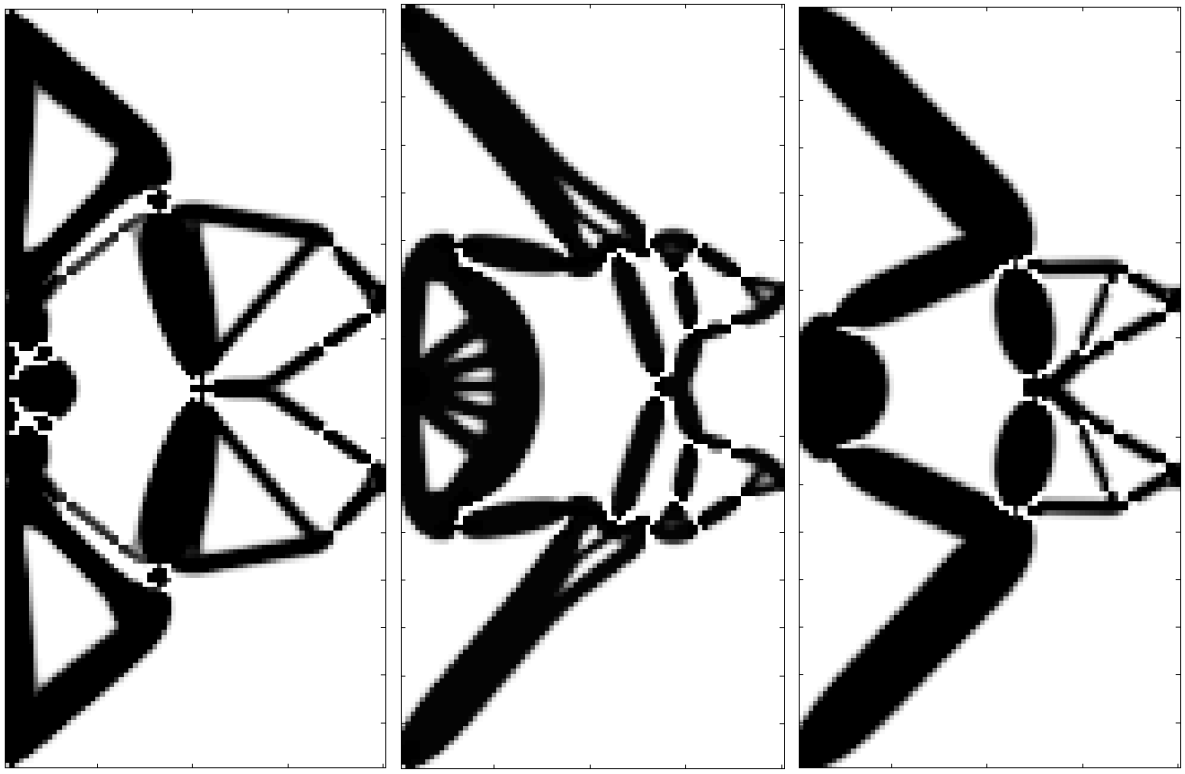

(a)$n_{\text{OC}} = 1$, $n_{\text{GCMMA}} = 1$ (b)$n_{\text{OC}} = 2, n_{\text{GCMMA}} = 2$ (c)$n_{\text{OC}} = 10, n_{\text{GCMMA}} = 4$

Figure 3.26: Final topologies with vertical output motion path using Eqs. (3.107) and (3.108)

gies. However, all three topologies meet the performance specifications and, thus, result in topologies that meet the motion requirements. All parasitic motions u_{out1}^{Stagg} stay within the specified limits and the desired vertical motion u_{out2}^{Stagg} is maximized with a parasitic error less than 0.32%.

It was observed that larger intervals reduce the advantages of staggering both algorithms. Small values of n_{OC} keep the (interim) solutions close to the (additional) motion constraints whereas high values almost guarantee robust behavior. Too high values of n_{GCMMA} reduce the stability. However, the number of intervals of the OC and GCMMA algorithms seems to play a minor role and, thus, it is not further investigated.

3.3.4.2 Single criterion objective function

The simple OC algorithm and the staggered OC-GCMMA algorithm are applied to the load case illustrated in Fig. 3.27 leading to a compliant gripping device based on a single criterion objective function given by the formulation $(\mathbb{P})^I_{\text{OC}}$ and $(\mathbb{P})^I_{\text{GCMMA}}$ in Eqs. (3.107) and (3.108) in Sect. 3.2.3.1.

In case of the OC algorithm, only the vertical output motions $\boldsymbol{u}_{out} = (0; u_{out2})$ are maximized without limiting the parasitic output motions $\boldsymbol{u}_{out\perp} = (u_{out1}; 0)$. In the staggered topology optimization process, the parasitic output motions $\boldsymbol{u}_{out\perp}$ are limited and, thus, the output motion $\boldsymbol{u}_{out}$ is forced to follow a vertical path within the specified corridor.

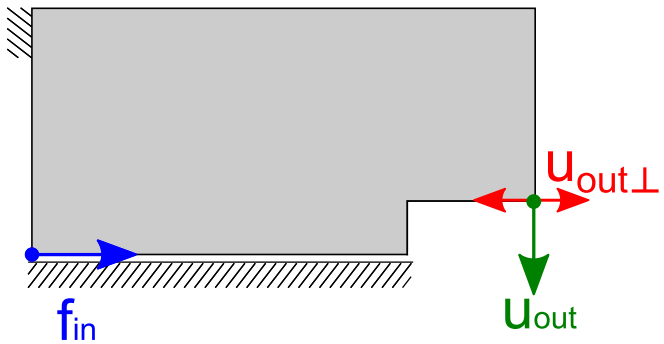

Figure 3.27: Initial design domain with specified boundary conditions, an input force $\boldsymbol{f}_{in}$, a desired output motion $\boldsymbol{u}_{out}$ and a motion constraint $\boldsymbol{u}_{out\perp}$ aiming to synthesize a compliant gripping device

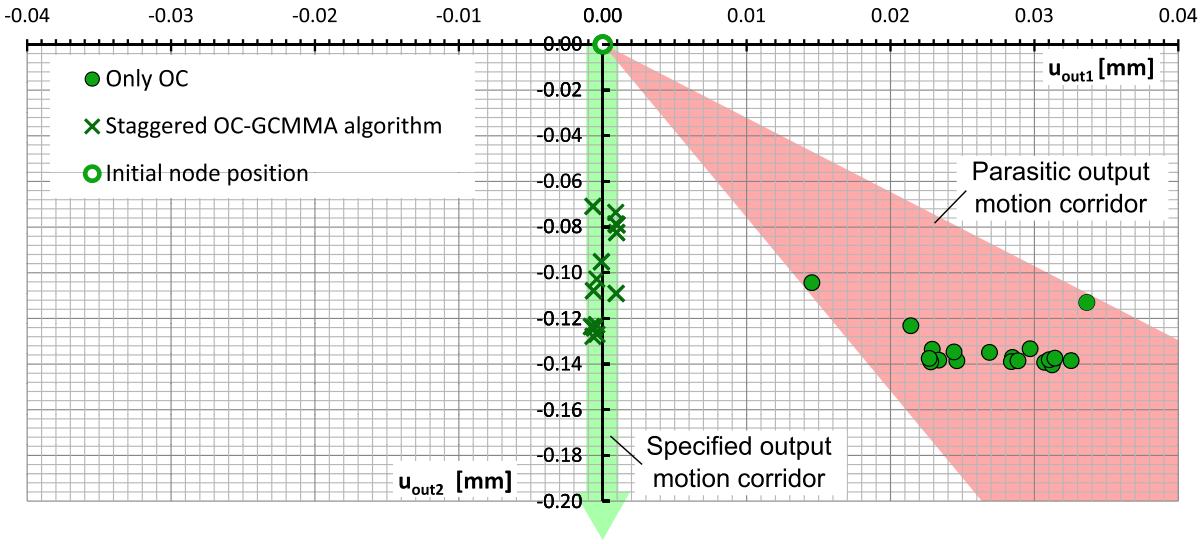

Figure 3.28: Output motion $\boldsymbol{u}_{out}$, i.e. displacement of the output node, of final topologies obtained by a pure OC algorithm and a staggered OC-GCMMA algorithm for optimization problem (3.107) and (3.108) for several mesh sizes

Fig. 3.28 shows the output motion $\boldsymbol{u}_{out}$, i.e. displacement of the output node, of the final topologies obtained by the simple OC algorithm in comparison to the staggered OC-GCMMA algorithm for the optimization problem given in Eqs. (3.107) and (3.108) for several FE mesh sizes. The output node of the final topology in its initial (unchanged) position is plotted at the local coordinates $(u_{out1}; u_{out2}) = (0; 0)$. The output motions obtained by the OC algorithm $\boldsymbol{u}_{out}^{OC}$ and the staggered OC-GCMMA algorithm $\boldsymbol{u}_{out}^{Stagg}$ are plotted in circles and crosses, respectively.

It can be seen that the output motions $\boldsymbol{u}_{out}^{OC}$ lay in a parasitic output motion corridor (red cone), i.e. the desired (vertical) motion u_{out2} is superposed by a dominant, undesired (horizontal) motion u_{out2} leading to an overall motion that is hardly controllable due to the parasitic influence. Thus, the topologies obtained by a pure OC algorithm fail to meet the specific motion requirements in terms of a precise output motion.

In contrast to this, it can be seen that all the output motions $\boldsymbol{u}_{out}^{Stagg}$ lay in a specific output motion corridor (green bold arrow) specified by lower and upper bounds of the parasitic output motion $-u_{out1}^{\min} = u_{out1}^{\max} =$

Table 3.3: Output displacements $\boldsymbol{u}_{\text{out}}$ and relative errors for optimization problem (3.107) and (3.108) for purely vertical output motion

N [−]	u_{out2}^{OC} [µm]	u_{out1}^{OC} [µm]	Parasitic error [−]	u_{out2}^{Stagg} [µm]	u_{out1}^{Stagg} [µm]	Parasitic error [−]
400	-104.3	14.5	-13.9%	-79.0	1.0	-1.3%
900	-113.0	33.6	-29.8%	-123.6	-0.8	0.6%
1,600	-123.2	21.4	-17.4%	-127.0	-0.4	0.3%
2,500	-137.1	28.5	-20.8%	-102.8	-0.4	0.4%
3,600	-133.5	22.9	-17.2%	-95.2	-0.1	0.1%
4,900	-139.2	30.7	-22.1%	-122.8	-0.4	0.4%
8,100	-133.3	29.7	-22.3%	-127.9	-0.7	0.5%
10,000	-138.5	24.6	-17.8%	-124.1	-0.6	0.5%
12,100	-138.9	28.4	-20.4%	-109.1	0.9	-0.9%
14,400	-139.0	22.8	-16.4%	-82.4	1.0	-1.2%
16,900	-140.3	31.2	-22.3%	-73.6	0.9	-1.2%
19,600	-138.1	31.0	-22.5%	-107.9	-0.6	0.6%
22,500	-138.5	32.5	-23.5%	-78.6	0.9	-1.2%

1μm. Thus, the topologies obtained by the staggered OC-GCMMA algorithm meet the specific motion requirements in terms of reducing parasitic motion.

Remark. Note, that the abscissa and ordinate are scaled differently in Fig. 3.28.

Table 3.3 lists the detailed output displacements $\boldsymbol{u}_{\text{out}}$ and relative errors of the final topologies for optimization problem (3.107) and (3.108) for different numbers of FE. In columns 2-4 and 5-7 the displacements of the output node and the parasitic error are listed for the OC algorithm and the staggered OC-GCMMA algorithm, respectively. It can be seen that the parasitic motions of the topology obtained by the OC algorithm are higher than 20% and, thus, cannot be neglected. In contrast, the parasitic motions of the topology obtained by the staggered OC-GCMMA algorithm are less than 1.3% and stay within the upper and lower bounds $-u_{out1}^{\min} = u_{out1}^{\max} = 1\mu$m.

3.3.4.3 Multi criteria objective function

The staggered topology optimization based on a multi criteria objective function given by the formulation $(\mathbb{P})^{II}_{\text{OC}}$ and $(\mathbb{P})^{II}_{\text{GCMMA}}$ in Eqs. (3.111) and (3.112) in Sect. 3.2.3.2 is applied to the load case already illustrated in Fig. 3.18 leading to a compliant gripping device. Here, the output motion $\boldsymbol{u}_{out}$ is maximized while it is forced to follow on a specified output motion path $\boldsymbol{u}_{spec} = (u_{spec1}; u_{spec2})$.

Fig. 3.29 shows the output motion $\boldsymbol{u}_{out}$, i.e. displacement of the output node, of the final topologies obtained by the staggered OC-GCMMA algorithm for the optimization problem given in Eqs. (3.111) and (3.112) for several FE mesh sizes.

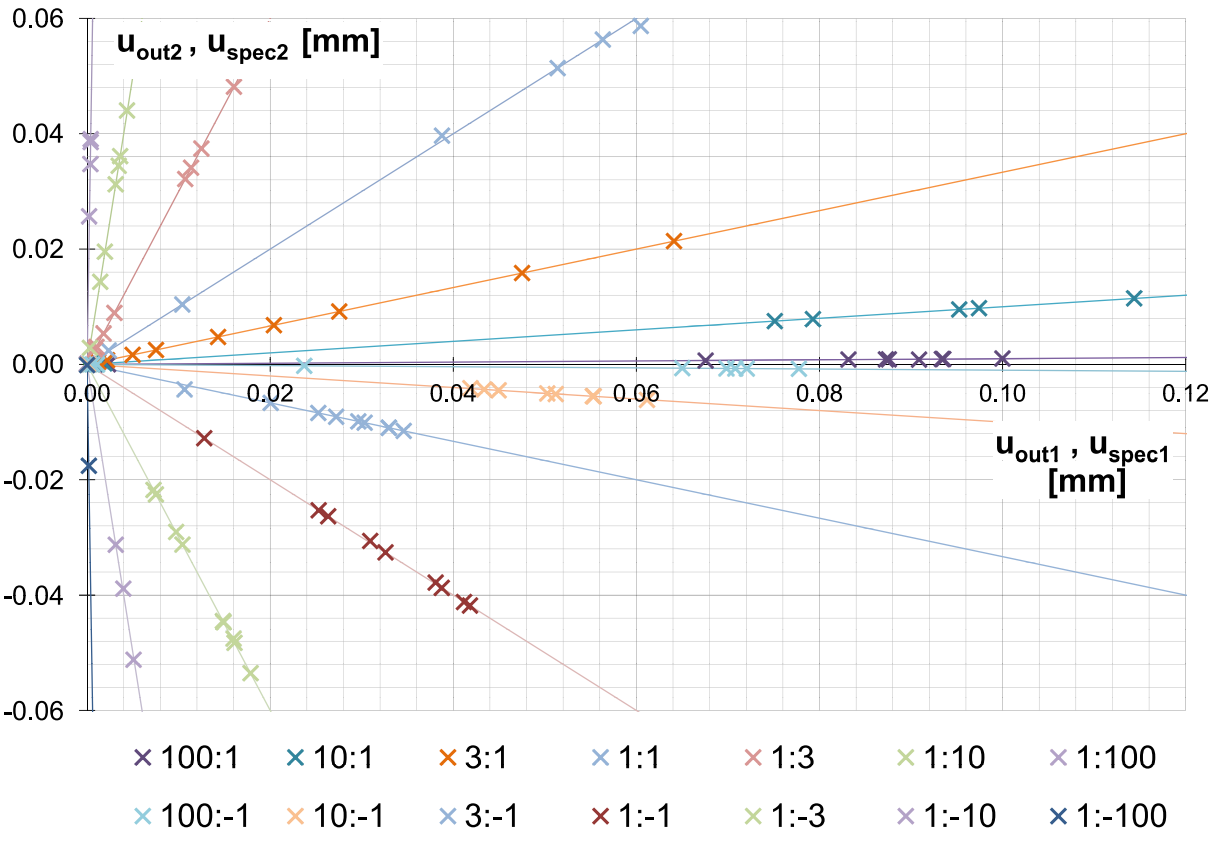

Figure 3.29: Displacements $\boldsymbol{u}_{out}$ of the output node for optimization problem (3.111) and (3.112) for different specified output motions $\boldsymbol{u}_{spec}$

The output node of the final topology in its initial (unchanged) position is plotted at the local coordinates $(u_{out1}; u_{out2}) = (0; 0)$. The desired, specified output motions $\boldsymbol{u}_{spec}$ are plotted as solid lines. The corresponding output motions obtained by the staggered OC-GCMMA algorithm $\boldsymbol{u}_{out}^{Stagg}$ are plotted as crosses. For instance, the entries highlighted as "x $1; -1$" represent the obtained output displacements $\boldsymbol{u}_{out}$ for a specified output motion $\boldsymbol{u}_{spec} = (1; -1)$.

It can be seen that all the obtained output motions $\boldsymbol{u}_{out}^{Stagg}$ lie on the specific output direction and vary only in the distance to the origin. Thus, the topologies obtained by the OC-GCMMA algorithm based on the multi-criteria method meet all considered motion requirements.

Table 3.4 lists in detail the corresponding output displacements $\boldsymbol{u}_{out}$ and parasitic errors for optimization problem (3.111) and (3.112) for different specified output motions $\boldsymbol{u}_{spec}$ for different numbers of FE. Further results are given in the Appendix A.5. In column two, the specified output direction $(u_{spec1}; u_{spec2})$ are listed. In column 3-6, the obtained displacements of the output node, the directions $(u_{out1}; u_{out2})$ and the parasitic errors are listed for the staggered OC-GCMMA algorithm.

Again, it can be seen that all parasitic motions of the topologies obtained by the staggered OC-GCMMA algorithm are very small and do not exceed 3%. Considering fine FE meshes with $N > 5,000$, the parasitic error is less than 0.1%.

Thus, the proposed staggered topology optimization algorithm generates successfully CM that meet specific output motion requirements.

Table 3.4: Output displacements $\boldsymbol{u}_{out}$ and relative errors for optimization problem (3.111) and (3.112) for different specified output motions $\boldsymbol{u}_{spec}$

N [−]	$u_{spec1} : u_{spec2}$ [−]	u_{out1}^{Stagg} [µm]	u_{out2}^{Stagg} [µm]	$u_{out1}^{Stagg} : u_{out2}^{Stagg}$ [−]	Parasitic error [−]
400	10:1	1.89	0.19	10.00	0.0%
900	10:1	97.42	9.76	9.99	-0.1%
1,600	10:1	114.37	11.45	9.99	-0.1%
2,500	10:1	0.95	0.09	10.04	0.4%
3,600	10:1	-146.51	-14.66	10.00	0.0%
4,900	10:1	79.28	7.86	10.09	0.9%
6,400	10:1	75.11	7.51	10.00	0.0%
8,100	10:1	0.07	0.01	9.99	-0.1%
10,000	10:1	95.26	9.53	9.99	-0.1%
400	3:1	1.21	0.40	3.00	0.0%
900	3:1	64.10	21.38	3.00	-0.1%
1,600	3:1	27.54	9.18	3.00	0.0%
2,500	3:1	20.40	6.80	3.00	0.0%
3,600	3:1	14.31	4.76	3.00	0.1%
4,900	3:1	7.52	2.51	3.00	0.0%
6,400	3:1	2.18	0.73	3.00	0.0%
8,100	3:1	47.51	15.85	3.00	-0.1%
10,000	3:1	4.97	1.66	3.00	-0.1%
400	1:1	60.48	58.69	1.03	3.0%
900	1:1	69.08	69.09	1.00	0.0%
1,600	1:1	2.35	2.42	0.97	-2.7%
2,500	1:1	56.33	56.33	1.00	0.0%
3,600	1:1	38.76	39.67	0.98	-2.3%
4,900	1:1	51.39	51.38	1.00	0.0%
6,400	1:1	0.03	0.03	1.00	0.1%
8,100	1:1	10.40	10.40	1.00	0.0%
10,000	1:1	61.17	61.16	1.00	0.0%

3.4 Summary

In this chapter, the non-intuitive topology optimization of large-displacement CM with specified output motion was addressed. After describing the relevant fundamentals of continuum mechanics, linear and nonlinear FEA, and topology optimization methods, a robust and efficient staggered topology optimization scheme, based on optimality criteria method and globally convergent method of moving asymptotes, was implemented. A single criterion objective function and a multi criteria objective function were formulated, implemented, applied and compared.

First, the topology optimization process was illustrated in a stepwise manner. It could be seen, that CM were generated without any intuition starting from an initial material domain with specified boundary conditions. The obtained results based on the own OC algorithm agree well with those of other research groups.

Second, the results based on linear and nonlinear FEA were compared in terms of computation time and quality. It could be seen, that a combination of linear and nonlinear FEA guarantees a time-efficient *and* accurate topology synthesis. Therefore, all optimization processes in this thesis are started out with linear FEA and, then, are finalized using nonlinear FEA. The final results of this linear-nonlinear FEA converged in all considered cases to the results obtained by the fully nonlinear computation but in significantly less time.

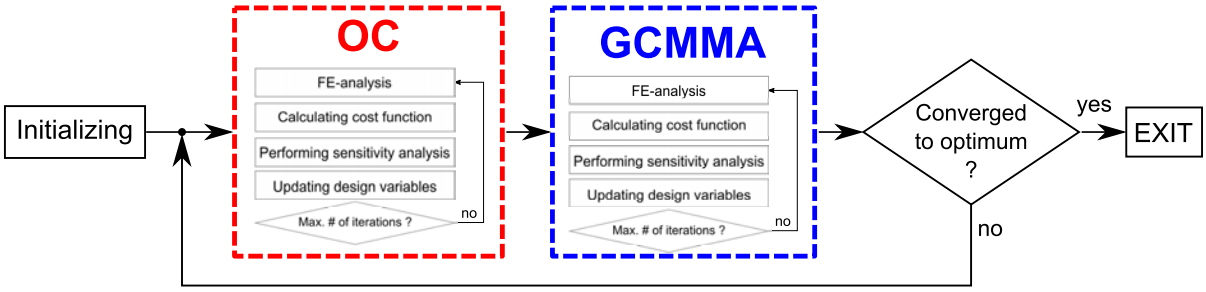

Figure 3.30: Proposed staggered optimization scheme combining Optimality Criteria (OC) method and Globally Convergent Method of Moving Asymptotes (GCMMA)

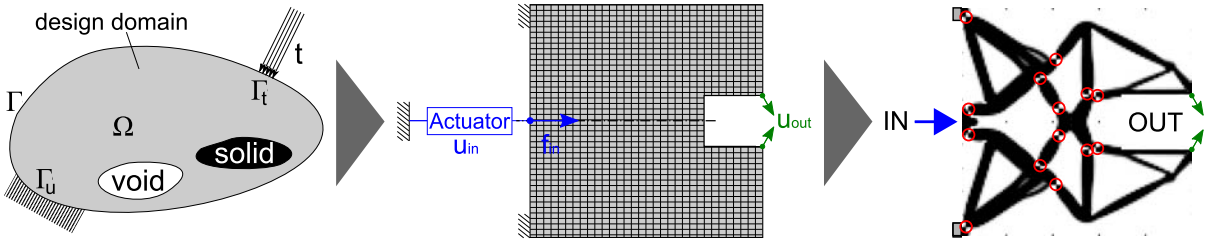

Figure 3.31: Three steps of the applied topology optimization: Starting out from a general material domain (left), transforming into a discretized design domain (center) and obtaining an optimized topology (right)

Third, adding and tuning stiffnesses of the actuator at the input node or the work piece at the output node yield successfully specifically tailored CM meeting the requirements in terms of motion, stroke and forces of different applications.

Fourth, the proposed staggered OC-GCMMA topology optimization algorithm is superior to a simple OC algorithm and provides a robust and broadly-functional method to generate CM with specified output motions. The objective function was formulated and applied as a single criterion objective function as well as a multi criteria objective function. Both formulations result in equally satisfying results, i.e. the generated CM meet the specified output motion requirements. In fact, all output motions coincide with the specified directions and the parasitic errors stay below 3%.

As a key result of the topology optimization process, the positions of the hinges can be gathered from the final topology of the CM as illustrated in Fig. 3.31. The application of a developed hinge detection algorithm is briefly discussed later in Sect. 5.3. However, an optimal shape of the hinges cannot be achieved. The hinges are represented by single nodes (one-node hinges) in finite element analysis leaving doubts on the physical meaning as well as an uncertainty in the manufacturing process.

In order to overcome this one-node hinge problem of mathematically optimized compliant mechanisms' topologies, one-node hinges need to be replaced by real flexure hinges providing desired deflection range and the ability to bear internal loads without failure.

4 Flexure hinges: key elements of compliant mechanisms

Flexure hinges (FH) are key elements of compliant mechanisms (CM) enabling CM's overall motion based on the elastic deflection of each individual FH. Their function is similar to conventional pin-joint hinges, i.e. to connect different stiff bodies or material areas with each other and, thus, providing flexibility. However, the overall motion is not obtained by a relative movement, but of the elastic deflection of certain "thin" parts. These areas with a thin cross-section are called FH. In contrast to their conventional counterparts, FH have no bearing play and, thus, are highly suitable for ultra-precision applications, as mentioned in Sect. 2.2.

However, the performance of FH varies significantly depending on the geometric shape of the hinges, i.e. differently shaped FH, as shown earlier in Fig. 2.6 possess different mechanical properties. Desired, relevant mechanical properties are named in Sect. 4.1. Analytical expressions are derived in Sect. 4.2 and Sect. 4.3. The set-ups of the numerical simulations and experimental studies are described in Sect. 4.4. Results from the analytical, numerical and experimental studies are compared and discussed in Sect. 4.5 . Finally, a conclusion is drawn in Sect. 4.6.

Remark. The influence of the geometric imperfections due to different manufacturing techniques is discussed in detail in [172] and, thus, is not further described here.

4.1 Relevant mechanical properties of flexure hinges

In order to incorporate appropriate planar FH into CM, the following static and dynamic mechanical properties are highly relevant and need to be calculated beforehand based on different loading conditions as illustrated in Fig. 4.1:

- **Mechanical stresses** $\sigma(x,z)$, $\tau(x,z)$, to identify critical regions that are not apparent.
- **Displacements** $u(x,z)$, $w(x)$, to gain a better understanding of the deflection of the entire FH.
- **Stiffness** k_z and **bending stiffness** c_ψ, to be able to model FH in an efficient manner.
- **Maximum (elastic) deflection**, to identify deflection limits and avoid material failure.
- **Precision**, i.e. **center of rotation** $\boldsymbol{P}_{eff}^{01}$ and its motion with deflection, to identify and compensate a change of kinematics.
- **Natural frequencies** f, to understand the behavior under dynamic load conditions and to check the quality of numerical simulations against experimental data.
- **Fatigue strengths** S_f, to avoid expensive experimental studies and to minimize the risk of unexpected fatigue failure.

Analytical expressions on the aforementioned properties are derived using a standard x-z-coordinate system, as shown in Fig. 4.1. If possible, numerical and experimental data are used to validate the analytical calculations. Since FH are mainly used in CM to allow rotational motion, the main focus is on axial bending caused by external nodal forces F_x, F_z and moment $M_y(x)$ also illustrated in Fig. 4.1.

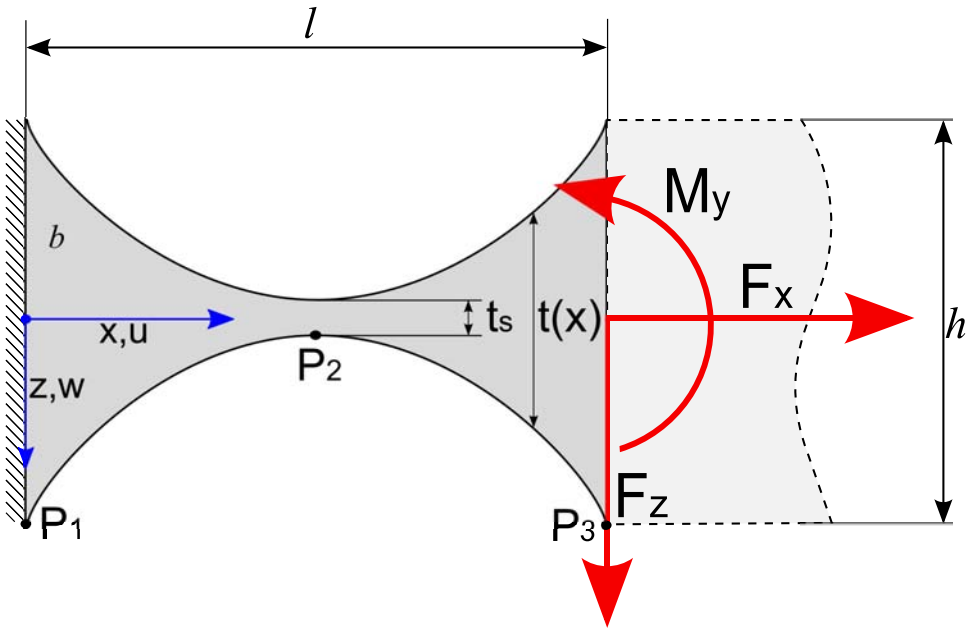

Figure 4.1: Planar, flexure hinge characterized by length l, depth b, height h, variable thickness $t(x) \geq t_s$ and common points P_1, P_2, P_3 to resist external loads F_x, F_z, M_y.

More importance is given to practice-oriented flexure hinge types that are more cost-saving in terms of manufacturability and mathematical convenience, i.e. planar flexure hinges are examined: rectangular, circular and parabolic flexure hinges, denoted by superscripts R, C and P, respectively.

Remark. Circular FH are approximated by a parabolic function using Taylor expansion to avoid complicated expressions. A detailed mathematical derivation is given in the Appendix A.7.

The geometry of flexure hinges is described by length l, height h and variable thickness $t(x) \geq t_s$ as well as common points $P_1(0, h/2)$, $P_2(l/2, t_s/2)$ and $P_3(l, h/2)$, as shown in Fig. 4.1. The depth is set to uniform $b = 10mm$ over the entire FH, which is sufficient for the majority of planar applications.

Key aspect for the following calculations is the geometric shape given by the variable thickness $t(x)$ of rectangular FH

$$t^R(x) = t_s, \tag{4.1}$$

for parabolic FH

$$\begin{aligned} t^P(x) = & \quad 2\left(c_1 + c_2 x + c_3 x^2\right) \\ = & \quad h - \frac{4x(h-t_s)}{l} + \frac{4x^2(h-t_s)}{l^2}, \end{aligned} \tag{4.2}$$

and for circular FH

$$\begin{aligned} t^C(x) = & \quad 2(z_M + \sqrt{r^2 - (x - x_M)^2}) \\ = & \quad \frac{h^2 - t_s^2 + l^2}{4(h-t_s)} - \sqrt{\frac{\left(l^2 + (h-t_s)^2\right)^2}{(4(h-t_s))^2} - \frac{(l-2x)^2}{4}}. \end{aligned} \tag{4.3}$$

The expressions of parabolic and circular FH are first written in a general form denoted by polynomial coefficients c_1, c_2, c_3 and circle's center coordinates x_M, z_M and radius r, respectively. Second, relevant geometric boundary conditions for parabolic FH

$$c_1 = \frac{h}{2}, \qquad c_2 = \frac{-2(h-t_s)}{l}, \qquad c_3 = \frac{2(h-t_s)}{l^2}, \tag{4.4}$$

and circular FH

$$x_M = \frac{l}{2}, \qquad z_M = \frac{t_s}{2} + r, \qquad r = \frac{l^2 + (h-t_s)^2}{4(h-t_s)}, \tag{4.5}$$

are applied.

Throughout this thesis, the formulations $t^{R,P,C} = t^{R,P,C}\ (x, h, l, t_s)$ are used to keep the solution adaptable to specific problems.

4.2 Analytical calculation of static and quasi-static mechanical properties

Explicit expressions for static and quasi-static mechanical properties, i.e. moments of area, mechanical stresses, displacements, stiffness and bending stiffness, maximum elastic deflection as well as the center of rotation, are derived analytically for differently shaped FH, in this section.

4.2.1 Moments of area

The moments of area for the considered flexure hinges are required to calculate the stresses in the following sections. The areas of the cross-section are

$$A^{R,P,C}(x) = bt^{R,P,C}(x). \tag{4.6}$$

The first moments of area $S_y(x,z) = \int_{A^*} z^* dA$ are

$$\begin{aligned} S_y^R(x,z) &= \frac{b}{8}(t_s^2 - 4z^2), \\ S_y^P(x,z) &= \frac{b}{8l^4}\left(\left(hl^2 + 4(h-t_s)(x^2-lx)\right)^2 - 4l^4z^2\right), \\ S_y^C(x,z) &= \frac{b}{2}\left(\left(z_M + \sqrt{r^2-(x-x_M)^2}\right)^2 - z^2\right). \end{aligned} \tag{4.7}$$

Remark. Note, that the first moment of area is calculated from z to $t(x)/2$.

The second moments of area $I_y(x) = \int_A z^2 dA$ are

$$\begin{aligned} I_y^R &= \frac{bt_s^3}{12}, \\ I_y^P(x) &= \frac{b}{12l^6}\left(h(l-2x)^2 + 4t_s(l-x)x\right)^3, \\ I_y^C(x) &= \frac{b}{12r^3}\left((x-x_M)^2 + 2r(z_M-r)\right)^3, \end{aligned} \tag{4.8}$$

where the thicknesses t_s and $t^{R,P,C}(x)$ are given in Eqs. (4.1) - (4.3). The listed moments of area are used to calculate nominal stresses and displacements in the upcoming section.

4.2.2 Mechanical stresses

The normal stresses $\sigma_x(x,z) = \frac{F_x}{A(x)} + \frac{M_y(x)}{I_y(x)}z$, and shear stresses $\tau_{xz} = \frac{F_z(x)S_y(x,z)}{I_y(x)b}$ depend on the external loads, moment of area $S_y(x,z)$, $I_y(x,z)$ and depth b, where a linear-elastic, isotropic stress-strain relation is assumed. Furthermore, the normal stresses σ_y, σ_z and shear stresses τ_{yz}, τ_{xy} in lateral direction are assumed to be negligible. Thus, the relevant normal stresses are

$$\begin{aligned}
\sigma_x^R(z) &= \frac{1}{bt_s}F_x + \frac{12(x-l)z}{bt_s^3}F_z + \frac{12z}{bt_s^3}M_y,\\
\sigma_x^P(x,z) &= \frac{l^2}{bh_*^3(x)}F_x + \frac{12l^6(x-l)z}{bh_*^9(x)}F_z + \frac{12l^6z}{bh_*^9(x)}M_y,\\
\sigma_x^C(x,z) &= \frac{1}{2bh_{**}(x)}F_x + \frac{3z(x-l)}{2bh_{**}^3(x)}F_z + \frac{3z}{2bh_{**}^3(x)}M_y,
\end{aligned} \tag{4.9}$$

and shear stresses are

$$\begin{aligned}
\tau_{xz}^R(z) &= \left(\frac{-6z^2}{bt_s^3} + \frac{3}{2bt_s}\right)F_z,\\
\tau_{xz}^P(x,z) &= \left(\frac{3l^2\left(-4l^4z^2 + h_*^6(x)\right)}{2bh_*^9(x)}\right)F_z,\\
\tau_{xz}^C(x,z) &= \frac{3\left(r^2 - z^2 - (x-x_M)^2 + \left(z_M - 2\sqrt{r^2-(x-x_M)^2}\right)z_M\right)}{4bh_{**}(x)}F_z,
\end{aligned} \tag{4.10}$$

where $h_*^3(x) = h(l-2x)^2 + 4(l-x)xt_s$ and $h_{**}(x) = z_M - \sqrt{r^2-(x-x_M)^2}$ are introduced to keep the expressions short.

Remark. Note, that any stress concentration effects are not yet taken into account as they will be considered later, in Sect. 4.2.5.

4.2.3 Displacements

The displacements $u(x,z)$, $w(x)$ due to external loads F_x, F_z, M_y, as already shown in Fig. 4.1, are calculated. Later, they are used to calculate stiffness and bending stiffness in Sect. 4.2.4.

In order to calculate displacements $u(x,z)$, $w(x)$ and bending slope $\psi(x)$, different beam theories are supposed to be applicable: *Euler-Bernoulli's* beam theory assumes that the (shear-indeformable) cross section remains perpendicular to the neutral axis and $\psi \approx \tan\psi = -w'(x)$, which is sufficient for slender beams (e.g. rectangular flexure hinges) undergoing small and moderate bending angles. *Elastica* beam theory lifts the latter limitation using the correct, non-linear expression $w''_E(x)/(1+(w'_E(x))^2)^{3/2} = -M_y(x)/EI_y(x)$ and, thus, it also holds for large bending angles. *Timoshenko's* beam theory holds for small and moderate bending angles, as Bernoulli's theory does, but it takes the shear deformation caused by arising shear stresses into account. Usually, this has a minor effect on the displacements considering "long" rectangular, leaf-type FH ($t(x) << l$). However, it cannot be neglected in the case of "thick", notch-type FH with an increased "effective" thickness $t^{eff} = 1/l \int t(x)dx \approx l$ compared to hinge length l, such as most circular and parabolic hinges. The influence of large deformations and shear stresses is further described in [218] and [219], respectively.

In this work, Timoshenko's beam theory is used to calculate the required displacements, since (a) FH do not undergo extremely large rotations as assumed in the Elastica beam theory and (b) shear deformation cannot be neglected as done in Bernoulli's beam theory. The relevant displacement expressions are

$$\begin{aligned} w'(x) &= -\psi(x) + \frac{F_z}{\alpha_S G A(x)}, \\ \psi'(x) &= \frac{M_y(x)}{EI_y(x)}, \\ u(x,z) &= z\,\psi(x) + \int_0^x \frac{F_x}{EA(x)}dx. \end{aligned} \tag{4.11}$$

Here, the angles $w'(x)$ and $\psi(x)$ differ by an additional shear deformation

term, where α_s is a shear correction factor compensating non-uniform shear stresses τ_{xs} in the cross section. Furthermore, the displacement $u(x,z)$ is expanded by an additional axial displacement term caused by axial forces F_x. Based on Eq. (4.11), the displacement expressions can be calculated for different types of flexure hinges.

The displacements for a rectangular flexure hinge based on Timoshenko's theory become

$$\begin{aligned} w^R(x) &= \frac{12(1+\nu)t_s^2 x + 30lx^2 - 10x^3}{5Ebt_s^3} F_z - \frac{6x^2}{Ebt_s^3} M_y, \\ \psi^R(x) &= -\frac{12lx - 6x^2}{Ebt_s^3} F_z + \frac{12x}{Ebt_s^3} M_y, \\ u^R(x,z) &= \frac{x}{Ebt_s} F_x - \frac{(12lx - 6x^2)z}{Ebt_s^3} F_z + \frac{12xz}{Ebt_s^3} M_y. \end{aligned} \tag{4.12}$$

The displacements of circular and parabolic FH are calculated in a general form and given in the Appendix A.6. The derived displacements expressions are used in Sect. 4.2.4 to calculate stiffness and bending stiffness of different flexure hinges.

Remark. Anti-clastic bending effects are neglected, as suggested in [220].

4.2.4 Stiffness and bending stiffness

The stiffnesses k_x, k_z and, in particular, the bending stiffness c_ψ of an FH is important for an efficient modeling of compliant mechanisms using discrete spring joints or reduced-order finite element models. The loads $\boldsymbol{f} = (F_z, M_y, F_x)^T$ and displacements $\boldsymbol{u} = (w(x), \psi(x), u(x,z))^T$ are coupled by the compliance expressions $\boldsymbol{u} = \mathbf{C}\ \boldsymbol{f}$ as given in Eq. (4.12). For modeling and topology optimization purposes, it is beneficial to invert this relation to

$$\boldsymbol{K}\boldsymbol{u} = \boldsymbol{f}. \tag{4.13}$$

The stiffness matrix $\boldsymbol{K}$ represents all mechanical properties (for static and quasi-static problems) that are crucial for modeling purposes, topology optimization problems and (embedded) finite element calculations using efficient, reduced-order finite element models.

Generally, these expressions are quite large, especially, for parabolic and circular flexure hinges. Due to conciseness, the stiffness matrix of a rectangular flexure hinge is presented solely. However, the stiffness matrices of parabolic and circular hinges can be calculated based on the displacement equation given in the Appendix A.6. Using the derived relations between loads and corresponding displacements given in Eq. (4.12) yield the stiffness matrix for rectangular FH

$$\boldsymbol{K}^R = Ebt_s^3 \begin{pmatrix} \frac{5}{l(12(1+\nu)t_s^2+5l^2)} & \frac{5}{24(1+\nu)t_s^2+10l^2} & 0 \\ \frac{5l}{2l(12(1+\nu)t_s^2+5l^2)} & \frac{10l^2+6(1+\nu)t_s^2}{l(12(1+\nu)t_s^2+5l^2)} & 0 \\ 0 & 0 & \frac{1}{lt_s^2} \end{pmatrix}, \tag{4.14}$$

where the diagonal entries represent k_z, c_ψ and k_x.

4.2.5 Maximum elastic deflection

Clearly, FH can undergo smaller rotational deflections than conventional pin joints that have practically no limit. The maximum elastic deflection of FH can be estimated by combining the occurring stresses, given in Eqs. (4.9) and (4.10), to an equivalent stress σ_V which has to be lower than the yield stress $S_{0.2}$: $\sigma_V \leq S_{0.2}$. Among various established yield criteria, the von-Mises yield criterion $\sigma_V = \sqrt{\sigma_x^2 + 3\tau_{xz}^2}$ is mainly used for ductile materials for quasi-static loading conditions and, thus, applicable to the majority of materials in compliant mechanisms.

The maximum normal stress $\sigma_{x,max}$ can be found at the thinnest cross section $x = x(t = t_s)$ at the upper or lower edge $z = \pm t_s/2$. Whereas the maximum shear stresses $\tau_{xz,max}$ occur at the *center* of the thinnest cross section $x = x(t = t_s)$ at $z = 0$ and is zero at the edges $\tau_{xz}(z = \pm t_s/2) = 0$. Typically in applications considered here, normal stresses are more dominant than shear stresses suggesting to neglect shear stress. However, maximum shear stresses are taken into account in the equivalent stress due to safety reasons. Therefore, the equivalent stresses

become

$$\begin{aligned}\sigma_{V,max}^{R,P,C} &= \sqrt{\left(\sigma_{max,x}K_{tt} + \sigma_{max,b}K_{tb}\right)^2 + 3\tau_{max}^2} \\ &= \sqrt{\left(\frac{F_x}{bt_s}K_{tt} + \frac{6M_y(x)}{bt_s^2}K_{tb}\right)^2 + 3\left(\frac{F_z}{2bt_s}\right)^2},\end{aligned} \tag{4.15}$$

where stress concentration factors K_{tt} and K_{tb} for tensile and bending loads (second indices t, b) are introduced due to the stress concentration at the FH as illustrated in Fig. 4.2.

For rectangular FH, with uniform thickness $t(x) = t_s$, the critical section is solely determined by the maximum bending moment $M_{y,max}^R(x = 0) = M_y - lF_z$. In contrast to this, for parabolic and circular notch type hinges, the critical section is determined by the thinnest cross section t_s, as well, leading to a critical section very close to the thinnest cross section at $x \approx l/2$, where the bending moment becomes $M_{y,max}^{C,P}(x \approx l/2) = M_y - l/2\ F_z$. Thus, the maximum equivalent stresses are

$$\begin{aligned}\sigma_{e,max}^{R} &= \sqrt{\left(\frac{F_x}{bt_s}K_{tt}^{R} + \frac{6(M_y - lF_z)}{bt_s^2}K_{tb}^{R}\right)^2 + 3\left(\frac{F_z}{2bt_s}\right)^2}, \\ \sigma_{e,max}^{C,P} &= \sqrt{\left(\frac{F_x}{bt_s}K_{tt}^{C,P} + \frac{6(M_y - \frac{l}{2}F_z)}{bt_s^2}K_{tb}^{C,P}\right)^2 + 3\left(\frac{F_z}{2bt_s}\right)^2}.\end{aligned} \tag{4.16}$$

The stress concentration factors for rectangular leaf type hinges K_{tt}^R, K_{tb}^R strongly depend on the corner radius and can be found in [221]. For circular and parabolic hinges, stress concentration factors can be approximated following [222] as

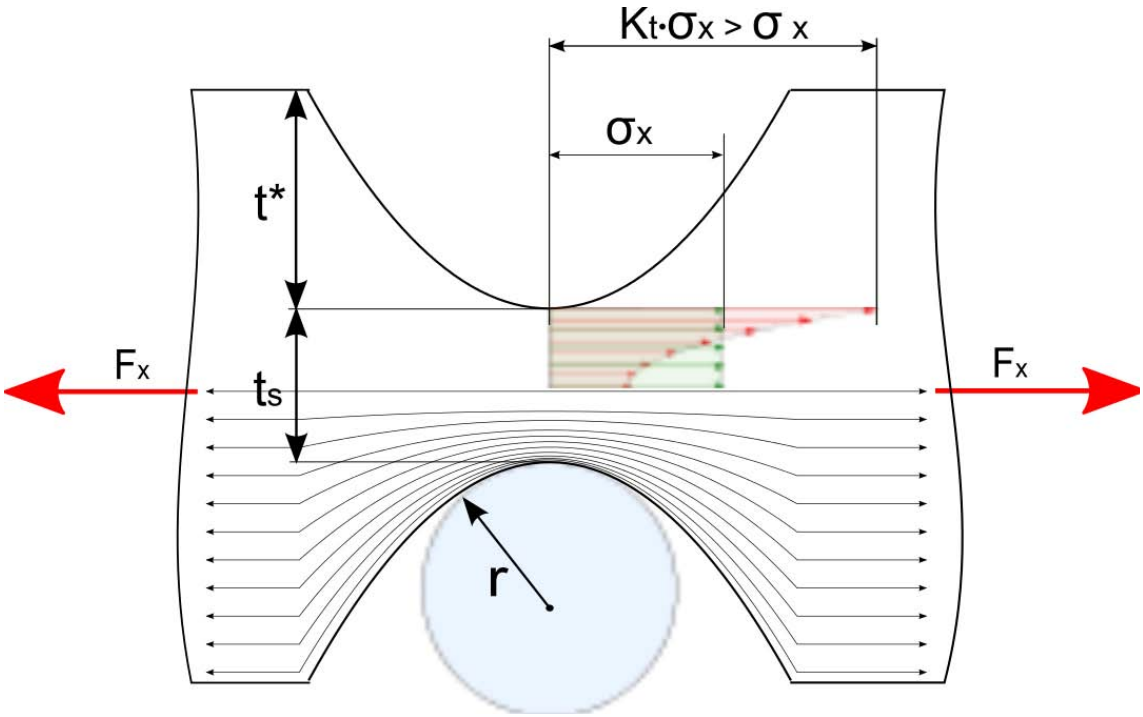

Figure 4.2: Stress concentration at flexure hinges due to notch effect

$$
\begin{aligned}
K_{tt}^{C,P} &= 1 + \left[0.1 \left(\frac{r}{t^*} \right) + 0.7 \left(1 + \frac{t_s}{2r} \right)^2 \left(\frac{t_s}{2r} \right)^{-3} \right. \\
&\qquad \left. +0.13 \left(\frac{t_s}{2r} \right) \left(\frac{t_s}{2r} + \frac{t^*}{r} \right)^{-1} \left(\frac{t^*}{r} \right)^{-1.25} \right]^{-\frac{1}{2}}, \\
K_{tb}^{C,P} &= 1 + \left[0.08 \left(\frac{r}{t^*} \right)^{0.66} + 2.2 \left(1 + \frac{t_s}{2r} \right)^{2.25} \left(\frac{t_s}{2r} \right)^{-3.375} \right. \\
&\qquad \left. +0.2 \left(\frac{t_s}{2r} \right) \left(\frac{t_s}{2r} + \frac{t^*}{r} \right)^{-1} \left(\frac{t}{r} \right)^{-1.33} \right]^{-\frac{1}{2}},
\end{aligned}
\tag{4.17}
$$

where $t^* = \frac{h-t_s}{2}$ and the radii of curvature r are

$$
r^C = \frac{l^2 + (h - t_s)^2}{4(h - t_s)} = const. \tag{4.18}
$$

and

$$r^P\left(x=\frac{l}{2}\right)=\frac{l^2}{4(h-t_s)}, \tag{4.19}$$

for circular and parabolic hinges as shown in Fig. 4.2. Here, the geometric properties given in Eqs. (4.1) – (4.3) and corresponding derivatives $t'(x)$, $t''(x)$ were applied to calculate the radius of a parabola $r^P(x) = \left|(1+t'(x)^2)^{3/2}/t''(x)\right|$.

Finally, the equivalent stresses can be calculated using Eq. (4.15) for all types of FH considered in this work. Based on the material dependent strength, the maximum values of axial and shear forces, F_x and F_z, as well as of the bending moment M_y that are applicable can be determined, which leads to the maximum elastic deformations by using Eq. (4.11).

4.2.6 Precision, i.e. center of rotation

The precision of FH is a significant performance indicator and refers – from a kinematical point of view – to the center of rotation and its motion with deflection of bodies connected by flexure hinges. It is crucial for a correct modeling of compliant mechanisms, i.e. ignoring the particular center of rotation of FH can lead to parasitic motion or failure of the entire mechanism due to unwanted behavior, such as snap through effects.

The center of rotation is usually considered for rigid-body-motions. However, many parts of a CM that are connected by FH are very stiff and can be treated in a similar way. In this work, the overall center of rotation $\boldsymbol{P}_{eff}^{01}$ refers to a fixed point considering undeformed (0) and maximum elastically deformed state (1) as illustrated in Fig. 4.3, whereas its motion refers to the herpolhode, i.e. the motion of the instantaneous center of rotation with deflection.

In order to calculate the center of rotation of a rigid body attached to an FH, the position of two single points P_A, P_B and the corresponding displacements $u_A = u(l,0)$, $w_A = w(l,0)$ and $u_B = u(l,-h/2)$ are considered. This yields an overall center of rotation

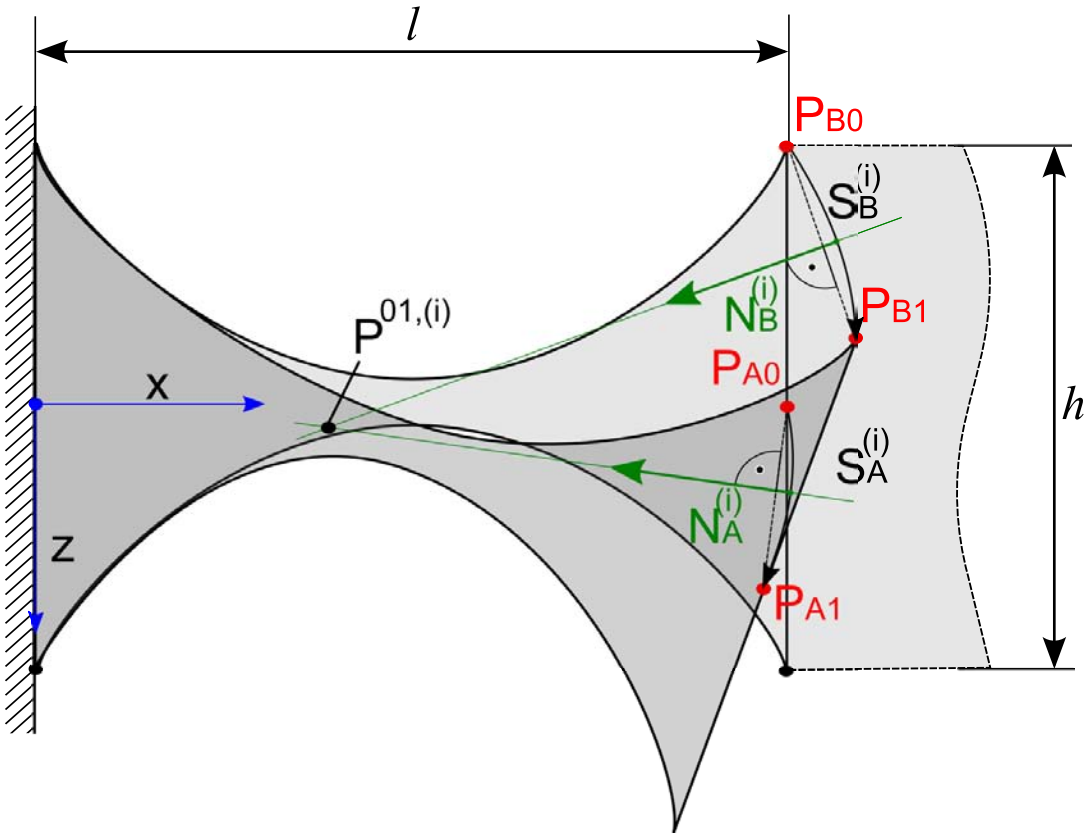

Figure 4.3: Determination of instantaneous center of rotation $P^{01,(i)}$ of a flexure hinge

$$\boldsymbol{P}_{eff}^{01} = \begin{pmatrix} P_{eff,x}^{01} \\ \\ P_{eff,z}^{01} \end{pmatrix} = \frac{1}{2} \begin{pmatrix} \frac{w_A}{u_A - u_B} h + u_A + u_B + 2l \\ \\ \frac{u_A}{u_B - u_A} h - \frac{u_A u_B}{w_A} + w_A \end{pmatrix}, \tag{4.20}$$

which holds for all types of flexure hinges.

The motion of the (instantaneous) center of rotation can be calculated considering an infinite number of intermediate steps between undeformed and maximum elastically deformed step. Therefore, the motion paths

$$\boldsymbol{S}_A^{(i)} = \boldsymbol{P}_A + \begin{pmatrix} u_A^{(i)} \\ w_A^{(i)} \end{pmatrix}, \qquad \boldsymbol{S}_B^{(i)} = \boldsymbol{P}_B + \begin{pmatrix} u_B^{(i)} \\ w_B^{(i)} \end{pmatrix}, \tag{4.21}$$

the tangent vectors

$$\boldsymbol{T}_A^{(i)} = \dot{\boldsymbol{K}}_{\boldsymbol{A}} = \begin{pmatrix} \dot{u}_A^{(i)} \\ \dot{w}_A^{(i)} \end{pmatrix}, \qquad \boldsymbol{T}_B^{(i)} = \dot{\boldsymbol{K}}_{\boldsymbol{B}} = \begin{pmatrix} \dot{u}_B^{(i)} \\ \dot{w}_B^{(i)} \end{pmatrix}, \tag{4.22}$$

and the corresponding normal vectors

$$\boldsymbol{N}_A^{(i)} = \begin{pmatrix} \dot{w}_A^{(i)} \\ -\dot{u}_A^{(i)} \end{pmatrix}, \qquad \boldsymbol{N}_B^{(i)} = \begin{pmatrix} \dot{w}_B^{(i)} \\ -\dot{u}_B^{(i)} \end{pmatrix}, \tag{4.23}$$

need to be calculated first where the operator $\dot{(\,)}$ refers to the change from the ith to the $(i{+}1)$th intermediate step. Determining the point of intersection of $\boldsymbol{N}_A^{(i)}$ and $\boldsymbol{N}_B^{(i)}$ leads to

$$\boldsymbol{P}^{01,(i)} = \begin{pmatrix} \frac{2(u_A+l)\dot{u}_A - 2(u_B+l)\dot{u}_B + h\dot{w}_A}{2(\dot{u}_A-\dot{u}_B)} \\ \\ w_A - \frac{2(u_A-u_B)\dot{u}_B + h\dot{w}_A}{2(\dot{u}_A-\dot{u}_B)\dot{w}_A}\dot{u}_A \end{pmatrix}, \tag{4.24}$$

which is the center of rotation for all intermediate steps i, i.e. the desired motion with deflection.

4.3 Analytical calculation of dynamic mechanical properties

The explicit expressions for dynamic mechanical properties, i.e. first natural frequency and fatigue strength, are derived analytically for differently shaped FH, in this section.

4.3.1 Natural frequency

The natural frequency of a system consisting of a rigid body connected to a flexure hinge as shown in Fig. 4.4 is relevant for compliant mechanisms under dynamic loading conditions. In addition, it is a good quality measure comparing analytical, numerical and experimental studies.

The natural frequencies are calculated analytically using the aforementioned Timoshenko's beam theory. Extending Eq. (4.11) to a dynamic state yield the differential equations:

$$\begin{aligned} \rho A(x)\ddot{w}(x) - \left(GA_*(x)(w'(x)+\psi)\right)' &= q, \\ \rho I_y(x)\ddot{\psi} - (EI_y(x)\psi')' + GA_*(w'+\psi) &= 0. \end{aligned} \tag{4.25}$$

Applying standard boundary conditions at fixed end $x = 0$

$$w = 0, \qquad \psi = 0, \tag{4.26}$$

and free end $x = l$

$$EI_y\psi' = \overline{M}, \qquad GA_*(w'+\psi) = \overline{F}, \tag{4.27}$$

the differential Eq. (4.25) can be solved, where the force $\overline{F}$ and the moment $\overline{M}$ depend on the (known) rigid body connected to the FH. However, solving these equations analytically for a variable, unspecified FH's thickness $t(x) \neq$ const. is not always possible. Therefore, a numerical approach, namely the Rayleigh quotient

$$\omega_1^2 = \frac{\max E_P}{\max E_k} \tag{4.28}$$

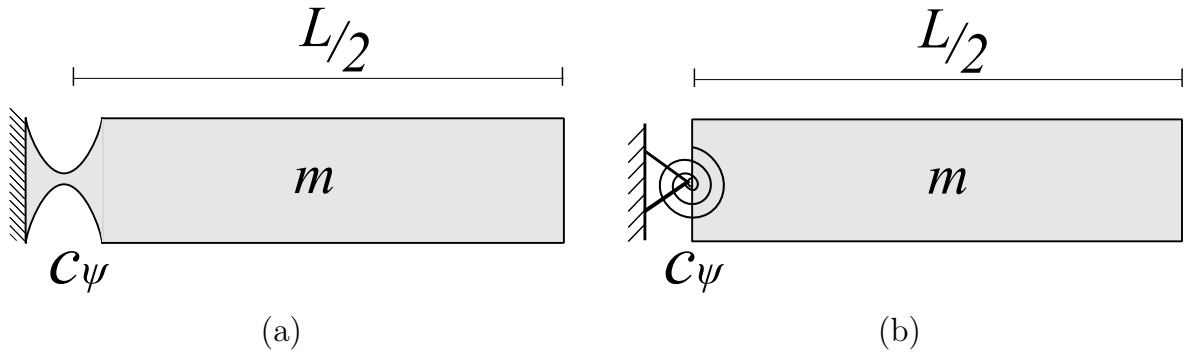

Figure 4.4: Continuous flexure hinge (a) and equivalent discrete torsion spring model (b)

is chosen, where the first natural circular frequency ω_1 is approximated by the ratio of maximum values of potential and kinetic energies E_p and E_k. Following [223] yields for the FH

$$\omega_1^2 = \frac{\int_0^l EI_y(x)\Psi'(x)^2 + GA_*(x)(W'(x) + \Psi(x))^2 dx}{\rho \int_0^l A(x)W(x)^2 + I_y(x)\Psi(x)^2 dx}, \tag{4.29}$$

where displacement and bending angle are described by appropriate test functions $\Psi(x)$ and $W(x)$. In order to determine $\Psi(x)$ and $W(x)$, the displacements and bending angle occurring from a uniform transverse load q_0 with a resulting bending moment $M_y(x) = -\frac{1}{2}q_0(l-x)^2$, as suggested in [224], are used. The Eq. (4.29) is applied in Sect. 4.5.4 to calculate the natural frequencies $f_{ana} = \omega_1/2\pi$ analytically.

The natural frequency of a *discrete* model can be calculated from

$$J\ddot{\psi}(t) + c_\psi \psi(t) = 0, \tag{4.30}$$

with $J = mL^2/12$ as the mass moment of inertia of the attached rigid body of the length $L/2$. Assuming a time-harmonic vibration $\psi(t) = a\sin(\omega t)$ yield $\left(c - J\omega^2\right)\sin(\omega t) = 0$, which must hold for all t. Substituting the circular frequency $\omega = 2\pi f$ and the mass of the half test specimen $m = \rho AL/2$ leads to $c_\psi = 32\pi^2 f_1^2/(3\rho AL^3)$ which leads to the final relation

$$f_1^{dm} = \sqrt{\frac{3\rho AL^3 c_\psi}{32\pi^2}}. \tag{4.31}$$

Thus, the natural frequency of the discrete model f_1^{dm} can be calculated from the torsion spring's stiffness, i.e. the bending stiffness of the FH.

4.3.2 Fatigue strength

The fatigue strengths of differently shaped FH are calculated using the stress-life approach. Accordingly, the occurring mechanical stresses are compared to the fatigue strength of a smooth test specimen which is then lowered by applying different reduction factors, often called "knock-down factors", accounting for nonzero mean stresses, notch effects and surface finish.

Remark. Thermal effects (both ambient and generated) are considered negligible for the applications of interest.

4.3.2.1 Stresses in flexural hinges

Since FH are mainly used in CM to allow rotational motion, the main focus is on axial bending caused by the external nodal forces F_x, F_z and the moment $M_y(x)$, as already described for the quasi-static case in Sect. 4.2. Here, dynamic effects are taken into account, where all loads are assumed to be time-harmonic, with constant mean and amplitude values, denoted by index m and index a, respectively. For example, $M_y = M_{my} \pm M_{ay}$ causes time-harmonic (bending) stresses $\sigma_b = \sigma_{mb} \pm \sigma_{ab}$.

According to standard literature, the largest principal tensile stress is the most significant stress component in fatigue analysis for the materials typically used in CM [225]. Assuming negligible normal stresses in lateral direction, i.e. $\sigma_y = \sigma_z = 0$, the largest principal tensile stress is given by the normal stress in the x-direction

$$\sigma_x(x,z) = \frac{F_x}{A(x)} + \frac{M_y(x)}{I_y(x)} z, \tag{4.32}$$

which depends on the external loads F_x, $M_y(x)$, cross-section $A(x)$, depth b, second area moment $I_y(x,z)$ and the z-coordinate, where a linear-elastic, isotropic stress-strain relation is assumed.

Recalling Eq. (4.9), the *relevant* nominal stresses within flexural hinges as shown in Fig. 4.1 are

$$\begin{aligned}
\sigma_x^R(z) &= \frac{1}{bt_s}F_x + \frac{12(x-l)z}{bt_s^3}F_z + \frac{12z}{bt_s^3}M_y, \\
\sigma_x^P(x,z) &= \frac{l^2}{bh_*^3(x)}F_x + \frac{12l^6(x-l)z}{bh_*^9(x)}F_z + \frac{12l^6z}{bh_*^9(x)}M_y, \\
\sigma_x^C(x,z) &= \frac{1}{2bh_{**}(x)}F_x + \frac{3z(x-l)}{2bh_{**}^3(x)}F_z + \frac{3z}{2bh_{**}^3(x)}M_y,
\end{aligned} \tag{4.33}$$

where $h_*^3(x) = h(l-2x)^2+4(l-x)xt_s$ and $h_{**}(x) = z_M - \sqrt{r^2-(x-x_M)^2}$ are introduced to keep the expressions concise.

In the ensuing sections, the axial force F_x causes a tensile stress σ_t whereas the moment M_y and the force F_z cause a bending stress, σ_b, within the cross-section of the FH. For both loading conditions, the resulting mean stresses $\sigma_m = (\sigma_{max} + \sigma_{min})/2$, amplitude stresses $\sigma_a = (\sigma_{max} - \sigma_{min})/2$ and ratio $R = \sigma_{min}/\sigma_{max}$ can be calculated using the nominal stresses $\sigma_{x,max}^{R,P,C}$ which occur at the thinnest cross section at the upper or lower edge substituting $x = l/2$ and $z = \pm t_s/2$ into Eq. (4.33).

4.3.2.2 Fatigue strength with zero mean stress

Fatigue strengths S_f have been determined by extensive experiments and, thus, are known for some materials. However, if bending fatigue strength S_{fb} and tensile fatigue strength S_{ft} are not available, they can be estimated in absence of mean stress ($\sigma_m = 0$) based on numerous experiments on unnotched standard test specimens. There are different methods to estimate the fatigue strengths. A classical approach is given by using the linear relation between tensile fatigue strength S_{ft} and ultimate tensile strength S_U

$$S_{ft} = \alpha S_U, \tag{4.34}$$

where the factors $\alpha = 0.5$ for steel and Titanium alloys, and $\alpha = 0.35$ for aluminum alloys are typically used. As mentioned in [225], this is not

Table 4.1: Material properties [227] and fatigue strengths in absence of mean stresses ($\sigma_m = 0$) of aluminum alloys mainly used in compliant mechanisms: experimental data $S_{f,exp}$ [227], a linear estimate [225], bending fatigue strength $S_{fb,Ra}$ and tensile fatigue strength $S_{ft,Ra}$ [226]

Name [−]	$S_{0.2}$ [MPa]	S_U [MPa]	$S_{f,exp}$ [MPa]	$S_{ft} = \alpha S_U$ [MPa]	$S_{fb,Ra}$ [MPa]	$S_{ft,Ra}$ [MPa]
Al 2024-O	75	185	90	65	74	63
Al 2024-T3	345	485	140	170	130	111
Al 2024-T351	325	470	140	165	130	111

necessarily a good measure and only provides an initial estimate. Another approach is suggested by Radaj [226], where the bending fatigue strength $S_{fb,Ra}$ is estimated for aluminum alloys possessing different tensile strengths for $N = 10^8$ life cycles by the following

$$S_{fb,Ra} \approx \begin{cases} 0.4 S_U & \text{for } S_U \leq 325\,\text{MPa} \\ 130\,\text{MPa} & \text{for } S_U \geq 325\,\text{MPa}, \end{cases} \tag{4.35}$$

and the tensile fatigue strengths $S_{ft,Ra}$ were further reduced to

$$S_{ft,Ra} \approx 0.85\ S_{fb,Ra}. \tag{4.36}$$

The different fatigue strengths in absence of any mean stresses ($\sigma_m = 0$) are listed in Table 4.1.

4.3.2.3 Fatigue strength with nonzero mean stress

Considering nonzero mean stresses, the maximum permissible stress amplitudes need to be formulated as a function of the mean stresses $S_{ai}(\sigma_m)$, i.e. the same number of life cycles can only be achieved for higher mean stresses σ_m by reducing the stress amplitudes σ_a. The index i is used for formulas which apply to both, tensile and bending load. Otherwise the indexes b for bending and t for tension are used separately.

Three established relations have been proposed by Gerber [228], Goodman [229] and Soderberg [230] respectively:

$$\text{Gerber:} \qquad S_{ai}(\sigma_m) = S_{fi}\left(1 - \left(\frac{\sigma_m}{S_U}\right)^2\right), \tag{4.37}$$

$$\text{Mod. Goodman:} \qquad S_{ai}(\sigma_m) = S_{fi}\left(1 - \frac{\sigma_m}{S_U}\right), \tag{4.38}$$

$$\text{Soderberg:} \qquad S_{ai}(\sigma_m) = S_{fi}\left(1 - \frac{\sigma_m}{S_{0.2}}\right), \tag{4.39}$$

as illustrated later in Fig. 4.8(a). According to Suresh [231], Soderberg provides a very conservative estimate, whereas Goodman and Gerber match experimental data well. Modified Goodman is suggested for aluminum alloys and, thus, further considered.

4.3.2.4 Notch effect

The fatigue strength of FH is significantly lower than it is for unnotched test specimens, due to stress concentrations that occur at the root of FH, causing nucleation of microcracks which possibly leads to failure. In a quasi-static analysis, the stress concentration factors K_{ti} are mainly used to account for the occurring higher peak stresses, compared to the nominal stresses, as shown in [232]. The stress concentration factors for tension $K_{tt}^{C,P}$ and bending $K_{tb}^{C,P}$ are already given for static calculations in Eq. (4.17).

In fatigue analysis, various experiments have suggested that the static stress concentration factors overestimate the notch severity of FH. Therefore, the "notch effect" is described more precisely by the fatigue strength reduction factor K_{fi}, also called fatigue notch factor, defined as the ratio of the fatigue strength of unnotched test specimens (as described in the previous section) and the fatigue strength of the notched specimens, i.e. the flexural hinge:

$$1 \leq \quad K_{fi} = \frac{S_{fi,TestSpecimen}}{S_{fi,FlexureHinge}} \quad \leq K_{ti}. \tag{4.40}$$

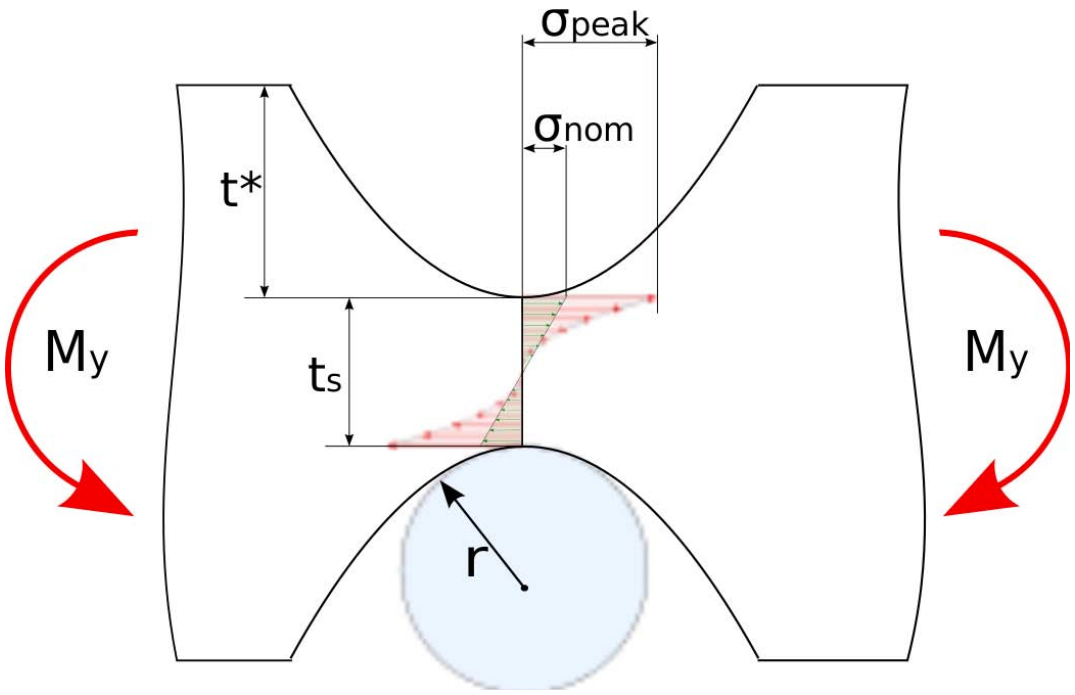

Figure 4.5: Peak stresses depending on the curvature at the root lead to a reduced fatigue strength of flexural hinges

The fatigue strength reduction factor K_{fi} can be calculated using the notch sensitivity q, which is defined as

$$q = \frac{K_{fi} - 1}{K_{ti} - 1}, \tag{4.41}$$

where q varies from zero (no notch effect: $K_{fi} = 1$) to one (full notch effect $K_{fi} = K_{ti}$) and can be determined from Fig. 4.6.

K_{fi} can also be determined from experiments or empirical measures as proposed by Peterson or Neuber:

$$\text{Peterson:} \qquad K_{fi} = 1 + \frac{K_{ti} - 1}{1 + A_P/r}, \tag{4.42}$$

$$\text{Neuber:} \qquad K_{fi} = 1 + \frac{K_{ti} - 1}{1 + \sqrt{A_N/r}}, \tag{4.43}$$

with A_P and A_N as material constants depending on the strength and ductility, e.g. $A_P \approx 0.66\,\text{mm}$ for aluminum alloys [233]. Thus, the

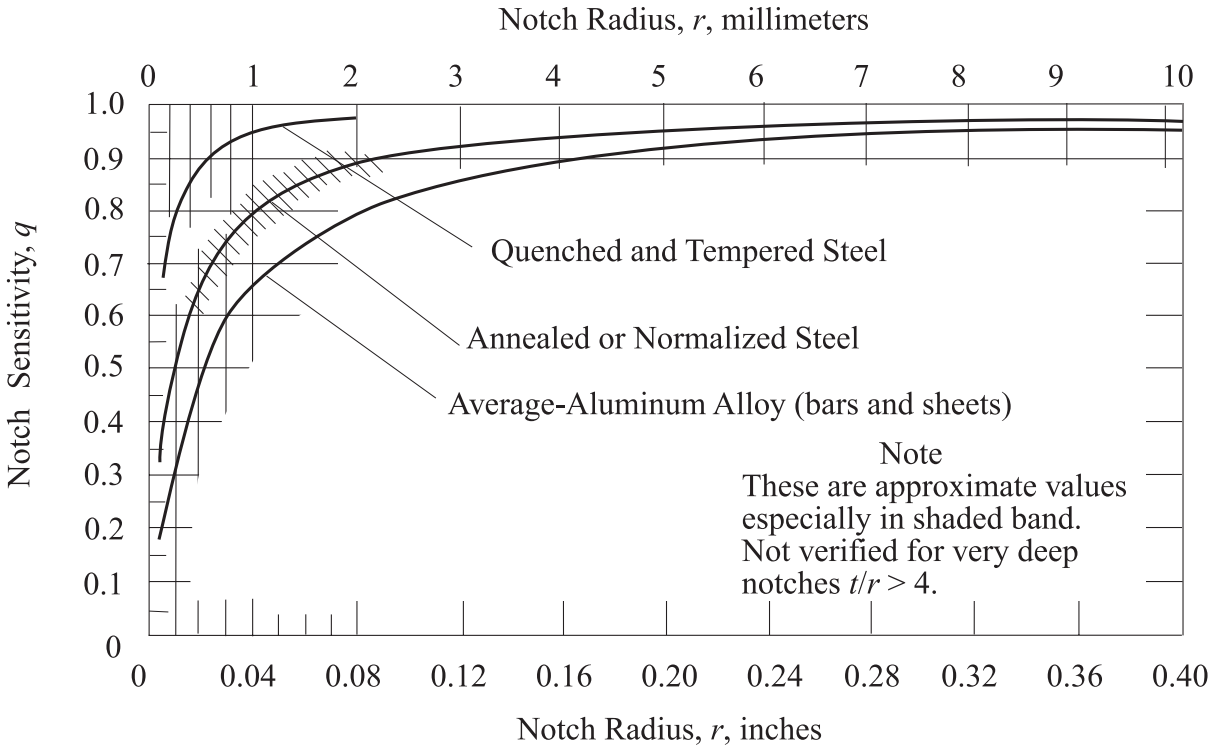

Figure 4.6: Notch sensitivity for different radii r [221]

reduced fatigue strength of flexural hinges is calculated by Eqs. (4.37) - (4.39) yielding, for example, following Goodman

$$S_{ai}(\sigma_m) = \frac{S_{fi}}{K_{fi}} \left(1 - \frac{\sigma_m}{S_U / K_{ti}} \right), \tag{4.44}$$

as illustrated in Fig. 4.8(b) where the ordinate and abscissa are scaled by $1/K_{ti}$ and $1/K_{fi}$, respectively.

4.3.2.5 Superposed bending and tension

Thus far, pure bending or pure tensile cyclic loads were considered. Although superposed bending and tension cause similar critical stresses, the overall fatigue life is unequally more complex due to different amplitudes, frequencies and phase relations. There are, to the authors' knowledge, neither material parameters nor precise methods known that hold for arbitrary loading conditions. However, a reasonable equivalent stress

$\sigma_{a,e}$ can be estimated following Issler [233] by choosing, for example, the tensile loading as a reference yielding

$$\sigma_{a,e} = \sigma_{at} + \kappa\sigma_{ab}, \tag{4.45}$$

with $\kappa = S_{at}/S_{ab}$ as a reference coefficient.

4.3.2.6 Surface effect

The surface roughness of the root of FH affects the fatigue strength significantly, due to possible crack nucleation and propagation on the surface. The surface roughness reduction factor γ accounts for different surface qualities obtained by different manufacturing technologies, such as polishing, grinding, milling and drilling. It is defined as the ratio of the fatigue strength of standard test specimens with a specific surface quality and the fatigue strength of a very smooth test specimens

$$\gamma = \frac{S_{fi}}{S_{fi,smooth}}. \tag{4.46}$$

It is assumed that the influence of the surface finish is similar for unnotched and notched test specimens. Therefore, values for γ, which were measured on unnotched test specimens are applied to FH, as well. The surface roughness reduction factor γ depending on the surface roughness R_t, also called total height of the profile, is shown in Fig. 4.7 for different aluminum alloys.

The absolute arithmetic *average* surface roughness R_a for electrical discharged machined (EDM) specimens is typically within a range of 1.6-5 µm [235]. There is no mathematical relation between R_t and R_a. However, an experience-based estimate is given in [236] by a factor of 8.7 yielding approximate values of $R_t \approx$ 14-44 µm. Assuming a reasonable surface roughness of $R_t \approx 20$ µm yields for Al wrought alloys mainly used in CM, e.g. Al 2024-T3 or Al 2024-T351, with a ratio $S_{0.2}/S_U \approx 0.7$ a surface reduction factor of $\gamma = 0.75$.

The fatigue strength of FH is further reduced to

$$S_{ai}(\sigma_m) = \frac{\gamma S_{fi}}{K_{fi}} \left(1 - \frac{\sigma_m}{S_U/K_{ti}}\right), \tag{4.47}$$

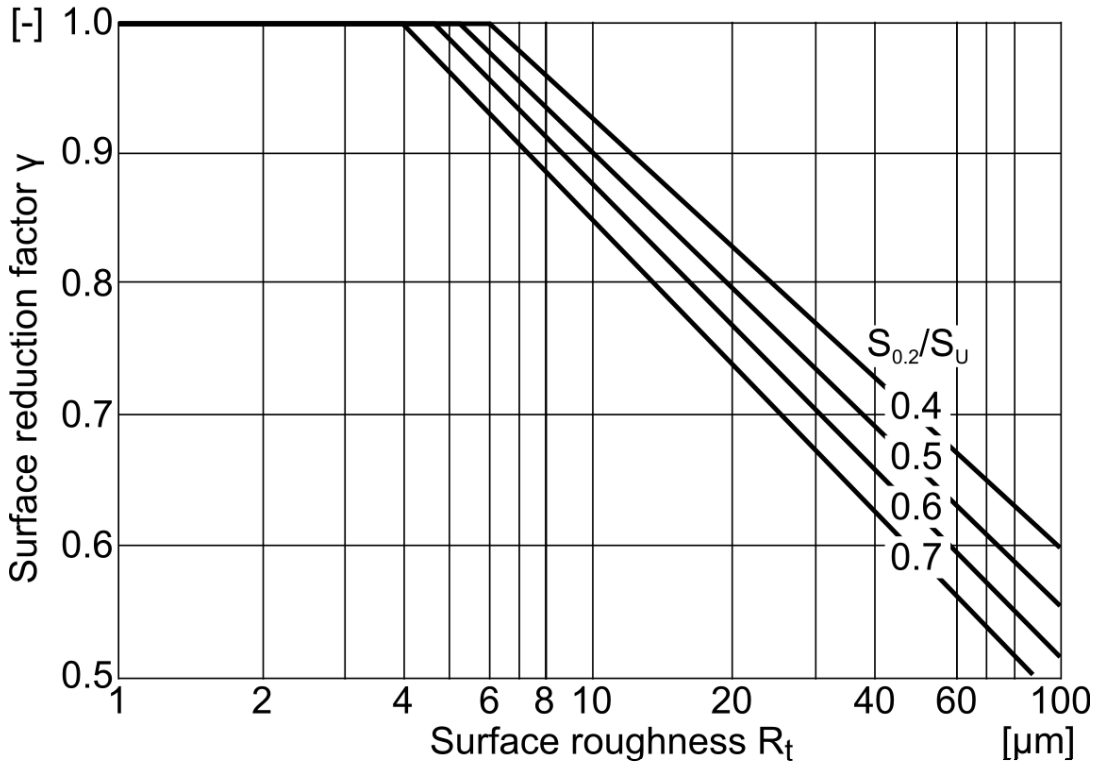

Figure 4.7: Surface roughness reduction factor γ for aluminum wrought alloys adopted and modified from [226] based on VDI guideline 2226 [234]

as illustrated in Fig. 4.8(b) where the ordinate and abscissa are further scaled by γ.

On the one hand, the geometry of FH can be designed for $N = 10^8$ life cycles using Eq. (4.47), where usually the material data and surface finish are known beforehand. On the other hand, the fatigue strength of an FH and a possible fatigue failure can be predicted. Basically, the occurring mean and amplitude stresses need to stay below the lowest graph in Fig. 4.8(b).

In Sect. 4.5.5, examples will illustrate the design process and the failure prediction process.

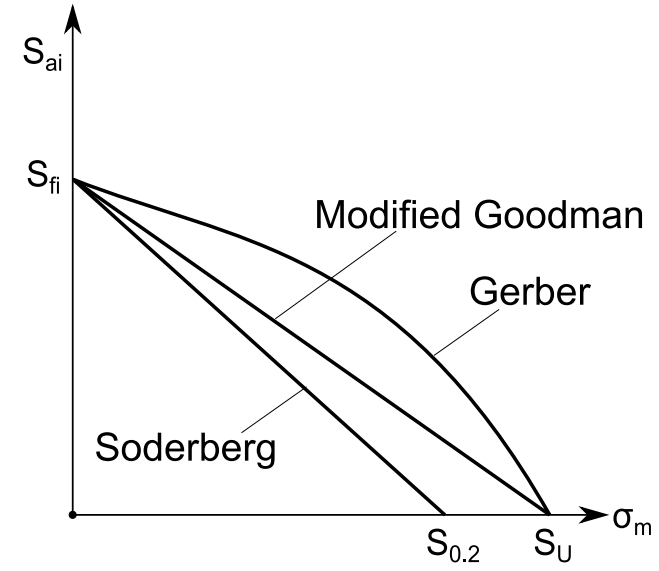

(a)

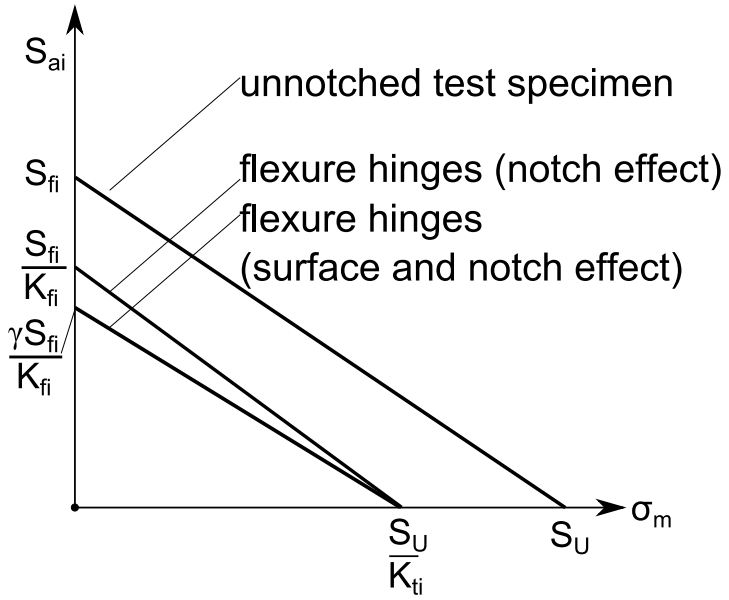

(b)

Figure 4.8: Fatigue diagrams: (a) three established relations, (b) reduced fatigue strength of flexural hinges using modified Goodman relation

4.4 Numerical simulation and experimental set-up

In order to validate the analytical calculations, the mechanical behavior of FH is examined by numerical simulations and experimental studies. First, the test specimens with incorporated FH of different geometries are described. Then, the numerical and experimental set-ups are explained.

Remark. The experimental studies were carried out and documented by several students under the author's supervision at the HSU [237–240].

4.4.1 Test specimens

All considered test specimens have a rectangular shape with the dimensions

$$L = 100\,\mathrm{mm}, \quad h_1 = 4\,\mathrm{mm}, \quad h_2 = 10\,\mathrm{mm}, \quad b = 10\,\mathrm{mm}, \qquad (4.48)$$

with incorporated FH at the center of each test specimen. Fig. 4.9(a) illustrates the test specimens with differently-shaped FH.

The relevant dimensions of all considered test specimens are listed in Table 4.2. The minimum thickness t_s varies from $0.2\,\mathrm{mm} \leq t_s \leq 2\,\mathrm{mm}$. All FH are symmetric but with different geometries, i.e. rectangular, circular or parabolic shape, as described in Eqs. (4.1) – (4.3) and shown in Fig. 4.9(b) – Fig. 4.9(e). Multiple sets of the described 21 different test specimens are investigated, to reduce the effect of manufacturing imperfections.

The test specimens are made of a high strength aluminum wrought alloy EN AW Al 2024 -T351 with approx. 4% copper, 1% magnesium and 0.5% manganese as the main alloying elements and less than a half percent of silicon, zinc, nickel, chromium, lead and bismuth. Its chemical notation is $AlCu_4Mg_1$. T351 is the temper of the material leading to its high strength mechanical properties. In applications of CM, these Al alloys are advantageous due to their high fatigue strength and their high elastic strain. The relevant material specifications are

$$E = 70\,\mathrm{GPa}, \quad \nu = 0.33, \quad \rho = 2790\,\mathrm{kg\,m^{-3}}.$$

(a) Test specimens with $h = 10\,\text{mm}$

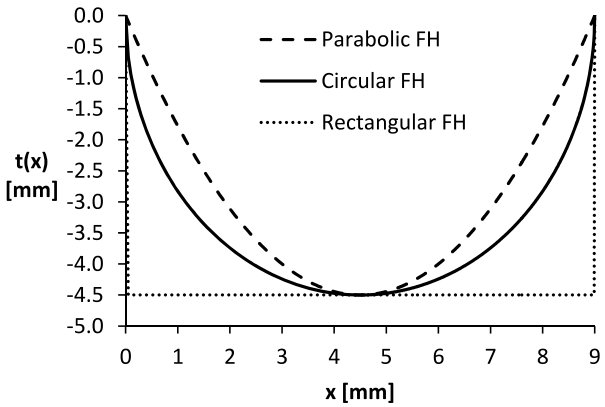

(b) Upper half of FH with $t_s = 1\,\text{mm}$

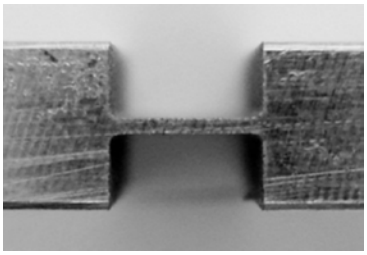

(c) Rectangular notch

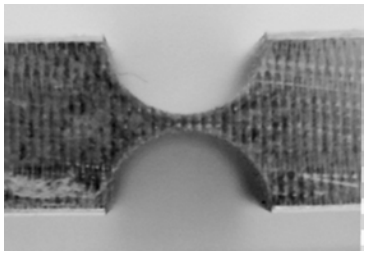

(d) Circular notch

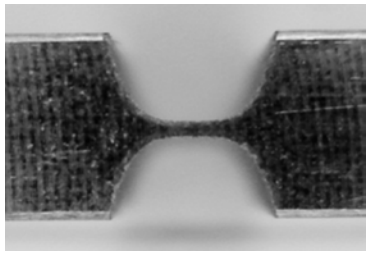

(e) Parabolic notch

Figure 4.9: Selected test specimens of differently shaped flexure hinges

A detailed description and a listing of in-depth material data of suitable aluminum alloys is given in [227].

4.4.2 Numerical simulation

The mechanical behavior of all test specimens with differently-shaped FH is simulated using the commercial software package Abaqus 6.8.1. Particularly, the occurring mechanical stresses, displacements, stiffness and bending stiffness and natural frequencies are simulated.

The test specimens are generated, modeled and meshed with a two-dimensional finite element (FE) model consisting of 8-node quadrilateral, plane stress elements (CPS8R) with quadratic shape functions. The numerical simulation is done considering the following aspects:

- The number of finite elements at the thinnest cross section is five

Table 4.2: Geometric data of 21 different test specimens with rectangular, circular and parabolic flexure hinges

shape [−]	L [mm]	b [mm]	h [mm]	FH's thickness t_s [mm]	FH's length l [mm]
			10	2	8
			10	1	9
			4	1	3
R	100	10	4	0.8	3.2
			4	0.6	3.4
			4	0.4	3.6
			4	0.2	3.8
			10	2	8
			10	1	9
			4	1	3
C	100	10	4	0.8	3.2
			4	0.6	3.4
			4	0.4	3.6
			4	0.2	3.8
			10	2	8
			10	1	9
			4	1	3
P	100	10	4	0.8	3.2
			4	0.6	3.4
			4	0.4	3.6
			4	0.2	3.8

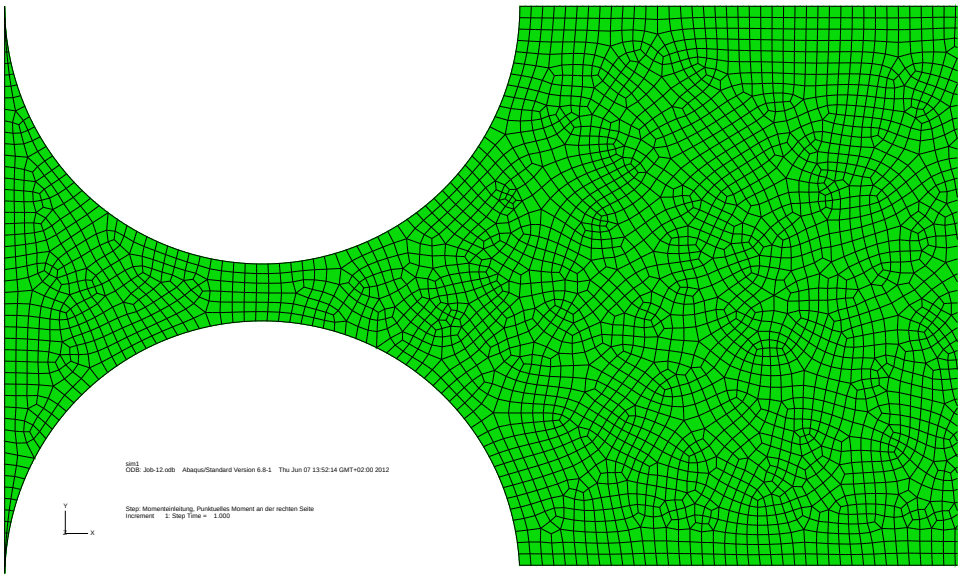

(a) Example mesh of flexure hinge

Figure 4.10: Numerical simulation of flexure hinges using Abaqus 6.8.1

or more.

- Distortion of finite elements is small.
- Areas without any noticeable displacements are not modeled, e.g. the clamped (left) side of the test specimens.

As an example, Fig. 4.10 shows a close-up of a meshed FE model of a circular FH before applying external loads. Later, Abaqus/Standard is used to compute the nodal displacements from the (quasi-static) equilibrium equations implicitly where a reduced 2×2 integration scheme is utilized for the geometric nonlinear analyses. The modal analysis is solved using the Lanczos solver. Further details are given in the Abaqus Documentation and in Lanczos' historical paper [241, 242].

Remark. An adaptive meshing would be more efficient than the uniform meshing applied here. However, the uniform meshing is chosen since the numerical computation is cheap and lasts only a couple of seconds due to the small number of degrees of freedom.

4.4.3 Experimental set-up

The mechanical behavior of all test specimens with differently-shaped FH is measured experimentally using the tensile testing machine TIRAtest 2810, the digital image correlation system Q400 and the scanning laser vibrometer PSV400. Particularly, the displacements due to a bending load are measured with the TIRAtest and Q400, and the stiffness, bending stiffness and precision are calculated afterwards. The natural frequencies are measured with the PSV400.

4.4.3.1 Tensile testing machine

The test specimens are clamped in a horizontal direction and loaded by a vertical force using the tensile testing machine TIRAtest 2810, as shown in Fig. 4.11. The applied load is controlled by a standard PC connected by an electronic drive control. The test specimen's deflection due to the applied load is measured immediately leading to stiffness k_z and bending stiffness c_ψ afterwards. In addition, the stepwise deflection is optically measured by the digital image correlation system Q400 at the same time.

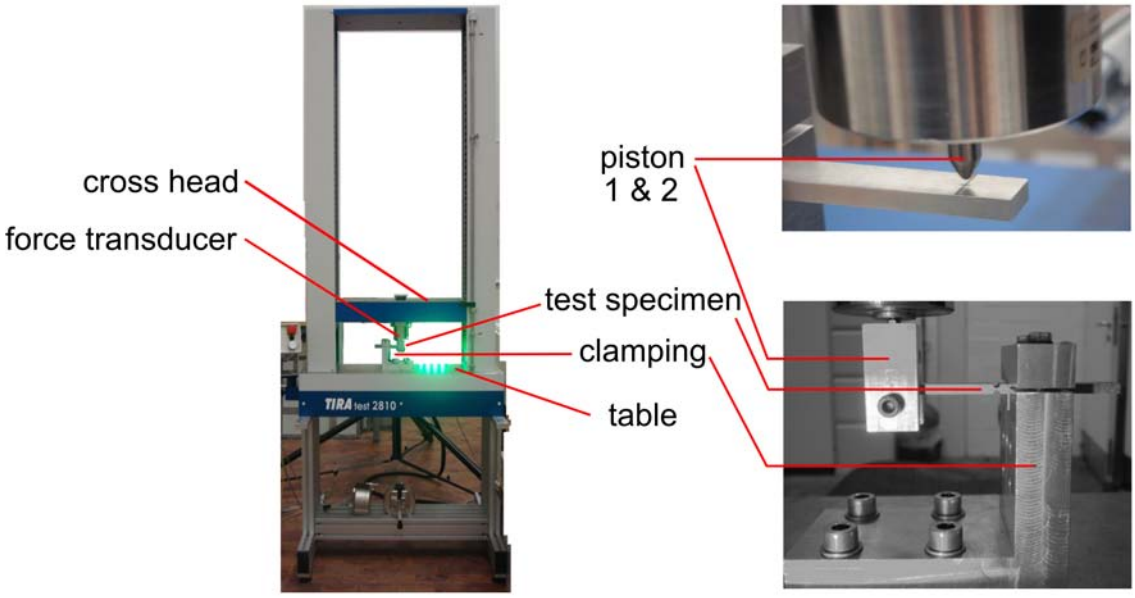

Figure 4.11: Tensile testing machine TIRAtest 2810 (left) and clamped test specimen (right).

4.4.3.2 Digital image correlation system

The deflection of each test specimen is measured optically in a stepwise manner by a Digital image correlation system Q400 from Dantec Dynamics. In order to enable the system to detect even the tiniest motions, fine, black and white varnishes were sprayed on the test specimens beforehand.

Based on the measured displacements $u(x, z)$ and $w(x, z)$ of each surface point of each test specimen, the deflection path and, thus, the center of rotation is determined afterwards.

Fig. 4.12(a) shows the main components of the Q400: a light source to illuminate the test specimen and a camera system with a (macro) objective aperture to record the displacements. Fig. 4.12(b) shows a close-up of the FH of a clamped test specimen that was sprayed beforehand.

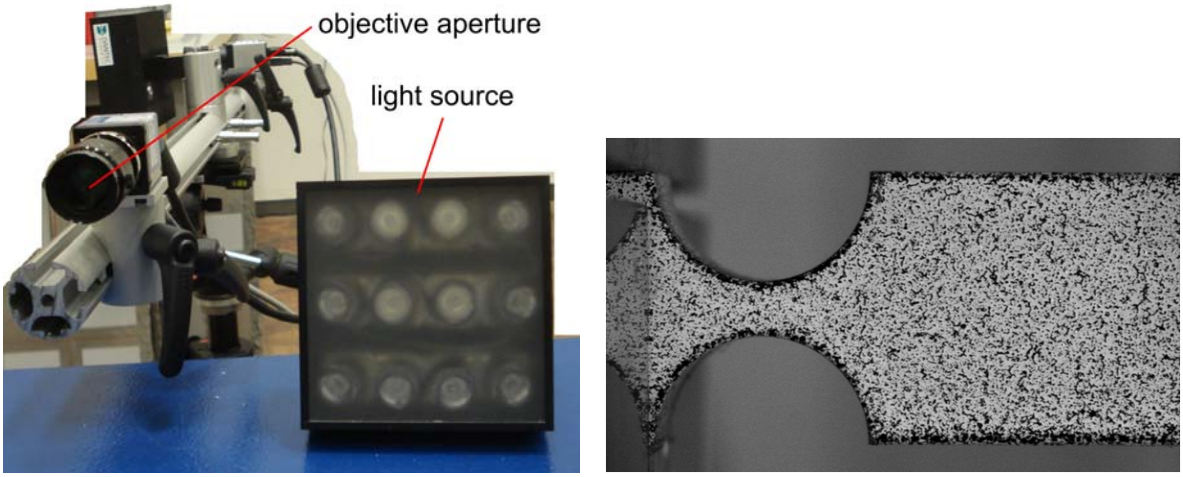

(a) Main components (b) Flexure hinge (optical)

Figure 4.12: Digital image correlation system Q400

4.4.3.3 Scanning laser vibrometer

The natural frequencies of each test specimen are measured optically using a scanning laser vibrometer PSV400 from Polytec. This system

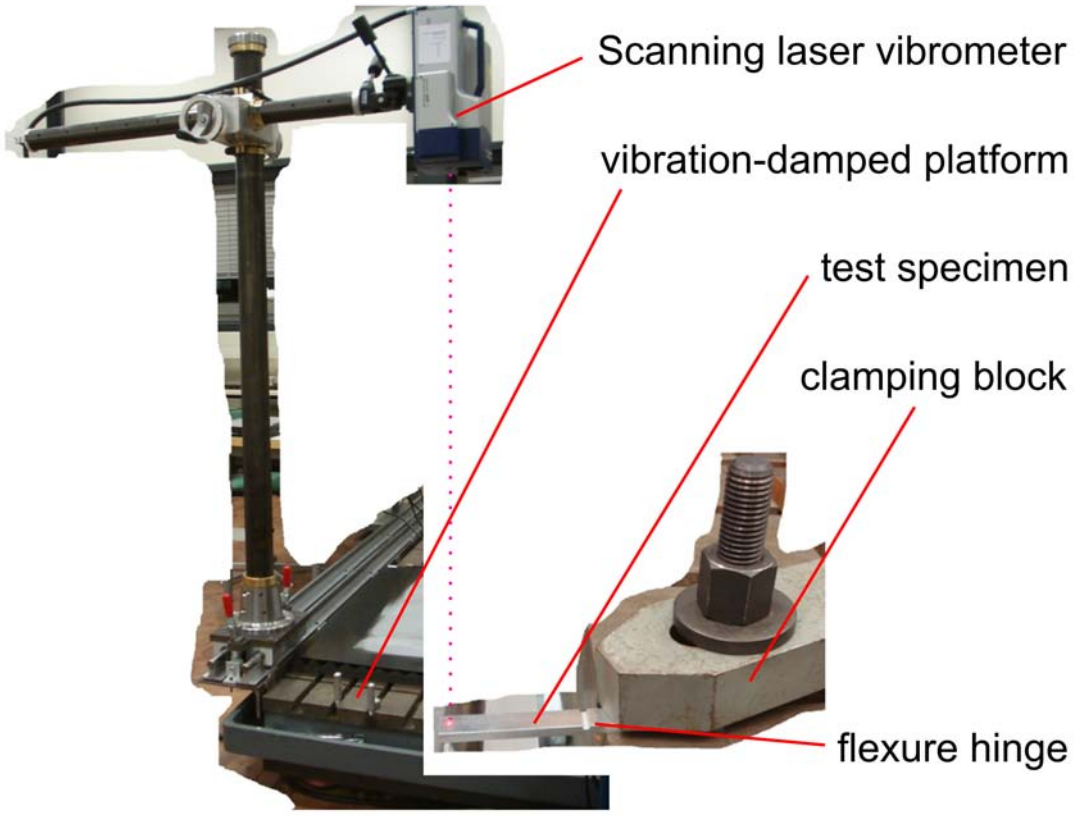

Figure 4.13: Scanning laser vibrometer PSV400

measures the surface velocity based on the principle of laser interferometry.

Each test specimen is clamped on one end on a vibration-damped platform and is pulse-excitated at the free end (with the FH). The oscillations are measured with a properly adjusted laser beam that is sent from the PSV400, reflected on the test specimen's (oscillating) surface and traced by the PSV400. Based on the recorded time signal of the (response) oscillation, the natural frequencies under the fixed-free boundary conditions can be determined after an automated Fourier transformation. The experimental set-up is illustrated in Fig. 4.13.

4.5 Results

The results of the analytical calculations on the mechanical behavior of differently-shaped FH, as described in Sect. 4.1 - 4.3, are shown and discussed in this section. Particularly, the maximum elastic deflection, the (bending) stiffness, the precision, the natural frequency and the prediction of fatigue strength and the optimal design of FH are addressed.

Additionally, the data of numerical simulations and experimental studies, as described in Sect. 4.4, are used to validate the analytical results.

4.5.1 Maximum elastic deflection

The maximum elastic deflection of FH is an important performance measure, in particular, in high stroke applications. As long as the occurring stresses do not exceed the (known) yield stress $S_{0.2}$, the deflection is considered to be elastic. The stresses in the FH are calculated analytically using Eq. (4.16), where the stress concentration factors $K_{tt} = K_{tt}\,(t(x))$ and $K_{tb} = K_{tb}\,(t(x))$ are calculated using Eq. (4.17) for all considered FH. The left end of the FH is clamped and the right end is free with a vertical Force F_z applied at $x = L$

In Table 4.3, the analytical results of the maximum elastic deflection w of differently sized parabolic and circular flexure hinges are listed for different lengths l and thinnest thicknesses t_s undergoing bending due to a pure shear force F_z. Some of the these results are presented in Fig. 4.14. The listed stress concentration factors result from the different hinge geometries $t^C(x)$ and $t^P(x)$. The maximum elastic deflection $w(l)$ and, more importantly, the corresponding maximum bending angle $\psi(l)$ at the end of the FH are shown.

Caused by the smaller radii of curvature of parabolic FH, the stress concentration is higher in parabolic FH than it is in circular FH, i.e. $K_{tt}^P > K_{tt}^C$ and $K_{tb}^P > K_{tb}^C$, respectively. This leads to smaller, applicable shear forces F_z and to smaller deflections $w(l)$ and slopes $\psi(l)$ at the end of parabolic FH. The stress concentration at all considered FH decreases for smaller and thinner FH, and is hardly noticeable for $t_s < 2\,\mathrm{mm}$.

Table 4.3: Maximum elastic deflection of circular (C) and parabolic (P) flexure hinges undergoing bending due to pure shear force F_z

	h [mm]	l [mm]	t_s [mm]	K_{tt} [−]	K_{tb} [−]	F_z [N]	$w(l)$ [µm]	$\psi(l)$ [°]
C	10	8	2	1.12	1.05	47.60	52.00	0.745
P	10	8	2	1.28	1.13	44.10	36.10	0.516
C	10	9	1	1.04	1.02	12.20	93.20	1.146
P	10	9	1	1.10	1.04	11.80	65.80	0.859
C	10	9.5	0.5	1.01	1.00	3.10	145.90	1.776
P	10	9.5	0.5	1.04	1.01	3.00	103.40	1.261
C	4	3.0	1.0	1.17	1.08	12.39	18.95	0.716
P	4	3.0	1.0	1.39	1.19	11.19	12.47	0.471
C	4	3.2	0.8	1.12	1.05	8.10	24.12	0.854
P	4	3.2	0.8	1.28	1.13	7.51	16.10	0.572
C	4	3.4	0.6	1.08	1.03	4.64	31.25	1.047
P	4	3.4	0.6	1.19	1.08	4.41	21.21	0.712
C	4	3.6	0.4	1.04	1.01	2.09	42.37	1.344
P	4	3.6	0.4	1.10	1.04	2.03	29.20	0.928
C	4	3.8	0.2	1.01	1.00	0.53	65.46	1.965
P	4	3.8	0.2	1.04	1.01	0.52	45.87	1.382
C	4	3.9	0.1	1.00	1.00	0.13	96.28	2.827
P	4	3.9	0.1	1.01	1.00	0.13	67.87	1.993
C	4	3.95	0.05	1.00	1.00	0.03	138.71	4.022
P	4	3.95	0.05	1.00	1.00	0.03	97.97	2.842

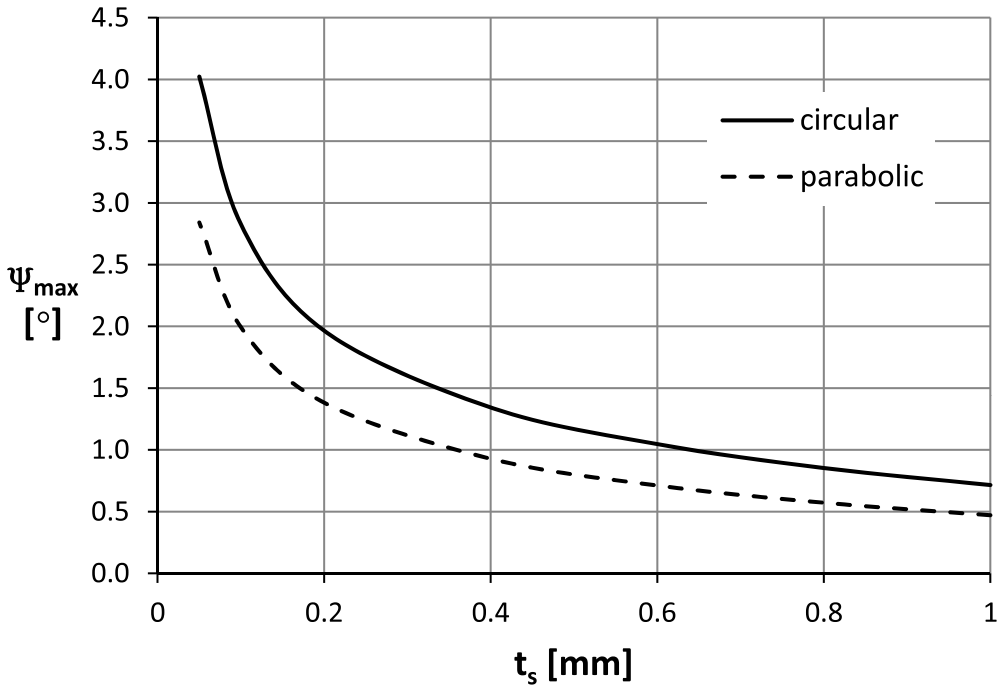

Figure 4.14: Maximum elastic deflection of differently sized circular and parabolic flexure hinges

In order not to exceed the yield stress, the maximum applicable loads become smaller for thinner FH by approximately $F_z \sim 1/t_s^2$. This results from the normal stress term in Eqs. (4.16) which becomes more dominant. However, the smaller loads yield higher deflections due to the term t_s^3 in the denominator in Eq. (4.12). Thus, the resulting maximum deflections and bending angles of thinner FH are significantly higher.

In Fig. 4.14, the maximum bending angle $\psi_{max} = \psi(l)$ is plotted over the thickness t_s for circular and parabolic FH. It can be noted, that circular FH provide a larger deflection range by approx. 35% than similarly sized, parabolic FH, i.e. if the same dimensions and the common points P_1, P_2 and P_3, as shown in Fig. 4.1, are kept.

Generally, the maximum elastic deflection are linked to the occurring stresses that depend directly on the radii of curvature, i.e. smaller radii of curvature result in higher stress concentration factors leading to higher stresses and a lower elastic deflection range. This is not a surprising result, however Eqs. (4.15) - (4.19) provide analytical expressions to

calculate the range of elastic deflection of common types of FH in CM prior to any modeling or manufacturing efforts.

Remark. Rectangular FH are **not examined** in terms of maximum elastic deflection due to an extreme deviation of the stress concentration caused by the uncertainness of the radii at the ends of the rectangular FH. Therefore, rectangular FH are not reliable, although they potentially provide very high deflections due to their long, thin cross section.

4.5.2 Stiffness and bending stiffness

The bending stiffness c_ψ of FH are crucial characteristics in the modeling and design process of CM. They are calculated analytically and measured experimentally based on the applied loads and the corresponding deflections, as described in Sect. 4.2.4 and Sect. 4.4.3, respectively.

In Table 4.4, the bending stiffness c_ψ of differently sized, rectangular, circular and parabolic FH are listed for different lengths l and thicknesses t_s. Analytical results $c_{\psi,ana}$, experimentally gathered data $c_{\psi,exp}$ and the relative error e are shown, for experimentally measured hinge dimensions. In addition, the analytical results $c^*_{\psi,ana}$ on the exact hinge dimensions l^* and t^* are listed. In Fig. 4.15, the analytical and experimental results on the bending stiffness of differently shaped FH is illustrated.

It can be noted for all hinge dimensions, that the analytical results match the experimental approximately and the error is reasonably small. In particular, for FH of small thicknesses $t_s < 0.6\,\text{mm}$ that are frequently used in CM, the analytical calculation yield accurate results.

In all considered FH, the rectangular FH yield the smallest bending stiffnesses caused by the high deflection due to its long, thin cross section. The circular and the parabolic FH yield considerably higher bending stiffnesses, where the parabolic FH possess the highest stiffnesses due to the short length of the thinnest cross section where $t(x) \approx t_s$.

Comparing the analytical results with the exact hinge dimensions, reveals that parabolic FH are stiffer by approximately 40% compared to circular FH.

Table 4.4: Bending stiffness c_ψ for rectangular (R), circular (C) and parabolic (P) flexure hinges: analytical calculations and experimental results

	h [mm]	l [mm]	t_s [mm]	$c_{\psi,ana}$ [N m rad^{-1}]	$c_{\psi,exp}$ [N m rad^{-1}]	l^* [mm]	t_s^* [mm]	$c^*_{\psi,ana}$ [N m rad^{-1}]
R	10	8.42	2.28	82.11	61.18	8	2	58.33
C	10	8.08	2.00	142.96	133.71	8	2	143.64
P	10	8.03	2.13	230.86	180.06	8	2	199.37
R	10	9.47	1.18	10.12	8.86	9	1	6.48
C	10	9.09	0.99	22.76	27.98	9	1	23.46
P	10	9.09	1.07	38.61	37.70	9	1	33.05
R	4	3.08	0.94	16.15	14.20	3	1	19.44
C	4	3.07	0.94	35.96	28.47	3	1	42.15
P	4	3.03	0.96	52.52	33.75	3	1	57.85
R	4	3.26	0.76	8.00	6.92	3.2	0.8	9.33
C	4	3.22	0.76	20.17	16.63	3.2	0.8	22.98
P	4	3.25	0.76	28.21	21.13	3.2	0.8	31.90
R	4	3.47	0.54	2.70	2.69	3.4	0.6	3.71
C	4	3.47	0.54	8.22	7.58	3.4	0.6	10.73
P	4	3.37	0.59	14.42	10.13	3.4	0.6	15.02
R	4	3.64	0.35	0.70	0.63	3.6	0.4	1.04
C	4	3.61	0.41	3.99	2.55	3.6	0.4	3.75
P	4	3.53	0.40	5.29	3.40	3.6	0.4	5.29
R	4	3.80	0.20	0.12	-	3.8	0.2	0.12
C	4	3.84	0.16	0.37	0.25	3.8	0.2	0.64
P	4	3.81	0.15	0.45	0.38	3.8	0.2	0.91

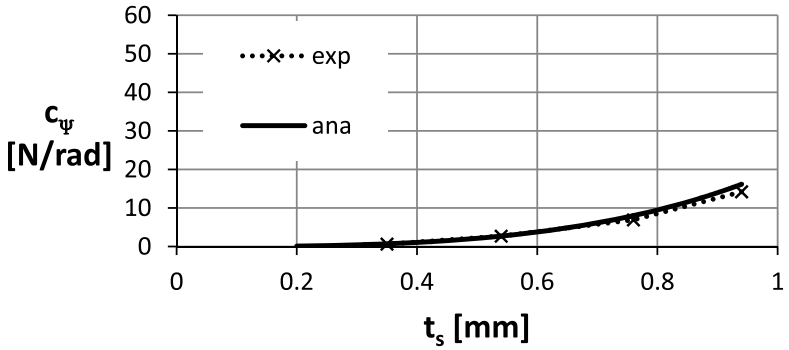

(a) Rectangular FH

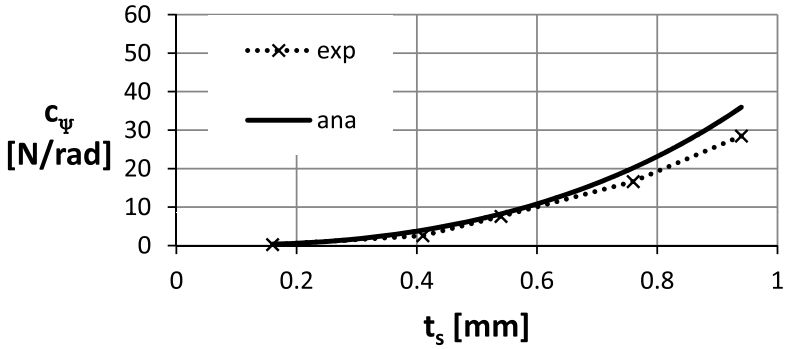

(b) Circular FH

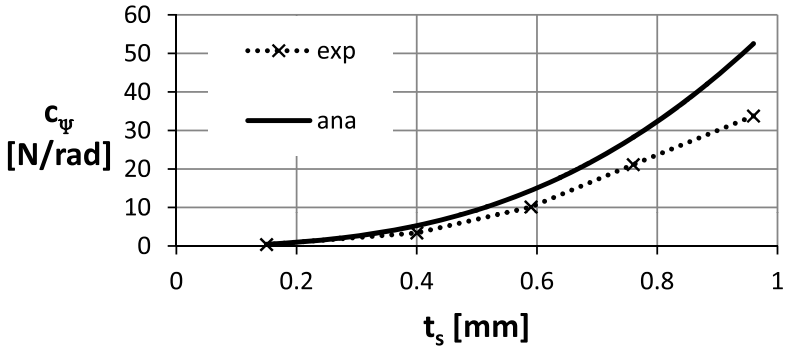

(c) Parabolic FH

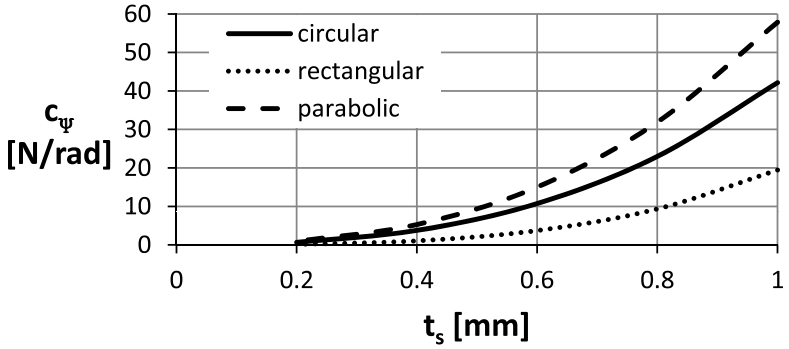

(d) Analytical results

Figure 4.15: Bending stiffness of differently shaped flexure hinges: (a)-(c) comparison of analytical and experimental results, and (d) comparison of different hinge geometries

4.5.3 Precision, i.e. center of rotation

The precision, i.e. the change of the position of the center of rotation of FH is a significant performance measure since CM with incorporated FH are primarily designed for high precision applications. The effective center of rotation P_{eff}^{01} of circular and parabolic FH is calculated analytically for different heights h, lengths l and thicknesses t_s, as described in Sect. 4.2.6. Two different bending cases are considered: First, a superposed bending due to a shear force F_z and a bending moment M_y. Second, a bending due to a pure bending moment M_y without any shear forces F_z. The same loads, i.e. F_z and/or $M_y = F_z L$, as applied to cause the maximum elastic deflection, as shown in Sect. 4.5.1 and listed in Table 4.3, are applied.

In Table 4.5, the Δx- and Δz-coordinates of the effective centers of rotation, $P_{eff,\Delta x}^{01}$ and $P_{eff,\Delta z}^{01}$ are listed. These coordinates refer to the geometric center of each FH where the different superscripts of P_{eff}^{01,F_z,M_y} and P_{eff}^{01,M_y} refer to the superposed bending and pure bending, respectively. In Fig. 4.16, the effective centers of rotation of rectangular, parabolic and circular FH are illustrated for both load cases.

It can be noted that for all considered FH, the effective center of rotation does not remain in the geometric center of the FH. For almost all parabolic and circular FH, it is shifted in the positive z-direction, i.e. in the bending direction and in the positive x-direction, i.e. where the load is applied. For rectangular FH, it is shifted in positive z-direction, and, in positive or negative x-direction depending on the load case: for pure bending moment it is shifted in positive x-direction whereas it is shifted in negative x-direction for superposed shear force and bending moment. For intermediate loading conditions (not shown), i.e. $0 < M_Y/(F_Z L) < 1$, the positions of the centers of rotation lie between the illustrated cases.

The shift in both directions decreases for lower loads and increases for smaller thicknesses, where the shift of parabolic FH is smaller than it is for circular or rectangular FH, i.e. parabolic hinges rotate closer around its geometric center than circular or rectangular FH. This means, that parabolic FH are more precise and, thus, better suited for in high-

Table 4.5: Precision, i.e. the coordinates of the overall center of rotation P_{eff}^{01} for rectangular (R), circular (C) and parabolic (P) flexure hinges

	h	l	t_s	$P_{eff,\Delta x}^{01,F_z,M_y}$	$P_{eff,\Delta z}^{01,F_z,M_y}$	$P_{eff,\Delta x}^{01,M_y}$	$P_{eff,\Delta z}^{01,M_y}$
	[mm]	[mm]	[mm]	[mm]	[mm]	[mm]	[mm]
R	10	8	2	-0.1547	0.0226	0.0049	0.0196
C	10	8	2	-0.0544	0.0260	0.0286	0.0229
P	10	8	2	-0.0574	0.0181	0.0199	0.0159
R	10	9	1	-0.1715	0.0580	0.0055	0.0493
C	10	9	1	0.0077	0.0456	0.0444	0.0400
P	10	9	1	0.0028	0.0320	0.0312	0.0281
R	10	9.5	0.5	-0.1867	0.1306	0.0059	0.1114
C	10	9.5	0.5	0.0535	0.0713	0.0657	0.0624
P	10	9.5	0.5	0.0380	0.0494	0.0455	0.0433
R	4	3	1	-0.0217	0.0069	0.0022	0.0065
C	4	3	1	-0.0046	0.0090	0.0115	0.0086
P	4	3	1	-0.0079	0.0062	0.0079	0.0059
R	4	3.2	0.8	-0.0217	0.0100	0.0024	0.0094
C	4	3.2	0.8	0.0013	0.0116	0.0138	0.0110
P	4	3.2	0.8	-0.0020	0.0081	0.0096	0.0077
R	4	3.4	0.6	-0.0224	0.0152	0.0026	0.0145
C	4	3.4	0.6	0.0081	0.0151	0.0170	0.0144
P	4	3.4	0.6	0.0042	0.0106	0.0119	0.0101
R	4	3.6	0.4	-0.0238	0.0258	0.0027	0.0243
C	4	3.6	0.4	0.0165	0.0207	0.0219	0.0197
P	4	3.60	0.40	0.0113	0.0146	0.0155	0.0140
R	4	3.80	0.20	-0.0258	0.0579	0.0029	0.0542
C	4	3.80	0.20	0.0308	0.0323	0.0324	0.0308
P	4	3.80	0.20	0.0221	0.0229	0.0230	0.0219
R	4	3.90	0.10	-0.0271	0.1225	0.0033	0.1304
C	4	3.90	0.10	0.0474	0.0478	0.0467	0.0456
P	4	3.90	0.10	0.0339	0.0339	0.0332	0.0323
R	4	3.95	0.05	-0.0278	0.2512	0.0030	0.2350
C	4	3.95	0.05	0.0692	0.0691	0.0667	0.0659
P	4	3.95	0.05	0.0492	0.0490	0.0473	0.0467

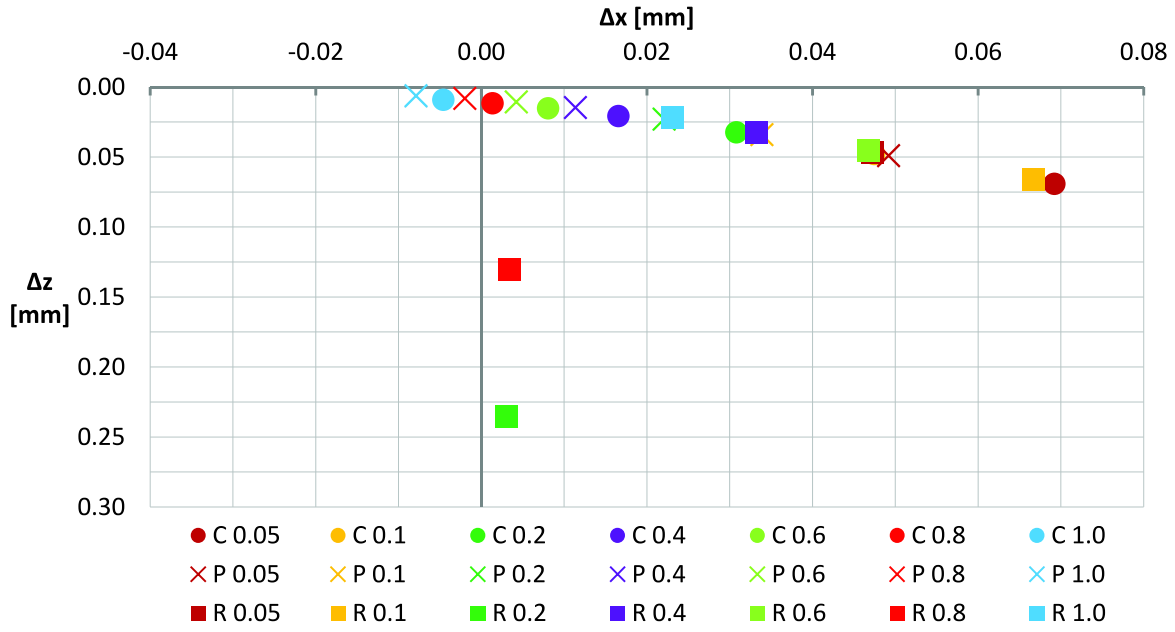

(a) Pure bending moment

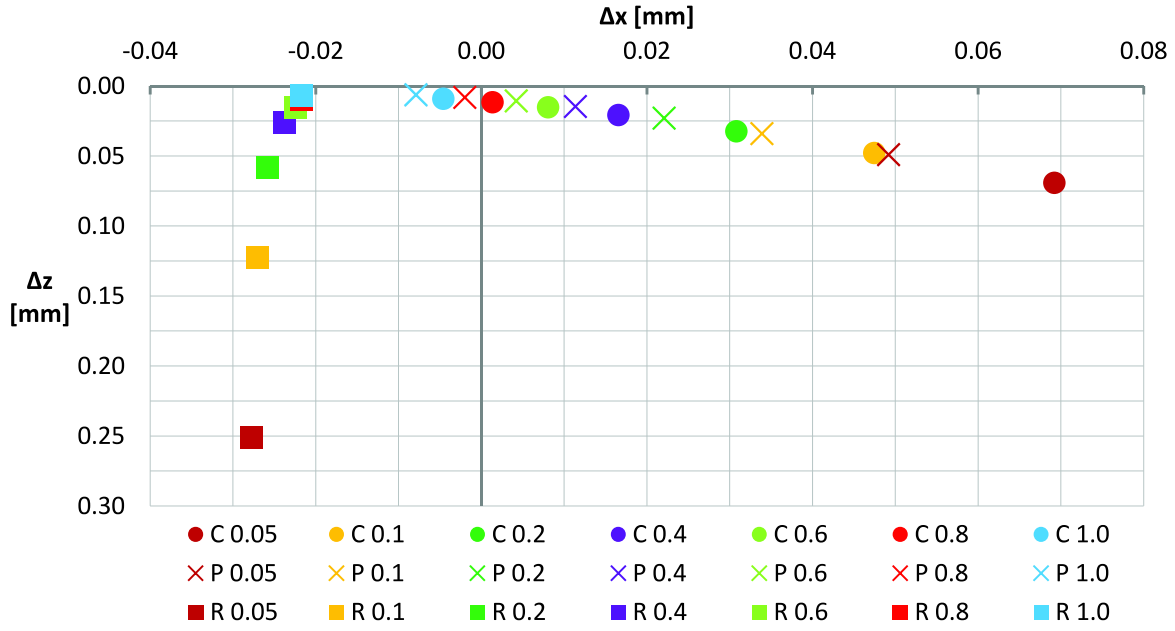

(b) Superposed shear force and bending moment

Figure 4.16: Precision, i.e. center of rotation of differently sized, circular and parabolic flexure hinges under different loading conditions: (a) pure bending moment, (b) superposed shear force and bending moment

precision applications.

Remark. The effective center of rotation of rectangular, leaf type FH can vary enormously from $x \approx l/3$ to $x \approx l/2$ depending on the shear force F_z and in z-direction depending on the bending moment M_y. Therefore, rectangular FH are usually not suitable for high precision applications.

4.5.4 Natural frequency

The natural frequencies of CM with incorporated, differently shaped FH is highly relevant for dynamic high precision applications, where unwanted vibrations should be avoided as early as possible in the design process. In addition, it is a valuable quality measure of the analytical and numerical model.

In Table 4.6, the first natural frequencies of fixed-free test specimens shown in Sect. 4.4.3 with incorporated differently shaped FH are listed for different lengths l and thicknesses t_s. Analytical, numerical and experimental results f_{ana}, f_{num}, f_{exp}, f_{exp}^{dm} are shown. The analytical calculations f_{ana} are based on Eq. (4.29) using Timoshenko's beam theory. The numerical results f_{num} are calculated by a modal analysis using the commercial software ABAQUS as described in Sect. 4.4.2. The experimental data f_{exp} is gathered using the scanning laser vibrometer, as described in Sect. 4.4.3.3. Independent from those results, the experimental data f_{exp}^{dm} is determined based on Eq. (4.31) for a discrete torsional spring, as illustrated earlier in Fig. 4.4, and the determined stiffness c_{exp} experimentally measured with the tensile testing machine, as described in Sect. 4.4.3.1. The results are shown in Fig. 4.17, too.

It can be noted, that the analytical calculations agree well with the numerical and experimental results for all considered types and dimensions of FH. The rectangular FH yield significantly lower natural frequencies than circular and parabolic FH $f^R < f^C < f^P$, which agrees well with the results on the bending stiffness recalling the proportionality $c \sim f^2$ given in Eq. (4.31).

Comparing the independently measured, experimental data f_{exp} and f_{exp}^{dm} with each other, a very small relative error e_{exp} of less than 4% can be

noted. This implies, that FH can be modeled appropriately by discrete torsional springs using the bending stiffness c_ψ shown in Sect. 4.5.2.

Table 4.6: First natural frequencies f of test specimens with incorporated rectangular (R), circular (C) and parabolic (P) flexure hinges: comparison of analytical, numerical and experimental results

	l [mm]	t_s [mm]	f_{ana} [Hz]	f_{num} [Hz]	f_{exp} [Hz]	f_{exp}^{dm} [Hz]	e_{exp} [-]
R	9.47	1.18	148.50	149.99	136.20	141.00	3.5%
C	9.09	0.99	224.14	216.71	238.40	242.50	1.7%
P	9.09	1.07	288.22	272.16	285.30	288.50	1.1%
R	8.42	2.28	420.66	418.14	368.10	370.00	0.5%
C	8.08	2.00	562.42	524.40	550.90	541.60	-1.7%
P	8.03	2.13	642.32	628.65	638.40	636.40	-0.3%
R	3.08	0.94	286.48	275.00	277.50	278.11	0.2%
C	3.07	0.94	428.66	398.40	404.40	393.80	-2.6%
P	3.03	0.96	497.73	445.54	439.40	428.79	-2.4%
R	3.26	0.76	204.54	198.42	193.80	194.08	0.1%
C	3.22	0.76	328.20	307.89	306.30	300.95	-1.7%
P	3.25	0.76	375.22	340.58	339.40	339.26	0.0%
R	3.47	0.54	119.61	116.93	118.80	121.01	1.9%
C	3.47	0.54	211.47	201.75	209.40	203.26	-2.9%
P	3.37	0.59	275.86	252.69	235.60	234.91	-0.3%
R	3.64	0.35	61.08	60.13	58.10	58.64	0.9%
C	3.61	0.41	148.29	143.23	116.90	117.88	0.8%
P	3.53	0.40	169.85	158.49	135.00	136.12	0.8%
R	3.80	0.20	26.28	25.68	13.80	-	-
C	3.84	0.16	44.85	44.27	36.90	36.98	0.2%
P	3.81	0.15	49.15	47.74	44.40	45.60	2.7%

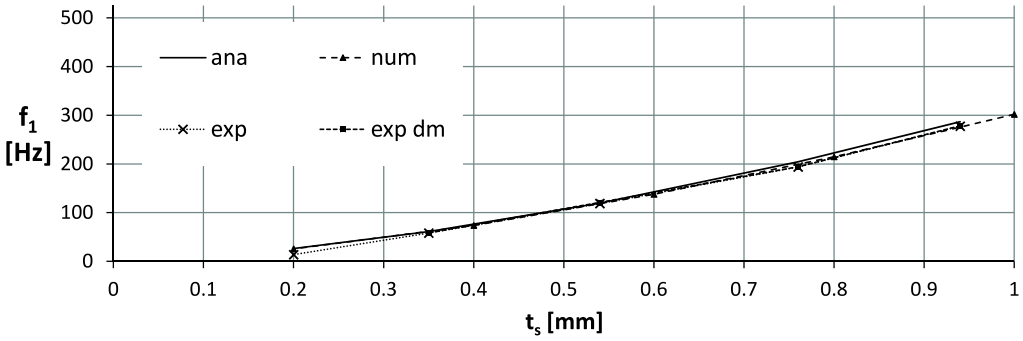

(a) Rectangular FH

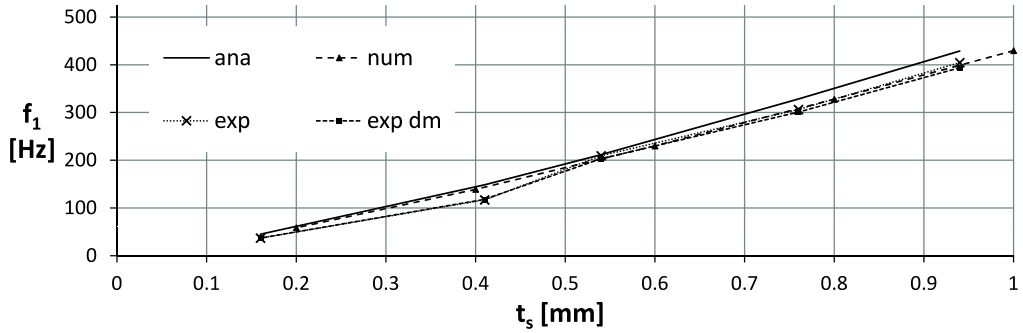

(b) Circular FH

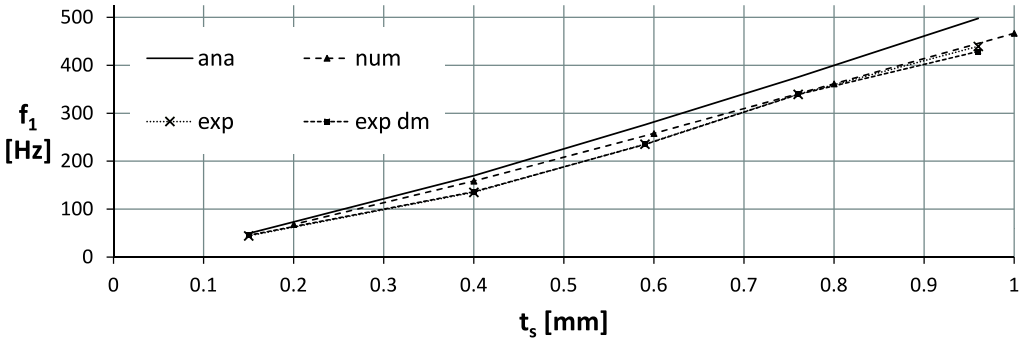

(c) Parabolic FH

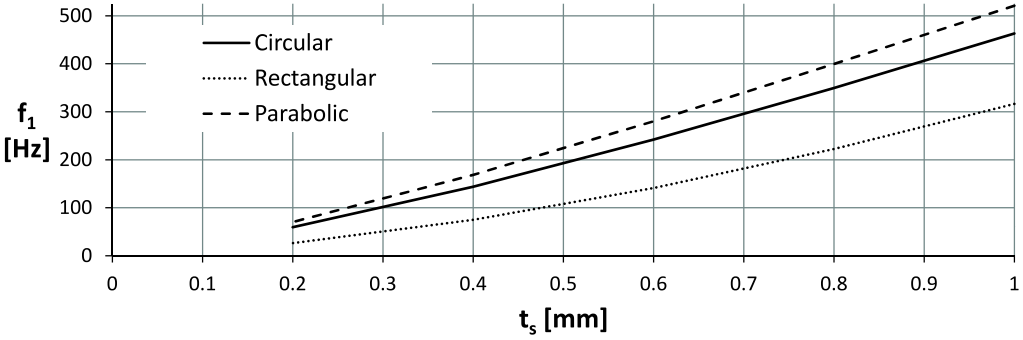

(d) Analytical results

Figure 4.17: First natural frequencies of test specimens with differently shaped flexure hinges: (a)-(c) comparison of analytical, numerical and experimental results, and (d) comparison of different hinge geometries.

4.5.5 Fatigue strength and optimal design

Flexure hinges are the weak spots of CM due to their frequent elastic deflection. In particular, fatigue failure of FH is a serious issue which is addressed in the following. In a first step, explicit, analytical expressions will be derived based on the equations already given in Sect. 4.3.2. In a second step, these equations will be applied to two example cases illustrating the analysis and design process.

4.5.5.1 Deriving explicit, analytical expressions

The resulting mean and amplitude stresses σ_m, σ_a that occur in FH can be calculated by Eq. (4.33) based on given loads, for example, from the topological synthesis. The highest capable stress amplitude for a given mean stress $S_{ai}(\sigma_m)$ is linked to the flexural hinges geometric and material properties by Eq. (4.47). The ratio of these values is typically referred as the safety factor S_D as

$$S_D = \frac{S_{at}(\sigma_m)}{\sigma_{a,e}}, \tag{4.49}$$

with $\sigma_{a,e}$ as defined in Eq. (4.45).

The optimal shape of circular and parabolic flexural hinges are calculated inversely based on the explicit expressions derived in the previous section and linked to the safety factor S_D. In any case, the maximum mean and amplitude stresses depend on the given loads as written in Eq. (4.33) and occur at $x = \frac{l}{2}$ and $z = \pm\frac{t_s}{2}$:

$$\begin{aligned} \sigma_{mb} &= \frac{6}{bt_s^2}M_{my} - \frac{3l}{bt_s^3}F_{mz}, & \sigma_{ab} &= \frac{6}{bt_s^2}M_{ay} - \frac{3l}{bt_s^3}F_{az}, \\ \sigma_{mt} &= \frac{1}{bt_s}F_{mx}, & \sigma_{at} &= \frac{1}{bt_s}F_{ax}. \end{aligned} \tag{4.50}$$

Remark. The hinge height h is substituted by the relation $h = 2t^* + t_s$. as illustrated in Fig. 4.5.

Circular flexural hinges

In order to connect the geometric properties of circular flexural hinges to the safety factor, the stress concentration factors are obtained by Eqs. (4.17) and (4.18):

$$K_{tb}^{C} = 1 + \left(\frac{0.32}{\left(4 + \frac{l^2}{t^{*2}}\right)^{0.66}} + \frac{0.01\left(l^2 + 4t^{*2}\right)^{1.33} t_s}{t^{2.66}(2t^* + t_s)} + \frac{0.02\left(l^2 + 4t^{*2}\right)^{1.13}\left(l^2 + 4t^*(t^* + t_s)\right)^{2.25}}{(t^* t_s)^{3.375}} \right)^{-0.5} \tag{4.51}$$

$$K_{tt}^{C} = 1 + \left(0.01 + \frac{0.013 l^2}{t^2} + \frac{0.01\left(l^2 + 4t^{*2}\right)^{1.25} t_s}{t^{2.5}(2t^* + t_s)} + \frac{0.01\left(l^2 + 4t^{*2}\right)\left(l^2 + t^*(4t^* + 4t_s)\right)^2}{t^{*3} t_s^3} \right)^{-0.5}. \tag{4.52}$$

The fatigue strengths become with Eqs. (4.42), (4.47) and (4.50)

$$\begin{aligned} S_{ab} &= \frac{S_{fb}\left(l^2 + 4t^*(2A_P + t^*)\right)\left(3F_{mz}K_{tb}^{C} l - 6K_{tb}^{C} M_{my} + bS_U t_s^2\right)\gamma}{bS_U\left(8A_P t + K_{tb}^{C}\left(l^2 + 4t^{*2}\right)\right) t_s^2}, \\ S_{at} &= \frac{S_{ft}\left(l^2 + 4t^*(2A_P + t^*)\right)\left(-F_{mx}K_{tt}^{C} + bS_U t_s\right)\gamma}{bS_U\left(8A_P t^* + K_{tt}^{C}\left(l^2 + 4t^2\right)\right) t_s}. \end{aligned} \tag{4.53}$$

Substituting Eq. (4.53) into Eq. (4.45) yield the equivalent stress

$$\sigma_{a,e} = \frac{1}{bt_s} F_{ax} + \kappa\left(\frac{6}{bt_s^2} M_{ay} - \frac{3l}{bt_s^3} F_{az}\right), \tag{4.54}$$

with

$$\kappa = \frac{S_{ft}\left(8A_P t^* + K_{tb}^{C}\left(l^2 + 4t^{*2}\right)\right) t_s\left(-F_{mx}K_{tt}^{C} + bS_U t_s\right)}{S_{fb}\left(8A_P t^* + K_{tt}^{C}\left(l^2 + 4t^{*2}\right)\right)\left(3F_{mz}K_{tb}^{C} l - 6K_{tb}^{C} M_{my} + bS_U t_s^2\right)}. \tag{4.55}$$

The safety factor becomes after substituting Eqs. (4.51) - (4.55) into Eq. (4.49):

$$\begin{aligned}\boldsymbol{S_D} = \\ \big[\gamma S_{fb} S_{ft} \left(\boldsymbol{l}^2 + 4\boldsymbol{t^*}(2A_p + \boldsymbol{t^*})(-F_{mx}K_{tt}^C + bS_U\boldsymbol{t_s}\right)\left(3F_{mz}K_{tb}^C\boldsymbol{l} - 6K_{tb}^C M_{my} + bS_U\boldsymbol{t_s^2}\right)\big]/ \\ \big[\left(3S_U S_{ft}(F_{az}\boldsymbol{l} - 2M_{ay}\right)\left(8A_P\boldsymbol{t^*} + K_{tb}^C(\boldsymbol{l}^2 + 4\boldsymbol{t^{*2}})\right)\left(F_{mx}K_{tt}^C - bS_U\boldsymbol{t_s}\right) \\ + F_{ax}S_{fb}\left(8A_P\boldsymbol{t^*} + K_{tt}^C(\boldsymbol{l}^2 + 4\boldsymbol{t^{*2}})\right)\left(3F_{mz}K_{tb}^C\boldsymbol{l} - 6K_{tb}^C M_{my} + bS_U\boldsymbol{t_s^2}\right)\big)\big] \quad (4.56)\end{aligned}$$

This expression explicitly links the safety factor S_D with the design variables of any circular FH, i.e. the thicknesses t_S, the root height t^* and the length l.

Remark. The relevant (scalar) variables are printed in bold and the dependencies, e.g. $K_{tt} = K_{tt}(t_s, t^*)$, are omitted for simplicity.

Parabolic flexural hinges

In order to connect the geometric properties of parabolic FH to the safety factor, the stress concentration factors are obtained by Eqs. (4.17) and (4.19)

$$K_{tb}^P = 1 + \left(\frac{0.32t^{*1.33}}{l^{1.33}} + \frac{0.01t_s l^{2.66}}{t^{*2.66}(2t^* + t_s)} + \frac{0.02\left(l^3 + 4lt^*t_s\right)^{2.25}}{(t^*t_s)^{3.375}}\right)^{-0.5} \quad (4.57)$$

and

$$\begin{aligned}K_{tt}^P = 1 + 3.67\Bigg(&\frac{1}{t^{*5.5}t_s^3(2.t^* + t_s)} l^{2.5}\left(0.29(lt^*)^{3.5}\right. \\ &+ \frac{t_s^2\left(4.71t^{5.5} + 2.69t^{4.5}t_s + 0.17t^{3.5}t_s^2\right)}{l^{0.5}} + 0.15l^{3.5}t^{*2.5}t_s + 0.13t^{*3}t_s^4 \\ &\left.+ l^{1.5}t_s\left(2.35t^{*4.5} + 1.18t^{*3.5}t_s\right) + \frac{t_s^2\left(4.71t^{*5.5} + 2.69t^{*4.5}t_s + 0.17t^{*3.5}t_s^2\right)}{l^{0.5}}\right)\Bigg)^{-0.5}.\end{aligned} \quad (4.58)$$

The fatigue strengths are calculated with Eqs. (4.42), (4.47) and (4.50)

$$\begin{aligned} S_{ab} &= \frac{\gamma\left(l^2+8t^*A_P\right)S_{fb}\left(3lF_{mz}K_{tb}^P-6K_{tb}^PM_{my}+bS_Ut_s^2\right)}{b\left(8t^*A_P+l^2K_{tb}^P\right)S_Ut_s^2}, \\ S_{at} &= \frac{\gamma\left(l^2+8t^*A_P\right)S_{ft}\left(-F_{mx}K_{tt}^P+bS_Ut_s\right)}{b\left(8t^*A_P+l^2K_{tt}^P\right)S_Ut_s}. \end{aligned} \tag{4.59}$$

The equivalent stress $\sigma_{a,e}$ becomes with Eq. (4.45):

$$\begin{aligned} \kappa &= \frac{\left(8t^*A_P+l^2K_{tb}^P\right)S_{ft}t_s\left(-F_{mx}K_{tt}^P+bS_Ut_s\right)}{\left(8t^*A_P+l^2K_{tt}^P\right)S_{fb}\left(3K_{tb}^P\left(lF_{mz}-2M_{my}\right)+bS_Ut_s^2\right)}, \\ \sigma_{a,e} &= \frac{1}{bt_s}F_{ax}+\kappa\left(\frac{6}{bt_s^2}M_{ay}-\frac{3l}{bt_s^3}F_{az}\right). \end{aligned} \tag{4.60}$$

The safety factor S_D is formulated after substituting Eqs. (4.57 - 4.60) into Eq. (4.49) as:

$$\begin{aligned} \boldsymbol{S_D} = \\ &\left[\gamma S_{fb}S_{ft}\boldsymbol{t_s^2}(\boldsymbol{l}^2+8t^*A_P)(-F_{mx}K_{tt}^P+bS_U\boldsymbol{t_s})\left(3K_{tb}^P(\boldsymbol{l}F_{mz}-2M_{my})+bS_U\boldsymbol{t_s^2}\right)\right]/ \\ &\left[S_U\boldsymbol{t_s}\left(3F_{x,a}\boldsymbol{t_s}K_{t_b}^P(8\boldsymbol{t^*}A_P+\boldsymbol{l}^2K_{tt}^P\right)(\boldsymbol{l}F_{mz}-2M_{my})S_{fb}+3(F_{az}\boldsymbol{l}- \right. \\ &2M_{ay})F_{mx}(8\boldsymbol{t^*}A_P+\boldsymbol{l}^2K_{tb}^P)K_{tt}^PS_{ft}\boldsymbol{t_s}+bS_U\boldsymbol{t_s^2}\left(F_{ax}t_s(8\boldsymbol{t^*}A_P+\boldsymbol{l}^2K_{tt}^P)\right. \\ &\left.\left.S_{fb}-3S_{ft}(F_{az}\boldsymbol{l}-2M_{ay})(8\boldsymbol{t^*}A_P+\boldsymbol{l}^2K_{tb}^P)\right)\right]. \end{aligned} \tag{4.61}$$

This expression links explicitly the safety factor S_D with the design variables of the parabolic flexural hinge, i.e. the thicknesses t_S, t^* and the length l.

Remark. Again, the relevant (scalar) variables are printed in bold and the dependencies, e.g. $K_{tt} = K_{tt}(t_s, t^*)$, are omitted for simplicity.

The Eqs. (4.56) and (4.61) are nonlinear functions, where t^*, t_s and l must meet given geometric specifications. Maximizing $S_D(t^*, t_s, l)$ results in FH with optimal geometric properties. In general, this problem can be solved numerically. However, plotting $S_D(t^*, t_s, l)$ as given in Eqs. (4.56) and (4.61) is not very costly and enables the analyst to easily pick optimal geometric parameters for different safety factors. Two examples are

given shortly. It can be seen, that circular hinges yield higher safety factors than parabolic hinges, for a given thinnest cross-section t_S, i.e. an infinite life is more likely using circular hinges. In other words, circular hinges can have a thinner cross-section than parabolic hinges for a given safety factor. However, the reader should be aware that circular flexural hinges are not necessarily the best choice in terms of deflection range and precision, as described in Sect. 4.5.1 and Sect. 4.5.3, respectively.

4.5.5.2 Example 1: Life cycle analysis

Consider a given parabolic flexural hinge ($h = 10\,\text{mm}$, $l = 8\,\text{mm}$, $b = 10\,\text{mm}$, $t_s = 0.5\,\text{mm}$) is undergoing a cyclic loading of $M_y = 20 \pm 30\,\text{N mm}$ and $F_x = 10 \pm 20\,\text{N}$. The monolithic CM is made of aluminum wrought alloy T3 and the hinges are manufactured by wire cutting-EDM (surface roughness $R_t = 20\mu\text{m}$). A check is made for infinite life (with a safety factor $S_D \geq 2$) by performing the following:

1. Calculate the maximum nominal stresses by Eq. (4.33):

$$\sigma_{mb} = \frac{6}{bt_s^2} M_{my} = 48\,\text{N mm}^{-2}, \quad \sigma_{ab} = \frac{6}{bt_s^2} M_{ay} = 72\,\text{N mm}^{-2},$$
$$\sigma_{mt} = \frac{1}{bt_s} F_{mx} = 2\,\text{N mm}^{-2}, \quad \sigma_{at} = \frac{1}{bt_s} F_{ax} = 4\,\text{N mm}^{-2}.$$

2. Determine the ultimate tensile strength and the fatigue strength of unnotched test specimens from Table 4.1:

$$S_U = 485\,\text{MPa}, \quad S_{fb,R} = 130\,\text{MPa}, \quad S_{ft,R} = 111\,\text{MPa}.$$

3. Calculate the fatigue strength reduction factor by Eq. (4.42) using Eq. (4.19):

$$r = 1.68\,\text{mm}, \quad K_{tb} = 1.02, \quad K_{tt} = 1.06,$$
$$K_{fb} = 1.01, \quad K_{ft} = 1.04.$$

4. Determine the surface roughness reduction factor by Fig. 4.7:

$$\gamma = 0.75.$$

5. Calculate the fatigue strength of the flexural hinge by Eq. (4.47) using the results from steps 2 - 4:

$$S_{ab} = 86.78\,\text{MPa}, \quad S_{at} = 79.73\,\text{MPa}.$$

6. Calculate the equivalent deflection stress σ_{ae} by Eq. (4.45):

$$\kappa = 0.92, \quad \sigma_{ae} = 70.2\,\text{N}\,\text{mm}^{-2}.$$

7. Calculate the safety factor using Eq. (4.49) and check with specifications:

$$S_D = 1.14 < 2.$$

Conclusion: Reliability of the parabolic flexural hinge against fatigue failure with a safety factor $S_D \geq 2$ cannot be guaranteed. A logical question is, how a flexural hinge can be designed to prevent fatigue failure, which is addressed in the second example.

4.5.5.3 Example 2: Optimal design

Consider a parabolic flexural hinge undergoing superposed tensile ($F_x = 10 \pm 20\,\text{N}$) and bending ($M_y = 120 \pm 50\,\text{N}\,\text{mm}$) cyclic loading. The monolithic CM is made of Al wrought alloy T351 and the flexural hinges are manufactured by drilling (surface roughness $R_t = 28\,\mu\text{m}$). The length l of the flexural hinge is rigorously limited to 1 mm so that it fits into the CM. The thinnest cross-section t_s and the notch depth t^* need to be determined in order to provide infinite life with safety factor $S_D \geq 2$ by performing the following steps:

1. Determine the surface roughness reduction factor by Fig. 4.7:

$$\gamma = 0.69.$$

2. Calculate the stress concentration factors by Eq. (4.57):

$$\begin{aligned} K_{tt}^{P} =& 1 + \left(t^{*3} t_s^3 \left(2.t^* + t_s\right)\right)^{0.5} * \left(0.01 t_s + 0.35 t^3 t_s^2 + 0.01 t^{*0.5} t_s^4 \right. \\ & \left. t^{*2} t_s \left(0.18 + 0.2 t_s^2\right) + t^* \left(0.02 + 0.09 t_s^2 + 0.01 t_s^4\right) \right)^{-0.5}, \\ K_{tb}^{P} =& 1 + \left(0.32 t^{*1.32} + \frac{0.01 t_s}{t^{*2.66} \left(2t^* + t_s\right)} + \frac{0.02 \left(1 + 4 t^* t_s\right)^{2.25}}{\left(t^* t_s\right)^{3.38}} \right)^{-0.5}. \end{aligned}$$

3. Calculate the safety factor using Eq. (4.61):

$$\begin{aligned} S_D = & \, 2.05(1 + 5.28 t^*)(K_{tt}^{P} - 485 t_s) \left(-72 K_{tb}^{P} + 485 t_s^2\right) / \\ & \left[t^* t_s (852746 + 66580.8 t_s) + K_{tb}^{P} (-2205 K_{tt}^{P} - 9884.16 t^* \right. \\ & \left. + 161505 t_s) + K_{tt}^{P} \left(-1758.24 t^* + 12610 t_s^2\right)\right]. \end{aligned} \quad (4.62)$$

Conclusion: The dependencies between the design variables, t_s and t^*, and the safety factor S_D are illustrated in Fig. 4.18 for parabolic and circular flexural hinges. The latter one was obtained by a similar (but not explicitly shown) calculation. Geometric parameters can be chosen to achieve optimal flexural hinges with infinite life for a desired safety factor, e.g. $t^* = 3.5\,\text{mm}$ and $t_S = 1.0\,\text{mm}$ for $S_D = 2$.

4.5.5.4 Overall result

In order to avoid fatigue failure of flexural hinges in compliant mechanisms, explicit analytical expressions for the fatigue life of circular and parabolic flexural hinges were derived, accounting for stress concentration, surface finish and non-zero mean stresses. Time-harmonic, constant amplitude loads, namely axial forces, shear forces and bending moments, were considered. Optimally designed FH with an infinite life were then obtained by an inverse solution of the derived explicit expressions for given loads.

Two example cases were described in detail to illustrate the proposed fatigue analysis and design process. Comparing circular and parabolic

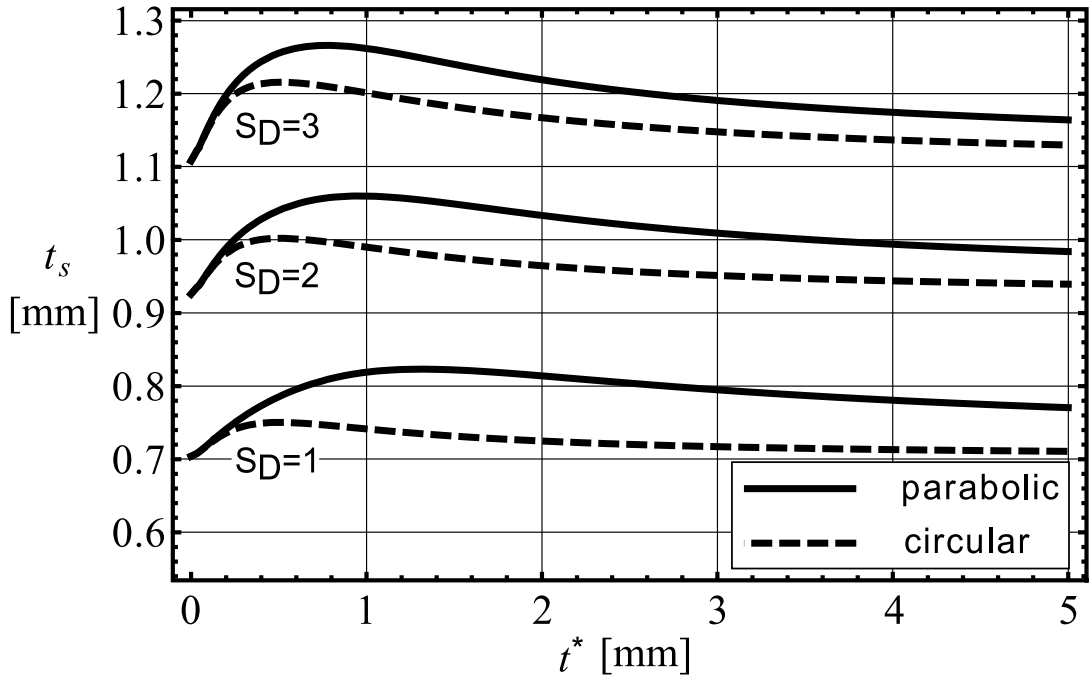

Figure 4.18: Safety factor S_D as a function of t^* and t_s for parabolic and circular flexural hinges as listed in Eq. (4.62)

hinges in terms of fatigue life, it was shown, that circular hinges provide a "safer" design than parabolic hinges for a given thinnest cross-section. Or in other words, circular hinges can have a thinner cross-section than parabolic hinges, while providing the same safety against fatigue failure.

Generally, the resulting fatigue strength of flexural hinges depend on the surface finish and on the notch effect that is linked directly with the radii of curvature, i.e. smaller radii of curvature result in lower fatigue strengths. This is not a surprising result, however Eq. (4.47) provides explicit analytical expressions to calculate the reduced fatigue strength of flexural hinges prior to any modeling or manufacturing efforts.

4.6 Summary

Relevant mechanical properties of differently shaped FH were examined. For this, analytical expressions on mechanical stresses, displacements, stiffnesses and bending stiffnesses, maximum elastic deflection, precisions, natural frequencies, fatigue strengths and optimal design of rectangular, circular and parabolic FH were derived and applied. Numerical simulations and experimental studies were conducted to validate the analytical results. The benefits of the derived explicit expressions relating the shape and mechanical properties of FH are illustrated in Fig. 4.19. The strengths and weaknesses of rectangular, circular and parabolic FH are summarized in Table 4.7.

A **high elastic deflection** is obtained by rectangular FH due to its long, thin cross section. However, a reliable, analytical prediction is hardly possible, since the occurring stresses vary by magnitudes with the very small root radius. Circular FH obtain moderate elastic deflections, whereas parabolic FH yield only small deflections.

A **high bending stiffness** is obtained by parabolic FH. Circular and rectangular FH possess moderate and low bending stiffness, respectively. The analytical calculations match the numerical and experimental data well. Therefore, the derived expressions are well suited to calculate the stiffness of FH or to design FH with specific stiffnesses.

A **high precision** is obtained by circular and, in particular, by parabolic FH. Rectangular FH provide poor performances in this field. In addition, the enormous influence of different superposed loadings leaves rectangular FH unsuitable for high precision applications. In contrast to this, circular and parabolic FH seems to be highly applicable.

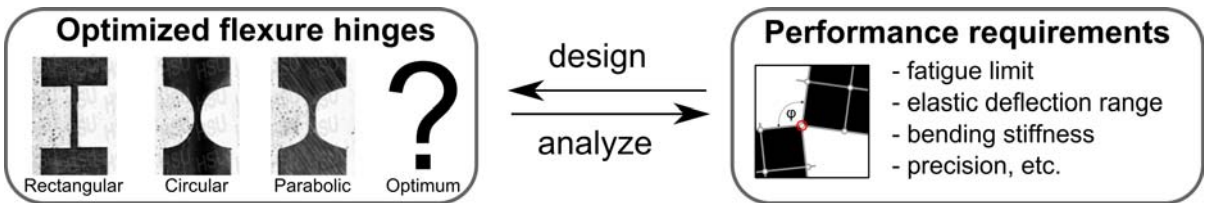

Figure 4.19: Benefits of explicit, analytical expressions linking flexure hinge's geometry with its corresponding mechanical properties

Table 4.7: Strengths and weaknesses of differently-shaped FH

	Rectangular FH	Circular FH	Parabolic FH
Maximum deflection	+ +	○	−
High bending stiffness	−	○	+
High precision	− −	+	+ +
High natural frequency	− −	+	+ +
High endurance	− −	+ +	+
Potential for design	−	+ +	+ +

A **high natural frequency** for a certain configuration is obtained by circular and, in particular, parabolic FH. Rectangular FH yield low natural frequencies. Again, the analytical results on all considered FH match the numerical and experimental data quite well. A discrete model, consisting of a torsional spring connected to a rigid bar, was introduced and a relation between stiffness and natural frequency was derived from the equation of motion. This relation was used to compare experimental data gathered by different, independent experimental setups. The measured and calculated bending stiffnesses match very well with a relative error of less than 4%.

A **high endurance** is obtained by parabolic FH and, in particular, by circular FH, whereas rectangular FH provide a poor performance. This means, that – given an infinite life – parabolic and circular FH are able to endure higher stress amplitudes and higher mean stresses than rectangular FH. The derivation of analytical, explicit and applicable expressions of differently shaped FH is highly relevant to many researchers and engineers, and, so far, not existent to the author´s knowledge. Experimental studies on the fatigue life of differently shaped FH were not conducted and, again, not known to the author.

A high **potential for optimal design** is provided by circular and parabolic FH, whereas rectangular FH are poorly suited due to an almost unpredictable, high stress concentration of real machined root radii.

From a topological synthesis standpoint, the derived, explicit, analytical expressions provide an effective analysis and design process, in order to incorporate optimal flexural hinges into compliant mechanisms for quasi-static and dynamic applications prior to any modeling or manufacturing efforts. These formulations eliminate unclear interpretation issues that would be encountered during any later manufacturing stage of a compliant mechanism.

5 A compliant mechanism with incorporated flexure hinges

In this chapter, the incorporation of flexure hinges into the topological design is illustrated by a sample case. For this purpose, the non-intuitive staggered topology optimization process and the gained knowledge of differently-shaped flexure hinges are now melted together as illustrated in Fig. 5.1. As an example, an optimized compliant gripping device with incorporated flexure hinges is designed, tested and rapid-prototyped.

First, the specifications in terms of geometric dimensions and desired motion performance are set. Second, the staggered OC-GCMMA topology optimization process is applied. Third, a hinge detection algorithm is implemented and applied to the final topology. Fourth, commercial computer-aided design (CAD) and FEA software tools are used to generate and examine a blue print of the CM. Finally, a rapid-prototyped CM is manufactured based on the previously generated CAD model.

5.1 Performance specifications

Starting from an initial, rectangular material design domain as shown in Fig. 5.2, a compliant gripping device with a *horizontal* input motion f_{in} at the left center and an output gripping on a specific output motion path u_{out} at the right border is desired.

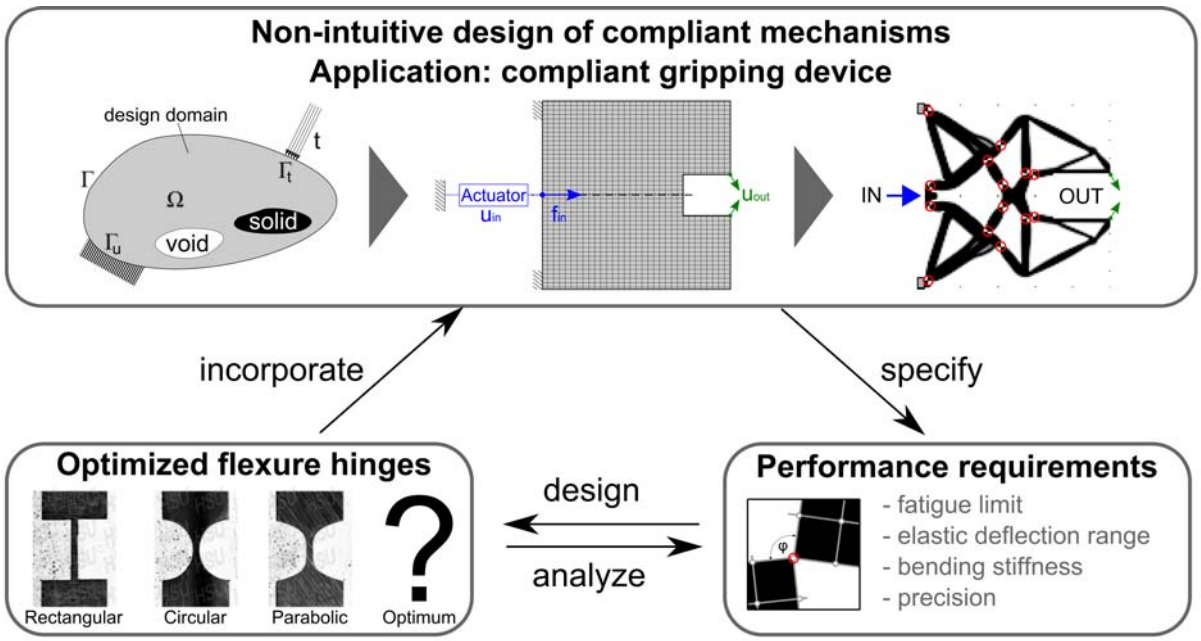

Figure 5.1: Multi-step synthesis of compliant mechanisms

Fixed boundary conditions are only set to the left upper and lower corner. The ratio of the overall length and height of the design domain is $L_d : H_d = 1 : 2$. The output height is set to $1/8\, H_d$, no void area is set.

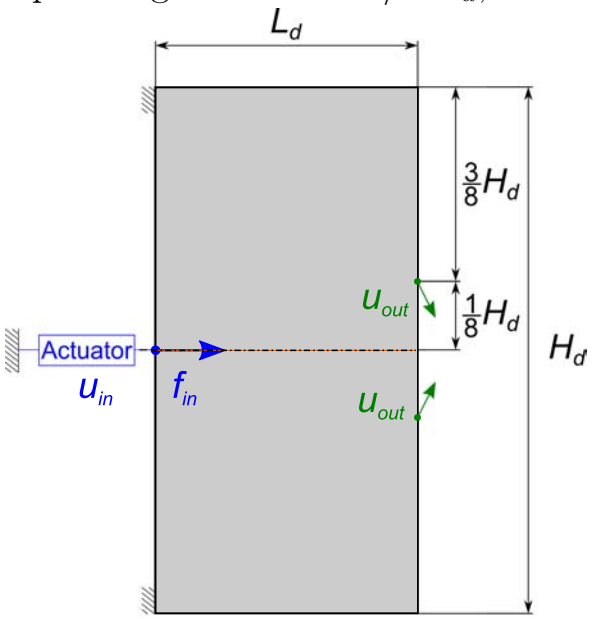

Figure 5.2: Initial design domain (length L_d, height H_d) with specified boundary conditions, an input force $\boldsymbol{f}_{in}$ and a desired output gripping $\boldsymbol{u}_{out}$ pointing in a specific output motion direction

5.2 Topology optimization process

The staggered OC-GCMMA topology optimization process, as described in Sect. 3 is applied here. Table 5.1 lists the relevant details of the staggered algorithm. The design domain is divided by its horizontal symmetry axis where the upper half of the design domain is discretized by $N = N_x \times N_y = 3,600$ FE. The interval lengths of the staggered optimization algorithm are set to be $n_{OC} = 2$ and $n_{GCMMA} = 2$ with a maximum number of iterations of $n_{max}^{Stagg} = 252$. The linear FEA switched over to nonlinear FEA at iteration number $n_{nonlinear} = 200$.

Table 5.1: Data of the staggered topology optimization process

N_x	N_y	N	n_{OC}	n_{GCMMA}	n_{max}^{Stagg}	$n_{nonlinear}$
[−]	[−]	[−]	[−]	[−]	[−]	[−]
60	60	3,600	2	2	250	200

Figure 5.3 shows the staggered topology optimization process of a compliant gripping device with 2×3,600 FE in a stepwise manner: starting from an initial, material design domain (Fig. 5.3(a)), running through several intermediate topologies (Fig. 5.3(b) - Fig. 5.3(g)) and resulting in a final topology (Fig. 5.3(h)).

At each selected iteration number, two plots show the current design after the GCMMA-algorithm (left) and after the concurrent OC-algorithm (right). It can be seen, that (a) the topology of the CM is designed stepwise and (b) the left and right topologies melt together after several iterations.

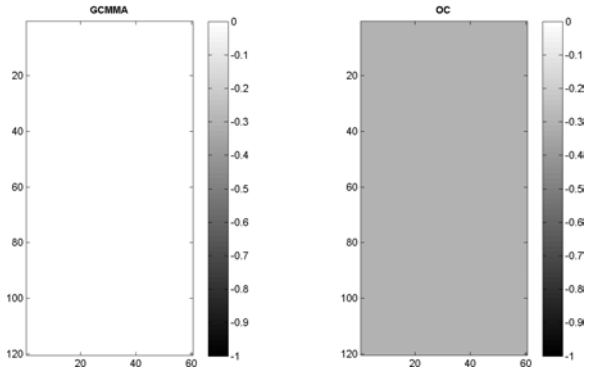

(a) Starting point

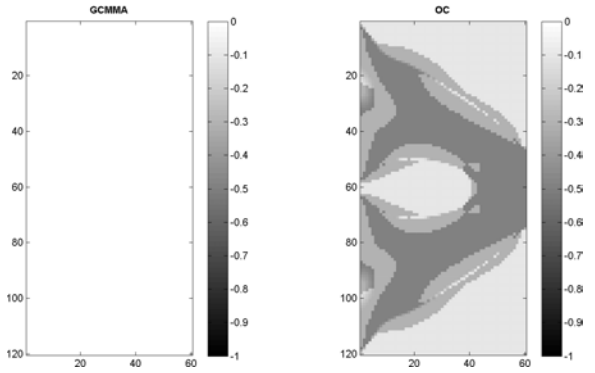

(b) 2nd iteration

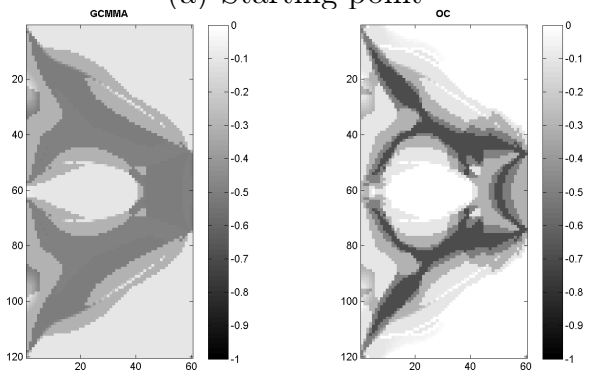

(c) 6th iteration

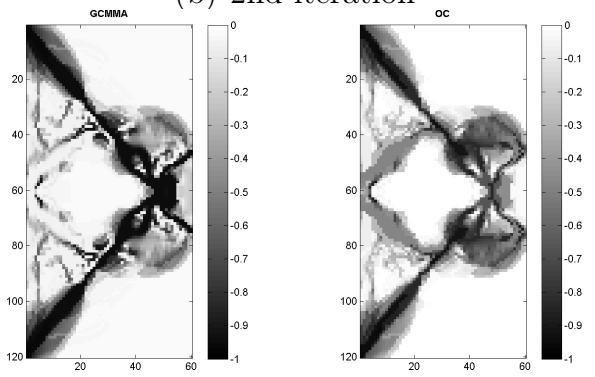

(d) 20th iteration

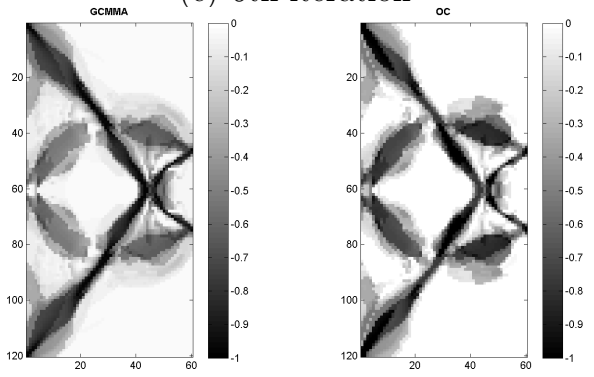

(e) 50th iteration

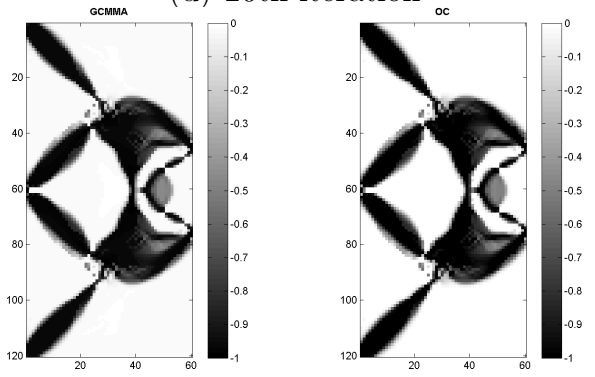

(f) 80th iteration

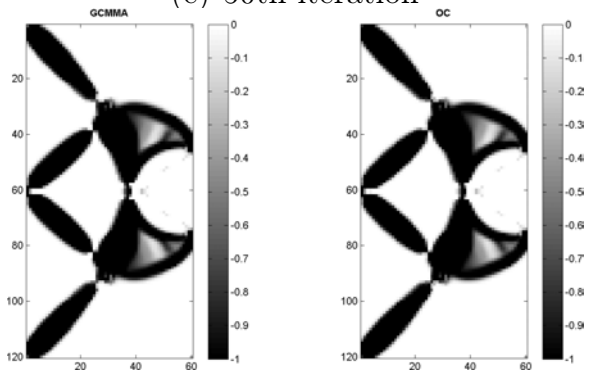

(g) 100th iteration

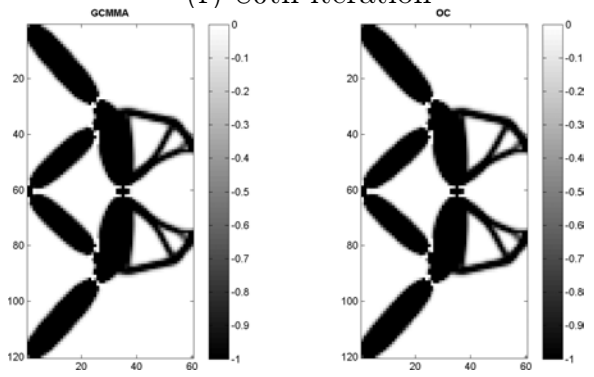

(h) 252nd iteration

Figure 5.3: Stepwise process of the staggered topology optimization algorithm: plots after GCMMA-algorithm (left) and after OC-algorithm (right) with an interval of $n_{GCMMA} = 2$ and $n_{OC} = 2$

5.3 Hinge detection

As mentioned in Sect. 3.4, one key result of the topology optimization process is that the "hinge areas" can be extracted from the final plot of the design variables, as shown by Fig. 5.3(h). In order to replace the "hinge areas" with real flexure hinges, the exact positions are determined by a *hinge detection algorithm* that scans the CM's final topology for one-node hinges and one-cell hinges that are illustrated in Fig. 5.4. Eventually, the final topology with highlighted hinges (green circle) as well as input and output nodes (red and blue x) is shown in Fig. 5.5(a).

Besides the positions of the FH, the *deflection* of each individual FH is required. Therefore, another (nonlinear) FEA with the known design variables, input displacements and output displacements is performed again yielding the nodal displacements and, thus, the maximum deflections of each individual hinge.

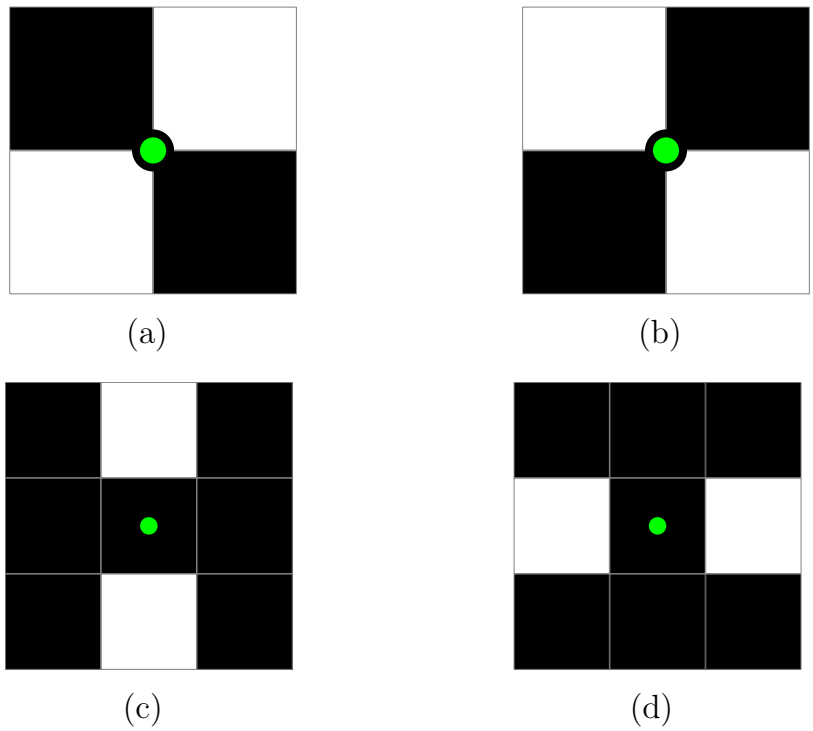

Figure 5.4: One-node hinges (a) and (b), and one-cell hinges (c) and (d) detected by hinge detection algorithm

5.4 Computer-aided design and finite element analysis

The relevant positions and geometrical data are passed to a commercial CAD software tool, namely Solid Works. Here, a 2D and 3D blueprint are generated automatically based on the submitted data where *circular* flexure hinges with the following geometry data are chosen

$$h = 5\,\text{mm}, \quad r = 2.3\,\text{mm}, \quad t_s = 0.4\,\text{mm}, \quad b = 15\,\text{mm}.$$

and incorporated in the CM. Fig. 5.5(a) shows the final topology with highlighted coordinates of the input (red) and output motion (blue) as well as of the flexure hinges. Fig. 5.5(b) shows the corresponding 3D blueprint.

The resulting CAD files are, then, passed to a commercial FEA software, namely ANSYS. Here, the same displacements that were calculated previously within the optimization procedure as described in Sect. 3, are computed. Fig. 5.5(c) and Fig. 5.5(d) show the meshed part and the corresponding y-displacement contour plot.

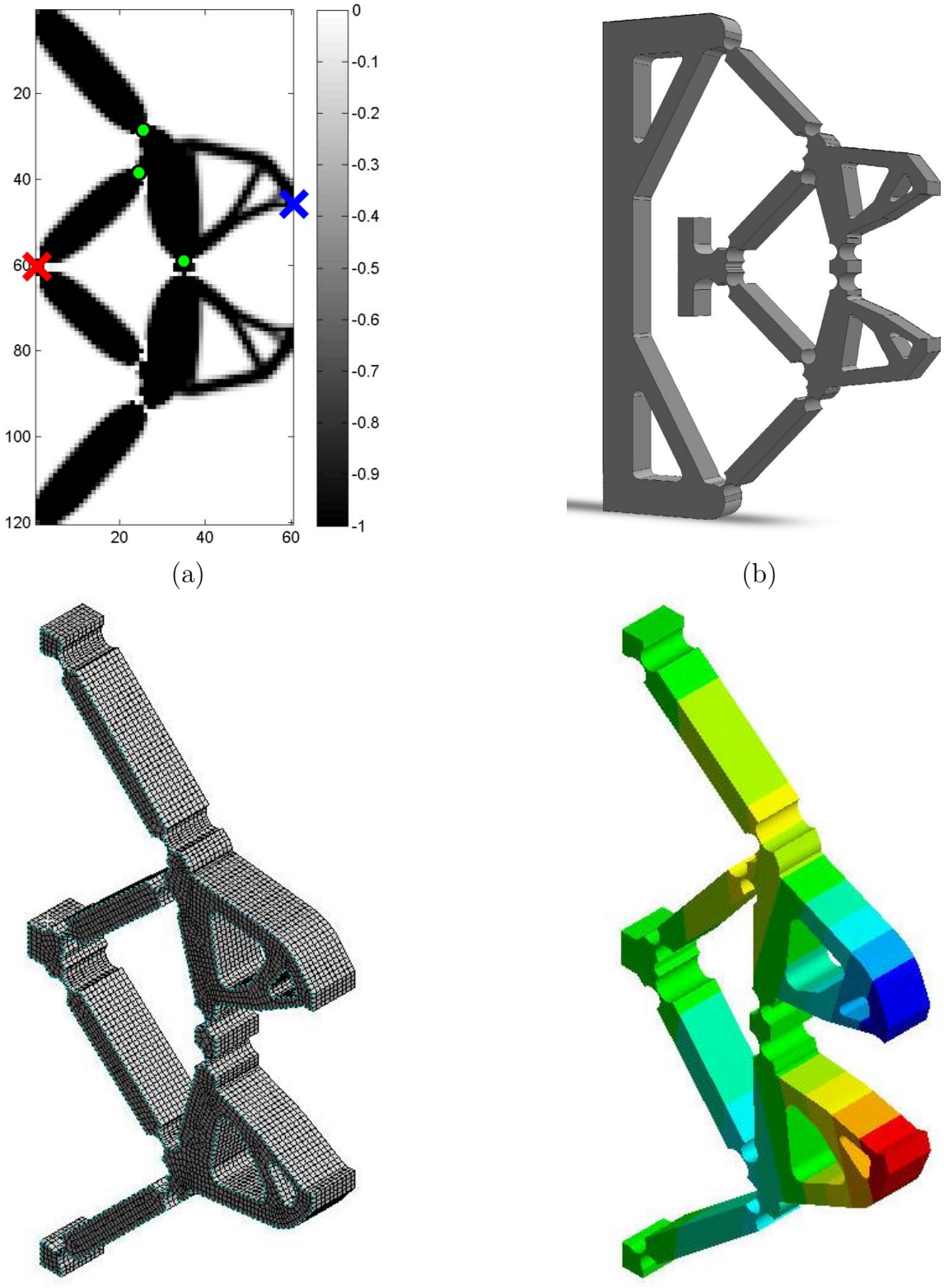

(a) (b)

(c) (d)

Figure 5.5: Post-processing of final topology of the compliant gripping device: starting from detected hinge's positions (a) and resulting in commercial CAD models (b) and FEA models (c) and (d)

5.5 A rapid-prototyped compliant mechanism

The CAD files are also passed to a rapid prototyping machine software where a real prototype is manufactured quickly. Fig. 5.6 shows the corresponding real prototype.

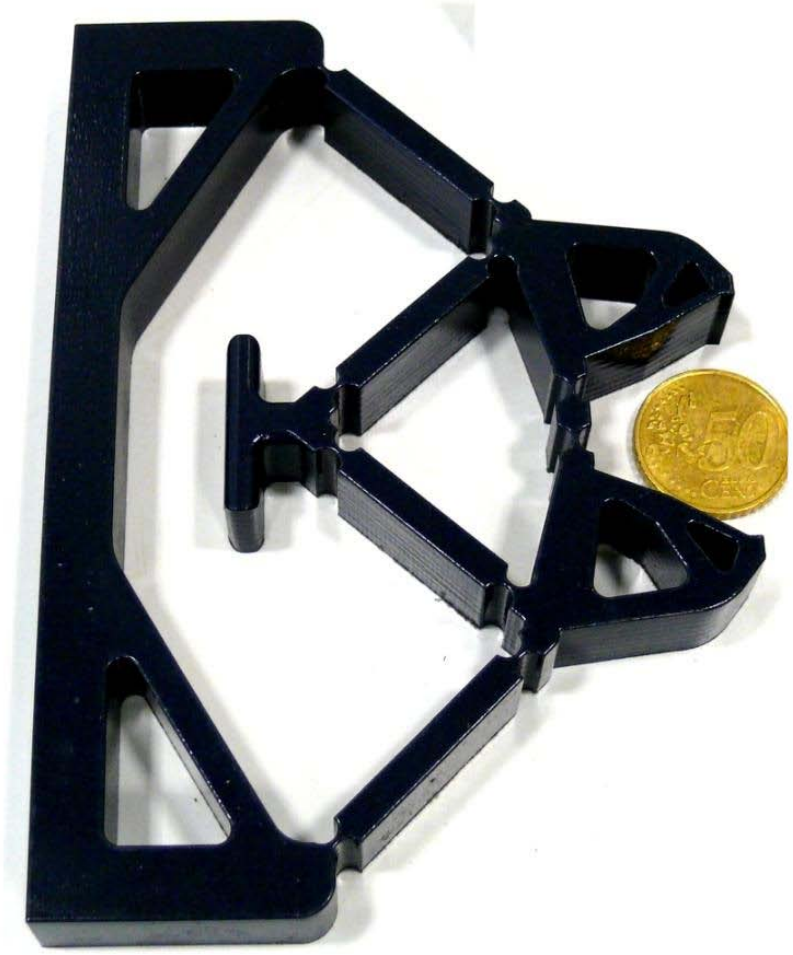

Figure 5.6: A rapid-prototyped compliant gripping device

This example demonstrates the systematic way of generating real CM with incorporated FH starting from a few geometric and material specifications, designing non-intuitively the optimal topology, detecting and incorporating FH and, finally, manufacturing a prototype.

6 Thesis' conclusion

In this final chapter, a summary of the thesis, its main achievements as well as future prospects are given.

6.1 Summary

As a part of the priority programme "Small machine tools for small work pieces" initiated by the German Research Foundation, this dissertation focused on the synthesis of compliant mechanisms. It addressed two major challenges: first, the difficult, non-intuitive design process and, second, the hardly-predictable influence of incorporated flexure hinges.

In order to address the first challenge, a staggered topology optimization algorithm that includes a nonlinear finite element analysis, optimality criteria method and globally convergent method of moving asymptotes, was developed. This algorithm was tested on different common load cases resulting in different topologies corresponding to the boundary conditions and motion specifications.

In order to address the second challenge, analytical expressions were derived and tested providing explicit relations between the hinge geometry and important mechanical properties. These relations were applied in both directions, i.e. the mechanical properties were determined directly from the geometry, and an optimal geometry was found meeting certain mechanical performance criteria including the highly desirable prediction on the fatigue life.

Finally, the appropriate flexure hinges were incorporated in the optimized topology yielding a prototype of a compliant gripping device.

6.2 Main achievements

Focussing on the non-intuitive and systematic synthesis of compliant mechanisms with incorporated appropriately-designed flexure hinges, the thesis' main achievements that contribute an advancement to present research work are:

- Developing a robust and broadly-applicable topology optimization method by staggering two different established optimization algorithms, namely OC and GCMMA, that yields the successful and robust generation of compliant mechanisms with desired output motions.

- Implementing a (self-written) nonlinear FEA code into the topology optimization algorithm accounting for a highly accurate and stable modeling of the large deformations occurring in CM.

- Bridging the gap between topology optimization synthesis and real-world flexure hinges by developing a broadly-applicable hinge detection algorithm that extracts the positions and deflections of FH from a final topology of a compliant mechanism enabling a rapid modeling with other (commercial) CAD and/ or FEA software.

- Deriving explicit, analytical expressions connecting relevant mechanical characteristics with the geometric dimensions of flexure hinges, and validating the analytical results regarding maximum elastic deformation, stiffness, precision as well as natural frequency by numerical simulations and experimental studies.

- Deriving novel and explicit analytical expressions connecting the important fatigue life of flexure hinges with their geometric dimensions and external loads. These equations provide a straightforward and powerful method (a) to predict the fatigue life of the highly- susceptible flexure hinges and (b) to optimally design long-lasting flexure hinges.

All in all, this dissertation improves and accelerates the design process of compliant mechanisms with incorporated flexure hinges by the proposed

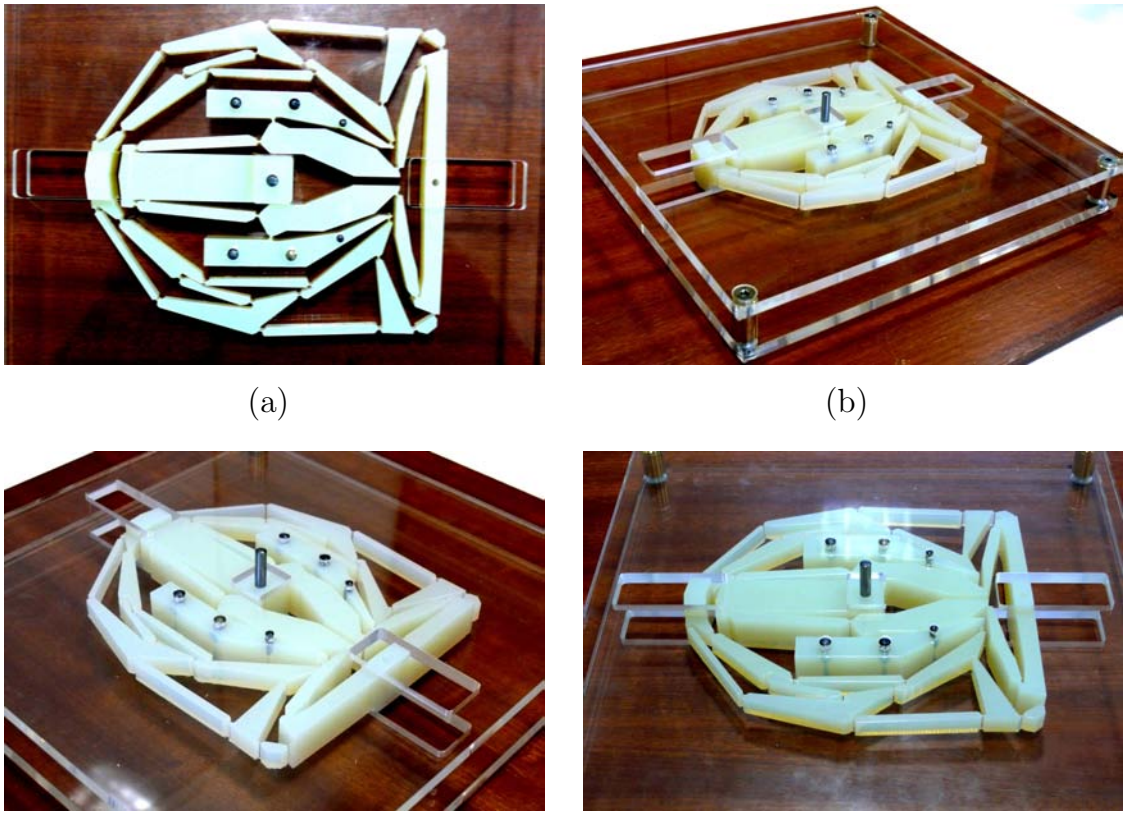

Figure 6.1: Compliant feed unit with optimized topology recently designed at HSU

topology optimization algorithm and the explicit analytical expressions that are ready to be applied prior to any modeling and manufacturing efforts.

As shown in Fig. 6.1, for instance, a prototype of a compliant feed unit providing a high stroke amplification designed for a piezoceramic actuator was generated, modeled and manufactured at the HSU in 2013, where numerous aspects of the proposed methodology have been applied.

In the future, the proposed topological synthesis of compliant mechanisms with appropriate flexure hinges can be applied to a variety of other applications, as well.

6.3 Future prospects

In order to continue and further develop the presented research work, the following future prospects seem to be reasonable:

- The flexure hinges can be modeled more efficiently by applying *model order reduction techniques* based on the equations provided in this work. These reduced models of FH could be implemented directly into the topology optimization process resulting in a significant reduction of computation time.

- For highly dynamic applications, the inertia of masses and the damping of the structure of the CM need to be taken into account. This can be done by extending the presented quasi-static FEA to a *dynamic FEA* within the topology optimization synthesis leading to time-dependent sets of equations. For this, powerful parallel programming techniques are necessary due to a required time-wise discretization that causes an enormous increase of computation time.

- In order to achieve a more compact design, actuators can be embedded directly into the material of the compliant mechanism. Combining different *smart materials* with individual strokes and frequency ranges could also reduce disturbing oscillations that effect the CM's precision.

The proposed future prospects would potentially lead to a further development and an advancement to present research work on the field of compliant mechanisms with incorporated flexure hinges.

Bibliography

[1] M. Sauter. *A graph-based optimization method for the design of compliant mechanisms and structures*. PhD thesis, Swiss Federal Institute of Technology Zurich, 2008.

[2] S. Shuib, M.I.Z. Ridzwan, A.H. Kadarman, S. Perai, and M. Penang. Methodology of compliant mechanisms and its current developments in applications: A review. *American Journal of Applied Sciences*, 4(3):160–167, 2007.

[3] M.P. Bendsøe and O. Sigmund. *Topology optimization: theory, methods, and applications*. Springer Verlag, 2003.

[4] K. Saitou, K. Izui, S. Nishiwaki, P. Papalambros, et al. A survey of structural optimization in mechanical product development. *Journal of Computing and Information Science in Engineering*, 5:214, 2005.

[5] L.L. Howell and A. Midha. A method for the design of compliant mechanisms with small-length flexural pivots. *Journal of Mechanical Design*, 116:280, 1994.

[6] L.L. Howell and A. Midha. A loop-closure theory for the analysis and synthesis of compliant mechanisms. *Journal of Mechanical Design*, 118:121, 1996.

[7] A. Midha, L.L. Howell, and T.W. Norton. Limit positions of compliant mechanisms using the pseudo-rigid-body model concept. *Mechanism and Machine Theory*, 35(1):99–115, 2000.

[8] C.A. Mattson, L.L. Howell, and S.P. Magleby. Development of commercially viable compliant mechanisms using the pseudo-rigid-body model: Case studies of parallel mechanisms. *Journal of Intelligent Material Systems and Structures*, 15(3):195, 2004.

[9] D.C. Handley, T.F. Lu, Y.K. Yong, and W.J. Zhang. A simple and efficient dynamic modeling method for compliant micropositioning mechanisms using flexure hinges. In *SPIE proceedings series*, volume 5276, pages 67–76, 2004.

[10] Y.Q. Yu, L.L. Howell, C. Lusk, Y. Yue, and M.G. He. Dynamic modeling of compliant mechanisms based on the pseudo-rigid-body model. *Journal of Mechanical Design*, 127:760, 2005.

[11] L.L. Howell. *Compliant mechanisms*. Wiley-Interscience, 2001.

[12] G.K. Ananthasuresh and S. Kota. Designing compliant mechanisms. *Mechanical Engineering*, 117(11):93–96, 1995.

[13] M. I. Frecker, G. K. Ananthasuresh, S. Nishiwaki, N. Kikuchi, and S. Kota. Topological synthesis of compliant mechanisms using multi-criteria optimization. *Journal of Mechanical Design*, 119(2):238–245, 1997.

[14] A. Saxena and G.K. Ananthasuresh. On an optimal property of compliant topologies. *Structural and Multidisciplinary Optimization*, 19(1):36–49, 2000.

[15] M.I. Frecker, S. Kota, and N. Kikuchi. Optimal design of compliant mechanisms for smart structures applications. In *Proceedings of SPIE*, volume 3323, page 234, 1998.

[16] M. Frecker, N. Kikuchi, and S. Kota. Topology optimization of compliant mechanisms with multiple outputs. *Structural and Multidisciplinary Optimization*, 17(4):269–278, 1999.

[17] M. Frecker and S. Canfield. Optimal design and experimental validation of compliant mechanical amplifiers for piezoceramic stack

actuators. *Journal of Intelligent Material Systems and Structures*, 11(5):360, 2000.

[18] M.I. Frecker. Recent advances in optimization of smart structures and actuators. *Journal of Intelligent Material Systems and Structures*, 14(4-5):207–216, 2003.

[19] G.K. Ananthasuresh. *Optimal synthesis methods for MEMS*. Kluwer Academic Publishers, 2003.

[20] A. Saxena and G.K. Ananthasuresh. A computational approach to the number of synthesis of linkages. *Journal of Mechanical Design*, 125:110, 2003.

[21] D.S. Ramrakhyani, M.I. Frecker, and G.A. Lesieutre. Hinged beam elements for the topology design of compliant mechanisms using the ground structure approach. *Structural and Multidisciplinary Optimization*, 37(6):557–567, 2009.

[22] S. Kota, J. Hetrick, Z. Li, and L. Saggere. Tailoring unconventional actuators using compliant transmissions: design methods and applications. *IEEE/ASME transactions on mechatronics*, 4(4):396–408, 1999.

[23] S. Kota, J. Joo, Z. Li, S.M. Rodgers, and J. Sniegowski. Design of compliant mechanisms: applications to MEMS. *Analog Integrated Circuits and Signal Processing*, 29(1):7–15, 2001.

[24] S. Kota, K.J. Lu, Z. Kreiner, B. Trease, J. Arenas, and J. Geiger. Design and application of compliant mechanisms for surgical tools. *Journal of Biomechanical Engineering*, 127:981, 2005.

[25] J. Joo, S. Kota, and N. Kikuchi. Topological synthesis of compliant mechanisms using linear beam elements. *Mechanics of Structures and Machines*, 28(4):245–280, 2000.

[26] J. Joo and S. Kota. Topological synthesis of compliant mechanisms using nonlinear beam elements. *Mechanics Based Design of Structures and Machines*, 32(1):17–38, 2004.

[27] C. Talischi, A. Pereira, I.F.M. Menezes, and G.H. Paulino. Topology optimization with Wachspress and Voronoi finite elements. In *International Conference on Engineering Optimization*, 2008.

[28] H.A. Eschenauer and N. Olhoff. Topology optimization of continuum structures: a review. *Applied Mechanics Reviews*, 54:331, 2001.

[29] Y.M. Xie and G.P. Steven. A simple evolutionary procedure for structural optimization. *Computers and Structures*, 49(5):885–896, 1993.

[30] Y.M. Xie. *Evolutionary structural optimization*. Springer (London and New York), 1997.

[31] X. Huang and M. Xie. *Evolutionary topology optimization of continuum structures: methods and applications*. Wiley, 2010.

[32] V. Young, O.M. Querin, G.P. Steven, and Y.M. Xie. 3D bi-directional evolutionary structural optimisation (BESO). *Oxbridge Press, Structural Optimisation(Australia)*, pages 275–282, 1998.

[33] O.M. Querin, G.P. Steven, and Y.M. Xie. Evolutionary structural optimisation using an additive algorithm. *Finite Elements in Analysis and Design*, 34(3):291–308, 2000.

[34] A. Lencus, O.M. Querin, G.P. Steven, and Y.M. Xie. Aircraft wing design automation with ESO and GESO. *International Journal of Vehicle Design*, 28(4):356–369, 2002.

[35] P. Tanskanen. A multiobjective and fixed elements based modification of the evolutionary structural optimization method. *Computer Methods in Applied Mechanics and Engineering*, 196(1-3):76–90, 2006.

[36] C.S. Edwards, H.A. Kim, and C.J. Budd. An evaluative study on ESO and SIMP for optimising a cantilever tiebeam. *Structural and Multidisciplinary Optimization*, 34(5):403–414, 2007.

[37] R. Ansola, E. Veguería, J. Canales, and J.A. Tárrago. A simple evolutionary topology optimization procedure for compliant mechanism design. *Finite Elements in Analysis and Design*, 44(1-2):53–62, 2007.

[38] M. Zhou and G.I.N. Rozvany. On the validity of ESO type methods in topology optimization. *Structural and Multidisciplinary Optimization*, 21(1):80–83, 2001.

[39] G.I.N. Rozvany. A critical review of established methods of structural topology optimization. *Structural and Multidisciplinary Optimization*, 37(3):217–237, 2009.

[40] J.A. Sethian and A. Wiegmann. Structural boundary design via level set and immersed interface methods. *Journal of Computational Physics*, 163(2):489–528, 2000.

[41] M.Y. Wang, X. Wang, and D. Guo. A level set method for structural topology optimization. *Computer Methods in Applied Mechanics and Engineering*, 192(1-2):227–246, 2003.

[42] X. Wang, M.Y. Wang, and D. Guo. Structural shape and topology optimization in a level-set-based framework of region representation. *Structural and Multidisciplinary Optimization*, 27(1):1–19, 2004.

[43] G. Allaire, F. Jouve, and A.M. Toader. A level-set method for shape optimization. *Comptes Rendus Mathematique*, 334(12):1125–1130, 2002.

[44] G. Allaire, F. Jouve, and A.M. Toader. Structural optimization using sensitivity analysis and a level-set method. *Journal of computational physics*, 194(1):363–393, 2004.

[45] J. Sokolowski and A. Zochowski. On the topological derivative in shape optimization. *SIAM Journal on Control and Optimization*, 37:1251, 1999.

[46] J.A. Norato, M.P. Bendsøe, R.B. Haber, and D.A. Tortorelli. A topological derivative method for topology optimization. *Structural and Multidisciplinary Optimization*, 33(4):375–386, 2007.

[47] G. Allaire and F. Jouve. A level-set method for vibration and multiple loads structural optimization. *Computer Methods in Applied Mechanics and Engineering*, 194(30-33):3269–3290, 2005.

[48] S. Wang and M.Y. Wang. Radial basis functions and level set method for structural topology optimization. *International Journal for Numerical Methods in Engineering*, 65(12):2060–2090, 2006.

[49] X. Xing, P. Wei, and M.Y. Wang. A finite element-based level set method for structural optimization. *International Journal for Numerical Methods in Engineering*, 82(7):805–842, 2010.

[50] L. Shu, M.Y. Wang, Z. Fang, Z. Ma, and P. Wei. Level set based structural topology optimization for minimizing frequency response. *Journal of Sound and Vibration*, 2011.

[51] M.Y. Wang, S. Chen, X. Wang, and Y. Mei. Design of multimaterial compliant mechanisms using level-set methods. *Journal of Mechanical Design*, 127:941, 2005.

[52] Z. Luo, L. Tong, M.Y. Wang, and S. Wang. Shape and topology optimization of compliant mechanisms using a parameterization level set method. *Journal of Computational Physics*, 227(1):680–705, 2007.

[53] J. Luo, Z. Luo, S. Chen, L. Tong, and M.Y. Wang. A new level set method for systematic design of hinge-free compliant mechanisms. *Computer Methods in Applied Mechanics and Engineering*, 198(2):318–331, 2008.

[54] Z. Luo, M.Y. Wang, S. Wang, and P. Wei. A level set-based parameterization method for structural shape and topology optimization. *International Journal for Numerical Methods in Engineering*, 76(1):1–26, 2008.

[55] S. Chen, W. Chen, and S. Lee. Level set based robust shape and topology optimization under random field uncertainties. *Structural and Multidisciplinary Optimization*, 41(4):507–524, 2010.

[56] M. Otomori, T. Yamada, K. Izui, and S. Nishiwaki. Level set-based topology optimisation of a compliant mechanism design using mathematical programming. *Mechanical Sciences*, 2, 2011.

[57] M. Otomori, T. Yamada, K. Izui, S. Nishiwaki, and J. Andkjær. A topology optimization method based on the level set method for the design of negative permeability dielectric metamaterials. *Computer Methods in Applied Mechanics and Engineering*, 2012.

[58] S. Nishiwaki, M.I. Frecker, S. Min, and N. Kikuchi. Topology optimization of compliant mechanisms using the homogenization method. *International Journal for Numerical Methods in Engineering*, 42(3):535–559, 1998.

[59] M.P. Bendsoe and N. Kikuchi. Generating optimal topologies in structural design using a homogenization method. *Computer Methods in Applied Mechanics and Engineering*, 71(2):197–224, 1988.

[60] R. Ansola, J. Canales, J.A. Tárrago, and J. Rasmussen. An integrated approach for shape and topology optimization of shell structures. *Computers and Structures*, 80(5-6):449–458, 2002.

[61] A.R. Díaaz and N. Kikuchi. Solutions to shape and topology eigenvalue optimization problems using a homogenization method. *International Journal for Numerical Methods in Engineering*, 35(7):1487–1502, 1992.

[62] Z.D. Ma, N. Kikuchi, and I. Hagiwara. Structural topology and shape optimization for a frequency response problem. *Computational Mechanics*, 13(3):157–174, 1993.

[63] Z.D. Ma, N. Kikuchi, H.C. Cheng, and I. Hagiwara. Topological optimization technique for free vibration problems. *Journal of Applied Mechanics*, 62:200, 1995.

[64] Z.D. Ma, N. Kikuchi, and H.C. Cheng. Topological design for vibrating structures. *Computer Methods in Applied Mechanics and Engineering*, 121(1-4):259–280, 1995.

[65] Z.D. Ma, N. Kikuchi, C. Pierre, and B. Raju. Multidomain topology optimization for structural and material designs. *Journal of Applied Mechanics*, 73:565, 2006.

[66] O. Sigmund. A 99 line topology optimization code written in Matlab. *Structural and Multidisciplinary Optimization*, 21(2):120–127, 2001.

[67] K. Suzuki and N. Kikuchi. A homogenization method for shape and topology optimization. *Computer Methods in Applied Mechanics and Engineering*, 93(3):291–318, 1991.

[68] Z. Hongwei, L. Kai, and M. Z-D. Homogenization topology optimization method based on continuous field. *Advances in Mechanical Engineering*, 2010, 2011.

[69] M.P. Bendsøe. *Optimization of Structural Topology, Shape, and Material*. Springer, 1995.

[70] B. Hassani and E. Hinton. A review of homogenization and topology optimization i: homogenization theory for media with periodic structure. *Computers and Structures*, 69(6):707–717, 1998.

[71] B. Hassani and E. Hinton. Review of homogenization and topology optimization ii- analytical and numerical solution of homogenization equations. *Computers and Structures*, 69(6):719–738, 1998.

[72] B. Hassani and E. Hinton. A review of homogenization and topology optimization iii–topology optimization using optimality criteria. *Computers and Structures*, 69(6):739–756, 1998.

[73] B. Hassani and E. Hinton. *Homogenization and structural topology optimization: theory, practice and software*. Springer, 1999.

[74] C.H. Le. *Developments in topology and shape optimization*. PhD thesis, University of Illinois at Urbana-Champaign, Available at http://www.ideals.illinois.edu/handle/2142/16064 (accessed on 5 November 2011), 2010.

[75] P.E. Gill, W. Murray, and M.H. Wright. *Practical optimization*. Academic press, 1981.

[76] R. Fletcher. *Practical Methods of Optimization: Vol. 2: Constrained Optimization*. Academic press, 1981.

[77] M. Zhou and G.I.N. Rozvany. DCOC: an optimality criteria method for large systems part I: theory. *Structural and Multidisciplinary Optimization*, 5(1):12–25, 1992.

[78] M. Zhou and G.I.N. Rozvany. DCOC: an optimality criteria method for large systems part II: algorithm. *Structural and Multidisciplinary Optimization*, 6(4):250–262, 1993.

[79] G. Chiandussi, M. Codegone, and S. Ferrero. Topology optimization with optimality criteria and transmissible loads. *Computers and Mathematics with Applications*, 57(5):772–788, 2009.

[80] M. Ghaemi. *Topology optimization problems using optimality criteria methods*. PhD thesis, Budapest University of Technology and Economics, Available at http://www.omikk.bme.hu/ collections/ phd/ Epitomernoki_Kar/2010/Mohsen_Ghaemi/ertekezes.pdf (accessed on 5 November 2011), 2009.

[81] S. Canfield and M. Frecker. Topology optimization of compliant mechanical amplifiers for piezoelectric actuators. *Structural and Multidisciplinary Optimization*, 20(4):269–279, 2000.

[82] M. Bremicker, P.Y. Papalambros, and H.T. Loh. Solution of mixed-discrete structural optimization problems with a new sequential linearization algorithm. *Computers and Structures*, 37(4):451–461, 1990.

[83] A.V. Kumar. A sequential optimization algorithm using logarithmic barriers: Applications to structural optimization. *Journal of Mechanical Design*, 122(3):271–277, 2000.

[84] J. Herskovits, G. Dias, G. Santos, and C.M. Mota Soares. Shape structural optimization with an interior point nonlinear programming algorithm. *Structural and Multidisciplinary Optimization*, 20(2):107–115, 2000.

[85] P. Morin, R.H. Nochetto, M.S. Pauletti, and M. Verani. Adaptive SQP method for shape optimization. *Numerical Mathematics and Advanced Applications*, pages 663–673, 2010.

[86] C. Fleury and V. Braibant. Structural optimization: a new dual method using mixed variables. *International Journal for Numerical Methods in Engineering*, 23(3):409–428, 1986.

[87] C. Fleury. Conlin: an efficient dual optimizer based on convex approximation concepts. *Structural and Multidisciplinary Optimization*, 1(2):81–89, 1989.

[88] K. Svanberg. The method of moving asymptotes - a new method for structural optimization. *International Journal for Numerical Methods in Engineering*, 24(2):359–373, 1987.

[89] K. Svanberg. A class of globally convergent optimization methods based on conservative convex separable approximations. *SIAM Journal on Optimization*, 12(2):555, 2002.

[90] K. Svanberg. MMA and GCMMA. *Report Available at http://www.math.kth.se/~krille/gcmma07.pdf(accessed on 15 October 2009)*, 2007.

[91] K. Schittkowski, C. Zillober, and R. Zotemantel. Numerical comparison of nonlinear programming algorithms for structural optimization. *Structural and Multidisciplinary Optimization*, 7(1):1–19, 1994.

[92] E. Kita and T. Toyoda. Structural design using cellular automata. *Structural and Multidisciplinary Optimization*, 19(1):64–73, 2000.

[93] M.M. Abdalla and Z. Gürdal. Structural design using optimality based cellular automata. In *Proceedings of 43rd AIAA/ASME/ASCE/AHS/ASC Structures, Structural Dynamics, and Materials Conference*, 2002.

[94] R. Kicinger, T. Arciszewski, and K.A. De Jong. Morphogenic evolutionary design: cellular automata representations in topological structural design. *Adaptive Computing in Design and Manufacture VI, IC Parmee, ed., Springer-Verlag, London, UK*, pages 25–38, 2004.

[95] R. Kicinger, T. Arciszewski, and K. De Jong. Morphogenesis and structural design: cellular automata representations of steel structures in tall buildings. In *Congress on Evolutionary Computation, 2004. CEC2004.*, volume 1, pages 411–418. IEEE, 2004.

[96] L.S. Guo, J. Huang, A. Tavor, and J.E. Renaud. Multidomain topology optimization for crashworthiness based on hybrid cellular automata. *Key Engineering Materials*, 486:250–253, 2011.

[97] M.M. Abdalla and Z. Gürdal. Structural design using cellular automata for eigenvalue problems. *Structural and Multidisciplinary Optimization*, 26(3):200–208, 2004.

[98] A. Tovar, N. Patel, A.K. Kaushik, G.A. Letona, J.E. Renaud, and B. Sanders. Hybrid cellular automata: a biologically-inspired structural optimization technique. In *10th AIAA/ISSMO Symposium on Multidisciplinary Analysis and Optimization*, 2004.

[99] A. Tovar, N.M. Patel, G.L. Niebur, and J.E. Renaud. Topology optimization using a hybrid cellular automation method with local control rules. *Journal of Mechanical Design*, 128:1205, 2006.

[100] A. Tovar, N.M. Patel, A.K. Kaushik, and J.E. Renaud. Optimality conditions of the hybrid cellular automata for structural optimization. *AIAA Journal*, 45(3):673, 2007.

[101] Z. Gürdal and T. Brian. Cellular automata for design of truss structures with linear and nonlinear response. *Atlanta*, 2000.

[102] B. Tatting and Z. Gürdal. Cellular automata for design of two-dimensional continuum structures. In *Proceedings of 8th AIAA/USAF/NASA/ISSMO Symposium on Multidisciplinary Analysis and Optimization*, 2000.

[103] C.L. Penninger, L.T. Watson, A. Tovar, and J.E. Renaud. Convergence analysis of hybrid cellular automata for topology optimization. *Structural and Multidisciplinary Optimization*, 40(1):271–282, 2010.

[104] S. Rajeev and C.S. Krishnamoorthy. Discrete optimization of structures using genetic algorithms. *Journal of Structural Engineering*, 118:1233, 1992.

[105] P. Hajela and C.Y. Lin. Genetic search strategies in multicriterion optimal design. *Structural and Multidisciplinary Optimization*, 4(2):99–107, 1992.

[106] P. Hajela and E. Lee. Genetic algorithms in truss topological optimization. *International Journal of Solids and Structures*, 32(22):3341–3357, 1995.

[107] S.J. Wu and P.T. Chow. Integrated discrete and configuration optimization of trusses using genetic algorithms. *Computers and Structures*, 55(4):695–702, 1995.

[108] S.J. Wu and P.T. Chow. Steady-state genetic algorithms for discrete optimization of trusses. *Computers and Structures*, 56(6):979–991, 1995.

[109] C.Y. Lin and P. Hajela. Genetic algorithms in optimization problems with discrete and integer design variables. *Engineering Optimization*, 19(4):309–327, 1992.

[110] M.J. Jakiela, C. Chapman, J. Duda, A. Adewuya, and K. Saitou. Continuum structural topology design with genetic algorithms. *Computer Methods in Applied Mechanics and Engineering*, 186(2-4):339–356, 2000.

[111] F. Erbatur, O. Hasançebi, et al. Optimal design of planar and space structures with genetic algorithms. *Computers and Structures*, 75(2):209–224, 2000.

[112] E. Zitzler and L. Thiele. Multiobjective evolutionary algorithms: A comparative case study and the strength pareto approach. *Evolutionary Computation, IEEE Transactions on*, 3(4):257–271, 1999.

[113] S. Botello, J.L. Marroquin, E. Onate, and J.V. Horebeek. Solving structural optimization problems with genetic algorithms and simulated annealing. *International Journal for Numerical Methods in Engineering*, 45(8):1069–1084, 1999.

[114] N. Srinivas and K. Deb. Multiobjective optimization using nondominated sorting in genetic algorithms. *Evolutionary computation*, 2(3):221–248, 1994.

[115] C.A.C. Coello et al. Treating constraints as objectives for single-objective evolutionary optimization. In *Engineering Optimization*. Citeseer, 1999.

[116] C.A. Coello and A.D. Christiansen. Multiobjective optimization of trusses using genetic algorithms. *Computers and Structures*, 75(6):647, 2000.

[117] K. Tai and J. Prasad. Target-matching test problem for multiobjective topology optimization using genetic algorithms. *Structural and Multidisciplinary Optimization*, 34(4):333–345, 2007.

[118] D.A. Van Veldhuizen. Multiobjective evolutionary algorithms: Classifications, analyses, and new innovations. Technical report, Evolutionary Computation, 1999.

[119] P. Nanakorn and K. Meesomklin. An adaptive penalty function in genetic algorithms for structural design optimization. *Computers and Structures*, 79(29-30):2527–2539, 2001.

[120] A.C.C. Lemonge and H.J.C. Barbosa. An adaptive penalty scheme for genetic algorithms in structural optimization. *International Journal for Numerical Methods in Engineering*, 59(5):703–736, 2004.

[121] O. Yeniay. Penalty function methods for constrained optimization with genetic algorithms. *Mathematical and Computational Applications*, 10(1):45–56, 2005.

[122] S.Y. Wang and K. Tai. Structural topology design optimization using genetic algorithms with a bit-array representation. *Computer Methods in Applied Mechanics and Engineering*, 194(36-38):3749–3770, 2005.

[123] K.S. Lee and Z.W. Geem. A new structural optimization method based on the harmony search algorithm. *Computers and structures*, 82(9-10):781–798, 2004.

[124] R. Balamurugan, CV Ramakrishnan, and N. Singh. Performance evaluation of a two stage adaptive genetic algorithm (TSAGA) in structural topology optimization. *Applied Soft Computing*, 8(4):1607–1624, 2008.

[125] S. Kirkpatrick, C.D. Gelatt Jr, and M.P. Vecchi. Optimization by simulated annealing. *Science*, 220(4598):671–680, 1983.

[126] A. Suppapitnarm, K.A. Seffen, G.T. Parks, and P.J. Clarkson. A simulated annealing algorithm for multiobjective optimization. *Engineering Optimization*, 33(1):59–85, 2000.

[127] R.E. Perez and K. Behdinan. Particle swarm approach for structural design optimization. *Computers and Structures*, 85(19-20):1579–1588, 2007.

[128] N. Padhye. Topology optimization of compliant mechanism using multi-objective particle swarm optimization. In *Proceedings of the 2008 GECCO conference companion on Genetic and evolutionary computation*, pages 1831–1834. Association for Computing Machinery, 2008.

[129] Y. Li and Q. Xu. Design and optimization of an XYZ parallel micromanipulator with flexure hinges. *Journal of Intelligent & Robotic Systems*, 55(4):377–402, 2009.

[130] C.V. Camp and B.J. Bichon. Design of space trusses using ant colony optimization. *Journal of Structural Engineering*, 130:741, 2004.

[131] C.V. Camp, B.J. Bichon, and S.P. Stovall. Design of steel frames using ant colony optimization. *Journal of Structural Engineering*, 131:369, 2005.

[132] A. Kaveh, B. Hassani, S. Shojaee, and S.M. Tavakkoli. Structural topology optimization using ant colony methodology. *Engineering Structures*, 30(9):2559–2565, 2008.

[133] R. Parsons and S.L. Canfield. Developing genetic programming techniques for the design of compliant mechanisms. *Structural and Multidisciplinary Optimization*, 24(1):78–86, 2002.

[134] A. Saxena. Synthesis of compliant mechanisms for path generation using genetic algorithm. *Journal of Mechanical Design*, 127:745, 2005.

[135] K.J. Lu and S. Kota. Design of compliant mechanisms for morphing structural shapes. *Journal of Intelligent Material Systems and Structures*, 14(6):379, 2003.

[136] K.J. Lu and S. Kota. Topology and dimensional synthesis of compliant mechanisms using discrete optimization. *Journal of Mechanical Design*, 128:1080, 2006.

[137] D. Sharma, K. Deb, and N.N. Kishore. Evolving path generation compliant mechanisms (PGCM) using local-search based multi-objective genetic algorithm. In *International Conference on Trends in Product Life Cycle, Modeling, Simulation and Synthesis (PLMSS)*, pages 227–238, 2006.

[138] D. Sharma, K. Deb, and N.N. Kishore. Towards generating diverse topologies of path tracing compliant mechanisms using a local search based multi-objective genetic algorithm procedure. In *Evolutionary Computation, CEC 2008*, pages 2004–2011. IEEE.

[139] D. Sharma, K. Deb, and N.N. Kishore. Advancement of path generating compliant mechanisms (PGCM) topologies by initial population strategy of customized evolutionary algorithm. 2009.

[140] D. Sharma, K. Deb, and N.N. Kishore. Domain-specific initial population strategy for compliant mechanisms using customized genetic algorithm. *Structural and Multidisciplinary Optimization*, pages 1–14, 2011.

[141] Y. Liu and J. McPhee. Automated type synthesis of planar mechanisms using numeric optimization with genetic algorithms. *Journal of Mechanical Design*, 127:910, 2005.

[142] N.D. Lagaros, M. Papadrakakis, and G. Kokossalakis. Structural optimization using evolutionary algorithms. *Computers and structures*, 80(7-8):571–589, 2002.

[143] Y. Li, B. Heng, L. Kong, and W. Yang. Review of algorithms of structural optimization with discrete variables. *World Journal of Engineering*, 8(3):231–236, 2011.

[144] T.A. Poulsen. A simple scheme to prevent checkerboard patterns and one-node connected hinges in topology optimization. *Structural and Multidisciplinary Optimization*, 24(5):396–399, 2002.

[145] G.H. Yoon, Y.Y. Kim, M.P. Bendsøe, and O. Sigmund. Hinge-free topology optimization with embedded translation-invariant differentiable wavelet shrinkage. *Structural and Multidisciplinary Optimization*, 27(3):139–150, 2004.

[146] O. Sigmund. Manufacturing tolerant topology optimization. *Acta Mechanica Sinica*, 25(2):227–239, 2009.

[147] B.P. Trease, Y.M. Moon, and S. Kota. Design of large-displacement compliant joints. *Journal of Mechanical Design*, 127:788, 2005.

[148] P. Kohrs. *Entwicklung und Erprobung einer neuen Vorschubeinheit für kleine Werkzeugmaschinen*. PhD thesis, Helmut-Schmidt-University/ University of the Federal Armed Forces Hamburg, 2011.

[149] J.M. Paros and L. Weisbord. How to design flexural hinges. *Machine Design*, 25:151–156, 1965.

[150] W. Xu and T. King. Flexure hinges for piezoactuator displacement amplifiers: flexibility, accuracy, and stress considerations. *Precision Engineering*, 19(1):4–10, 1996.

[151] N. Lobontiu, J.S.N. Paine, E. Garcia, and M. Goldfarb. Corner-filleted flexure hinges. *Journal of Mechanical Design*, 123:346, 2001.

[152] Y.M. Tseytlin. Notch flexure hinges: an effective theory. *Review of Scientific Instruments*, 73(9):3363–3368, 2002.

[153] Y. Wu and Z. Zhou. Design calculations for flexure hinges. *Review of Scientific Instruments*, 73:3101, 2002.

[154] N. Lobontiu, E. Garcia, M. Hardau, and N. Bal. Stiffness characterization of corner-filleted flexure hinges. *Review of Scientific Instruments*, 75:4896, 2004.

[155] N. Lobontiu, J.S.N. Paine, E. Garcia, and M. Goldfarb. Design of symmetric conic-section flexure hinges based on closed-form compliance equations. *Mechanism and Machine Theory*, 37(5):477–498, 2002.

[156] N. Lobontiu, J.S.N. Paine, E. O'Malley, and M. Samuelson. Parabolic and hyperbolic flexure hinges: flexibility, motion precision and stress characterization based on compliance closed-form equations. *Precision Engineering*, 26(2):183–192, 2002.

[157] Y. Tian, B. Shirinzadeh, and D. Zhang. Closed-form compliance equations of filleted V-shaped flexure hinges for compliant mechanism design. *Precision Engineering*, 34(3):408–418, 2010.

[158] S.T. Smith, V.G. Badami, J.S. Dale, and Y. Xu. Elliptical flexure hinges. *Review of Scientific Instruments*, 68:1474, 1997.

[159] G. Chen, X. Shao, and X. Huang. A new generalized model for elliptical arc flexure hinges. *Review of Scientific Instruments*, 79(9):095103, 2008.

[160] G. Chen, X. Liu, H. Gao, and J. Jia. A generalized model for conic flexure hinges. *Review of Scientific Instruments*, 80(5):055106, 2009.

[161] Y. Tseytlin. Tractable model for concave flexure hinges. *Review of Scientific Instruments*, 82(1):015106–015106, 2011.

[162] Z. Zhang and Y. Yuan. Design calculation and analysis of half corner-filleted flexure hinge. *Optics and Precision Engineering*, 3, 2007.

[163] G. Chen and L.L. Howell. Two general solutions of torsional compliance for variable rectangular cross-section hinges in compliant mechanisms. *Precision Engineering*, 33(3):268–274, 2009.

[164] F.Z. Hsiao and T.W. Lin. Analysis of a novel flexure hinge with three degrees of freedom. *Review of Scientific Instruments*, 72(2):1565–1573, 2001.

[165] N. Lobontiu, M. Cullin, M. Ali, and J.M.F. Brock. A generalized analytical compliance model for transversely symmetric three-segment flexure hinges. *Review of Scientific Instruments*, 82:105116, 2011.

[166] N. Lobontiu. *Compliant mechanisms: design of flexure hinges*. CRC, 2003.

[167] S.T. Smith. *Flexures: elements of elastic mechanisms*. CRC, 2000.

[168] Y.K. Yong, T.F. Lu, and D.C. Handley. Review of circular flexure hinge design equations and derivation of empirical formulations. *Precision Engineering*, 32(2):63–70, 2008.

[169] Y.K. Yong, T.F. Lu, et al. Comparison of circular flexure hinge design equations and the derivation of empirical stiffness formulations. 2009.

[170] Y. Tian, B. Shirinzadeh, D. Zhang, and Y. Zhong. Three flexure hinges for compliant mechanism designs based on dimensionless graph analysis. *Precision Engineering*, 34(1):92–100, 2010.

[171] Y.K. Yong and T.F. Lu. The effect of the accuracies of flexure hinge equations on the output compliances of planar micro-motion stages. *Mechanism and Machine Theory*, 43(3):347–363, 2008.

[172] J.W. Ryu and D.G. Gweon. Error analysis of a flexure hinge mechanism induced by machining imperfection. *Precision Engineering*, 21(2):83–89, 1997.

[173] A.E. Guérinot, S.P. Magleby, L.L. Howell, and R.H. Todd. Compliant joint design principles for high compressive load situations. *Journal of Mechanical Design*, 127:774, 2005.

[174] F.E. Scire and E.C. Teague. Piezodriven 50-μm range stage with subnanometer resolution. *Review of Scientific Instruments*, 49(12):1735–1740, 1978.

[175] M. Goldfarb and N. Celanovic. A flexure-based gripper for small-scale manipulation. *Robotica*, 17(2):181–187, 1999.

[176] M.N.M. Zubir, B. Shirinzadeh, and Y. Tian. Development of a novel flexure-based microgripper for high precision micro-object manipulation. *Sensors and Actuators A: Physical*, 150(2):257–266, 2009.

[177] B.J. Yi, G.B. Chung, H.Y. Na, W.K. Kim, and I.H. Suh. Design and experiment of a 3-DOF parallel micromechanism utilizing flexure hinges. *Robotics and Automation, IEEE Transactions on*, 19(4):604–612, 2003.

[178] S.B. Choi, S.S. Han, Y.M. Han, and B.S. Thompson. A magnification device for precision mechanisms featuring piezoactuators and flexure hinges: design and experimental validation. *Mechanism and Machine Theory*, 42(9):1184–1198, 2007.

[179] Y. Tian, B. Shirinzadeh, D. Zhang, and G. Alici. Development and dynamic modelling of a flexure-based Scott-Russell mechanism for nano-manipulation. *Mechanical Systems and Signal Processing*, 23(3):957–978, 2009.

[180] J.W. Ryu, D.G. Gweon, and K.S. Moon. Optimal design of a flexure hinge based< i> xy</i> φ wafer stage. *Precision Engineering*, 21(1):18–28, 1997.

[181] P. Gao, S.M. Swei, and Z. Yuan. A new piezodriven precision micropositioning stage utilizing flexure hinges. *Nanotechnology*, 10:394, 1999.

[182] T.F. Niaritsiry, N. Fazenda, and R. Clavel. Study of the sources of inaccuracy of a 3 dof flexure hinge-based parallel manipulator. In *Robotics and Automation, Proceedings. ICRA. 2004 IEEE International Conference on Robotics and Automation*, volume 4, pages 4091–4096. IEEE, 2004.

[183] D. Kim, D. Kang, J. Shim, I. Song, and D. Gweon. Optimal design of a flexure hinge-based XYZ atomic force microscopy scanner for minimizing Abbe errors. *Review of Scientific Instruments*, 76(7):073706, 2005.

[184] Y. Tian, B. Shirinzadeh, and D. Zhang. A flexure-based five-bar mechanism for micro/nano manipulation. *Sensors and Actuators A: Physical*, 153(1):96–104, 2009.

[185] S.H. Chang and B.C. Du. A precision piezodriven micropositioner mechanism with large travel range. *Review of Scientific Instruments*, 69:1785, 1998.

[186] Y.K. Yong and T.F. Lu. Kinetostatic modeling of 3-rrr compliant micro-motion stages with flexure hinges. *Mechanism and Machine Theory*, 44(6):1156–1175, 2009.

[187] Q. Yao, J. Dong, and P.M. Ferreira. Design, analysis, fabrication and testing of a parallel-kinematic micropositioning XY stage. *International Journal of Machine Tools and Manufacture*, 47(6):946–961, 2007.

[188] X. Tang and I.M. Chen. A large-displacement 3-DOF flexure parallel mechanism with decoupled kinematics structure. In *Intelligent Robots and Systems, 2006 IEEE/RSJ International Conference on*, pages 1668–1673. IEEE, 2006.

[189] X. Tang, I.M. Chen, and Q. Li. Design and nonlinear modeling of a large-displacement XYZ flexure parallel mechanism with decoupled kinematic structure. *Review of Scientific Instruments*, 77:115101, 2006.

[190] H.W. Ma, S.M. Yao, L.Q. Wang, and Z. Zhong. Analysis of the displacement amplification ratio of bridge-type flexure hinge. *Sensors and Actuators A: Physical*, 132(2):730–736, 2006.

[191] J.H. Kim, S.H. Kim, and Y.K. Kwak. Development of a piezoelectric actuator using a three-dimensional bridge-type hinge mechanism. *Review of Scientific Instruments*, 74:2918, 2003.

[192] M. Callegari, A. Cammarata, A. Gabrielli, M. Ruggiu, and R. Sinatra. Analysis and design of a spherical micromechanism with flexure hinges. *Journal of Mechanical Design*, 131:5, 2009.

[193] J.J. Parise, L.L. Howell, and S.P. Magleby. Ortho-planar linear-motion springs. *Mechanism and Machine Theory*, 36(11-12):1281–1299, 2001.

[194] L.L. Howell, S. Thomson, J.A. Briscoe, J.J. Parise, S. Lorenc, J.B. Larsen, C.R. Huffmire, N. Burnside, and T.A. Gomm. Compliant, ortho-planar, linear motion spring, June 30 2003. US Patent App. 10/258,568.

[195] K.W. Chae, W.B. Kim, and Y.H. Jeong. A transparent polymeric flexure-hinge nanopositioner, actuated by a piezoelectric stack actuator. *Nanotechnology*, 22:335501, 2011.

[196] A. Raatz. *Stoffschlüssige Gelenke aus pseudo-elastischen Formgedächtnislegierungen in Pararellrobotern.* Vulkan-Verlag GmbH, 2006.

[197] P.R. Ouyang, R.C. Tjiptoprodjo, W.J. Zhang, and G.S. Yang. Micro-motion devices technology: The state of arts review. *The International Journal of Advanced Manufacturing Technology*, 38(5):463–478, 2008.

[198] P.W. Christensen and A. Klarbring. *An introduction to structural optimization*, volume 153. Springer, 2008.

[199] A. Schumacher. *Optimierung mechanischer Strukturen: Grundlagen und industrielle Anwendungen*. Springer, 2004.

[200] G.A. Holzapfel. *Nonlinear solid mechanics: a continuum approach for engineering*. John Wiley & Sons Inc, 2000.

[201] T. Belytschko, W.K. Liu, and B. Moran. *Nonlinear finite elements for continua and structures*. Wiley New York, 2000.

[202] R. Lammering. *Strukturmechanik – Vorlesungsskript*. Helmut-Schmidt-University / University of the Federal Armed Forces Hamburg, 2012.

[203] T. Berg. Design of movement restricted compliant mechanisms. Technical report, Helmut-Schmidt University / University of the Federal Armed Forces Hamburg, 2012. Advisor: F. Dirksen.

[204] K. Svanberg. The method of moving asymptotes (MMA) with some extensions. *Optimization of Large Structural Systems*, pages 555–566, 1993.

[205] K. Svanberg. *GCMMA code and documentation*, 16. November 2009. Provided electronically.

[206] M.P. Bendsøe and O. Sigmund. Material interpolation schemes in topology optimization. *Archive of Applied Mechanics (Ingenieur Archiv)*, 69(9):635–654, 1999.

[207] M. Stolpe and K. Svanberg. An alternative interpolation scheme for minimum compliance topology optimization. *Structural and Multidisciplinary Optimization*, 22(2):116–124, 2001.

[208] M.B. Fuchs, S. Jiny, and N. Peleg. The SRV constraint for 0/1 topological design. *Structural and Multidisciplinary Optimization*, 30(4):320–326, 2005.

[209] O. Sigmund. Morphology-based black and white filters for topology optimization. *Structural and Multidisciplinary Optimization*, 33(4):401–424, 2007.

[210] W.C. Rheinboldt. *Methods for solving systems of nonlinear equations*. SIAM, 1998.

[211] K.K. Choi and N.H. Kim. *Structural sensitivity analysis and optimization 1: linear systems*. Springer, 2004.

[212] K.K. Choi and N.H. Kim. *Structural Sensitivity Analysis and Optimization 2: Nonlinear Systems and Applications*. New York, NY: Springer Science+ Business Media, Inc., 2005.

[213] Michael Yu Wang. Mechanical and geometric advantages in compliant mechanism optimization. *Frontiers of Mechanical Engineering in China*, 4(3):229–241, 2009.

[214] Gang-Won Jang, Myung-Jin Kim, and Yoon Young Kim. Design optimization of compliant mechanisms consisting of standardized elements. *Journal of Mechanical Design*, 131:121006, 2009.

[215] T. Buhl, C.B.W. Pedersen, and O. Sigmund. Stiffness design of geometrically nonlinear structures using topology optimization. *Structural and Multidisciplinary Optimization*, 19(2):93–104, 2000.

[216] Zhen Luo, Liping Chen, Jingzhou Yang, Y Zhang, and K Abdel-Malek. Compliant mechanism design using multi-objective topology optimization scheme of continuum structures. *Structural and Multidisciplinary Optimization*, 30(2):142–154, 2005.

[217] S. Rahmatalla and C.C. Swan. Sparse monolithic compliant mechanisms using continuum structural topology optimization. *International Journal for Numerical Methods in Engineering*, 62(12):1579–1605, 2005.

[218] A.E.H. Love. *A treatise on the mathematical theory of elasticity*. University Press, 1920.

[219] C.M. Wang, J.N. Reddy, and K.H. Lee. *Shear deformable beams and plates*. Elsevier Amsterdam, 2000.

[220] H.D. Conway and W.E. Nickola. Anticlastic action of flat sheets in bending. *Experimental Mechanics*, 5(4):115–119, 1965.

[221] D.F. Pilkey. *Peterson's stress concentration factors*. Wiley, 2008.

[222] E. Haibach. *Betriebsfestigkeit: Verfahren und Daten zur Bauteilberechnung*. Springer New York, 2006.

[223] B. Tabarrok and B.H. Karnopp. Analysis of the oscillations of the Timoshenko beam. *Zeitschrift für Angewandte Mathematik und Physik*, 18(4):580–587, 1967.

[224] S.S. Rao. *Vibration of continuous systems*. John Wiley and Sons Inc, 2007.

[225] J. Schijve. *Fatigue of structures and materials*. Springer Netherlands, 2001.

[226] D. Radaj and M. Vormwald. *Ermüdungsfestigkeit: Grundlagen für Ingenieure*. Springer Verlag, 2007.

[227] J.G. Kaufman. *Properties of aluminum alloys: fatigue data and the effects of temperature, product form, and processing*. ASM Intl, 2008.

[228] H. Gerber. Bestimmung der zulässigen Spannungen in Eisenkonstruktionen. *Zeitschrift des Bayerischen Architeckten und Ingenieur-Vereins*, 6:101–110, 1874.

[229] J. Goodman. *Mechanics applied to engineering*. Longman, Green and Co., London, 1899.

[230] C.R. Soderberg. Factor of safety and working stress. *Transactions of ASME*, 52:13–28, 1939.

[231] S. Suresh. *Fatigue of materials*. Cambridge University Press, 1998.

[232] F. Dirksen and R. Lammering. On mechanical properties of planar flexure hinges of compliant mechanisms. *Mechanical Sciences*, 2(1):109–117, 2011. Special Issue – Future directions in compliant mechanisms.

[233] L. Issler, H. Ruoß, and P. Häfele. *Festigkeitslehre - Grundlagen*. Springer Verlag, 2nd edition, 2005.

[234] Richtlinie, VDI. 2226. *Empfehlung für die Festigkeitsberechnung metallischer Bauteile, VDI-Verlag GmbH Düsseldorf*, 1965.

[235] J. Paolo Davim, editor. *Surface Integrity in Machining*. Springer, 1st edition edition, 2010.

[236] Service engineering bulletin sb021 - surface finish. www.engineaustralia.com.au/default/service_bulletin, (accessed on Nov 15, 2011).

[237] J.E.O. Burger. Experimentelle Untersuchung von elastischen Festkörpergelenken mittels optischem Korrelationsmesssystem Q400. Technical report, Helmut-Schmidt-University/ University of the Federal Armed Forces, 2010. Advisor: F. Dirksen.

[238] S. Baum. Experimentelle Untersuchung von elastischen Festkörpergelenken mittels der Zugprüfmaschine TIRA 2810. Technical report, Helmut-Schmidt-University/ University of the Federal Armed Forces, 2010. Advisor: F. Dirksen.

[239] J. Burock. Experimentelle Untersuchung von elastischen Festkörpergelenken. Technical report, Helmut-Schmidt-University/ University of the Federal Armed Forces, 2011. Advisor: F. Dirksen.

[240] M. Gottwald. Experimental investigations on thin flexure hinges. Technical report, Helmut-Schmidt-University/ University of the Federal Armed Forces, 2012. Advisor: F. Dirksen.

[241] C. Lanczos. An iteration method for the solution of the eigenvalue problem of linear differential and integral operators. *Journal of Research of the National Bureau of Standards*, 45(4), 1950.

[242] Dassault Systèmes Simulia Corp. *ABAQUS 6.8.1 Documentation*, 2012.

List of Symbols and Abbreviations

Roman letters

A	Area of cross section	m^2
A_*	Area of cross section with shear correction	m^2
A_N	Material constant (Neuber)	m
A_P	Material constant (Peterson)	m
b	Depth of flexure hinge in Chap. 4	m
b_e^k	Substitute variable for OC method	-
$\boldsymbol{\mathcal{B}}_0$	Matrix containing derivatives (reference configuration)	-
$\boldsymbol{B}_0$	Matrix containing derivatives with deformation gradient	-
$[\boldsymbol{C}]$	Reduced elasticity matrix	$\mathrm{N\,m^{-2}}$
$\mathbb{C}$	Fourth-order elasticity tensor	$\mathrm{N\,m^{-2}}$
$\mathbf{C}$	Compliance matrix	$\mathrm{m\,N^{-1}}$
C	Superscript denoting circular flexure hinge	-
c_ψ	Bending stiffness of flexure hinge in x-z-plane	$\mathrm{N\,rad^{-1}}$
$\boldsymbol{E}$	Green strain tensor	-
$\boldsymbol{e}$	Almansi strain tensor	-
E	Young's modulus	$\mathrm{N\,m^{-2}}$

e	Error	-
E_K	Kinetic energy	$\mathrm{kg\,m^2\,s^{-2}}$
$\boldsymbol{E}_{lin}$	Linearized Green strain tensor	-
$\boldsymbol{e}_{lin}$	Linearized Almansi strain tensor	-
E_P	Potential energy	$\mathrm{kg\,m^2\,s^{-2}}$
$\boldsymbol{f}$	Load vector	N, N m
$\boldsymbol{F}$	Deformation gradient	-
f	Natural frequency of flexure hinge	Hz
f_0, g_0	Objective function	-
f^{dm}	Natural frequency of discrete model of flexure hinge	Hz
$\boldsymbol{f}^{ext}$	External load vector	N
f_i, g_i	Constraints ($i \geq 1$)	-
$\boldsymbol{f}^{int}$	Internal load vector	N
$\boldsymbol{f}^{int}_{geo}$	Internal load vector for geometric tangent stiffness	N
$\boldsymbol{f}^{int}_{mat}$	Internal load vector for material tangent stiffness	N
F_x, F_z	Forces in x- and z-direction	N
G	Shear modulus	$\mathrm{N\,m^{-2}}$
h	Height of flexure hinge	m
h_*, h_{**}	Abbreviatory heights	m
$\boldsymbol{I}$	Identity matrix	-
I_y	Second moment of area	$\mathrm{m^4}$
$\boldsymbol{J}$	Jacobian matrix	-
J	Jacobian	-

$\boldsymbol{K}$	Global stiffness matrix	$\mathrm{N\,m^{-1}}$, $\mathrm{N\,rad^{-1}}$
$\boldsymbol{K}^e_{lin}$	Element stiffness matrix (linear FEA)	$\mathrm{N\,m^{-1}}$
$\boldsymbol{K}^e_{nonlin}$	Element stiffness matrix (nonlinear FEA)	$\mathrm{N\,m^{-1}}$
$\boldsymbol{K_D}$	Diagonalized stiffness matrix	$\mathrm{N\,m^{-1}}$, $\mathrm{N\,rad^{-1}}$
K_f	Fatigue strength reduction factor	-
$\boldsymbol{K}_T$	Tangent stiffness matrix	$\mathrm{N\,m^{-2}}$
K_{tb}, K_{tt}	Stress concentration factors	-
k_x	Stiffness of flexure hinge in x-direction	$\mathrm{N\,m^{-1}}$
k_z	Stiffness of flexure hinge in z-direction	$\mathrm{N\,m^{-1}}$
$\mathcal{L}$	Lagrangian function	-
l	Length of flexure hinge	m
M	Bending moment	N m
m	Mass	kg
M_y	Bending moment in x-z-plane	N m
$\boldsymbol{N}$	Matrix containing shape functions	-
$\boldsymbol{n}$	Outward normal vector	-
N	Number of finite elements	-
N_i	Shape functions	-
$\boldsymbol{N}_A^{(i)}$, $\boldsymbol{N}_B^{(i)}$	Normal vectors of points A and B at i-th step	$\mathrm{m\,s^{-1}}$
N_D	Life cycles until fatigue failure	-
N_{elx}	Number of finite elements in x-direction	-
N_{ely}	Number of finite elements in y-direction	-
n_{GCMMA}	Interval length, i.e. number of iterations GCMMA	-

$n_{nonlinear}$	Number of iterations denoting sole nonlinear FEA	-
n_{OC}	Interval length, i.e. number of iterations OC	-
$\boldsymbol{P}$	First Piola-Kirchhoff stress tensor	$\mathrm{N\,m^{-2}}$
$\mathbb{P}$	Optimization problem	-
P	Superscript denoting parabolic flexure hinge	-
$\boldsymbol{P}^{01,(i)}$	Center of rotation for the i-th step	m
$\boldsymbol{P}_{eff}^{01}$	Overall center of rotation	m
P_1, P_2, P_3	Geometric points	-
P_A, P_B	Geometric points for center of rotation	m
q	Notch sensitivity	-
$\boldsymbol{R}$	Residual vector	N
R	Ratio of extremal stresses in Sect. 4.3.2.1	-
R	Superscript denoting rectangular flexure hinge	-
r	Radius of circular flexure hinge	m
R_a	Average surface roughness	m
R_t	Surface roughness	m
$\boldsymbol{S}$	Second Piola-Kirchhoff stress tensor	$\mathrm{N\,m^{-2}}$
$S_{0.2}$	Yield strength	$\mathrm{N\,m^{-2}}$
$\boldsymbol{S}_A^{(i)}$, $\boldsymbol{S}_B^{(i)}$	Motion paths of points A and B at i-th step	$\mathrm{m\,s^{-1}}$
S_a	Stress amplitude	$\mathrm{N\,m^{-2}}$
S_{ab}	Amplitude bending strength	$\mathrm{N\,m^{-2}}$
S_{at}	Amplitude tensile strength	$\mathrm{N\,m^{-2}}$
S_f	Fatigue stress limit	$\mathrm{N\,m^{-2}}$

S_{fb}	Bending fatigue strength	$\mathrm{N\,m^{-2}}$
S_{ft}	Tensile fatigue strength	$\mathrm{N\,m^{-2}}$
S_m	Mean stress	$\mathrm{N\,m^{-2}}$
S_U	Ultimate tensile strength of a material	$\mathrm{N\,m^{-2}}$
S_y	First moment of area	$\mathrm{m^3}$
$\boldsymbol{T}$	Transformation matrix	-
$\boldsymbol{t}$	Stress vector	$\mathrm{N\,m^{-2}}$
T	Computation time	s
t	Thickness of flexure hinge	m
$\boldsymbol{T}_A^{(i)}$, $\boldsymbol{T}_B^{(i)}$	Tangent vectors of points A and B at i-th step	$\mathrm{m\,s^{-1}}$
t_s	Minimal thickness	m
t^*	Height of notch	m
$\boldsymbol{u}$, $\boldsymbol{v}$	Displacement vectors	m, rad
u, v, w	Displacements in x-, y- and z-direction	m
$\delta\boldsymbol{v}$	Test function (vector-valued)	m
V	Overall volume fraction	-
w_i, w_j	Gauss weights	-
$W(x)$	Test function	m
$\boldsymbol{X}$	Material coordinates	m
$\boldsymbol{x}$	Spatial coordinates	m
x, y, z	Cartesian coordinates	m
x_M, z_M	Center coordinates of circular flexure hinge	m
y_e	Intervening variable for OC method	-

Greek letters

α, β, θ	Dimensions and rotation angle of unit cell in Fig. 2.5(c)	-
α	Positive scalar-valued variable for convex approximations	-
α	Material factor in Sect. 4.3.2.2	-
α_{IJ}	Scalar value in geometric tangent stiffness matrix	$\mathrm{N\,m^{-2}}$
α_s	Shear correction factor	-
Γ	Boundary of design domain	-
γ	Surface roughness reduction factor	-
$\boldsymbol{\partial}$	Matrix containing derivative operators	-
ϵ	Small strain tensor	-
κ	Reference coefficient for superposed bending	-
λ	Lagrange multiplier	-
λ, μ	Lamé constants	$\mathrm{N\,m^{-2}}$
λ_1, λ_2, λ_3	Eigenvalues	-
∇	Derivative operator	-
ν	Poisson's ratio	-
ξ, η	Cartesian coordinates (master element)	
$\Psi(x)$	Test function	-
η	Numerical damping term for OC method	-
ρ	Design variable	-
$\underline{\rho}$	Minimum value of design variable	-
$\overline{\rho}$	Maximum value of design variable	-
ρ_e	Design value of element e	-

ρ_{spec}	Specified value of design variable	-
σ	Local stress	$\mathrm{N\,m^{-2}}$
σ_a	Stress amplitude	$\mathrm{N\,m^{-2}}$
$\sigma_{a,e}$	Equivalent stress amplitude	$\mathrm{N\,m^{-2}}$
$\boldsymbol{\sigma}$	Cauchy stress tensor	$\mathrm{N\,m^{-2}}$
σ_m	Mean stress	$\mathrm{N\,m^{-2}}$
σ_{nom}	Nominal stress	$\mathrm{N\,m^{-2}}$
σ_{peak}	Peak stress	$\mathrm{N\,m^{-2}}$
σ_e	Equivalent stress	$\mathrm{N\,m^{-2}}$
σ_x	Normal stresses in x-direction	$\mathrm{N\,m^{-2}}$
τ	Shear stress	$\mathrm{N\,m^{-2}}$
τ_{xz}	Shear stresses on x-surface in z-direction	$\mathrm{N\,m^{-2}}$
$\boldsymbol{\phi}$	Motion	m
ϕ	Dual function	-
Ω	Design domain	-
Ω_0	Design domain (reference configuration)	-
ω_1	Circular frequency	$\mathrm{rad\,s^{-1}}$

Abbreviations

ACO	Ant colony optimization
ana	Analytical data
ASME	American Society of Mechanical Engineers
BC	Boundary condition
BESO	Bi-directional evolutionary structural optimization

CA	Cellular automata
CM	Compliant mechanisms
CONLIN	Convex linearization
CPS8R	Eight-noded biquadratic plane-stress with reduced intergration
CRC	Chemical Rubber Company
DAAD	German Academic Exchange Service (Deutscher Akademischer Austauschdienst)
EDM	Electrical discharge machining
ESO	Evolutionary structural optimization
exp	Experimental data
FEA	Finite element analysis
FH	Flexure hinge
GA	Genetic algorithm
GA	Geometrical amplification
GCMMA	Globally convergent method of moving asymptotes
geo	Geometric
HSU	Helmut-Schmidt-University/ University of the Federal Armed Forces
IEEE	Institute of Electrical and Electronics Engineers
inf	Infimum
ISSMO	International Society for Structural and Multidisciplinary Optimization
KIT	Karlsruhe Institute of Technology
LHS	Left-hand side
lin	Linear computation

LS	Level set
MA	Mechanical amplification
mat	Material
max	Maximum
MBB	Messerschmitt-Bölkow-Blohm
MEMS	Micro-electrical-mechanical-systems
MESO	Modified evolutionary structural optimization
min	Minimum
MMA	Method of moving asymptotes
MPE	Mutual potential energy
NASA	National Aeronautics and Space Administration
NATO	North Atlantic Treaty Organization
nonlin	Nonlinear computation
NSPA	NATO Support Agency
num	Numerical data
OC	Optimality criteria
PAMM	Proceedings of Applied Mathematics and Mechanics
PC	Personal computer
PRBM	Pseudo rigid body model
PSO	Particle swarm optimization
Q4	Quad 4: Rectangular, bilinear four-node finite element
RHS	Right-hand side
RRR	Three revolute, or hinged, joints
SA	Simulated annealing

SE	Strain energy
SLP	Sequential linear programming
SPIE	International Society for Optics and Photonics
SQP	Sequential quadratic programming
USAF	United States Air Force
VDI	Association of German Engineers (Verein Deutscher Ingenieure)
WS	Workstation

List of Figures

List of Tables

Index

A Further details and results

A.1 Voigt notation

In FE formulations, symmetric second-order tensors are often written as column matrices which is called the Voigt notation. The Voigt rule for *kinetic* tensors such as stresses is in 2D

$$\boldsymbol{S} = \begin{bmatrix} S_{11} & S_{12} \\ S_{21} & S_{22} \end{bmatrix} \Longrightarrow \{\boldsymbol{S}\} = \begin{Bmatrix} S_{11} \\ S_{22} \\ S_{12} \end{Bmatrix} = \begin{Bmatrix} S_1 \\ S_2 \\ S_3 \end{Bmatrix}. \tag{A.1}$$

The Voigt rule for *kinematic* tensors such as strains is in 2D

$$\boldsymbol{E} = \begin{bmatrix} E_{11} & E_{12} \\ E_{21} & E_{22} \end{bmatrix} \Longrightarrow \{\boldsymbol{E}\} = \begin{Bmatrix} E_{11} \\ E_{22} \\ 2E_{12} \end{Bmatrix} = \begin{Bmatrix} E_1 \\ E_2 \\ E_3 \end{Bmatrix}. \tag{A.2}$$

The Voigt notation for *higher-order* tensors such as the fourth-order material tensor using a linear elastic constitutive law in plane strain becomes a matrix as

$$[\boldsymbol{C}] = \begin{bmatrix} C_{11} & C_{12} & C_{13} \\ C_{21} & C_{22} & C_{23} \\ C_{31} & C_{32} & C_{33} \end{bmatrix} = \begin{bmatrix} C_{1111} & C_{1122} & C_{1112} \\ C_{2211} & C_{2222} & C_{2212} \\ C_{1211} & C_{1222} & C_{1212} \end{bmatrix}. \tag{A.3}$$

A.2 Sensitivity analysis

The objective function g_0 is expressed as a function of the displacements $\boldsymbol{u}(\boldsymbol{\rho})$ and the design variables $\boldsymbol{\rho}$ itself

$$g_0(\boldsymbol{\rho}) = f\left(\boldsymbol{u}(\boldsymbol{\rho}), \boldsymbol{\rho}\right). \tag{A.4}$$

The sensitivity expression is obtained by differentiating with respect to each component ρ_i of $\boldsymbol{\rho}$

$$\frac{dg_0}{d\rho_i} = \frac{\partial f}{\partial \boldsymbol{u}} \frac{d\boldsymbol{u}}{d\rho_i} + \frac{\partial f}{\partial \rho_i}, \tag{A.5}$$

where $\frac{\partial f}{\partial \boldsymbol{u}}$ and $\frac{\partial f}{\partial \rho_i}$ are explicit derivatives, and $\frac{d\boldsymbol{u}}{d\rho_i}$ is an implicit derivative which can be calculated by direct differentiation or by adjoint method.

A.2.1 Direct differentiation sensitivities

The implicit derivative $\frac{d\boldsymbol{u}}{d\rho_i}$ is evaluated using the residual vector of the (nonlinear) FEA $\boldsymbol{R}$ given in Eq. (3.98)

$$\boldsymbol{R}\left(\boldsymbol{u}(\boldsymbol{\rho}), \boldsymbol{\rho}\right) = \boldsymbol{0}, \tag{A.6}$$

that vanishes after each FEA. Taking the derivative with respect to the design variables yields

$$\frac{d\boldsymbol{R}}{d\rho_i} = \frac{\partial \boldsymbol{R}}{\partial \boldsymbol{u}} \frac{d\boldsymbol{u}}{d\rho_i} + \frac{\partial \boldsymbol{R}}{\partial \rho_i}, \tag{A.7}$$

which is zero since $\boldsymbol{R}\left(\boldsymbol{u}(\boldsymbol{\rho}), \boldsymbol{\rho}\right) = \boldsymbol{0} = const.$ This leads to

$$\frac{d\boldsymbol{u}}{d\rho_i} = -\left(\frac{\partial \boldsymbol{R}}{\partial \boldsymbol{u}}\right)^{-1} \frac{\partial \boldsymbol{R}}{\partial \rho_i}, \tag{A.8}$$

where the inverse term is calculated using the decomposed tangent stiffness matrix given by Eq. (3.100). By plugging Eq. (A.8) into Eq. (A.5) the desired sensitivities can be computed.

Remark. The direct differentiation method can be computationally cheap since it uses the previously calculated tangent stiffness matrix. However, in this work it was tested against the adjoint method yielding a slower performance.

A.2.2 Adjoint sensitivities

The sensitivities are obtained using the Lagrange multiplier method, which eliminates the implicit derivative $\frac{d\boldsymbol{u}}{d\rho_i}$ by introducing an augmented function

$$\hat{g}_0(\boldsymbol{\rho}) = f\left(\boldsymbol{u}(\boldsymbol{\rho}), \boldsymbol{\rho}\right) - \boldsymbol{\lambda}(\boldsymbol{\rho})\boldsymbol{R}\left(\boldsymbol{u}(\boldsymbol{\rho}), \boldsymbol{\rho}\right), \tag{A.9}$$

where $\boldsymbol{\lambda}$ is the Lagrange multiplier. Since the added constraint term $\boldsymbol{R}\left(\boldsymbol{u}(\boldsymbol{\rho}), \boldsymbol{\rho}\right)$ is zero, the objective function remains equal, i.e. $g_0 = \hat{g}_0$. Differentiating the augmented function with respect to the individual design parameter ρ_i result in

$$\frac{d\hat{g}_0}{d\rho_i} = \frac{\partial f}{\partial \boldsymbol{u}}\frac{d\boldsymbol{u}}{d\rho_i} + \frac{\partial f}{\partial \rho_i} - \frac{d\boldsymbol{\lambda}}{d\rho_i}\boldsymbol{R} - \boldsymbol{\lambda}\left(\frac{\partial \boldsymbol{R}}{\partial \boldsymbol{u}}\frac{d\boldsymbol{u}}{d\rho_i} + \frac{\partial \boldsymbol{R}}{\partial \rho_i}\right). \tag{A.10}$$

The differentiated constrained expression is equal to the unconstrained expression, i.e. $\frac{dc}{d\rho_i} = \frac{d\hat{c}}{d\rho_i}$, since $\boldsymbol{R} = \boldsymbol{0}$ and $\frac{\partial \boldsymbol{R}}{\partial \boldsymbol{u}}\frac{d\boldsymbol{u}}{d\rho_i} + \frac{\partial \boldsymbol{R}}{\partial \rho_i} = \boldsymbol{0}$. Rewriting Eq. (A.10) yields

$$\frac{d\hat{g}_0}{d\rho_i} = \underbrace{\frac{\partial f}{\partial \rho_i} - \boldsymbol{\lambda}\frac{\partial \boldsymbol{R}}{\partial \rho_i}}_{\text{explicit term}} + \underbrace{\frac{d\boldsymbol{u}}{d\rho_i}\left(\frac{\partial f}{\partial \boldsymbol{u}} - \left(\frac{\partial \boldsymbol{R}}{\partial \boldsymbol{u}}\right)^T \boldsymbol{\lambda}\right)}_{\text{implicit term}} + \underbrace{\frac{d\boldsymbol{\lambda}}{d\rho_i}\boldsymbol{R}}_{=\boldsymbol{0}} \tag{A.11}$$

The implicit term is eliminated by choosing the Lagrange multiplier λ such that

$$\left(\frac{\partial \boldsymbol{R}}{\partial \boldsymbol{u}}\right)^T \boldsymbol{\lambda} = \frac{\partial f}{\partial \boldsymbol{u}}, \tag{A.12}$$

where the decomposed tangent stiffness matrix is used to solve for the adjoint response $\boldsymbol{\lambda}$ in an efficient manner. Finally, the sensitivity expression reduces to

$$\frac{d\hat{g}_0}{d\rho_i} = \frac{\partial f}{\partial \rho_i} - \boldsymbol{\lambda}\frac{\partial \boldsymbol{R}}{\partial \rho_i}. \tag{A.13}$$

Remark. The adjoint method was tested to be very efficient for a single cost function and a large number of design variables. If there exist several cost functions resulting in several adjoint problems, direct differentiation is preferable.

A.3 Specified output motion vector

The desired output motion is described by a specified output motion vector $\boldsymbol{u}_{spec}$ as illustrated in Fig. A.1.

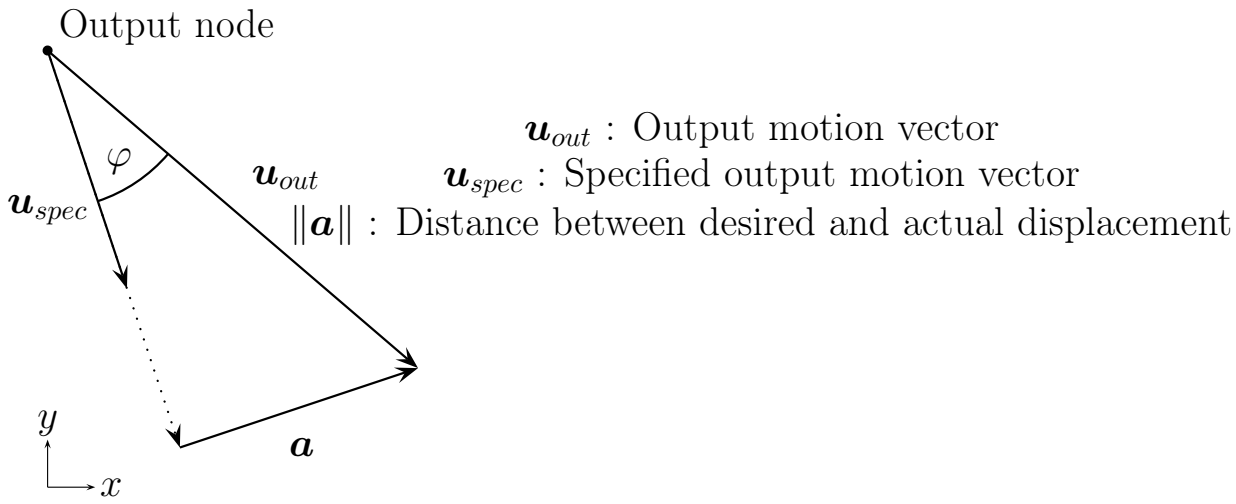

Figure A.1: Distance between desired and actual displacement vectors

This yields the following optimization problem

$$(\mathbb{P})_{\text{GCMMA}} = \begin{cases} \max\limits_{\rho} & g_0(\boldsymbol{\rho}) = \dfrac{\|\boldsymbol{u}_{out}\|}{\|\boldsymbol{u}_{out} - \alpha \boldsymbol{u}_{spec}\|} \\ \text{s.t.} & g_1(\boldsymbol{\rho}) = \sum_{e=1}^{N} (\rho_e - V) \leq 0 \\ & \boldsymbol{K}(\boldsymbol{\rho})\boldsymbol{u}(\boldsymbol{\rho}) = \boldsymbol{F} \\ & \{\boldsymbol{\rho} \in \mathbb{R}^N : \underline{\rho} \leq \rho_e \leq \overline{\rho}, e = 1, \ldots, N\}, \end{cases} \tag{A.14}$$

Considering coordinate-wise displacement expressions yields

$$u_{out,1} = \boldsymbol{v}(\boldsymbol{\rho})^T \boldsymbol{K}(\boldsymbol{\rho})\boldsymbol{u}(\boldsymbol{\rho}), \tag{A.15}$$

$$u_{out,2} = \boldsymbol{v}(\boldsymbol{\rho})_{\perp}^T \boldsymbol{K}(\boldsymbol{\rho})\boldsymbol{u}(\boldsymbol{\rho}). \tag{A.16}$$

Thus, the denominator becomes

$$\begin{aligned}
\|\boldsymbol{u}_{out} - \alpha \boldsymbol{u}_{spec}\| &= \left\| \begin{pmatrix} \boldsymbol{v}^{\boldsymbol{T}} \boldsymbol{K}\ \boldsymbol{u} \\ \boldsymbol{v}_{\perp}^{\boldsymbol{T}} \boldsymbol{K}\ \boldsymbol{u} \end{pmatrix} - \left(\frac{\boldsymbol{v}^{\boldsymbol{T}} \boldsymbol{K}\ \boldsymbol{u} \cdot u_{spec,1} + \boldsymbol{v}_{\perp}^{\boldsymbol{T}} \boldsymbol{K}\ \boldsymbol{u} \cdot u_{spec,2}}{\|\boldsymbol{u}_{spec}\|^2} \right) \boldsymbol{u}_{spec} \right\| \\
&= \left\| \begin{pmatrix} \boldsymbol{v}^{\boldsymbol{T}} \boldsymbol{K}\ \boldsymbol{u} \\ \boldsymbol{v}_{\perp}^{\boldsymbol{T}} \boldsymbol{K}\ \boldsymbol{u} \end{pmatrix} - \frac{1}{\|\boldsymbol{u}_{spec}\|^2} \begin{pmatrix} \boldsymbol{v}^{\boldsymbol{T}} \boldsymbol{K}\ \boldsymbol{u} \cdot u_{spec,1}^2 + \boldsymbol{v}_{\perp}^{\boldsymbol{T}} \boldsymbol{K}\ \boldsymbol{u} \cdot u_{spec,1} u_{spec,2} \\ \boldsymbol{v}^{\boldsymbol{T}} \boldsymbol{K}\ \boldsymbol{u} \cdot u_{spec,1} u_{spec,2} + \boldsymbol{v}_{\perp}^{\boldsymbol{T}} \boldsymbol{K}\ \boldsymbol{u} \cdot u_{spec,2}^2 \end{pmatrix} \right\| \\
&= \left\| \begin{pmatrix} u_{out,1} - \dfrac{u_{out,1} u_{spec,1}^2 + u_{out,2} u_{spec,1} u_{spec,2}}{\|\boldsymbol{u}_{spec}\|^2} \\ u_{out,2} - \dfrac{u_{out,1} u_{spec,1} u_{spec,2} + u_{out,2} u_{spec,2}^2}{\|\boldsymbol{u}_{spec}\|^2} \end{pmatrix} \right\|
\end{aligned}$$

$$\|\boldsymbol{u}_{out} - \alpha \boldsymbol{u}_{spec}\| = \left(\left(u_{out,1} - \frac{u_{out,1} u_{spec,1}^2 + u_{out,2} u_{spec,1} u_{spec,2}}{\|\boldsymbol{u}_{spec}\|^2} \right)^2 + \right. \tag{A.17}$$

$$\left. \left(u_{out,2} - \frac{u_{out,1} u_{spec,1} u_{spec,2} + u_{out,2} u_{spec,2}^2}{\|\boldsymbol{u}_{spec}\|^2} \right)^2 \right)^{\frac{1}{2}}. \tag{A.18}$$

Finally, the cost function can be computed as

$$\begin{aligned}
g_0(\boldsymbol{x}) = &- \left(u_{out,1}^2 + u_{out,2}^2 \right)^{\frac{1}{2}} \\
&\cdot \left(\left(u_{out,1} - \frac{u_{out,1} u_{spec,1}^2 + u_{out,2} u_{spec,1} u_{spec,2}}{\|\boldsymbol{u}_{spec}\|^2} \right)^2 + \right. \\
&\left. \left(u_{out,2} - \frac{u_{out,1} u_{spec,1} u_{spec,2} + u_{out,2} u_{spec,2}^2}{\|\boldsymbol{u}_{spec}\|^2} \right)^2 \right)^{-\frac{1}{2}}.
\end{aligned} \tag{A.19}$$

The volume constraint can be computed as

$$g_1(\boldsymbol{\rho}) = \sum_{e=1}^{N} \left(\rho_e - V \right). \tag{A.20}$$

The required sensitivities are:

$$\begin{aligned}
\frac{\partial g_0}{\partial \rho_i} &= \frac{\frac{\partial \|\boldsymbol{u}_{out}\|}{\partial \rho_i}\|\boldsymbol{u}_{out}-\alpha\boldsymbol{u}_{spec}\| - \|\boldsymbol{u}_{out}\|\frac{\partial\|\boldsymbol{u}_{out}-\alpha\boldsymbol{u}_{spec}\|}{\partial\rho_i}}{\|\boldsymbol{u}_{out}-\alpha\boldsymbol{u}_{spec}\|^2} \\
&= \frac{1}{\|\boldsymbol{u}_{out}-\alpha\boldsymbol{u}_{spec}\|}\left(\frac{1}{2}\left(u_{out,1}^2+u_{out,2}^2\right)^{-\frac{1}{2}}\left(-2u_{out,1}p\rho_i^{p-1}\boldsymbol{v_i^T}\boldsymbol{K_i}\ \boldsymbol{u}_i - 2u_{out,2}p\rho_i^{p-1}\boldsymbol{v_{\perp i}^T}\boldsymbol{K_i}\ \boldsymbol{u}_i\right)\right) \\
&- \frac{\|\boldsymbol{u}_{out}\|}{\|\boldsymbol{u}_{out}-\alpha\boldsymbol{u}_{spec}\|^2}\frac{1}{2}\left(\left(u_{out,1}-\frac{u_{out,1}u_{spec,1}^2+u_{out,2}u_{spec,1}u_{spec,2}}{\|\boldsymbol{u}_{spec}\|^2}\right)^2+\right. \\
&\left.\left(u_{out,2}-\frac{u_{out,1}u_{spec,1}u_{spec,2}+u_{out,2}u_{spec,2}^2}{\|\boldsymbol{u}_{spec}\|^2}\right)^2\right)^{-\frac{1}{2}} \\
&\cdot\left[2\left(u_{out,1}\left(1-\frac{u_{spec,1}^2}{\|\boldsymbol{u}_{spec}\|^2}\right)-u_{out,2}\frac{u_{spec,1}u_{spec,2}}{\|\boldsymbol{u}_{spec}\|^2}\right)\cdot\left(\left(1-\frac{u_{spec,1}^2}{\|\boldsymbol{u}_{spec}\|^2}\right)(-p)\rho_i^{p-1}\boldsymbol{v_i^T}\boldsymbol{K_i}\ \boldsymbol{u}_i\right.\right. \\
&\left.-\frac{u_{spec,1}u_{spec,2}}{\|\boldsymbol{u}_{spec}\|^2}(-p)\rho_i^{p-1}\boldsymbol{v_{\perp i}^T}\boldsymbol{K_i}\ \boldsymbol{u}_i\right)+2\left(u_{out,2}\left(1-\frac{u_{spec,2}^2}{\|\boldsymbol{u}_{spec}\|^2}\right)-u_{out,1}\frac{u_{spec,1}u_{spec,2}}{\|\boldsymbol{u}_{spec}\|^2}\right) \\
&\left.\cdot\left(\left(1-\frac{u_{spec,2}^2}{\|\boldsymbol{u}_{spec}\|^2}\right)(-p)\rho_i^{p-1}\boldsymbol{v_{\perp i}^T}\boldsymbol{K_i}\ \boldsymbol{u}_i-\frac{u_{spec,1}u_{spec,2}}{\|\boldsymbol{u}_{spec}\|^2}(-p)\rho_i^{p-1}\boldsymbol{v_i^T}\boldsymbol{K_i}\ \boldsymbol{u}_i\right)\right]
\end{aligned} \tag{A.21}$$

$$\begin{aligned}
\frac{\partial g_0}{\partial \rho_i} &= \frac{p\rho_i^{p-1}\left(-u_{out,1}\boldsymbol{v_i^T}\boldsymbol{K_i}\ \boldsymbol{u}_i - u_{out,2}\boldsymbol{v_{\perp i}^T}\boldsymbol{K_i}\ \boldsymbol{u}_i\right)}{\|\boldsymbol{u}_{out}\|\|\boldsymbol{u}_{out}-\alpha\boldsymbol{u}_{spec}\|} - \frac{\|\boldsymbol{u}_{out}\|}{\|\boldsymbol{u}_{out}-\alpha\boldsymbol{u}_{spec}\|^3} \\
&\cdot\left[\left(\boldsymbol{u}_{out}-\alpha\boldsymbol{u}_{spec}\right)_1\cdot\left(p\rho_i^{p-1}\left(\frac{u_{spec,1}u_{spec,2}}{\|\boldsymbol{u}_{spec}\|^2}\boldsymbol{v_{\perp i}^T}\boldsymbol{K_i}\boldsymbol{u_i}-\left(1-\frac{u_{spec,1}^2}{\|\boldsymbol{u}_{spec}\|^2}\right)\boldsymbol{v_i^T}\boldsymbol{K_i}\ \boldsymbol{u_i}\right)\right)\right. \\
&\left.+\left(\boldsymbol{u}_{out}-\alpha\boldsymbol{u}_{spec}\right)_2\cdot\left(p\rho_{\mathrm{i}}^{p-1}\left(\frac{u_{spec,1}u_{spec,2}}{\|\boldsymbol{u}_{spec}\|^2}\boldsymbol{v_i^T}\boldsymbol{K_i}\ \boldsymbol{u}_i-\left(1-\frac{u_{spec,1}^2}{\|\boldsymbol{u}_{spec}\|^2}\right)\boldsymbol{v_{\perp i}^T}\boldsymbol{K_i}\ \boldsymbol{u}_i\right)\right)\right]
\end{aligned} \tag{A.22}$$

$$\frac{\partial g_1}{\partial \rho_i} = 1. \tag{A.23}$$

These equations are implemented in the GCMMA algorithm.

Remark. In order to obtain output motions in the second and third quadrant, an additional constraint such as $g_2(\boldsymbol{\rho}) = -\mathrm{sgn}(u_{spec1})\, u_{out1} \leq 0$ needs to be added. Otherwise, it cannot be distinguished between $\boldsymbol{u}_{spec} = (1;-1)^T$ and $\boldsymbol{u}_{spec} = (-1;1)^T$, or $\boldsymbol{u}_{spec} = (1;1)^T$ and $\boldsymbol{u}_{spec} = (-1;-1)^T$ due to the appearance of u_{spec1}^2, u_{spec2}^2 and $u_{spec1}\, u_{spec2}$ in Eq. (A.19).

A.4 Specified output motion path

The objective function and the constraint equations are calculated based on the displacements $\boldsymbol{u}_{out}$, $\boldsymbol{v}$ and $\boldsymbol{v}_{\perp}$ caused by the real load $\boldsymbol{f}_{in}$, dummy load $\boldsymbol{f}_{out}$ and perpendicular dummy load $\boldsymbol{f}_{out,\perp}$, and the specified motion path $\boldsymbol{u}_{spec}$:

$$\begin{aligned} g_0(\boldsymbol{\rho}) &= u_{out}(\boldsymbol{\rho}) \\ &= \left(\left(\boldsymbol{v}^{\boldsymbol{T}} \boldsymbol{K}\ \boldsymbol{u} \right)^2 + \left(\boldsymbol{v}_{\perp}^{\boldsymbol{T}} \boldsymbol{K}\ \boldsymbol{u} \right)^2 \right)^{\frac{1}{2}}, \qquad \text{(A.24)} \\ g_1(\boldsymbol{\rho}) &= \left(\boldsymbol{u}_{spec} - \boldsymbol{u}_{out} \right)^2 - \epsilon \leq 0 \\ &= \left(f\left(\boldsymbol{v}^{\boldsymbol{T}} \boldsymbol{K}\ \boldsymbol{u} \right) - \boldsymbol{v}_{\perp}^{\boldsymbol{T}} \boldsymbol{K}\ \boldsymbol{u}\ \right)^2 - \epsilon, \qquad \text{(A.25)} \\ g_2(\boldsymbol{\rho}) &= \sum_{e=1}^{N} \left(\rho_e - V \right) \leq 0. \qquad \text{(A.26)} \end{aligned}$$

The corresponding sensitivities can be calculated as

$$\frac{\partial g_0}{\partial \rho_i} = \left(u_{out,1}^2 + u_{out,2}^2 \right)^{-\frac{1}{2}} \cdot p \rho_i^{p-1} \left(u_{out,1} \boldsymbol{v_i^T K_i}\ \boldsymbol{u_i} + u_{out,2} \boldsymbol{v_{\perp i}^T K_i}\ \boldsymbol{u_i} \right), \qquad \text{(A.27)}$$

$$\frac{\partial g_1}{\partial \rho_i} = 2 \cdot \left(f(u_{out,1}) - u_{out,2} \right) \cdot \left(\frac{\partial f(u_{out,1})}{\partial \rho_i} + p \rho_i^{p-1} \boldsymbol{v_{\perp i}^T K_i}\ \boldsymbol{u_i} \right) \qquad \text{(A.28)}$$

$$\begin{aligned} &\text{e.g. for } f(u_{out,1}) = -u_{out,1}^2 \\ &= -2 \cdot \left(+u_{out,1}^2 + u_{out,2} \right) \cdot p \rho_i^{p-1} (2 u_{out,1} \boldsymbol{v_i^T K_i}\ \boldsymbol{u_i} + \boldsymbol{v_{\perp i}^T K_i}\ \boldsymbol{u_i}), \qquad \text{(A.29)} \end{aligned}$$

$$\frac{\partial g_2}{\partial \rho_i} = 1. \qquad \text{(A.30)}$$

The Eq. (A.24)-(A.30) are implemented in the GCMMA algorithm.

A.5 Further results on topology optimization

In Table A.1 - Table A.5, further results of the staggered topology optimization process based on specified output motions as discussed in Sect. 3.3.4.3 are listed.

Table A.1: Output displacements $\boldsymbol{u}_{out}$ and relative errors for optimization problem (3.111) and (3.112) for different specified output motions $\boldsymbol{u}_{spec}$

# of FE [–]	$u_{spec1} : u_{spec2}$ [–]	u_{out1}^{Stagg} [μm]	u_{out2}^{Stagg} [μm]	$u_{out1}^{Stagg} : u_{out2}^{Stagg}$ [–]	Parasitic error [–]
400	100:1	93.36	0.93	100.01	0.0%
900	100:1	83.16	0.85	97.95	-2.1%
1,600	100:1	87.57	0.88	99.67	-0.3%
2,500	100:1	90.87	0.83	108.87	8.9%
3,600	100:1	67.56	0.66	101.82	1.8%
4,900	100:1	87.25	0.87	100.01	0.0%
6,400	100:1	99.98	1.02	97.93	-2.1%
8,100	100:1	93.52	0.94	99.98	0.0%
10,000	100:1	2.28	0.02	99.82	-0.2%
400	10:1	1.89	0.19	10.00	0.0%
900	10:1	97.42	9.76	9.99	-0.1%
1,600	10:1	114.37	11.45	9.99	-0.1%
2,500	10:1	0.95	0.09	10.04	0.4%
3,600	10:1	-146.51	-14.66	10.00	0.0%
4,900	10:1	79.28	7.86	10.09	0.9%
6,400	10:1	75.11	7.51	10.00	0.0%
8,100	10:1	0.07	0.01	9.99	-0.1%
10,000	10:1	95.26	9.53	9.99	-0.1%
400	3:1	1.21	0.40	3.00	0.0%
900	3:1	64.10	21.38	3.00	-0.1%
1,600	3:1	27.54	9.18	3.00	0.0%
2,500	3:1	20.40	6.80	3.00	0.0%
3,600	3:1	14.31	4.76	3.00	0.1%
4,900	3:1	7.52	2.51	3.00	0.0%
6,400	3:1	2.18	0.73	3.00	0.0%
8,100	3:1	47.51	15.85	3.00	-0.1%
10,000	3:1	4.97	1.66	3.00	-0.1%

Table A.2: Output displacements $\boldsymbol{u}_{out}$ and relative errors for optimization problem (3.111) and (3.112) for different specified output motions $\boldsymbol{u}_{spec}$

# of FE [−]	$u_{spec1} : u_{spec2}$ [−]	u_{out1}^{Stagg} [μm]	u_{out2}^{Stagg} [μm]	$u_{out1}^{Stagg} : u_{out2}^{Stagg}$ [−]	Parasitic error [−]
400	1:1	60.48	58.69	1.03	3.0%
900	1:1	69.08	69.09	1.00	0.0%
1,600	1:1	2.35	2.42	0.97	-2.7%
2,500	1:1	56.33	56.33	1.00	0.0%
3,600	1:1	38.76	39.67	0.98	-2.3%
4,900	1:1	51.39	51.38	1.00	0.0%
6,400	1:1	0.03	0.03	1.00	0.1%
8,100	1:1	10.40	10.40	1.00	0.0%
10,000	1:1	61.17	61.16	1.00	0.0%
400	1:3	-3.97	-11.61	0.34	2.5%
900	1:3	2.98	8.93	0.33	0.0%
1,600	1:3	1.80	5.36	0.34	0.5%
2,500	1:3	10.72	32.15	0.33	0.0%
3,600	1:3	1.02	3.05	0.33	0.0%
4,900	1:3	11.35	34.11	0.33	-0.1%
6,400	1:3	0.85	2.56	0.33	0.0%
8,100	1:3	12.48	37.44	0.33	0.0%
10,000	1:3	16.04	48.15	0.33	-0.1%
400	1:10	3.44	34.45	0.10	0.0%
900	1:10	1.94	19.56	0.10	-0.8%
1,600	1:10	0.30	2.87	0.10	4.3%
2,500	1:10	0.00	0.03	0.10	0.9%
3,600	1:10	3.12	31.23	0.10	-0.1%
4,900	1:10	1.43	14.33	0.10	0.0%
6,400	1:10	-3.70	-36.67	0.10	0.8%
8,100	1:10	4.35	44.04	0.10	-1.1%
10,000	1:10	3.61	36.11	0.10	0.0%

Table A.3: Output displacements $\boldsymbol{u}_{out}$ and relative errors for optimization problem (3.111) and (3.112) for different specified output motions $\boldsymbol{u}_{spec}$

# of FE [–]	$u_{spec1} : u_{spec2}$ [–]	u_{out1}^{Stagg} [μm]	u_{out2}^{Stagg} [μm]	$u_{out1}^{Stagg} : u_{out2}^{Stagg}$ [–]	Parasitic error [–]
400	1:100	-0.14	-14.29	0.01	0.8%
900	1:100	0.00	0.02	0.01	0.2%
1,600	1:100	0.39	39.06	0.01	-1.2%
2,500	1:100	0.00	0.02	0.01	11.0%
3,600	1:100	0.00	0.02	0.01	11.8%
4,900	1:100	0.21	25.68	0.01	-16.8%
6,400	1:100	0.38	38.56	0.01	-0.2%
8,100	1:100	0.00	0.13	0.01	8.0%
10,000	1:100	0.36	34.74	0.01	3.1%
400	100:-1	69.84	-0.70	-100.13	0.1%
900	100:-1	0.26	0.00	-100.06	0.1%
1,600	100:-1	72.06	-0.72	-99.99	0.0%
2,500	100:-1	0.57	-0.01	-99.70	-0.3%
3,600	100:-1	65.01	-0.65	-100.15	0.1%
4,900	100:-1	1.10	-0.01	-100.02	0.0%
6,400	100:-1	77.75	-0.75	-103.41	3.4%
8,100	100:-1	23.72	-0.24	-98.19	-1.8%
10,000	100:-1	70.80	-0.71	-100.12	0.1%
400	10:-1	44.95	-4.49	-10.00	0.0%
900	10:-1	61.16	-6.15	-9.94	-0.6%
1,600	10:-1	43.37	-4.33	-10.01	0.1%
2,500	10:-1	0.09	-0.01	-10.00	0.0%
3,600	10:-1	50.27	-5.03	-10.00	0.0%
4,900	10:-1	55.24	-5.49	-10.05	0.5%
6,400	10:-1	41.87	-4.13	-10.15	1.5%
8,100	10:-1	51.18	-5.14	-9.95	-0.5%
10,000	10:-1	55.34	-5.53	-10.01	0.1%

Table A.4: Output displacements $\boldsymbol{u}_{out}$ and relative errors for optimization problem (3.111) and (3.112) for different specified output motions $\boldsymbol{u}_{spec}$

# of FE [–]	$u_{spec1} : u_{spec2}$ [–]	u_{out1}^{Stagg} [μm]	u_{out2}^{Stagg} [μm]	$u_{out1}^{Stagg} : u_{out2}^{Stagg}$ [–]	Parasitic error [–]
400	3:-1	20.05	-6.67	-3.01	0.2%
900	3:-1	27.20	-9.08	-3.00	-0.1%
1,600	3:-1	10.64	-4.33	-2.46	-18.1%
2,500	3:-1	32.96	-10.98	-3.00	0.0%
3,600	3:-1	25.25	-8.42	-3.00	0.0%
4,900	3:-1	29.63	-9.88	-3.00	0.0%
6,400	3:-1	32.95	-10.98	-3.00	0.1%
8,100	3:-1	34.58	-11.53	-3.00	0.0%
10,000	3:-1	30.31	-10.10	-3.00	0.0%
400	1:-1	12.79	-12.80	-1.00	0.0%
900	1:-1	26.34	-26.33	-1.00	0.0%
1,600	1:-1	32.59	-32.60	-1.00	0.0%
2,500	1:-1	25.29	-25.30	-1.00	0.0%
3,600	1:-1	30.92	-30.61	-1.01	1.0%
4,900	1:-1	41.17	-41.20	-1.00	-0.1%
6,400	1:-1	38.74	-38.74	-1.00	0.0%
8,100	1:-1	41.82	-41.81	-1.00	0.0%
10,000	1:-1	38.07	-37.83	-1.01	0.6%
400	1:-3	7.51	-22.55	-0.33	0.0%
900	1:-3	7.25	-21.76	-0.33	0.0%
1,600	1:-3	17.85	-53.54	-0.33	0.0%
2,500	1:-3	9.73	-29.05	-0.33	0.4%
3,600	1:-3	14.83	-44.49	-0.33	0.0%
4,900	1:-3	16.00	-47.54	-0.34	0.9%
6,400	1:-3	10.41	-31.24	-0.33	0.0%
8,100	1:-3	16.10	-48.28	-0.33	0.0%
10,000	1:-3	14.91	-44.72	-0.33	0.0%

Table A.5: Output displacements $\boldsymbol{u}_{out}$ and relative errors for optimization problem (3.111) and (3.112) for different specified output motions $\boldsymbol{u}_{spec}$

# of FE [−]	$u_{spec1} : u_{spec2}$ [−]	u_{out1}^{Stagg} [μm]	u_{out2}^{Stagg} [μm]	$u_{out1}^{Stagg} : u_{out2}^{Stagg}$ [−]	Parasitic error [−]
400	1:-10	3.95	-38.88	-0.10	1.7%
900	1:-10	3.13	-31.26	-0.10	0.0%
1,600	1:-10	-3.42	34.23	-0.10	0.0%
2,500	1:-10	-3.11	31.38	-0.10	-0.9%
3,600	1:-10	-0.09	0.93	-0.10	0.0%
4,900	1:-10	5.07	-51.21	-0.10	-1.0%
6,400	1:-10	-3.45	34.45	-0.10	0.0%
8,100	1:-10	-3.14	31.37	-0.10	0.0%
10,000	1:-10	-2.98	30.11	-0.10	-1.0%
400	1:-100	0.19	-17.57	-0.01	8.0%
900	1:-100	-0.02	2.30	-0.01	-8.6%
1,600	1:-100	-0.11	10.64	-0.01	4.6%
2,500	1:-100	-0.38	39.27	-0.01	-2.3%
3,600	1:-100	-0.31	31.08	-0.01	-1.6%
4,900	1:-100	0.00	0.02	-0.01	-0.7%
6,400	1:-100	0.00	-0.11	-0.01	20.1%
8,100	1:-100	0.00	0.30	-0.01	-0.9%
10,000	1:-100	-0.32	32.22	-0.01	-2.1%

A.6 Displacements of parabolic and circular flexure hinges

$$
\begin{aligned}
w(x) = {} & \frac{3}{20c_1^2 b\left(-c_2^2+4c_1c_3\right)^{5/2}(c_1+x(c_2+c_3x))E}\Bigg\{ \\
& \bar{M}_y \cdot \Bigg[\frac{\left[1-100c_1^2 b\left(c_2^2-4c_1c_3\right)^3 x(c_1+x(c_2+c_3x))\left(2c_1^2c_3(3c_2-2c_3x)-c_2^3x(c_2+c_3x)+c_1c_2c_3x(11c_2+10c_3x)\right)E\right]}{20c_1^2 b\left(-c_2^2+4c_1c_3\right)^{5/2}(c_1+x(c_2+c_3x))E} \\
& +60c_1^2c_3(c_2+2c_3x)(c_1+x(c_2+c_3x))\left(\operatorname{ArcTan}\left[\frac{c_2}{\sqrt{-c_2^2+4c_1c_3}}\right]-\operatorname{ArcTan}\left[\frac{c_2+2c_3x}{\sqrt{-c_2^2+4c_1c_3}}\right]\right)\Bigg] \\
& +\bar{F}_y \cdot \Bigg[5\sqrt{-c_2^2+4c_1c_3x}\left(-4c_1^3c_3+c_2^3lx(c_2+c_3x)-c_1c_2x(c_2(c_2+11c_3l)+c_3(c_2+10c_3l)x)-2c_1^2\left(c_2^2+2c_3^2x(-l+2x)+c_2c_3(3l+4x)\right)\right) \\
& -4c_1^2(c_1+x(c_2+c_3x))\left(15c_2c_3(l+x)+4c_2^4(1+\nu)+c_2^2(5-32c_1c_3(1+\nu))+2c_3\left(5c_1+15c_3lx+32c_1^2c_3(1+\nu)\right)\right) \\
& \left(\operatorname{ArcTan}\left[\frac{c_2}{\sqrt{-c_2^2+4c_1c_3}}\right]-\operatorname{ArcTan}\left[\frac{c_2+2c_3x}{\sqrt{-c_2^2+4c_1c_3}}\right]\right)\Bigg]\Bigg\}
\end{aligned}
\tag{A.31}
$$

$$
\begin{aligned}
\psi(x) = &-\frac{3}{4c_1^2 b\left(-c_2^2+4c_1c_3\right)^{5/2}(c_1+x(c_2+c_3x))^2E}\Bigg\{\\
&\bar{M}_y\cdot\Bigg[-\sqrt{-c_2^2+4c_1c_3}x\left(20c_1^3c_3^2+c_2^3x(c_2+c_3x)^2-2c_1^2c_3\left(8c_2^2+c_2c_3x-6c_3^2x^2\right)+2c_1c_2(c_2+c_3x)\left(c_2^2-5c_2c_3x-5c_3^2x^2\right)\right)\\
&\quad+24c_1^2c_3^2(c_1+x(c_2+c_3x))^2\left(\text{ArcTan}\left[\frac{c_2}{\sqrt{-c_2^2+4c_1c_3}}\right]-\text{ArcTan}\left[\frac{c_2+2c_3x}{\sqrt{-c_2^2+4c_1c_3}}\right]\right)\Bigg]\\
&+\bar{F}_z\cdot\Bigg[\sqrt{-c_2^2+4c_1c_3}x\left(2c_1^3c_3(-3c_2+10c_3l-8c_3x)+c_2^3lx(c_2+c_3x)^2-c_1c_2(c_2+c_3x)\left(-2c_2^2l+c_2(c_2+10c_3l)x+c_3(c_2+10c_3l)x^2\right)\right.\\
&\quad\left.+c_1^2c_3\left(4c_3^2(3l-2x)x^2-c_2^2(16l+x)-2c_2c_3x(l+5x)\right)\right)+12c_1^2c_3(c_2+2c_3l)(c_1+x(c_2+c_3x))^2\\
&\quad\left(-\text{ArcTan}\left[\frac{c_2}{\sqrt{-c_2^2+4c_1c_3}}\right]+\text{ArcTan}\left[\frac{c_2+2c_3x}{\sqrt{-c_2^2+4c_1c_3}}\right]\right)\Bigg]\Bigg\}
\end{aligned}
\tag{A.32}
$$

$$
\begin{aligned}
u(x,z) &= \psi^T(x)\cdot z+\int_0^x\frac{F_x(u_{out})}{E\cdot A(u_{out})}\,\mathrm{c}_3u_{out}\\
&= \psi^T(x)\cdot z+\bar{F}_x\cdot\frac{\left(-\text{ArcTan}\left[\frac{c_2}{\sqrt{-c_2^2+4c_1c_3}}\right]+\text{ArcTan}\left[\frac{c_2+2c_3x}{\sqrt{-c_2^2+4c_1c_3}}\right]\right)}{b\sqrt{-c_2^2+4c_1c_3}E}
\end{aligned}
\tag{A.33}
$$

A.7 Taylor expansion on circular flexure hinges

In order to avoid mathematically inconvenient root terms, a Taylor expansion of $t_C(x)$ given in Eq. (4.3) at $x_0 = \frac{l}{2} = x_M$ is beneficial. Since differentiability is given, the general form can be written as

$$t_C(x) = \sum_{j=0}^{\infty} \frac{t_k^{(j)}(x_M)}{k!} \cdot (x - x_M)^j. \tag{A.34}$$

The Taylor expansion for $n_{Taylor} = 2$ yields

$$t_C(x) = (-2r + 2z_M) + \frac{(x - x_M)^2}{r} + \mathcal{O}(x - x_M)^3, \tag{A.35}$$

where third order terms (and higher) $\mathcal{O}(x - x_M)^3$are neglected leading to

$$t_{C,2}(x) = (-2r + 2z_M) + \frac{(x - x_M)^2}{r}, \tag{A.36}$$

which equals t_P with the following parameters

$$a = z_M - r + \frac{x_M^2}{2r}, \qquad c = \frac{-x_M}{r}, \qquad d = \frac{1}{2r}, \tag{A.37}$$

In order to check the error, i.e. the residuum $\mathcal{O}(x - x_M)^{n_{Taylor}+1} = R_n(x, x_0)$, the Lagrange polynomials are further considered

$$R_{n_{Taylor}}(x, x_0) = \frac{1}{(n_{Taylor} + 1)!} \cdot (x - x_0)^{(n_{Taylor}+1)} \cdot t_k^{(n_{Taylor}+1)}(z), \tag{A.38}$$

which leads in the case of $n_{Taylor} = 2$ at $x_0 = x_M$ to

$$\begin{aligned} R_2(x, x_M) &= \frac{1}{3!} \cdot (x - x_M)^3 \cdot t_C^{(3)}(z) \\ &= \frac{1}{3!} \cdot (x - x_M)^3 \cdot \frac{6r^2(x - x_M)}{((r + x - x_M)(r - x + x_M))^{5/2}}. \end{aligned} \tag{A.39}$$

The (absolute) maximum residuum can be found at $x = 0$ und $z = 0$ by

$$|R_2(0, x_M)| = |R_{2,max}| \leq \frac{1}{3!} \cdot |x_M|^3 \cdot |\frac{6r^2 x_M}{((r - x_M)(r + x_M))^{5/2}}|, \tag{A.40}$$

Substituting r and x_M results in

$$|R_{2,max}| \leq |\frac{4l^4\left(l^2+(H-t_s)^2\right)^2(H-t_s)^3}{(H^2-l^2-2Ht_s+t_s^2)^5}|, \tag{A.41}$$

which is further simplified since $H > t_s$ to

$$|R_{2,max}| \leq |\frac{4l^4\left(l^2+H^2\right)^2H^3}{(H^2-l^2)^5}|. \tag{A.42}$$

It can be noted, that the residuum increases for $H \approx l$. In order to calculate the overall error, an integrated formulations is introduced

$$R_n(x) = \int_{x_0}^{x} \frac{(x-t)^n}{n!} \cdot t_k^{(n+1)}(t)\,\mathrm{d}t, \tag{A.43}$$

which becomes for $n_{Taylor} = 2$

$$\begin{aligned} R_2(x) =& -\frac{(x-x_m)^2+2r\left(-r+\sqrt{(r+x-x_m)(r-x+x_m)}\right)}{r} \\ =& \frac{1}{2}\left(H+\frac{l^2}{H-t_s}-\frac{2(l-2x)^2(H-t_s)}{l^2+(H-t_s)^2}-t_s\right. \\ & \left.-\frac{\sqrt{16lx(H-t_s)^2-16x^2(H-t_s)^2+(H^2-l^2-2Ht_s+t_s^2)^2}}{H-t_s}\right) \end{aligned} \tag{A.44}$$

Example A.7.1. *The maximum overall error of a Taylor expanded, circular FH with the geometric properties*

$$l = 8\,\mathrm{mm} \qquad H = 10\,\mathrm{mm} \qquad t_s = 1\,\mathrm{mm}$$

is to be evaluated.

Substituting these values into Eq. (A.44) *results in a maximum residuum* $R_2(0) = 3.1\,\mathrm{mm}$ *with* $x = 0$*, i.e. an relative thickness error of approx. 30% at the beginning of the circular FH.*

Clearly, the occurring errors can not be neglected at the first sight. However, the mathematical convenience of the Taylor expanded expressions outweighs the occurring errors at the "thick" edges of the FH, since the approximation at the more relevant, "thinnest" cross section in the center of the FH remains excellent.

B Curriculum vitae

Professional background

Senior Technical Officer (2012 – present)
Federal Armed Forces of Germany

Research Assistant, Ph.D. candidate (2009 – 2012)
Helmut-Schmidt-University/
University of the Federal Armed Forces Hamburg, Germany

Visiting Research Scholar (2009, 2010, 2011)
University of California, Berkeley, USA

Aircraft Technical Officer (2002 – 2009)
Federal Armed Forces of Germany

Educational background

Master of Science in Mechanical Engineering (2006 – 2007)
University of California, Berkeley, USA

Diplom-Ingenieur in Computational Engineering (2003 – 2007)
Helmut-Schmidt-University/
University of the Federal Armed Forces Hamburg, Germany

General qualification for university entrance (1993 – 2002)
Europagymnasium "Richard von Weizsäcker", Thale, Germany

Awards and honors

Elected for NATO International Logistics programme (2013)
NATO Support Agency, Luxembourg

Honor for outstanding achievement (2012)
German Joint Forces Command

Post-graduate Research Scholarship Award (2010)
German Academic Exchange Service

Best Diploma of the year / Böttcher Award (2007)
Helmut-Schmidt-University/
University of the Federal Armed Forces Hamburg, Germany

Honor for outstanding academic achievement (2007)
German Joint Forces Command

Graduate Study Scholarship Award (2006/07)
German Academic Exchange Service

Best Pre-Diploma of the year / Pre-Diploma Award (2005)
Helmut-Schmidt-University/
University of the Federal Armed Forces Hamburg, Germany

Miscellaneous

Appointed reviewer
Precision Engineering, Elsevier (2013 – present)
Mechanical Sciences (2011 – present)

Date and place of birth
December 10, 1982 in Meißen, Germany

C List of own publications and presentations

Selected peer-reviewed publications

1. **F. Dirksen**, M. Anselmann, T.I. Zohdi, R. Lammering
   Incorporation of flexural hinge fatigue-life cycle criteria into the topological design of compliant small-scale devices,
   Precision Engineering, Elsevier, Vol. 37, No. 3, 531-541, 2013.

2. **F. Dirksen**, T. Berg, R. Lammering, T.I. Zohdi
   Topology synthesis of large-displacement compliant mechanisms with specific output motion paths, Proceedings of Applied Mathematics and Mechanics, Wiley-VCH Verlag, Vol. 12, No.1, 801-804, 2012.

3. **F. Dirksen**, R. Lammering
   On mechanical properties of planar flexure hinges of compliant mechanisms, Special Issue – Future directions in compliant mechanisms, Mechanical Sciences, Vol. 2, No. 1, 109-117, 2011.

4. **F. Dirksen**, T.I. Zohdi
   On Effective Energy Reflectance of Particulate Materials, International Journal of Fracture, Springer, Vol. 145, No. 4, 341-347, 2007.

Selected academic presentations

1. **F. Dirksen**
   (Chair of Computational Mechanics Session)
   Structural Optimization of Large-Displacement, Path-Following Compliant Mechanisms with Optimally Designed Flexure Hinges,
   8th European Solid Mechanics Conference, Graz, Austria, 2012.

2. **F. Dirksen**, T. Berg, R. Lammering, T.I. Zohdi
   (Invited speaker in Structural Optimization Session)
   Topology synthesis of large-displacement compliant mechanisms with specific output motion paths,
   GAMM, Darmstadt, Germany, 2012.

3. **F. Dirksen**
   Systematic Design of Compliant Mechanisms with optimized flexure hinges to prevent fatigue failure,
   DFG SPP 1476, Dresden, Germany, 2012.

4. **F. Dirksen**
   On mechanical properties of planar flexure hinges for topology optimization purposes of compliant mechanisms,
   2nd International Symposium on Compliant Mechanisms, Delft, The Netherlands, 2011.

5. **F. Dirksen**
   Non-intuitive Design and Optimization of Compliant Mechanisms,
   DFG SPP 1476, Braunschweig, Germany, 2011.

6. **F. Dirksen**
   Non-intuitive Design and Optimization of Compliant Mechanisms,
   University of California, Berkeley, USA, 2010.